Modelling and simulation of the movement of thin structures in a viscous fluid : application to the muco-ciliary transport

Loïc Lacouture

Université Paris-Saclay

École doctorale de mathématiques Hadamard (EDMH, ED 574)

Établissement d'inscription : Université Paris-Sud

Laboratoire d'accueil : Laboratoire de mathématiques d'Orsay, UMR 8628 CNRS

THÈSE DE DOCTORAT ÈS MATHÉMATIQUES

Spécialité : Mathématiques appliquées

Loïc LACOUTURE

Modélisation et simulation du mouvement de structures fines dans un fluide visqueux : application au transport mucociliaire

Date et lieu de soutenance : jeudi 23 juin 2016 à Orsay.

Après avis favorables des rapporteurs : Franck BOYER (Toulouse)
Emmanuel MAITRE (Grenoble)

Jury de soutenance :

Franck BOYER	(Toulouse) Rapporteur
Astrid DECOENE	(Orsay) Codirectrice de thèse
Angelo IOLLO	(Bordeaux) Examinateur
Emmanuel MAITRE	(Grenoble) Rapporteur
Sébastien MARTIN	(Paris) Codirecteur de thèse
Bertrand MAURY	(Orsay) Codirecteur de thèse
Philippe PONCET	(Pau) Président du jury

NNT : 2016SACLS139

Thèse préparée sous la direction d'Astrid Decoene,
de Sébastien Martin et de Bertrand Maury,
au Laboratoire de Mathématiques d'Orsay (CNRS-UMR 8628)
équipe "Analyse numérique et équations aux dérivées partielles"
Université Paris-Sud,
91405 Orsay Cedex

À Lana, ma filleule née le même jour que cette thèse

Remerciements

Mes premiers remerciements vont à mes directeurs de thèse. Merci Bertrand de m'avoir proposé ce sujet passionnant, et merci pour tes nombreuses et précieuses idées qui m'ont permis d'avancer chaque fois que j'en avais besoin. C'est toi aussi qui m'a dirigé vers Astrid et Sébastien. Je vous remercie chaleureusement tous les deux pour votre encadrement complémentaire qui a été très bénéfique pour moi. Vous avez toujours été très disponibles, sans compter les heures, et avez répondu à (toutes) mes questions et incertitudes. Je vous suis profondément reconnaissant pour votre indéfectible soutien tant au niveau enseignement et recherche qu'au niveau personnel. Je n'aurais pas pu espérer meilleurs directeurs de thèse, et ce à tous les niveaux.

J'adresse mes plus sincères remerciements à Franck Boyer et Emmanuel Maitre qui ont eu la gentillesse de rapporter cette thèse. Desidero ringraziare Angelo Iollo per avere accetato di fare parte della commissione, et je remercie aussi Philippe Poncet de me faire l'honneur de complèter ce jury.

Je remercie tous ceux avec qui j'ai eu l'occasion de collaborer durant ces quatres années, à commencer par les membres de l'équipe ANEDP du Laboratoire de Mathématiques d'Orsay. Je remercie en particulier Loïc Gouarin avec qui j'ai longuement travaillé pendant ma thèse et sans qui je n'aurais jamais pu me familiariser avec le code CAFES. Je le remercie aussi pour l'ensemble de ses interventions lors de mes nombreux "soucis informatiques", remerciements qu'il partagera avec Sylvain Faure que j'ai embêté au moins aussi souvent que lui. J'en profite pour remercier également Frédéric Lagoutière avec qui j'ai eu le plaisir de partager la majeure partie de l'enseignement pendant mon monitorat, et qui m'a peut-être plus appris sur le cours de "Mécanique et Modélisation" que nous en avons appris aux étudiants.

Je remercie l'ensemble de l'équipe du MAP5 qui m'a si bien accueilli lors de cette quatrième et dernière année de thèse. À cet égard, je remercie en particulier Annie Raoult et Clémence Misseboukpo qui ont largement œuvré en ma faveur. J'y ai trouvé une équipe pédagogique fort sympathique et avec qui ce fut un plaisir d'enseigner.

La liste de mes collaborateurs ne serait pas complète si je ne remerciais pas Silvia Bertoluzza. Merci Silvia pour l'intérêt que tu as porté à notre travail et surtout le rôle clé que tu as joué dans la résolution de notre problème.

Je remercie Nathalie, Valérie, Catherine, Estelle, Florence et Marie-Hélène, qui ont rendu les tâches administratives beaucoup moins pénibles et chronophages.

Parce qu'un cadre de travail serein et agréable est plus que nécessaire pour préparer une thèse dans de bonnes conditions, je remercie l'ensemble de mes collègues doctorants et docteurs d'Orsay et du MAP5. Les moments les plus difficiles ont vite été effacés par la bonne ambiance et la cohésion des différents bureaux. Un merci spécial à mon petit frère de thèse Fabien avec qui j'aurais dû travailler mais que je laisse de toute façon entre de bonnes mains.

Merci à Émi♡♡lie pour notre "duo de choc" au séminaire des doctorants.

Un grand merci à Céline et Mélina qui diront sans doute qu'elles n'ont "rien fait du tout", mais dont les conseils avisés m'ont permis de si bien réussir mon audition de PRAG.

Je tiens à remercier l'ensemble de mes amis du basket et du tennis. Dès mon arrivée à Paris pour le basket, et un peu plus tard quand je me suis mis au tennis, j'ai trouvé comme une deuxième famille, si bien que mes longues soirées de rédaction où je n'ai pas pu vous voir cette dernière année, comme j'avais l'habitude de le faire avant, ont été d'autant plus difficiles pour moi. Malgré tout, votre soutien et votre compréhension auront été sans faille. Des remerciements particuliers pour Éric, Pascal, Paulo et Vincent dont le brunch du dimanche midi va me manquer. Je remercie aussi le groupe Anne-Laure, David, Massimo et les deux Nicolas pour les soirées plus folles les unes que les autres, et surtout Grégoire pour tout ce que tu m'as apporté. J'ajouterai Élodie et Justine, mon duo de rousses préféré, et Clémence avec qui je refaisais le monde régulièrement. Enfin, je remercie Élise et Morty pour ce qu'elles sont pour moi, et sans qui les vacances de Noël et d'été ne seraient pas pareilles. Bref, je remercie toute la sphère non mathématique qui m'entoure, qui ne comprend pas grand chose à ce que je fais ("Tu l'as démontré à qui le théorème ?") mais qui m'apporte l'équilibre dont j'ai besoin.

Je voudrais aussi remercier ma famille au grand complet. En particulier ma marraine, avec qui j'ai tant partagé, des soirées théâtre aux fêtes de Mont De quand j'étais censé lire et/ou rédiger des articles, et ma sœur, que je ne peux dissocier de mes deux nièces Jade et Lana, ou devrais-je dire mes "bouffées d'oxygène" à chaque fois que je redescends en vacances. Vos encouragements répétés ont eu beaucoup plus de poids que vous ne l'imaginez tout au long de mes (longues) études. Je remercie aussi mes cousins, Carole et Benjamin, dont les messages de soutien à chacune des étapes importantes m'ont toujours fait du bien (et je ne parle même pas des parties endiablées de tarot !). Enfin mes parents, vous m'avez toujours fait confiance, et je suis fier de pouvoir aujourd'hui vous raconter mon charabia.

Last but not least, mes derniers remerciements sont pour Christèle. Difficile de résumer en quelques lignes tout ce que tu m'as apporté chaque jour pendant ma thèse, merci d'être toi, tout simplement.

Modélisation et simulation du mouvement de structures fines dans un fluide visqueux : application au transport mucociliaire

Résumé

Une grande part des muqueuses à l'intérieur du corps humain sont recouvertes de cils qui, par leurs mouvements coordonnés, conduisent à une circulation de la couche de fluide nappant la muqueuse. Dans le cas de la paroi interne des bronches, ce processus permet l'évacuation des impuretés inspirées à l'extérieur de l'appareil respiratoire.

Dans cette thèse, nous nous intéressons aux effets du ou des cils sur le fluide, en nous plaçant à l'échelle du cil, et on considère pour cela les équations de Stokes incompressible. Due à la finesse du cil, une simulation directe demanderait un raffinement important du maillage au voisinage du cil, pour un maillage qui évoluerait à chaque pas de temps. Cette approche étant trop onéreuse en terme de coûts de calculs, nous avons considéré l'asymptotique d'un diamètre du cil tendant vers 0 et d'une vitesse qui tend vers l'infini : le cil est modélisé par un Dirac linéique de forces en terme source. Nous avons montré qu'il était possible de remplacer ce Dirac linéique par une somme de Dirac ponctuels distribués le long du cil. Ainsi, nous nous sommes ramenés, par linéarité, à étudier le problème de Stokes avec en terme source une force ponctuelle. Si les calculs sont ainsi simplifiés (et leurs coûts réduits), le problème final est lui plus singulier, ce qui motive une analyse numérique fine et l'élaboration d'une nouvelle méthode de résolution.

Nous avons d'abord étudié une version scalaire de ce problème : le problème de Poisson avec une masse de Dirac en second membre. La solution exacte étant singulière, la solution éléments finis est à définir avec précaution. La convergence de la méthode étant dégradée dans ce cas-là, par rapport à celle dans le cas régulier, nous nous sommes intéressés à des estimations locales. Nous avons démontré une convergence quasi-optimale en norme H^s ($s \geqslant 1$) sur un sous-domaine qui exclut la singularité. Des résultats analogues ont été obtenus dans le cas du problème de Stokes.

Pour palier les problèmes liés à une mauvais convergence sur l'ensemble du domaine, nous avons élaboré une méthode pour résoudre des problème elliptiques avec une masse de Dirac ou une force ponctuelle en terme source. Basée sur celle des éléments finis standard, elle s'appuie sur la connaissance explicite de la singularité de la solution exacte. Une fois données la position de chacun des cils et leur paramétrisation, notre méthode rend possible la simulation directe en 3d d'un très grand nombre de cils. Nous l'avons donc appliquée au cas du transport mucociliaire dans les poumons. Cet outil numérique nous donne accès à des informations que l'on ne peut avoir par l'expérience, et permet de simuler des cas pathologiques comme par exemple une distribution éparse des cils.

Mots clés

Problèmes de Poisson et de Stokes, mesures de Dirac, éléments finis, estimations d'erreur locales, cils, transport mucociliaire.

Modelling and computing of the movement of thin structures in a viscous fluid: application to the muco-ciliary transport

Abstract

Numerous mucous membranes inside the human body are covered with cilia which, by their coordinated movements, lead to a circulation of the layer of fluid coating the mucous membrane, which allows, for example, in the case of the internal wall of the bronchi, the evacuation of the impurities inspired outside the respiratory system.

In this thesis, we integrate the effects of the cilia on the fluid, at the scale of the cilium. For this, we consider the incompressible Stokes equations. Due to the very small thickness of the cilia, the direct computation would request a time-varying mesh grading around the cilia. To avoid too prohibitive computational costs, we consider the asymptotic of a zero diameter cilium with an infinite velocity: the cilium is modelled by a lineic Dirac of force in source term. In order to ease the computations, the lineic Dirac of forces can be approached by a sum of punctual Dirac masses distributed along the cilium. Thus, by linearity, we have switched our initial problem with the Stokes problem with a punctual force in source term. Thus, we simplify the computations, but the final problem is more singular than the initial problem. The loss of regularity involves a deeper numerical analysis and the development of a new method to solve the problem.

We have first studied a scalar version of this problem: Poisson problem with a Dirac right-hand side. The exact solution is singular, therefore the finite element solution has to be defined with caution. In this case, the convergence is not as good as in the regular case, and thus we focused on local error estimates. We have proved a quasi-optimal convergence in H^1-norm ($s \leqslant 1$) on a sub-domain which does not contain the singularity. Similar results have been shown for the Stokes problem too.

In order to recover an optimal convergence on the whole domain, we have developped a numerical method to solve elliptic problems with a Dirac mass or a punctual force in source term. It is based on the standard finite element method and the explicit knowledge of the singularity of the exact solution. Given the positions of the cilia and their parametrisations, this method permits to compute in 3d a very high number of cilia. We have applied this to the study of the mucociliary transport in the lung. This numerical tool gives us information we do not have with the experimentations and pathologies can be computed and studied by this way, like for example a small number of cilia.

Keywords

Poisson and Stokes problems, Dirac measures, finite element methods, local error estimates, cilia, muco-ciliary transport.

TABLE DES MATIÈRES

INTRODUCTION

Une grande part des muqueuses à l'intérieur du corps humain sont recouvertes de cils qui, par leurs mouvements coordonnés, conduisent à une circulation de la couche de fluide nappant la muqueuse. Dans le cas de la paroi interne des bronches, ce processus permet l'évacuation des impuretés inspirées à l'extérieur de l'appareil respiratoire : c'est la clairance mucociliaire (on parle aussi de transport mucociliaire). L'efficacité du transport est basée sur l'interaction entre les cils et le fluide environnant, ce qui rend complexe la modélisation mathématique de ce phénomène biologique. Mais mieux comprendre la rhéologie du système est capital pour l'étude de cas pathologiques, telle la mucoviscidose. La thèse porte sur la simulation directe en 3D du mouvement de cils dans un fluide visqueux. Par simulation directe, nous entendons prise en compte des mécanismes à l'échelle où ils se produisent, à savoir celle du cil. L'objectif est de décrire en détail le mouvement d'un ou plusieurs cils en interaction avec le fluide environnant, en se basant sur l'observation que le cil est une structure fine dont la fréquence de battement est très grande. Nous nous plaçons donc dans l'asymptotique où le rapport entre épaisseur et longueur du cil tend vers 0, mais où la résultante de la force appliquée par les cils sur le fluide reste constante. Cette approche conduit à l'étude de problèmes mathématiques singuliers, motivant une analyse numérique fine et l'élaboration d'une nouvelle méthode de résolution. L'enjeu est de développer un outil numérique pour la simulation du transport mucociliaire, capable en particulier de simuler un très grand nombre de cils battant dans un fluide complexe. Cet outil permettrait de mieux comprendre les mécanismes mis en jeu, et en jouant sur les différents paramètres, d'évaluer leur influence sur l'efficacité du processus de transport. Ce travail a bénéficié d'un financement public Investissement d'avenir, référence ANR-11-LABX-0056-LMH, LabEx LMH (Laboratoire de Mathématiques Hadamard).

Présentation du problème

Dans les poumons, la paroi des bronches est recouverte d'un film liquide visqueux dont le rôle est double :

- il capture les impuretés inhalées et les fait remonter le long des bronches, puis le long de la trachée, d'où elles basculent dans l'œsophage et sont éliminées dans l'estomac.
- il protège la paroi des bronches des agents pathogènes (particules de pollution, bactéries, etc.).

Ce film protecteur est composé de deux couches superposées. La première, contre la paroi des bronches, est la couche périciliaire (PCL, pour *periciliary layer* en anglais), essentiellement composée d'eau. Le mucus, la couche en contact avec l'air, est composé d'eau et de lipides, les mucines. Ces deux fluides forment une barrière d'une dizaine de micromètres d'épaisseur. Les impuretées piégées dans le mucus sont transportées hors de l'appareil respiratoire grâce à des cils baignant essentiellement dans la couche périciliaire, et dont le battement permet la propulsion du mucus vers le haut de la trachée (voir Figure 1 pour une photo des cils). L'ensemble de ce mécanisme est appelé clairance mucociliaire (ou transport mucociliaire).

Une des grandes difficultés dans l'étude du transport mucociliaire est le manque de données expérimentales. La structure dyadique de l'arbre bronchique rend impossible les mesures *in vivo* à partir de la sixième génération. Par ailleurs, ces mesures sont très peu précises car les techniques employées sont souvent trop invasives. La culture *in vitro* de cils n'est pas plus facile à cause de la dégradation du matériel biologique vivant après prélèvement [64]. C'est pourquoi il est intéressant de développer un outil numérique donnant accès à des mesures de vitesses par exemple, que l'on ne peut que difficilement obtenir via l'expérience.

Une autre difficulté provient des différentes échelles de longueur que l'on peut considérer : moléculaire, ciliaire, bronchiale, etc. La Figure 1 illustre les différentes échelles mises en jeu.

Enfin, la complexité structurelle du transport mucociliaire rend son étude mathématique difficile. Beaucoup de paramètres sont à prendre en compte :

- le fluide nappant la paroi des bronches n'est pas homogène, il est composé de deux fluides de viscosités très différentes (le mucus est 50 fois plus visqueux que la couche périciliaire), et donc la dynamique de l'interface entre ces deux fluides peut faire l'objet d'une étude approfondie.
- les cils sont très fins, donc difficiles à prendre en compte numériquement, et la fréquence de battement est élevée.
- l'interaction entre l'air inspiré ou expiré et le mucus, sachant que les deux phénomènes ont des échelles de temps caractéristiques très différentes : les cils battent à une fréquence de l'ordre de 15Hz tandis que la fréquence de la respiration est de l'ordre de 0.25Hz.
- l'influence des agents pathogènes piégés dans le mucus qui peut aboutir à une modification de la rhéologie de l'écoulement bifluide.

Les travaux théoriques et numériques foisonnent sur le sujet et, malgré tout, la simulation du transport mucociliaire reste un enjeu important. La complexité du processus, dont

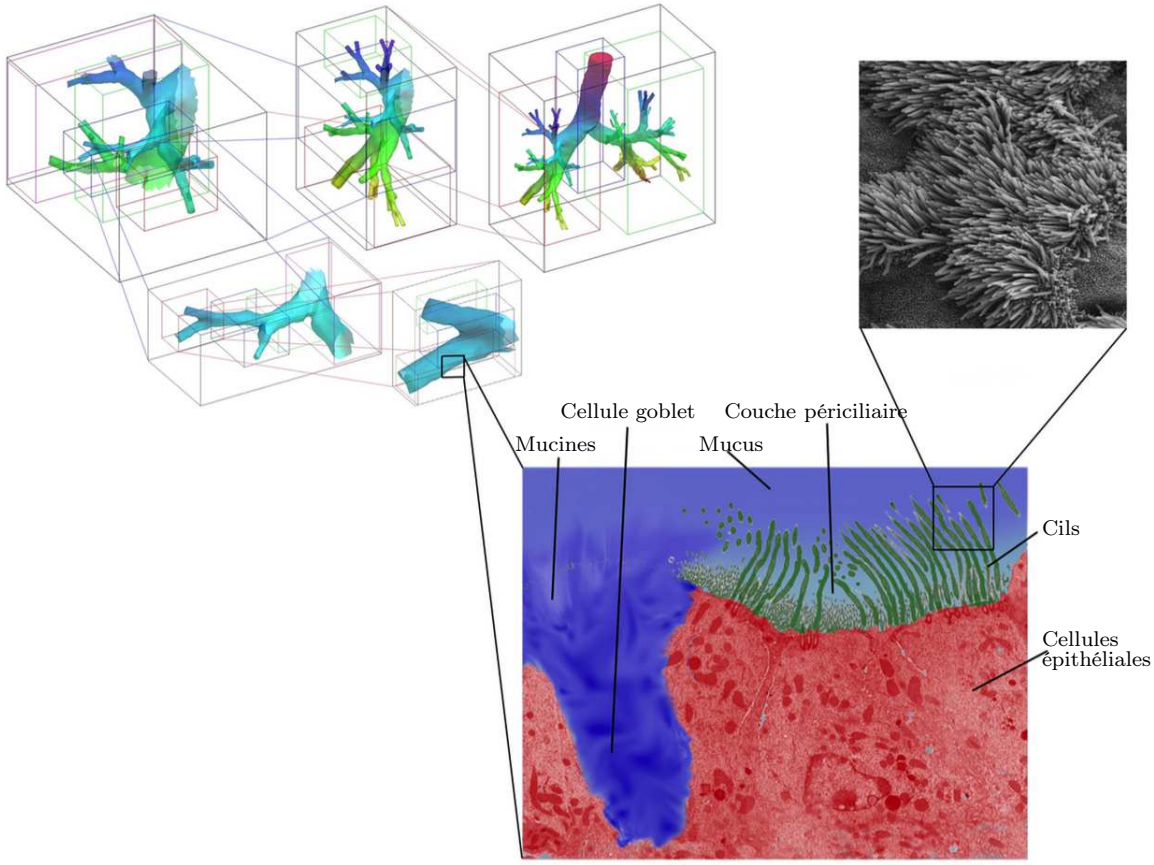

FIGURE 1: Schéma multi-échelle du poumon humain, des premières générations de bronches ($\simeq$ 1 cm) aux cellules épithéliales ($\simeq$ 5 μm). Adapté à partir de [30].

une liste non exhaustive des difficultés est donnée ci-dessus, rend le modèle numérique complet hors de portée des scientifiques à l'heure actuelle [29]. Dès lors, la compréhension du processus requiert une combinaison de méthodes qui incluent la modélisation mathématique, l'analyse des problèmes résultants et le calcul scientifique. Des modèles très différents mais complémentaires ont été proposés par les différentes auteurs, voir [108] pour en avoir une synthèse détaillée.

L'objectif de la thèse est la simulation directe en 3D du mouvement d'un très grand nombre de cils dans un écoulement bifluide. La modélisation présentée dans la section suivante est guidée par la volonté de limiter les coûts de calculs, qui peuvent vite devenir exhorbitants, tout en essayant de faire le minimum d'hypothèses possible.

Choix du modèle

Comme expliqué précédemment, il n'est pas raisonnable (voire impossible) de prendre en compte toute la complexité du problème. Il est donc important de bien construire son modèle, et pour cela, des hypothèses doivent être formulées.

Modèle fluide. Dans la littérature, les gens s'accordent sur le fait que la couche périciliaire est essentiellement de l'eau et a donc un comportement newtonien, même si cette affirmation a récemment été mise en cause par Boucher [17]. En revanche, pour le mucus, les modèles proposés peuvent être très différents : du modèle newtonien [30], au modèle viscoélastique [86, 107], et même parfois un fluide viscoplastique [37]. Pour notre modèle, nous avons choisi de considérer un fluide newtonien, pour la couche périciliaire et pour le mucus. Cependant, nous tenons compte de la différence de viscosité entre les deux fluides, et modélisons l'ensemble par un modèle bifluide, dont l'interface entre les deux fluides est supposée plane et invariante (voir Figure 2). Cette hypothèse se vérifie expérimentalement [96] et a été confirmée par les simulations [40], même si cette hypothèse peut être relaxée.

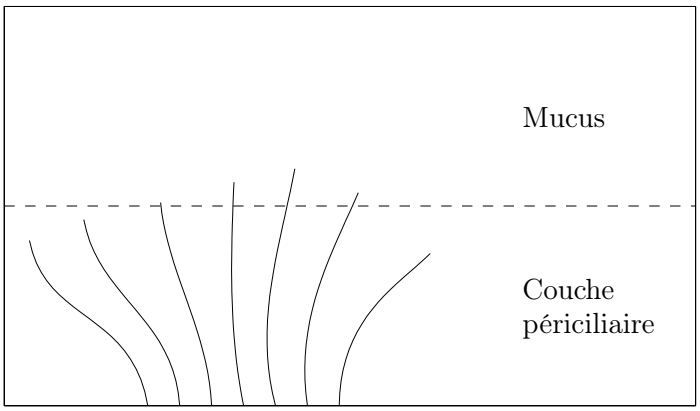

FIGURE 2: Bifluide.

La modélisation de l'écoulement d'un fluide newtonien incompressible et homogène conduit aux équations de Navier-Stokes

$$\left\{ \begin{array}{rcl} \rho \left(\dfrac{\partial \mathbf{u}}{\partial t} + \mathrm{div}(\mathbf{u} \otimes \mathbf{u}) \right) - \mu \triangle \mathbf{u} + \nabla p & = & \mathbf{F}_e, \\ \mathrm{div}(\mathbf{u}) & = & 0, \end{array} \right.$$

où ρ est la masse volumique, $\mathbf{u}$ la vitesse, μ la viscosité, p la pression et $\mathbf{F}_e$ les forces extérieures qui s'exercent sur le fluide. La première équation correspond à la conservation de la quantité de mouvement, et la seconde à la conservation de la masse. Dans sa forme adimensionnée, la première équation s'écrit

$$Re \left(\frac{\partial \widetilde{\mathbf{u}}}{\partial \widetilde{t}} + \mathrm{div}(\widetilde{\mathbf{u}} \otimes \widetilde{\mathbf{u}}) \right) - \triangle \widetilde{\mathbf{u}} + \nabla \widetilde{p} = \widetilde{\mathbf{F}}_e$$

où $\widetilde{\mathbf{u}}$, $\widetilde{t}$, $\widetilde{p}$ et $\widetilde{\mathbf{F}}_e$ sont les quantités correspondantes sans dimensions, et Re est le nombre de Reynolds :

$$Re = \frac{\rho L U}{\mu},$$

avec L et U respectivement la longueur et la vitesse caractéristiques de l'écoulement. Contrairement au nageur humain, pour lequel on a $Re \sim 10^6$, la longueur caractéristique dans le cas du transport mucociliaire est le micromètre et la vitesse le micromètre par seconde, de sorte que le nombre de Reynolds est de l'ordre de 10^{-6}, rendant ainsi les termes inertiels négligeables dans les équations de Navier-Stokes. On considère donc les équations de Stokes

$$\begin{cases} -\mu\triangle\mathbf{u} + \nabla p &= \mathbf{F}_e, \\ \operatorname{div}(\mathbf{u}) &= 0. \end{cases}$$

Ces équations étant complètement réversibles en temps, les cils bronchiques doivent produire un battement non réversible en temps sous peine d'avoir un effet moyen nul sur le fluide au cours d'une période.

Modèle pour le cil. Le but de cette thèse est de simuler en 3D et de manière directe toute une forêt de cils bronchiques, pour mesurer leur effet sur le mucus. La faisabilité des calculs, autrement dit éviter des coûts numériques exhorbitants, constitue notre ligne de conduite dans le choix du modèle pour le cil. Les deux modèles, dits de "cils discrets", les plus intuitifs sont :

- le domaine fluide exclut les cils, et on impose des conditions d'adhérence sur le bord de chaque cil $\mathbf{u}_{fluide} = \mathbf{u}_{cil}$.
- on immerge les cils dans le fluide, et on traite les cils par pénalisation en posant dans le volume du cil $\mathbf{u}_{fluide} = \mathbf{u}_{cil}$.

Dans les deux modèles décrits ci-dessus, le maillage doit être très précis au niveau des cils pour pouvoir prendre en compte les effets des cils et leur structure. Comme le cil est très fin, un raffinement de maillage est nécessaire au niveau du cil. Si la simulation de quelques cils en 3D est envisageable, il devient compliqué de simuler toute une forêt de cils. De plus, le premier modèle exige la construction d'un nouveau maillage à chaque pas de temps, ce qui devient vite très coûteux, là où le second modelè autorise un maillage cartésien fixe au cours des itérations en temps. Toujours dans l'objectif de limiter au maximum les coûts de calculs, nous avons choisi de considérer une nouvelle approche. En partant du constat que les cils battent très vite et qu'ils sont très fins, nous nous plaçons dans l'asymptotique où la vitesse du cil tend vers l'infini pendant que le diamètre du cil tend vers 0. À la limite, il reste du cil une distribution linéique de forces, portée par l'axe central du cil. Pour des raisons purement numériques, car il est plus facile d'évaluer une fonction en un point que de l'intégrer le long d'une courbe, nous avons approché cette distribution linéique de forces par une somme de forces ponctuelles distribuées le long du cil (voir Figure 3). Les liens entre ces modèles seront discutés dans ce manuscrit. Dans cette étude, on s'intéresse à l'écoulement produit par des cils dont le battement et la fréquence sont imposés.

Paramétrisation du cil. Pour compléter ce modèle, il reste à définir les x_i, points où sont localisées les forces ponctuelles, ainsi que les c_i, intensité de ces forces ponctuelles. En d'autres termes, on doit choisir une paramétrisation du cil et définir la force en chaque point du cil. La paramétrisation que nous avons choisie a été établie par Fulford

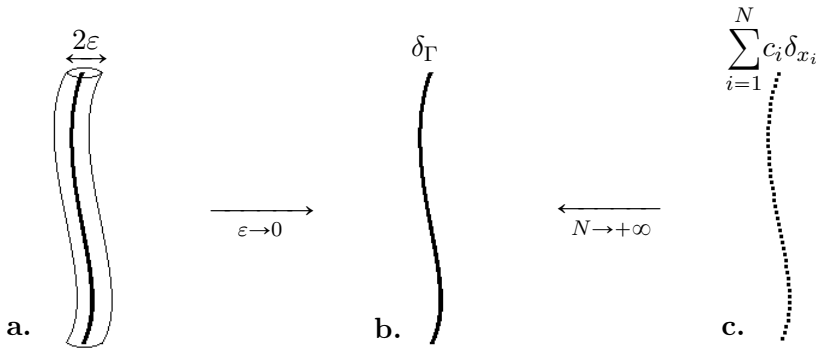

FIGURE 3: Modélisation du cil : **a.** Cil volumique de rayon ε et de force ε^{-2}, de sorte que la masse totale reste constante quand ε tend vers 0. **b.** Distribution linéique de forces portée par la courbe Γ du cil. **c.** Une somme de N forces ponctuelles distribuées le long du cil.

et Blake [48]. C'est une décompositon en série de Fourier du battement de cil à partir d'images obtenues par Sanderson et Sleigh [96]. Plus précisément, à chaque pas de temps t, le cil est représenté par la courbe paramétrée

$$\boldsymbol{\xi}(s,t) = L\left[\frac{1}{2}\mathbf{a}_0(s) + \sum_{n=1}^{6} \mathbf{a}_n(s)\cos(2n\pi ft) + \mathbf{b}_n(s)\sin(2n\pi ft)\right],$$

où s est la longueur d'arc depuis la base du cil, L et f sont respectivement la longueur et la fréquence de battement du cil. Les coefficients de Fourier $\mathbf{a}_n$, $\mathbf{b}_n$ sont des vecteurs polynomiaux de degré 3 en s.

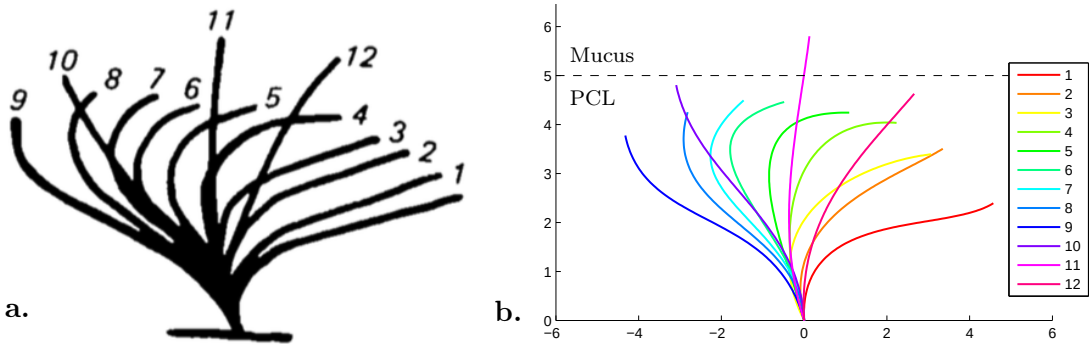

FIGURE 4: Trajectoire d'un cil pendant un battement. **a.** Description faite par Sanderson et Sleigh [96]. **b.** Paramétrisation établie par Fulford et Blake [48].

La Figure 4 illustre bien la correspondance entre les travaux expérimentaux [96] et les travaux théoriques [48] concernant la description du battement d'un cil bronchique. On peut déjà remarquer que le cil traverse l'interface mucus-couche périciliaire à l'aller, pendant la phase effective, mais reste complètement immergé pendant la phase de retour. Cette remarque est primordiale : le mouvement du cil n'est pas à moyenne nulle, ce qui est accentué par cette pénétration du cil dans le mucus, l'irréversibilité en temps étant nécessaire dans un fluide de Stokes pour permettre un transport du mucus efficace.

Paramétrisation d'une forêt de cils. L'article de Fulford et Blake [48] indique aussi comment paramétrer toute une forêt de cils. Deux paramètres sont à prendre en compte : l'espacement ℓ_0 entre deux cils et la longueur d'onde λ de l'onde métachronale qui naît de la synchonisation des cils. Considérons une forêt de $n_x \times n_y$ cils, où n_x et n_y sont respectivement les nombres de cils dans les direction x et y, le cil (i, j) est représenté par

$$\boldsymbol{\xi}_{i,j}(s,t) = i\ell_0\mathbf{e}_x + j\ell_0\mathbf{e}_y + \boldsymbol{\xi}\left(s, \frac{i\ell_0}{f\lambda} + t\right),$$

Dans notre modèle, comme c'est toujours le cas dans la littérature, on supposera que cette onde métachronale se propage seulement dans la direction du transport de mucus (direction x), mais dans le sens opposé.

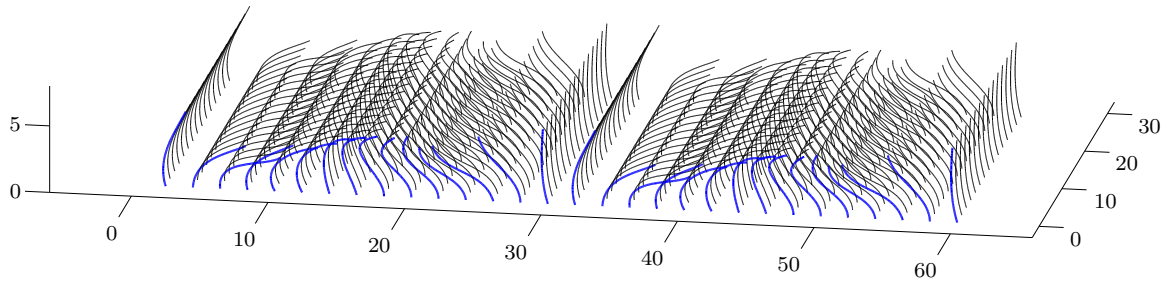

FIGURE 5: Dessin en 3D d'une forêt de cils (avec $\ell_0 = 2\mu$m au lieu de 0.3μm).

Distribution de forces le long du cil. Pour définir la distribution de forces le long du cil, deux options s'offrent à nous : la première est la "resistive-force theory", développée par Gray et Hancock [53] dans le cas de flagelles, qui suppose que la force hydrodynamique est proportionnelle à la vitesse locale du cil, mais cette théorie reste inconsistante dans le cas où les effets visqueux sont dominants [74] ; la seconde, que nous avons choisie, est la "slender-body theory". Notre modèle est dû à Cox [36] qui a établi un développement asymptotique de la force lorsque le rapport L/r_0 tend vers l'infini (longueur du cil divisée par son rayon). Toujours en notant $\boldsymbol{\xi}$ la paramétrisation du cil, l'expression de la force en chaque point est approchée par

$$\mathbf{f}(s,t) = \frac{2\pi\mu}{\ln(L/r_0)}\left(2\mathbb{I}_3 - \frac{\dot{\boldsymbol{\xi}}(s,t)\otimes\dot{\boldsymbol{\xi}}(s,t)}{\|\dot{\boldsymbol{\xi}}(s,t)\|^2}\right)\mathbf{u}_{\text{cil}}(s,t),$$

où $\dot{\boldsymbol{\xi}}$ est la dérivée de $\boldsymbol{\xi}$ par rapport à s et $\mathbf{u}_{\text{cil}}$ est la dérivée par rapport à t. Cette expression a été établie en confrontant deux approches : la première consiste à considérer la vitesse tellement proche du cil qu'on distingue son rayon mais sa longueur L paraît tendre vers l'infini ; la seconde au contraire considère la vitesse loin du cil, sa longueur est donc finie mais son diamètre paraît nul tellement il est fin. Dans les deux cas, le rapport L/r_0 tend vers l'infini.

Conditions aux bords. Nous allons maintenant fixer les conditions aux bords. La boîte de calcul que l'on considère est un parallèlépipède rectangle dont le bord inférieur

correspond à la paroi des bronches et la bord supérieur à l'interface entre le mucus et l'air. On suppose que la couche périciliaire adhère à la paroi des bronches, donc on y impose une vitesse nulle. Comme c'est souvent le cas dans les divers travaux menés sur le sujet, on suppose que la surface supérieure du mucus reste plane, ce qu'on modélise par une condition de non sortie du fluide et un glissement sans frottements (on néglige les effets de l'air sur le mucus). À l'échelle des cils, la fenêtre de calcul se focalise sur une longueur d'onde de l'onde métachronale, c'est-à-dire une centaine de cils. Les conditions aux bords les plus naturelles dans la direction du transport du mucus et celle qui lui est perpendiculaire sont donc des conditions bipériodiques, de façon à prendre en compte le battement des cils à l'extérieur de la boîte. Les conditions aux bords considérées sont rassemblées en Figure 6.

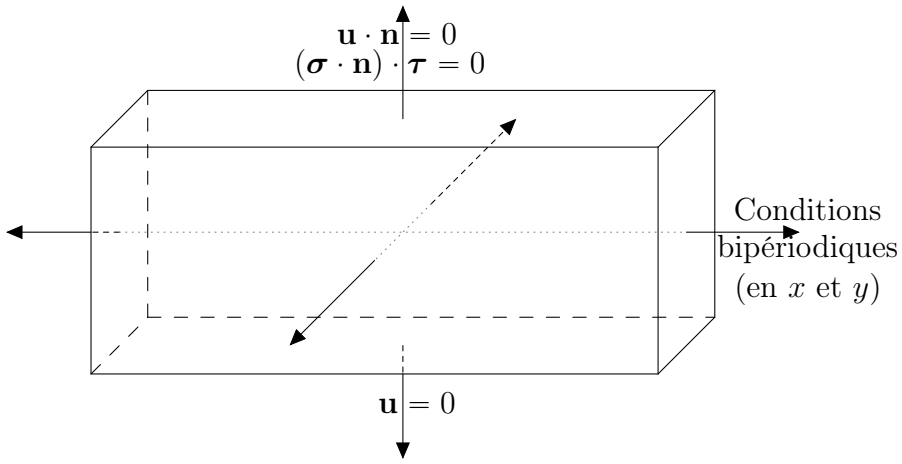

FIGURE 6: Illustration of the boundary conditions.

Problème mathématique résultant. Ce paragraphe est la conclusion de l'ensemble de la modélisation présentée précédemment. Le modèle considéré, par linéarité des équations de Stokes, conduit au problème mathématique suivant :

$$\begin{cases} -\mu\triangle\mathbf{u} + \nabla p &= \delta_{\mathbf{x}_0}\mathbf{F} \quad \text{on } \Omega, \\ \operatorname{div}(\mathbf{u}) &= 0 \quad \text{on } \Omega, \\ \mathbf{u} &= 0 \quad \text{on } \partial\Omega, \end{cases} \tag{0.0.1}$$

où $\mathbf{x}_0$ est le point du domaine qui porte la force ponctuelle $\mathbf{F}$. Les conditions aux bords décrites précédemment n'ont pas été prises en compte ici, mais elles le seront lors des calculs. En fait, les conditions aux bords choisies ne changent pas la régularité de la solution du problème résultant, et c'est pourquoi, dans un souci de simplicité et de clarté, l'analyse numérique sera étudiée en considérant des conditions aux bords de type Dirichlet homogènes. De même, si la viscosité variable peut poser des soucis pour la résolution numérique du problème, ce problème est indépendant du problème de la singularité du second membre. Ainsi s'affranchit-on de ces difficultés lors de l'étude théorique du problème de Stokes avec une terme source singulier

Analyse numérique de problèmes elliptiques singuliers

Le modèle présenté au paragraphe précédent a été choisi pour pouvoir simuler de manière directe toute une forêt de cils en 3D. Le modèle permet en effet de s'affranchir des conditions de raffinement de maillage puisqu'un maillage (structuré ou non) peut être envisagé indépendamment du nombre de cils. En contrepartie, un soin extrême doit être apporté à l'analyse numérique du problème résultant qui n'est pas usuel : le terme source du problème de Stokes est une force ponctuelle, terme source singulier en 2D et plus encore en dimension 3. Avant de s'intéresser au problème de Stokes, l'analyse numérique est menée dans le cas du problème de Poisson avec une masse de Dirac en second membre : ce problème est la version scalaire du problème de Stokes et, tout en étant plus simple, plusieurs résultats obtenus dans ce cas sont adaptables au problème de Stokes singulier.

Analyse numérique du problème de Poisson singulier. Le problème que l'on considère est le suivant

$$\begin{cases} -\triangle u &= \delta_{x_0} \quad \text{dans } \Omega \\ u &= 0 \quad \text{sur } \partial\Omega, \end{cases}$$

où Ω est un domaine régulier et x_0 est un point de ce domaine. La solution de ce problème n'étant pas dans $H^2(\Omega)$, les résultats classiques de convergence des méthodes éléments finis ne sont plus garantis, à savoir une convergence à l'ordre 1 en norme $H^1(\Omega)$ et à l'ordre 2 en norme $\mathbb{L}^2(\Omega)$. En fait la solution n'est même pas dans $H^1(\Omega)$, ce qui fait que les méthodes ne sont *a priori* pas définies. Si l'on considère des éléments finis continus (comme c'est très souvent le cas), la solution numérique a bien un sens et on peut alors s'intéresser à la convergence de cette solution numérique vers la solution exacte. Ce problème a largement été étudié dans la littérature. Parmi les résultats principaux on compte celui de Scott [99], qui a montré une convergence en norme $\mathbb{L}^2(\Omega)$ en $h^{d/2}$ où h est la taille caractéristique du maillage et d la dimension. Au moyen d'un raffinement du maillage autour de la singularité, Apel et ses co-auteurs [2] ont recouvré une convergence $\mathbb{L}^2$ à l'ordre 2 en 2D, mais avec un maillage équivalent à du h^2 près de la singularité : ce résultat rejoint celui de Scott mais apporte l'information qu'un raffinement de maillage local seulement suffit.

De notre côté, nous nous sommes intéressés au comportement de la solution numérique "loin" du Dirac, c'est-à-dire que nous avons étudié la convergence de la méthode sur un sous-ensemble Ω_0 qui exclut la singularité. Parallèlement à des travaux de Köppl et Wohlmuth [66], qui ont montré une convergence optimale en norme $\mathbb{L}^2(\Omega_0)$, nous avons prouvé une convergence quasi-optimale en norme $H^s(\Omega_0)$, $s \geqslant 1$. Plus précisément, le résultat que nous avons prouvé en 2D est le suivant :

Theorem. *Soient $\Omega_0 \subset\subset \Omega_1 \subset\subset \Omega$ tels que $x_0 \notin \Omega_1$ et $1 \leqslant s \leqslant k$. On note u la solution du problème de Poisson avec un Dirac en second membre, et u_h sa projection de Galerkin sur l'espace éléments finis V_h^k. Alors, il existe h_1 tel que pour tout $0 < h < h_1$,*

$$\|u - u_h\|_{1,\Omega_0} \leqslant C(\Omega_0, \Omega_1, \Omega) h^k \sqrt{|\ln h|},$$

où k est l'ordre d'approximation de l'espace V_h^k. De plus, pour $s \geqslant 2$, si on suppose en plus que les éléments finis sont H^k-conformes, on a

$$\|u - u_h\|_{s,\Omega_0} \leqslant C(\Omega_0, \Omega_1, \Omega) h^{k+1-s} \sqrt{|\ln h|}.$$

Ce résultat est vrai dès que l'espace éléments finis V_h^k vérifie quelques hypothèses très classiques et vérifiées par une grande classe d'espaces éléments finis, incluant tous les éléments finis définis sur des maillages quasi-uniformes. En particulier, les éléments finis de Lagrange et de Hermite, ou encore les ondelettes vérifient ces hypothèses. Elles sont écrites plus en détail dans le Chapitre 2.

La preuve de ce théorème s'appuie fortement sur le Théorème de Nitsche et Schatz [88], qui donne une estimation de l'erreur locale optimale (comme dans le cas régulier) moyennant l'erreur dans une norme aussi faible que l'on veut. Pour estimer cette erreur en norme faible, nous avons démontré une version faible du Lemme d'Aubin Nitsche. On se ramène alors au contrôle de l'erreur en norme $W^{1,q}(\Omega)$, avec $q < 2$, que l'on obtient grâce à une égalité *inf-sup* discrète.

En 3D, le résultat obtenu n'est plus quasi-optimal puisque la convergence que l'on obtient n'est plus en $h^k\sqrt{|\ln h|}$ mais en $h^{k-1}\sqrt[3]{|\ln h|}^2$. En fait, les arguments donnés en 2D fonctionnent car la solution est dans $W^{1,2-\tau}(\Omega)$, pour tout $\tau > 0$, c'est-à-dire à la limite d'être dans $H^1(\Omega)$. En 3D, la solution est dans $W^{1,3/2-\tau}(\Omega)$, elle est bien plus singulière, et cela suffit à mettre en défaut la preuve présentée en 2D.

Dans le cas particulier des éléments finis de Lagrange $\mathbb{P}_1$, nous avons montré un résultat légèrement plus fort :

$$\|u - u_h\|_{1,\Omega_0} \leqslant C(\Omega_0, \Omega_1, \Omega)h.$$

Ce résultat s'obtient encore grâce au Théorème de Nitsche et Schatz, mais avec d'autres arguments que ceux présentés dans le cas précédents : la clé réside en le fait que les fonctions test sont harmoniques sur chaque maille. Malheureusement, cette preuve ne s'étend ni au cas des éléments finis $\mathbb{P}_k$, $k \geqslant 2$, ni au cas de la dimension 3, ni au problème de Stokes.

Analyse du problème de Stokes singulier. Comme dit dans le préambule de cette partie, certains résultats obtenus dans le cas du problème de Poisson singulier peuvent être montrés dans le cas du problème de Stokes avec une force ponctuelle en terme source. Cette fois-ci encore, la solution n'est pas suffisamment régulière pour espérer une convergence optimale des méthodes éléments finis sur l'ensemble du domaine. À l'image de l'étude menée dans le cas du problème de Poisson, nous nous sommes intéressés aux erreurs locales des méthodes éléments finis classiques, et plus particulièrement aux éléments $\mathbb{P}_k/\mathbb{P}_{k-1}$, pour $k \geqslant 2$, et $\mathbb{P}_1\mathrm{b}/\mathbb{P}_1$ pour le cas $k = 1$. Le résultat que nous avons montré toujours en 2D est le suivant :

Theorem. *Soient $\Omega_0 \subset\subset \Omega_1 \subset\subset \Omega$ tels que $x_0 \notin \Omega_1$, $k \geqslant 1$, $1 \leqslant q < 2$, considérons $(\mathbf{u}, p) \in W_0^{1,q}(\Omega) \times \mathbb{L}_0^q(\Omega)$ la solution du problème de Stokes avec une force ponctuelle en terme source et $(\mathbf{u}_h, p_h)$ sa projection de Galerkin sur l'espace éléments finis $V_h^k \times W_h^k$ telle que $\int_\Omega p_h = 0$ et*

$$\begin{aligned} \int_\Omega \nabla(\mathbf{u} - \mathbf{u}_h) :: \nabla\boldsymbol{\eta} - \int_\Omega (p - p_h)\mathrm{div}(\boldsymbol{\eta}) &= 0 \quad \textit{for all } \boldsymbol{\eta} \in V_h^k, \\ \int_\Omega \mathrm{div}(\mathbf{u} - \mathbf{u}_h)\xi &= 0 \quad \textit{for all } \xi \in W_h^k. \end{aligned}$$

Sous l'hypothèse $(\mathbf{u}, p) \in H^{k+1}(\Omega_1)^2 \times H^k(\Omega_1)$*, il existe* h_1 *tel que pour tout* $0 < h \leqslant h_1$*,*

$$\|\mathbf{u} - \mathbf{u}_h\|_{1,\Omega_0} + \|p - p_h\|_{0,\Omega_0} \leqslant C(\Omega_0, \Omega_1, \Omega) h^k \sqrt{|\ln h|}.$$

La preuve est présentée dans le Chapitre 3. Elle s'appuie sur le Théorème d'Arnold et Liu [4], qui est un résultat équivalent à celui de Nitsche et Schatz, mais pour le problème de Stokes. Bien que l'ajout de la pression complique les choses, le squelette de la preuve est sensiblement le même que dans le cas du problème de Poisson. Quelques généralisations de ce résultat sont données à la suite de la preuve. Cependant, comme dans le cas du problème de Poisson, le second membre étant plus singulier encore, et les estimations obtenues en 3D ne sont plus quasi-optimales.

Une méthode numérique pour la résolution de problèmes elliptiques singuliers

Nous avons prouvé que la convergence des méthodes éléments finis classiques était optimale (ou quasi-optimale) sur un sous-domaine qui exclut la singularité. Mais nous savons aussi que sur l'ensemble du domaine la convergence est mauvaise. Pour pallier ces problèmes de convergence, nous proposons une nouvelle méthode numérique, dite de "soustraction", qui permet de retrouver un ordre de convergence optimal sur l'ensemble du domaine, sans raffinement. Cette méthode est basée sur la constat que, dans le cas de la masse de Dirac ou de la force ponctuelle, on connaît explicitement la singularité. Il suffit alors d'extraire la singularité de la solution et de se ramener à un problème auxiliaire régulier, dont l'analyse numérique conduit à une convergence optimale, quel que soit l'ordre d'approximation des éléments finis considérés.

Par exemple, dans le cas du problème de Stokes, une solution fondamentale est donnée par la Stokeslet $(\mathbf{u}_\delta, p_\delta)$:

$$\begin{cases} -\mu \triangle \mathbf{u}_\delta + \nabla p_\delta &= \delta_{\mathbf{x}_0} \mathbf{F} & \text{dans } \mathbb{R}^d, \\ \operatorname{div}(\mathbf{u}_\delta) &= 0 & \text{dans } \mathbb{R}^d, \end{cases}$$

où d est la dimension de l'espace, et $\mathbf{F}$ la force ponctuelle localisée au point $\mathbf{x}_0$. Pour extraire la singularité de la Stokeslet, concentrée au point $\mathbf{x}_0$, nous allons la multiplier par une fonction plateau χ régulière qui vaut 1 sur un voisinage de $\mathbf{x}_0$. Plus précisément, soient $0 < a < b < \operatorname{dist}(\mathbf{x}_0, \partial\Omega)$:

- χ est supposée régulière, $\chi \in H^{2+k}(\mathbb{R}^d)$.
- χ vaut 1 "près" de $\mathbf{x}_0$, $\chi|_{B(\mathbf{x}_0, a)} = 1$.
- χ vaut 0 "loin" de $\mathbf{x}_0$, $\chi|_{B(\mathbf{x}_0, b)^c} = 0$.

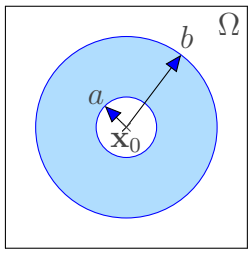

FIGURE 7: Support de χ.

On pose alors $\mathbf{u}_0 = \chi \mathbf{u}_\delta$ et $p_0 = \chi p_\delta$, et on calcule $-\mu\triangle\mathbf{u}_0 + \nabla p_0$ et $\mathrm{div}(\mathbf{u}_0)$:

- sur $B(\mathbf{x}_0, a)$, $\chi = 1$ donc

$$-\mu\triangle\mathbf{u}_0 + \nabla p_0 = -\mu\triangle\mathbf{u}_\delta + \nabla p_\delta = \delta_{\mathbf{x}_0}\mathbf{F} \quad \text{et} \quad \mathrm{div}(\mathbf{u}_0) = \mathrm{div}(\mathbf{u}_\delta) = 0.$$

- sur $B(\mathbf{x}_0, b)^c$, $\chi = 0$ donc

$$-\mu\triangle\mathbf{u}_0 + \nabla p_0 = 0 \quad \text{et} \quad \mathrm{div}(\mathbf{u}_0) = 0.$$

En fait, $(\mathbf{u}_0, p_0)$ est solution de

$$\left\{ \begin{array}{rcll} -\mu\triangle\mathbf{u}_0 + \nabla p_0 & = & \delta_{\mathbf{x}_0}\mathbf{F} + \mathbf{g} & \text{dans } \Omega, \\ \mathrm{div}(\mathbf{u}_0) & = & h & \text{dans } \Omega, \\ \mathbf{u}_0 & = & 0 & \text{sur } \partial\Omega, \end{array} \right.$$

où les termes sources réguliers $\mathbf{g}$ et h sont connus explicitement et à support dans la couronne centrée en $\mathbf{x}_0$, de rayon intérieur a et de rayon extérieur b (voir Figure 7). Ainsi, en notant $(\mathbf{v}, q)$ la solution exacte du problème

$$\left\{ \begin{array}{rcll} -\mu\triangle\mathbf{v} + \nabla q & = & -\mathbf{g} & \text{dans } \Omega, \\ \mathrm{div}(\mathbf{v}) & = & -h & \text{dans } \Omega, \\ \mathbf{v} & = & 0 & \text{sur } \partial\Omega, \end{array} \right.$$

et $\mathbf{v}_h$ la solution numérique associée, on obtient une solution numérique $\mathbf{u}_h$ du problème initial en posant $\mathbf{u}_h = \mathbf{u}_0 + \mathbf{v}_h$. La solution approchée $\mathbf{u}_h$ ainsi définie converge vers la solution exacte $\mathbf{u}$ à l'ordre optimal, quel que soit l'ordre d'approximation des éléments finis utilisés, car l'erreur $\mathbf{u} - \mathbf{u}_h$ est égale à $\mathbf{v} - \mathbf{v}_h$, l'erreur obtenue en résolvant numériquement le problème auxiliaire régulier.

La méthode de soustraction a été présentée dans le cas du problème de Stokes mais peut être généralisée à beaucoup de problèmes elliptiques, dès lors qu'on en connaît une solution fondamentale (exemple : le problème de Poisson). Elle se généralise aussi à d'autres cas de conditions aux bords plus complexes que des conditions de Dirichlet homogènes, comme celles que nous avons fixées pour notre modèle de transport mucociliaire (voir Figure 6). Enfin, la méthode a été décrite dans le cas d'un fluide de viscosité constante, mais peut être facilement adaptée au cas d'un écoulement bifluide.

Simulation directe en 3D d'une forêt de cils

La méthode de soustraction présentée précédemment permet de simuler en 3D et de manière directe toute une forêt de cils : par linéarité du problème de Stokes, considérer une seule force ponctuelle ou un très grand nombre revient au même dans le sens où on ne résout qu'un seul problème numérique à chaque itération en temps. Pour les calculs, nous utilisons le code CAFES, écrit en C/C++ et développé par Benoît Fabrèges pendant sa

thèse en collaboration avec Loïc Gouarin et Bertrand Maury. Le code est notamment utilisé pour sa partie solveur de Stokes parallèle et notre contribution a été l'implémentation de la méthode de soustraction décrite ci-dessus, de la construction du second membre à la correction de la solution numérique obtenue en résolvant le problème auxiliaire régulier.

Nous avons tout d'abord testé la méthode sur le cas modéré d'un petit paquet de cils : 15 dans la direction x et 15 dans la direction y (voir Figure 8). Notons quand même que ce "petit" cas test représente déjà beaucoup plus de cils que ce qu'ont pu considérer certains travaux [40, 71]. Pour ce premier test, on considère un fluide de viscosité constante : l'idée est d'observer la différence d'efficacité du transport pendant les phases effective et de retour des cils (voir Figure 8).

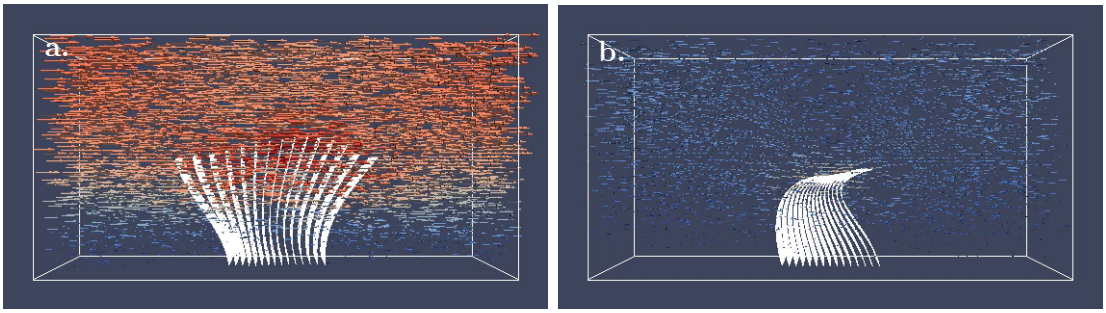

FIGURE 8: Simulation 3D d'une mini forêt. **a.** Phase effective. **b.** Phase de retour.

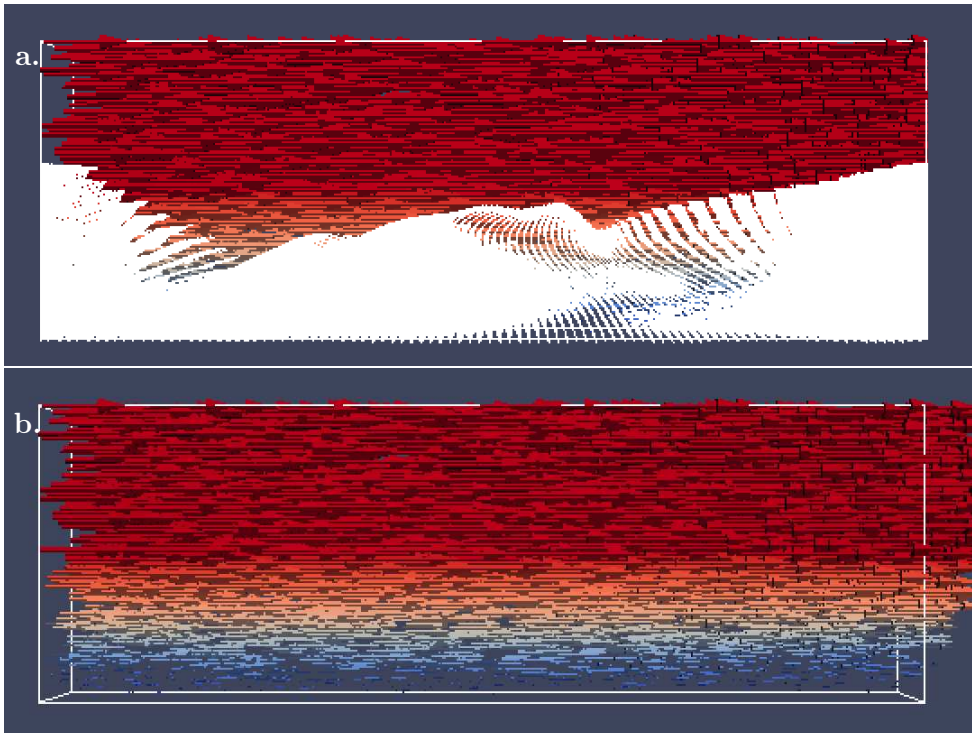

FIGURE 9: Simulation directe en 3D d'une forêt de 6885 cils. **a.** Affichage avec cils. **b.** Affichage sans cils.

Après avoir constaté l'efficacité de la méthode sur quelques centaines de cils, nous

avons testé sa robustesse sur des milliers de cils. Pour le calcul suivant, on se place dans des conditions réelles : simulation directe en 3D d'une forêt de cils complète, battant dans un écoulement bifluide et avec les conditions aux bords réalistes. La Figure 9 illustre ce calcul qui sera en fait le cas témoin auquel les calculs suivants seront comparés. Deux remarques immédiates émergent de ce calcul : le mucus se déplace à vitesse constante tel un "bloc" glissant sur la couche périciliaire, et la vitesse dans la couche périciliaire croît linéairement, comme déjà observé dans divers travaux [84, 108].

L'outil numérique que nous avons développé permet donc non seulement la simulation directe en 3D d'un très grand nombre de cils, mais aussi la simulation de certaines pathologies liées au processus de clairance mucociliaire. Nous avons pu, entre autres, simuler une hauteur de la couche périciliaire anormalement élevée (cas où les cils n'atteignent jamais le mucus), ou au contraire anormalement basse (cas où les cils atteignent le mucus aussi dans la phase de retour). L'influence de la densité de cils a aussi été étudiée, de façon à mesurer les effets de seuil de densité sur l'efficacité du transport.

Plan de la thèse

La thèse porte sur la modélisation et la simulation directe en 3D d'une forêt de cils. Elle est divisée en 4 chapitres, un chapitre de présentation et modélisation, 2 chapitres d'analyse numérique, et un dernier axé calcul scientifique.

Nous commençons le premier chapitre par une présentation d'ensemble du phénomène qui est étudié, à savoir la clairance mucociliaire. Les principales caractéristiques biologiques et mécaniques des cils, du mucus et de la couche périciliaire y sont décrits. Après un état de l'art des différentes études menées sur le sujet, nous y décrivons notre modèle pour le fluide et les cils. La fin du chapitre est consacrée à l'étude théorique de deux problèmes elliptiques singuliers : le problème de Stokes avec une force ponctuelle en terme source, problème résultant de la modélisation choisie, et le problème de Poisson avec une masse de Dirac en second membre, une version scalaire du problème de Stokes singulier.

Le deuxième chapitre est dédié à l'analyse numérique de la résolution du problème de Poisson avec une masse de Dirac en second membre par des méthodes éléments finis classiques. Plus précisément, on montre pour des éléments finis très généraux que la solution numérique converge à l'ordre quasi-optimal sur tout sous-domaine qui exclut la singularité. En d'autres termes, la convergence de la méthode est altérée par la singularité du second membre, mais l'erreur se concentre autour de la singularité, pour une bonne convergence "loin" du Dirac.

Des résultats analogues de convergence sont montrés dans le troisième chapitre dans le cas du problème de Stokes avec une force ponctuelle en terme source. Cette fois-ci, l'étude est menée dans le cas des éléments $\mathbb{P}_k/\mathbb{P}_{k-1}$, pour $k \geqslant 2$, et $\mathbb{P}_1\mathrm{b}/\mathbb{P}_1$ pour le cas $k = 1$, puis généralisée ensuite.

Le quatrième et dernier chapitre est divisé en deux grandes sections. La première présente une nouvelle méthode numérique, dite de soustraction, qui permet de recouvrir une convergence optimale sur l'ensemble du domaine quel que soit l'ordre d'approximation

des éléments. Cette méthode est ensuite généralisée à des cas plus compliqués comme un modèle bifluide, des conditions aux bords non homogènes, etc. La seconde section met en application cette méthode de soustraction et présente les résultats numériques obtenus dans le cas du transport mucociliaire. L'influence de plusieurs facteurs importants est testée comme l'importance de l'écoulement bifluide, la densité de cils ou la hauteur du mucus.

CHAPTER 1

FROM THE MUCOCILIARY TRANSPORT TO THE STOKES PROBLEM

Contents

1.1 Some biological data

1.1.1 The respiratory system

The respiratory system is the largest organ of human body. The volume that it occupies (from 5 to 7 litres) is essentially air. Half a litre is blood and less than another half forms the various tissues. It is composed of:

- the structure areas, among them the rib cage, the diaphragm, intercostal muscles, pleural area...
- the bronchial tree, with the trachea, the bronchi and the bronchioli.
- the respiratory areas formed by the alveoli, where the gaseous exchanges with the blood occur.

Through the breathing process, its role is to supply the body with oxygen (distributed by the blood) and to evacuate the carbon dioxide it products. To help in this process, a maximal air-blood exchange area is necessary: the exchange area is the boundary of a huge collection of small balls (around 300 million units), called *alveoli*, the diameter of which is about a quarter millimeter. That makes an exchange area (membrane of those alveoli) of about 100 m^2. The alveoli are connected to the outside world through the respiratory tract, which has a very particular spatial structure of tree (see Figure 1.1).

Figure 1.1: Bronchial tree mouding, created by E. R. Weibel [117]. Zoom on the little bronchi.

Indeed, the respiratory tract is an assembly of interconnected pipes following a very dyadic-tree structure. The overall tree can be described as follows: the trachea (with a diameter around 2 cm) divides into two sub-branches, which divide further onto smaller branches, and so on, up to around 23 levels of bifurcations. The word “around” is important: the aim is to occupy the whole available space in the rib cage, and some branches stop before the 23rd generation whereas others divide after [118]. The first generations are purely conductive, exchanges do not take place before generation 16 or 17. Beyond

that point, all branches are lined up with alveoli, up to the last generation. With 300 million alveoli, the exchange area is around 100 m^2 in human adults.

As said previously, the exchange area must be sufficiently large to allow the required quantity of oxygen to be transferred by passive diffusion. Therefore preserving the lung from the inhaled impurities is necessary: they could obstruct the bronchi and limit the exchange area. The breathed products which could settle in the bronchopulmonary system are eliminated thanks to three principal mecanisms:

- the cough.
- the mucociliary transport (or mucociliary escalator).
- the alveolar clearance.

Although it is not the aim of this thesis to discuss the mecanism and results of coughing in any detail, the relationship of cough to mucociliary transport deserves a mention. During cough, the respiratory muscles of the rib cage and diaphragm contract to expel air violently from the lungs, and this expulsion is accompagnied by a narrowing of the larger airways and an oscillation of the tissues and linings of the airway wall [72]. Gases may be expelled from the mouth at 10 $L.s^{-1}$ or more, implying gas velocities well in excess of 10 $m.s^{-1}$, even in narrow airways, and estimated speeds in regions of airway compression range as high as 250 $m.s^{-1}$, which is three quarters of the speed of sound.

In a few words, the alveolar clearance is the process during which particles are removed from the alveoli. This clearance can take many forms: phagocytosis by macrophages, elimination of the dust-loaded macrophages towards the ciliated airways, detention in the interstitium and transport to the lymphatic nodes [70].

In this thesis, we focus on the mucociliary transport and its mecanisms.

1.1.2 The mucociliary transport

The lining of the bronchi is napped with a *mucus* film whose role is to catch the inhaled impurities (dust, pollution particles, bacteria, fungus...). The mucus traps the pathogens, reduces microbial access to the epithelial cells, cells which compose the lining of the bronchi, and prevent them from accumulating in the bronchi and obstructing the lung. The mucus and the trapped impurities are transported outside the lung by means of the beat of submerged *cilia*, until the junction with the oesophagus to be eliminated in the stomach.

More precisely, at the scale of the cilium, on the lining of the bronchi (see Figure 1.2) the fluid is biphasic [81]. The lower layer is the *periciliary layer* (commonly called PCL). It contains the cilia. The upper layer is the mucus. The lining epithelium of the respiratory tract is thicker in its upper parts, where it is underlain by a thick submucosal zone [98]. The epithelia of ciliated regions are known to be complex, at least in part: in addition to the easily distinguishable ciliated cells, there are several types of epithelial cells, as described by Jeffrey and Reid [61], among them the goblet cells responsible for secreting

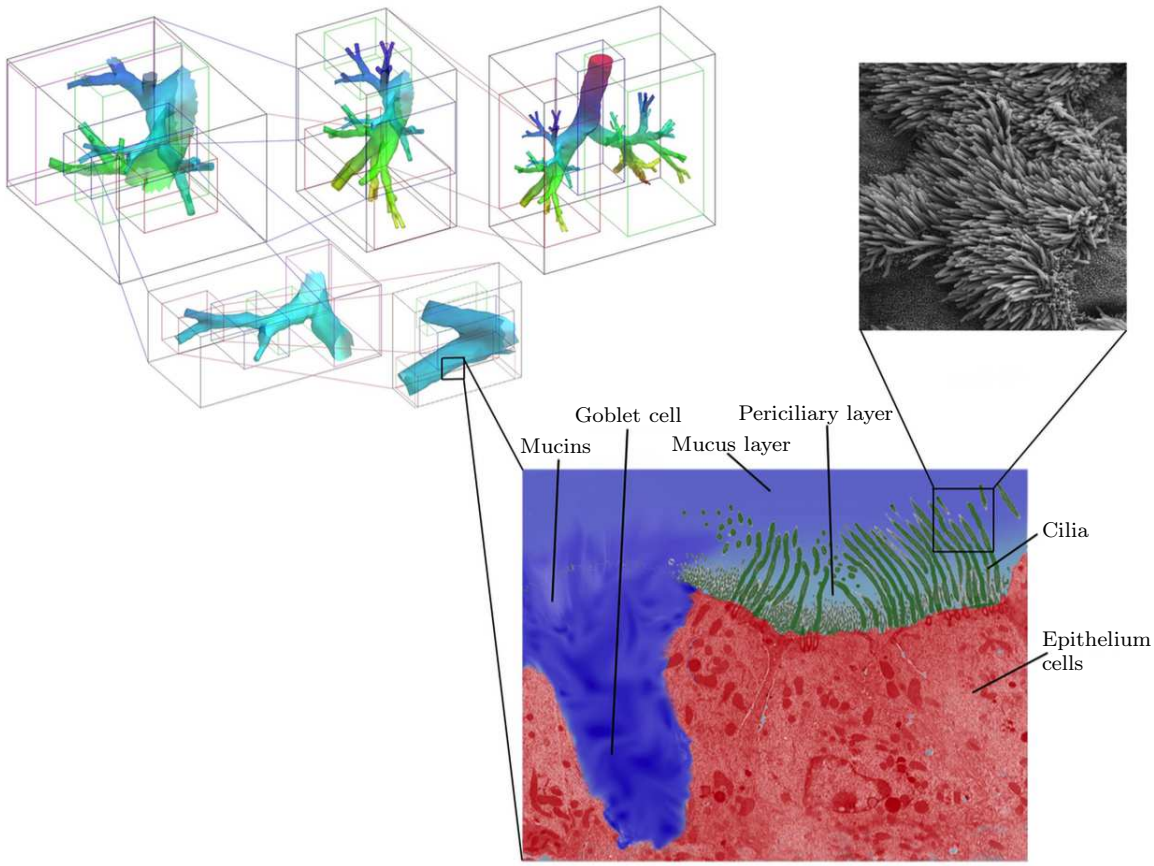

Figure 1.2: Multi-scales schema of human lung, from the trachea and the first generations of bronchi ($\simeq$ 1 cm) to the epithelial cells ($\simeq$ 5 μm). Modified from [30].

the proteins which compose the mucus. In the large airways, the apices of ciliated cells may form a more or less continuous cover at the surface of the epithelium. For instance, the tracheal epithelium may have only 1 goblet cell for every 5 ciliated cells. But, in the smaller airways, the proportion increases and there may be numerous intermediate cells.

Mucociliary transport depends upon a successful relationship between these three components: the cilia, the mucus and the periciliary fluid. The characteristics of transport may be altered by changes in any of these three components, and such changes may be used to regulate transport or changes resulting from disease may interfere with transport. Let us introduce some detailed aspects of the mucociliary transport which is the focus of this work from the mathematical point of view.

1.1.2.1 The mucus

There are two different types of biological fluids: the ones which flow in a closed circuit, like for instance the blood and the lymph, and the ones which flow in an open circuit, like mucus, saliva, sperm... Although the functions of each of these fluids are very different, they are all essentially composed of water and some other specific components: proteins,

cells, nutriments...

Respiratory airway mucus is a complex mixture of several proteins (glycoproteins, proteoglycans, lactoferrin, lysozyme...), lipids and salt [34, 80]. This mixture imparts protective properties to the lung: some proteins enhances the capture of bacteria and reduces microbial access to the epithelia; some remove iron required by many bacteria while others kill these bacteria [33]. Microorganisms are also trapped by the various lipids attached to some proteins, and the more diverse the lipids, the wider their binding properties. Mucus macromolecules absorb many kinds of foreign molecules avidly, and sulphated groups interact with viruses.

The glycoproteins appear to be the most important component conferring viscoelastic properties to the mucus. The rheological behavior of the mucus is important [78, 79, 80]. When cilia beat in water, the rate of flow increases linearly with the force exerted by the cilia because the viscosity remains constant [103]; such fluids show Newtonian behavior. Some other fluids, including mucus, are non-Newtonian and behave as shear-thinning fluids in which the viscosity, although much greater than water, decreases as the applied force is increased, so the more forcefully the cilia beat, the more easily the mucus moves. But mucus has also elastic properties. When it is stretched and released, it may return to near its original shape using energy stored in it by the original deformation, although some energy is also dissipated in overcoming the viscous forces. The time taken to use up the stored energy against viscous resistance is a measure of the relaxation time, which relates the moduli of elasticity and viscosity. Experiments suggest that the relaxation time for mucus is quite long (perhaps 30 s [51]). Thus, when cilia, which beat at rates of 10 to 20 Hz, exert propulsive forces on the mucus, stretching forces are applied to the mucus at much shorter time intervals than the relaxation time. The mucus is therefore seen by the cilia as an elastic structure able to accept efficient energy transfer from the cilia and relaxing very little between successive beats.

It has been observed that the mucus forms a blanket in the larger airways, but is more broken in smaller airways [56, 110]. In the smaller bronchioli, the mucus is present in the form of droplets [58]. These droplets are more numerous in the larger bronchioli and more likely in the larger airways to aggregate into flakes. In the bronchi and the trachea, the mucus seems to be a more continuous sheet. It appears possible that the mucus is normally only secreted in response to stimulation, and that the small droplets, flakes or plaques are bearing away trapped particules, perhaps bacteria or macrophages. Certainly one might expect a larger number of particules to be filtered out by inertial impact against the epithelium in the larger airways, and larger mucous plaques would be required to support them on the ciliary escalator. Let us note that flakes and plaques of mucus are more abundant in many infections and diseases of human respiratory tracts.

Finally, the mucus is the upper layer of the fluid napping the lining of the bronchi. It traps the inhaled impurities and transports them outside the lung. The mucus is a viscoelastic fluid but the relaxation time is long, so that we can model the mucus as a Newtonian viscous fluid.

1.1.2.2 The periciliary layer

The cilia of the respiratory tract beat in a low viscosity periciliary layer whose depth is a little less than the extended ciliary length when mucus is present. Although it is believed that the cilia achieve little net transport of periciliary fluid beneath the mucus, there is no quantitative data. Mathematical modeling suggests that at least the lower part of the periciliary layer shows minimal net flow. Clearly, the layer of fluid immediately below the mucus must flow at the same speed as the mucus, but we do not know anything about the relative depths of these two regions of the periciliary layer. Recently, it has been suggested that a further role of the PCL is to prevent the adherence of epithelial cells with the overlying mucus layer [65].

The activity of cilia may play a part in maintaining and controlling the depth of the periciliary layer. If the periciliary fluid layer becomes too deep, the cilia will be detached from the mucus during their effective strokes (see below), leading to lower transport rates until excess fluid is removed by cilia and they reach the mucus once again. In dry air, the loss of fluid by evaporation may reduce the depth of periciliary fluid and damage the cilia.

1.1.2.3 The cilia

The ciliary component is the best understood of the three components (mucus, periciliary layer and cilia). The first comprehensive account of cilia seems to be due to Sharpey in 1835 [101], who not only gave detailed descriptions of the actions of cilia in a wide variety of animals but also reported the discovery of ciliary motion in the respiratory systems of mammals. Since then a long period of active research, notably by Lucas who studied ciliary function in the upper respiratory tract [81]. As well as providing detailed confirmation of the role of cilia in mucociliary transport, this work led to the important conclusion that mucus is propelled by the tips of the cilia which themselves move in a low viscosity layer beneath the mucus.

Length of cilium	L	6 μm
Cross-sectional radius	r_0	0.1 μm
Beat frequency	f	15 Hz
Cilia spacing	ℓ_0	0.3 μm
Metachronal wavelength	λ	30 μm

Table 1.1: Summary of data for cilia in the lung, from [48].

Cilia fixed on the epithelial cells in the bronchi are thin structures whose length L is about 6 μm in the larger airways (reduced to 5 μm or a little less in the smaller bronchioli) and radius r_0 is 0.1 μm. They beat at an average frequency f of 15 Hz (see Table 1.1 for a summary of these data). We are talking about an "average frequency" because ciliary beat frequency depends on several parameters, among them the temperature and the humidity of the environment. Fluctuations in secretion of mucus can also stimulate the activity of

the cilia [92, 109], secretion which can be increased or decreased by some drugs [87]. As it will be explained below, the cilia do not beat alone but take part of a *metachronal wave* which propagates to the surface of a carpet of 0.3 μm-spaced cilia with a wavelength of 30 μm.

The complete modelling of the polymerization of a cilium is still an open problem at this time. A sectional view of a cilium (see Figure 1.4) shows a normal 9 + 2 axonemal structure of fibrils: a doublet of fibrils (called "axoneme") is encircled with nine other doublets of fibrils. Moreover, they are unusual in the possession of a crown of 3 to 7 short "claws" 25 to 35 nm long (see Figure 1.3), projecting from a dense cap at their tips [46]. The ciliary basal body is of a common type with a basal foot, short striated rootlets, and attached cytoplasmic microtubules, which together provide anchorage. This structure is characteristic of the cilia.

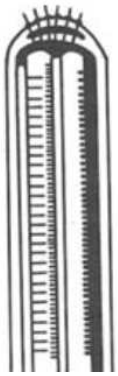

Figure 1.3: Crown of "claws" attached to the tips of the cilium, modified from [105].

Bending movements are produced as the outer nine microtubules doublets of the ciliary axoneme actively slide against one another when propelled by molecular bridges of dynein that project from one doublet towards the next. Dynein is a ATPase protein that uses energy from ATP in performing cyclical shape changes that produce the active sliding movements. The machinery of motility is spread along the whole length of the cilium, and different patterns of sliding along the length of the nine doublets are responsible for the differences in shape of the cilium during its beat. Radial connections between axonemal fibrils are assumed to resist the sliding and contribute to the formation of bends. A detailed description of the mechanism of motility has been given by Gibbons [50].

The beat of a cilium can be broken down into two parts: a recovery stroke and an effective stroke. These two phases does not counterbalance one with the other. This point is very important. Indeed, mucus and periciliary layer are viscous fluids at the scale of a cilium, and these fluids have reversibility property: a reversible movement of the cilium would not permit the mucus to be transported (see Section 1.3.1.2). Between two cycles, the cilium is at rest. At the start of the beat cycle, the cilium is in the rest position r (see Figure 1.5). In the recovery stroke the cilium unrolls clockwise (in the top view) from its rest position to the starting position for the effective strokes, remaining close to the cell surface. In the effective strokes, the cilium is fully extended and bends over to reach the rest position. Both side and top views show the beat is 3-dimensional, even if the effective

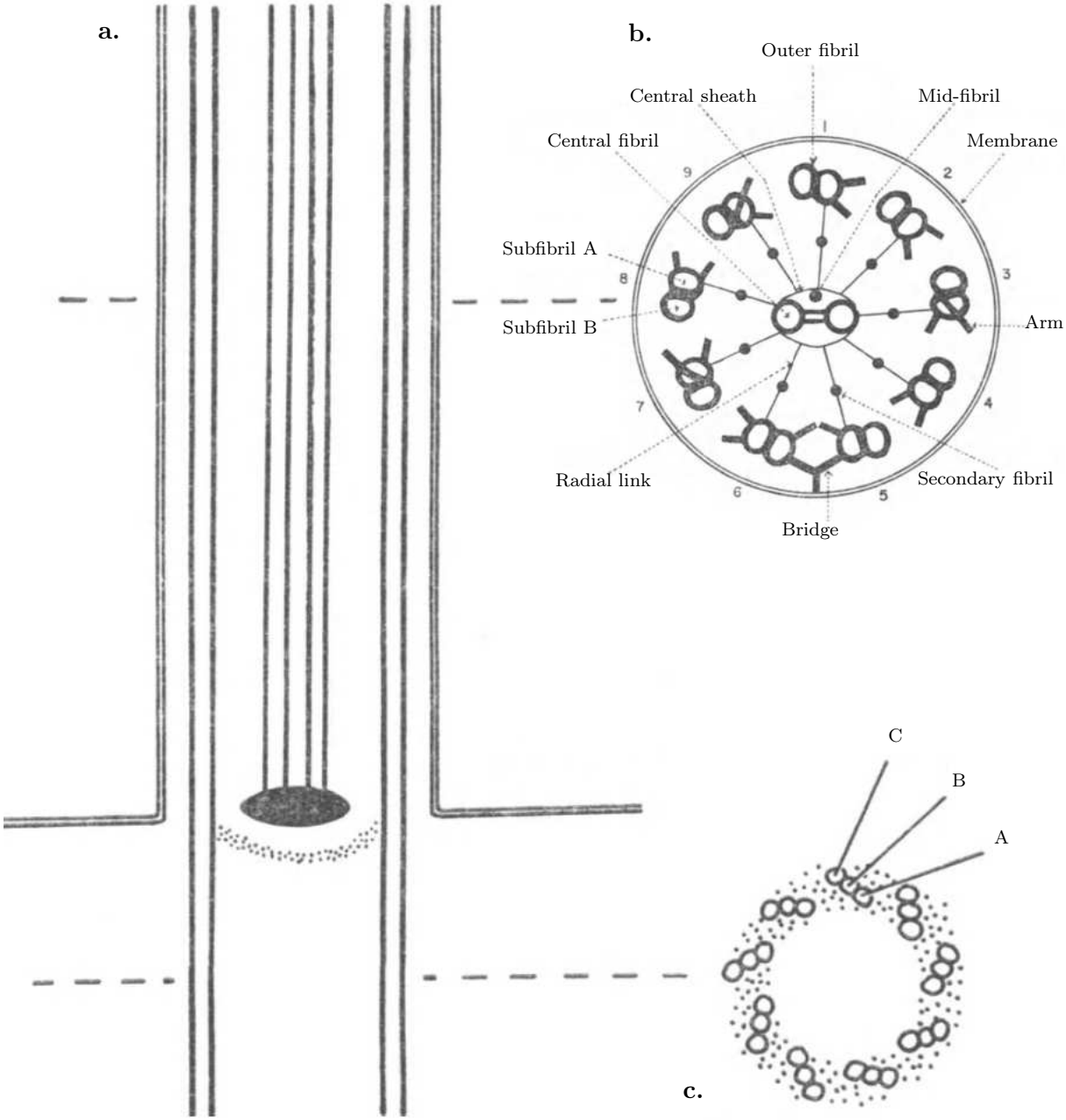

Figure 1.4: Diagrams showing the structure of a cilium. **a.** Structures seen in a longitudinal section. **b.** Transverse section of the ciliary shaft with the typical arrangement of internal fibrils. **c.** The arrangement of fibril triplets in the basal body, showing the position of the third subfibril C, and the twist of the peripheral triplets. Modified from Warner [116].

stroke is nearly planar and in a plane perpendicular to the cell surface, during which the cilium swings through an arc of about 110 degrees.

The different motion of the cilium between the effective and recovery strokes can be well understood if we consider the motion of a needlelike body in a viscous liquid. The force acting on a needlelike body moving perpendicular to the axis of symmetry is almost twice the force acting on the same needlelike body moving in the axial direction. Thus, it would be highly desirable for the cilium to have a "perpendicular mode" of motion in its effective stroke (thus generating a greater force) as against a "tangential mode" of motion during the recovery strokes. In addition, the force is linearly dependent on the velocity; thus, a larger velocity implies a larger force, which is clearly obvious in the ciliary beat pattern with the fast effective strokes. Indeed, according to Sanderson and Dirksen [95], the effective stroke is two or three times faster than the recovery stroke and the rest phase.

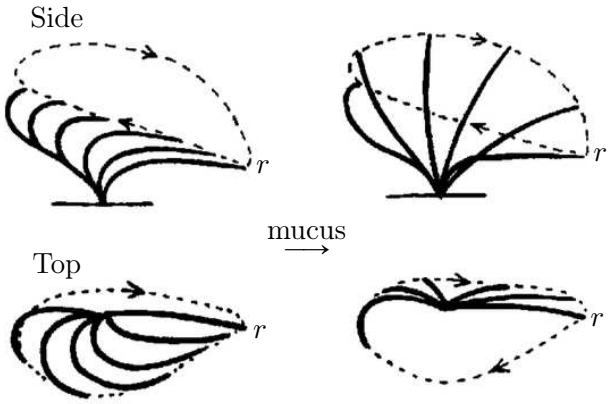

Figure 1.5: The 3D-beat cycle of a tracheal cilium seen from the side and from above. On the left the recovery stroke and on the right the effective stroke. Modified from [105].

When mucus is present, floating on top of the periciliary layer, it comes within reach of the ciliary tips during the effective stroke of the ciliary beat cycle, but the cilia will move beneath the mucus for the rest of the cycle. At the start of the effective stroke, cilia are often still slightly bent forward and may therefore enter the overlying mucus the tip first rather than being bent backwards and presenting the side of the cilium to the mucus (Figures 1.6**a** and 1.6**b**). At this stage, the cilia may push upwards on the mucus, raising it a little away from the cell surface. As the effective stroke proceeds, the cilium engages with the mucus and imparts propulsive force to the mucus. Towards the end of the effective stroke, the ciliary tip must begin to swing downwards once more and its forward movement decreases. The mucus continues to move forward as it is propelled by surrounding cilia and is pulled away from the decelerating ciliary tip. Then, decelerating cilia finish at the rest position. The resting cilium projects in the direction of mucus transport, and an area of resting cilia could act as a "nonreturn surface", discouraging a backward flow of mucus over the area (Figure 1.6**d**).

A cilium that is propelling mucus is subjected to a different distribution of forces from that of a cilium propelling water. In a homogeneous fluid, the viscous resistance to movement of a cilium increases towards the tip only because of increasing velocity of movement. However, a mucus-propelling cilium in its effective stroke is surrounded by

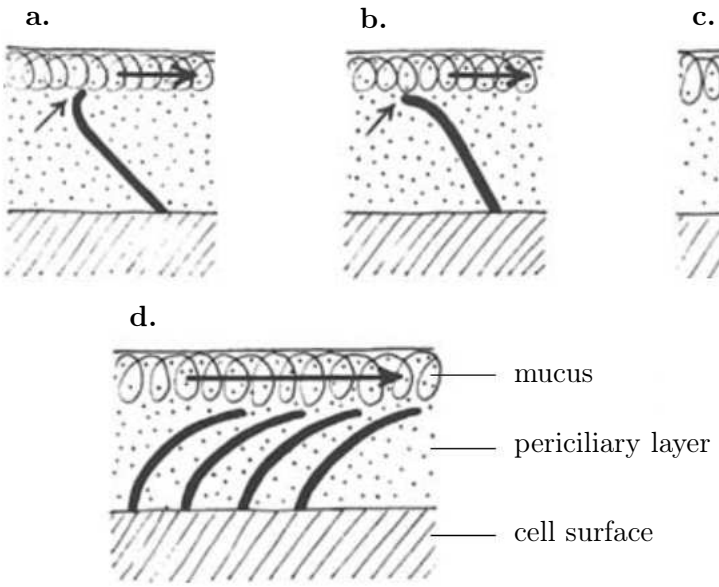

Figure 1.6: Mucus and cilia in different situations. Modified from [105].

low viscosity fluid throughout most of its length, but meets the much greater resistance of mucus in the distal 0.5 μm or so at the tip. Propulsive force for ciliary movement is generated throughout the ciliary length, and when a cilium meets resistance it will tend to bend backwards, the backward bend increasing as the distance of the effective resistance from the ciliary base increases. If a cilium bends backwards too far it will no longer be able to propel mucus effectively (Figure 1.6**c**). That is why there should be an optimal length for a mucus-propelling cilium at which it can exert a reasonable force and yet not bend too much when it meets a mucus load [103].

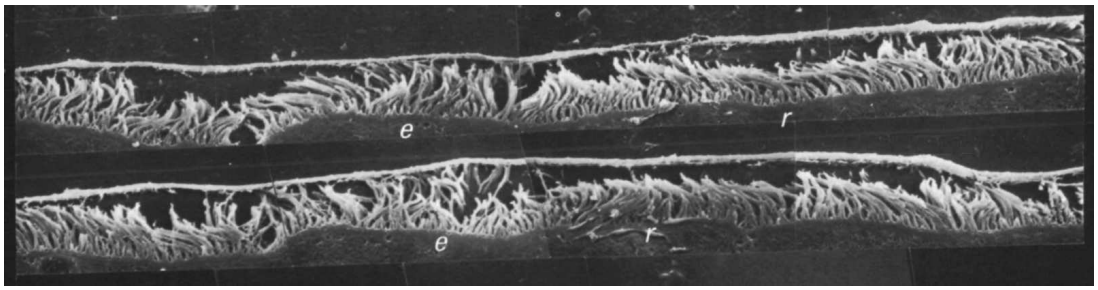

Figure 1.7: Two adjacent 1-μm-thick sections of cultured rabbit tracheal epithelium examined by scanning electron microscopy. Note the difference in orientation of the cilia during the effective (e) and recovery (r) phases of the beat cycle. Modified from [96].

Cilia that propel mucus do not work alone but as members of a metachronal wave. They take advantage of the recovery stroke to coordinate. If two cilia lie close enough together, they will interfere with one another and will adjust their frequency and phase of beating so as to minimize this interference [102]. According to the positional relationship between them relative to their plane of beating, they may end up beating in phase with one another, or with a constant phase difference. When many cilia interfere with their

neighbors in such a way, their beating will become organized into coordinated metachronal waves (see Figure 1.7). We can imagine that changes in the viscosity of the medium, or in the length, or in the spacing of the cilia, will have a deep influence on the characteristics of the metachronal wave. Its wavelength is of the order of a hundred of cilia, namely around 30 μm (see Table 1.1).

Even a small raft of flake of mucus would be likely to be propelled by several metachronal waves. A cilium performing its effective stroke will therefore normally come into contact with mucus that is already moving at perhaps 200 μm.s^{-1} [115]. Because the ciliary tip would move at 4 or 5 times this speed in the absence of mucus, it will exert a force on the mucus tending to accelerate the mucus. However, the highly viscous nature of the mucus will resist the propulsive force of the cilium and as a consequence will slow down the local speed of the cilium. Other cilia of the metachronal wave moving behind will join the first cilium and add their propulsive effort, and the slower the mucus moves, the larger the number of cilia within each metachronal wave that contribute effective strokes at any instant because they are slowed down to the speed of the mucus.

Based on the works of Sanderson and Sleigh [96] on the rabbit, waves may be small circular patches of activity, as in Figures 1.8**c** and 1.8**d**, or longer areas as seen in Figures 1.8**a**, 1.8**b** and 1.8**e**. In either case, they are limited in space and propagated for only a short distance on the cultured epithelium. In Figures 1.8**c** and 1.8**d**, some cilia are performing a clockwise recovery stroke (r), others an effective stroke (e) in the direction of mucus transport. The resultant metachronal wave (m) moves in a different direction.

The pattern of ciliary activity represented in Figure 1.9 indicates the metachronal relationships of the component cilia at an instant during the extension and propagation of the wave across the epithelium. The metachronal wave has originated from a single cilium. Each cilium begins its movement with a clockwise recovery stroke that has two components of hydrodynamic coupling which induce the movement of neighbouring cilia. With respect to the direction of the effective stroke (e) (which is the direction of the mucus transport), this coupling by sideways and backward forces, acting respectively downwards and to the left, as indicated by the short arrow (m). The effective stroke returns the cilia to the resting position by moving in the direction of the arrow (e) and has little influence on the metachronism. The metachronal wave therefore travels at an obtuse angle ($\sim 135^\circ$) to the effective stroke. The line of synchrony (s) is at 90° to the direction of the main line of metachrony.

Since there can be several metachronal waves, even if they can be located on small circular patches of ciliary activity (Figure 1.8**b**), their contribution to the propulsion of an area of mucus will carry the mucus over any irregularities or nonciliated areas of the epithelium, and smooth out any minor differences in rate or direction of beat of the small metachronal fields that go to make up the whole surface. These works on the rabbit were confirmed by Marino and Aiello [82], whose studies on human bronchial biopsies showed similar restricted metachronal fields. These are interpreted as being limited by the irregularities of the epithelial surface, or probably narrow nonciliated areas or other discontinuities across which mechanical communication of the wave does not easily take place.

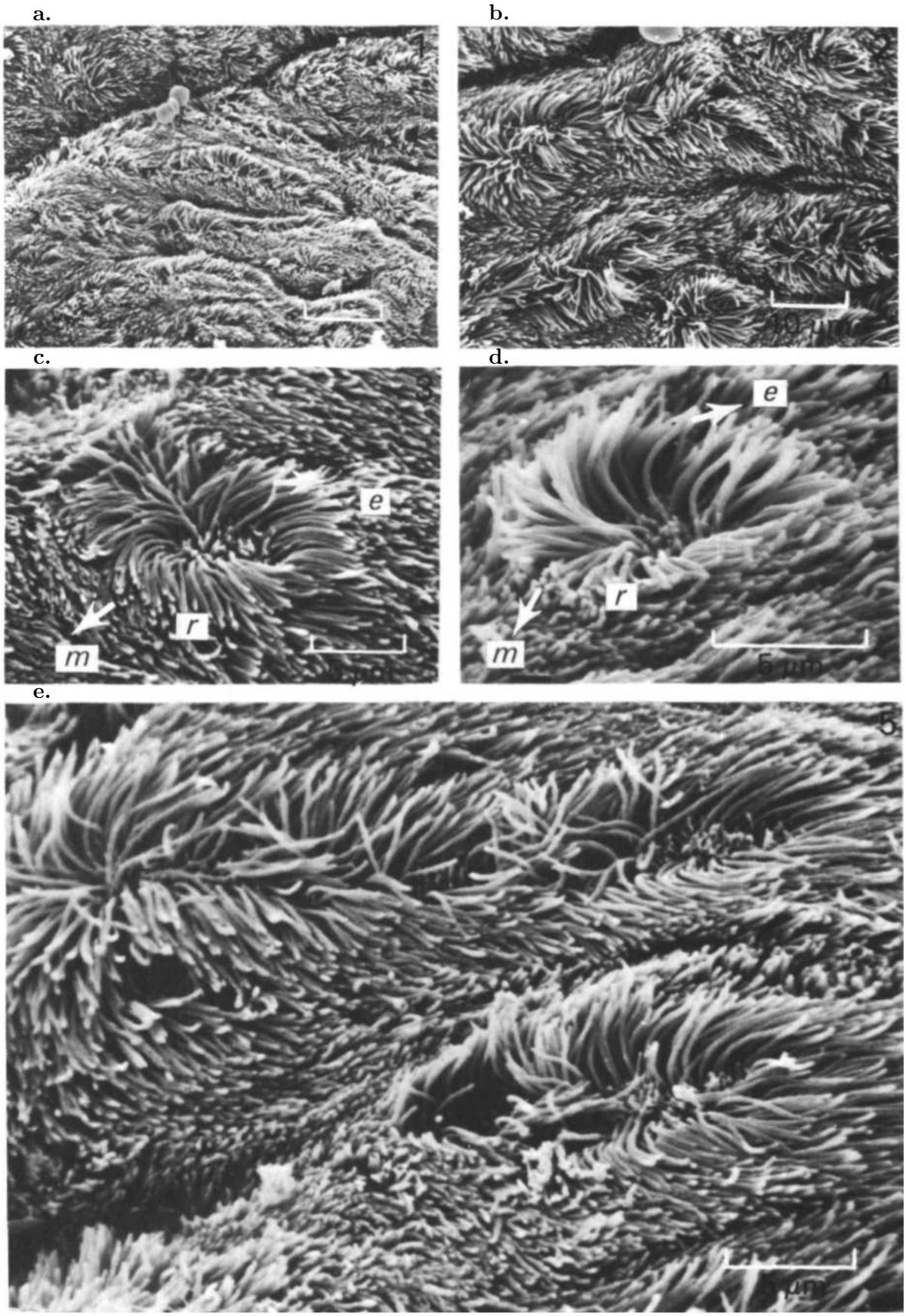

Figure 1.8: Scanning-electron micrographs of rabbit tracheal ciliated epithelia showing different areas of activity. Modified from [96].

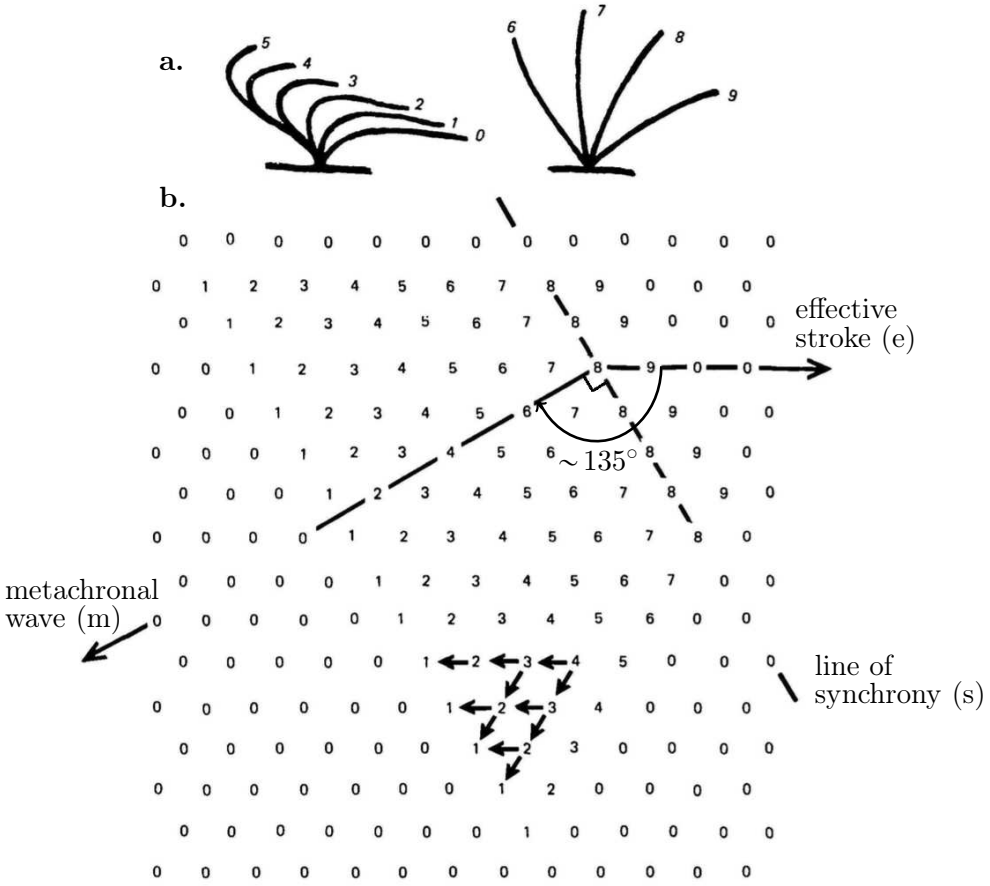

Figure 1.9: Interpretation of an area of ciliary activity on cultured rabbit tracheal epithelium represented by a model which is based upon a reconstructed 3-dimensional beat cycle (**a**) and upon a plan which indicates the spatial relationships of cilia on the epithelial surface. All cilia in the plan **b** are equally spaced (of 0.3 μm, see Table 1.1) and each one is represented by a single numeral, whose value denotes the phase of the cilium in its beat cycle (corresponding to schema **a**). Modified from [96].

Finally, the cilia are very slender bodies whose beats propel the mucus. They move in the periciliary layer, a low viscosity layer beneath the mucus. The beat of a cilium is a liking of a recovery stroke and an effective stroke, interspersed with rest phases, during which the cilium projects in the direction of mucus transport. Only tips of the cilia enter the mucus during the effective stroke to propel it. The cilium does not work alone but as member of a metachronal wave which emerges from the coordination of the cilia during the recovery stroke, and propagates in the opposite direction of mucus transport. All the data related to the cilia and the metachronal wave are given in Table 1.1.

1.1.2.4 Some pathologies

Before tackling the mathematical modellings for the mucociliary transport, let us mention some pathologies related to it. First, the cilia of persons who inherit the various forms of primary ciliary dyskinesia (immotile cilia syndrome) or Young's syndrome are either

totally nonmotile or have such defective motility that mucociliary clearance is absent or severely reduced [24, 89, 91]. In asthma [69], in infections with influenza [23] or cold viruses [90] and mycoplasmas [35], among others, substantial numbers of ciliated cells may be shed, and the propulsive machinery of mucociliary transport depleted. Disorientation of ciliated cells may occur in regeneration after infections, and it appears to be common in bronchitics [58], asthmatics, and smokers [104]. Hypertrophy of the mucous glands is a standard feature of disease, also seen most often in bronchitics [57], asthmatics [114], and smokers, and hypersecretion of mucus increases the amount to be cleared, perhaps by 10 or 20 times. Excessive mucin secretion by different secretory cell types is likely to be a major cause of the airway plugging associated with fatal asthma [55]. Finally, mucus viscosity can change too and disturb mucociliary clearance: it increases in diseases such as cystic fibrosis or when the mucosa becomes dehydrated, for example with a fever or excessive alcohol consumption; it decreases under emotional stress or if the subject has bronchitis or asthma.

1.2 Mucociliary transport, state of art

While numerous physiological and pathophysiological factors are known to influence mucociliary clearance and associated diseases, there are often insufficient data to evaluate each of their effects on the mucus transport [41], motivating theoretical and experimental modelling studies. Even if this phenomenon has already been widely studied, it is still a challenge for the scientific research. Several problems emerge from the complexity of the system: taking into account active thin strutures (cilia), the non-constant viscosity, the Newtonian or non-Newtonian behavior of the fluid, the interface between the two layers, the lining of the bronchi on the periciliary layer, the influence of the air on the mucus, the effects of the inhaled pathogens, etc. This complexity makes the full numerical problem be out of reach of scientists [29], but several complementary models have been developed to study the mucociliary clearance. This section is dedicated to the presentation of the literature related to the mucociliary transport in the lung. Mathematical models have been increasingly sophisticated and reflect many of the features found in the actual system, incorporating the effects of a large number of cilia together with the two-layer characteristic of the mucociliary fluid. Several of the more successful mucociliary transport models that have been developped are discussed below.

1.2.1 Envelope models

The concept of the envelope model is based on the idea that the main propulsive thrust comes from the instantaneous surface covering the tips of the undulating cilia (Figure 1.10). This idea was developed independently by Ross and Corrsin [94] for mucus transport and by Blake [10, 12] for free-swimming ciliated protozoa. The mucus transport model of Ross and Corrsin considered two layers: a “watery” periciliary layer and a linear viscoelastic mucous layer (Maxwell fluid). They predicted unrealistically low

mucus transport rates, but their theory did not allow contact between the envelope and the viscoelastic mucous layer. This work suggested that the mucous layer moves essentially like an elastic bloc. Moderate changes in the mucus viscosity did not appear to significantly alter transport. Conversely, they noted the significance of the viscosity of the periciliary layer, as any change can yield an appreciable change in mucus transport rate. The envelope model, while useful in gaining some understanding of mucociliary transport, is somewhat superficial in that it does not incorporate the essential physics of the ciliary beat cycle and the mechanical contact with highly viscous mucous layer. A more realistic model would take into account the action of the full length of the cilia and their asymetric beat pattern, which allows the inclusion of such important factors as the velocity and orientation of the cilium during the effective and recovery strokes.

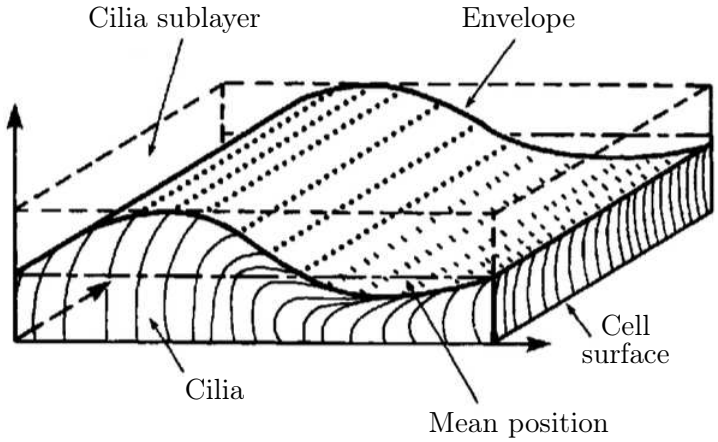

Figure 1.10: A schematic illustration of the envelope model. Modified from [105].

1.2.2 Sublayer models

A wide class of sublayer models have been developed taking into account the full length of the cilia to simulate the propulsion of mucus by cilia. On the one hand, there is the "traction-layer" model which uses a continuum representation for the cilia. On the other hand, there is the "discrete-cilia" model which employs an array of oscillating needlelike bodies to represent the cilia.

1.2.2.1 Traction-layer model

The action of a large number of cilia is modeled by a continuous distribution of forces per unit volume within the cilia sublayer. The volume force distribution is obtained by appropriate spatial averaging and Fourier analysis over a cycle of a particular ciliary beat pattern. In the model of Keller and coworkers [63], the averaging technique does not adequately discriminate between the effective and recovery strokes and predicts relatively

high oscillatory velocities as a consequence. A fairly constant stream flow in the upper part of the cilia sublayer could be observed. One of the characteristic results of this analysis is the almost total retardation of flow in the lower part of the cilia sublayer together with a "plug flow" in the mucous layer.

Recently Smith and coworkers [107] modeled in two-dimension the airway surface liquid by a three-layer model: the upper (the mucus) modeled as a Maxwell fluid, the lower one (the periciliary layer) and the middle one (kind of transition layer, rather thin) considered as Newtonian fluids. The cilia are treated as an active porus medium and their effects modeled by a volumique resistive force depending on the local velovity of the cilia. This model showed a quasi-uniform transport of the mucus layer but no collective movement in the periciliary layer emerges from this model.

1.2.2.2 Discrete-cilia model

Barton and Raynor [6] developed a mathematical analysis of ciliary propulsion, approximating the cilium by a rigid rod which automatically shortens during the recovery stroke. They used a simplified "resistance coefficient" approximation to the effect of the cilium on the surrounding fluid, and their model of the cilia motion did not include the experimental findings that were to emerge later. Their work allowed us to calculate realistic flow rates, and their characterization of the cilium as a rigid rod was exploited later in some models [15].

An alternate "discrete sublayer" approach utilizing the mathematical technique of slender-body theory was developed by Blake [13], initially for ciliated microorganisms. Due to their slenderness, individual cilia can be modelled by distributing force singularities along their centrelines. These ideas were extended in studies such as Liron and Mochon [76] and Fulford and Blake [48]. This theoretical approach gives estimates for the mean field velocity in both the periciliary layer and the mucous layer when both liquids are assumed to have Newtonian fluid properties. In all examples, the mean field velocity is very small in the lower part of the periciliary layer (which contains the recovery stroke) and increases very quickly close to the mucous layer, up to the mucous velocity.

Cilia seem to alter their beat pattern in the presence of mucus, or in a general way when subjected to a high viscosity environment. Calculations using a specified beat pattern do not strongly support the hypothesis that the penetration of the cilia into the mucous layer during their effective stroke is essential for mucus movement. Actually, they suggest that ample velocities of propulsion are obtained by the cilia even if there is no penetration, in the situation where the cilia densities are sufficiently high. Conversely, calculations based on models in which active cilia are sparsely distributed over the epithelium suggest that penetration of the cilia into the mucous layer would significantly enhance transport.

The form of the ciliary beating, especially during its effective stroke, is a determining factor for the velocity of the mucous layer. The ciliary beat described by Sanderson and Sleigh [96] is the more realistic as the cilia encounter the very large resistance of the mucus. Other theories have been developed, they include the tip penetration models, in which only the tips of the cilia penetrate the mucus [77], and the difficulties to determine

the deformation of the interface between two viscous fluids by the motion of a nearby slender body [14].

More recently, Smith and coworkers [106] discussed in detail techniques for modelling flows due to finite and infinite arrays of beating cilia. Cilia are modelled as curved slender ellipsoidal bodies by distributing Stokeslet and potential source dipole singularities along their centrelines, leading to an integral equation that can be solved using a simple and efficient discretization. They developed a more complex and detailed model of flow patterns in the periciliary layer of the airway surface liquid. Their results confirmed that shear flow of the mucus layer drives a significant volume of periciliary liquid in the direction of mucus transport even during the recovery stroke of the cilia. Lee and coworkers [71] considered in 2-dimension a two-layer Newtonian fluid model to investigate the important factors that may affect the mucociliary transport. The cilium is modeled by discrete Dirac delta function distributed all along the cilium. The numerical techinque implemented in this study is a projection method combined with the immersed boundary method in order to prescribe the ciliary beating patterns. Using the same computational techniques, Jayathilake and coworkers [60] simulated a 3-dimensional two-layer flow to better understand some pathological cases.

1.2.3 Non constant viscosity models

A few works consider a variable-viscosity model. Matar and Spelt [83] modeled in 2-dimension the viscosity as the solution of a reaction-advection-diffusion equation depending on the temperature, but the model of the flow is very simplified. A variable-viscosity model has been presented by Enault and coworkers [42] in the abscence of cilia, and by Mauroy and coworkers [85] at the scale of the bronchi for a Bingham fluid. Chatelin and Poncet [30] proposed a 3-dimensional model where the viscosity is the solution of a convection-diffusion equation. The movement of the cilia is imposed as the solution of an 1-dimensional transport equation on a parametric curve, and the effects of the cilia on the fluid are treated by penalization. To the best of our knowledge, in the other works which consider a variable viscosity, the viscosity is defined constant by part. In a recent study, Dillon and coworkers [40] used the immersed boundary method to simulate 2-dimensional flow due to three cilia, with a discrete model of the internal elastic and force-generating structures of the cilia. The mucus layer was simulated using a relatively thin elastic layer immersed in the fluid, a short distance above the cilia tips. Their results showed that the cilia are able to propel mucus without the need to engage with the mucus layer, and that elastic properties of the mucus layer prevent unphysical deformation of the mucus-periciliary liquid interface. This observation justifies the two-layers models (sometimes three) developed in several works [60, 71, 107], for which the interfaces are assumed invariable and flat.

For a more complete synthesis of the works on the mucociliary transport, we refer the reader to the review by Smith and coworkers [108]. An important conclusion of this state of art is that the complexity of the phenomenon leads us to consider several restrictive assumptions. The next section is devoted to the presentation of the mathematical model

of mucociliary transport. The aim is to simulate in 3D a whole forest of cilia in a two-viscosity fluid. We will especially pay attention to limit the computational costs related to the model, and at the same time, try to keep assumptions to the minimum.

1.3 Mathematical modelling of mucociliary transport

In discussing the fluid mechanical principles of mucociliary transport, it should be observed that there are several length scales of particular relevance to this study. There are:

- molecular length scales relative to the biochemical structure of the mucus.
- length scales associated with the cilium tip (0.1 to 1 μm).
- a length associated with the cilium length, cell size, ciliary wavelength and coherence of a mucous plaque (5 to 50 μm).
- a length scale associated with the length of an airway (5 to 10 mm).

In this study, we focus on the mucociliary transport phenomena at the scale of the cilium and ciliary wavelength.

1.3.1 Modeling of the fluid

1.3.1.1 A Newtonian fluid

All the notations introduced in the following developement are summarised in Table 1.2. As a first step, the fluid is assumed to be homogenous with constant viscosity. The mathematical modelling of fluid is classically based on the two conservation principles:

- mass conservation for an incompressible and homogeneous fluid,

$$\mathrm{div}(\mathbf{u}) = 0 \text{ on } \Omega,$$

- movement quantity conservation,

$$\rho\left(\frac{\partial \mathbf{u}}{\partial t} + \mathrm{div}(\mathbf{u}\otimes\mathbf{u})\right) = \mathrm{div}(\boldsymbol{\sigma}) + \mathbf{F}_e \text{ on } \Omega.$$

We assume that the fluid is Newtonian:

$$\boldsymbol{\sigma} = 2\mu\mathbb{D}(\mathbf{u}) - p\mathbb{I}_3 = \mu\left(\nabla\mathbf{u} + {}^t\nabla\mathbf{u}\right) - p\mathbb{I}_3, \tag{1.3.1}$$

which leads to the incompressible Navier-Stokes equations:

$$\left\{ \begin{array}{rcll} \rho\left(\dfrac{\partial \mathbf{u}}{\partial t} + \mathrm{div}(\mathbf{u}\otimes\mathbf{u})\right) - \mu\triangle\mathbf{u} + \nabla p & = & \mathbf{F}_e & \text{on } \Omega, \\ \mathrm{div}(\mathbf{u}) & = & 0 & \text{on } \Omega. \end{array} \right. \tag{1.3.2}$$

As it has been discussed in Section 1.1.2.1, the mucus is a viscoelastic fluid, and so we should work with a non-Newtonian fluid model. Nevertheless, the relaxation time is very high, which means that at the scale of the cilia beat, the elastic energy of the fluid is insignificant with regard to the viscous resistance. As a consequence, we have chosen to model the mucus as a Newtonian fluid, and use Equation (1.3.1) for the constraint tensor $\boldsymbol{\sigma}$.

Ω	Domain occupied by the fluid
$\mathbf{u}$	Velocity of the fluid
ρ	Density of the fluid
$\boldsymbol{\sigma}$	Constraint tensor
$\mathbf{F}_e$	External forces
μ	Viscosity of the fluid
$\mathbb{D}(\mathbf{u})$	Deformation tensor of $\mathbf{u}$
p	Pressure of the fluid
$\mathbb{I}_3$	Identity matrix of $\mathcal{M}_3(\mathbb{R})$

Table 1.2: Notations.

1.3.1.2 Stokes versus Navier-Stokes

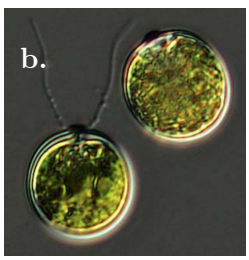

Figure 1.11: **a.** Simmer with a high Reynolds number: Jérémy Stravius at the World Swimming Championships in Barcelona, 2013.
b. Swimmer with a low Reynolds number: microalga *Chlamydomonas Reinhardtii*, picture found and modified from *http://www.fytoplankton.cz*.

Dividing Equations (1.3.2) by the fluid flow characteristic quantities, we get

$$Re\left(\frac{\partial\widetilde{\mathbf{u}}}{\partial\widetilde{t}}+\mathrm{div}(\widetilde{\mathbf{u}}\otimes\widetilde{\mathbf{u}})\right)-\triangle\widetilde{\mathbf{u}}+\nabla\widetilde{p}=\widetilde{\mathbf{F}}_e \tag{1.3.3}$$

where $\widetilde{\mathbf{u}}$, $\widetilde{t}$, $\widetilde{p}$ and $\widetilde{\mathbf{F}}_e$ are the corresponding dimensionless quantities, and Re is the Reynolds number. It is defined by

$$Re=\frac{\rho LU}{\mu},$$

with L and U respectively the flow characteristic length and velocity. Let us discuss two particular regimes:

- either the Reynolds number Re is high, which is true at the scale of the human swimmer (Figure 1.11**a**), for who Re is of the order of 10^6. In this case, inertial terms in Equation (1.3.3) preponderate over viscous terms. Note that these equations are not reversible in time because of the non-linear term, and the solution depends on the solution in the past.

- or the Reynolds number Re is low, which is true for micro-swimmers like *Chlamydomonas Reinhardtii* (Figure 1.11**b**), for which Re is of the order of 10^{-6}. This time, the inertial terms are dominated by the viscous terms and thus, the fluid can be modeled by the Stokes equations

$$\begin{cases} -\mu\triangle\mathbf{u}+\nabla p &= \mathbf{F}_e \quad \text{on } \Omega, \\ \mathrm{div}(\mathbf{u}) &= 0 \quad \text{on } \Omega. \end{cases} \tag{1.3.4}$$

  Let us note that the time-derivative does not appear in the Stokes equations, which results in an instantaneous balance of forces at each time: there is no dependance on the past, no memory effects, and the problem is completely reversible in time.

Regarding to mucociliary transport, the characteristic length and velocity are of the order of the micrometer and the micrometer per second, so that the Reynolds number Re in this case is of the order of 10^{-6}, like the micro-swimmer *Chlamydomonas Reinhardtii*. As a consequence, the Stokes equations are privileged. It is very important to underline that, because of the reversibility of the Stokes equations, the mucous transport is efficient only if the movement of the cilia is not reversible in time.

Much of the mucus propelled by cilia in the tracheobronchial tree moves against the pull of gravity, even if values of mucociliary transport appear similar irrespective of orientation. At the micrometric scale, the force of gravity ρg and of buoyancy $\triangle\rho g$ are insignificant. Moreover, for normal mucus depths ($\leqslant 10\ \mu$m), two factors negate the gravitational effects: first, the high-density array of cilia acting like a porous resistive medium, and second, the high viscosity and tensile forces within the mucus itself. The conclusion is that there is no external forces: $\mathbf{F}_e=0$.

1.3.1.3 Effects of the cilia on the fluid

It remains to take into account the interaction between the cilia and the mucus. Let us present two approaches:

- the easiest model is the "one-way" model, that is only one action is considered. Here, we model the effects of the cilia on the fluid, but we neglect the retroaction of the fluid on the cilia. In this case, the positions and the velocities of the cilia are given either by solving some mechanics equations or analytically imposed.
- the second model, more complex, is the "two-ways" model, when the two interactions are considered. The mechanical equations are coupled with the fluid mechanics equations (for example through the boundary conditions) and both the action of the cilia on the fluid and the action of the fluid on the cilia are modeled, leading to a strongly coupled fluid-structure interaction problem.

In this work, we consider only the action of the cilia on the mucus ("one-way" model) and we will see in Section 1.3.2.2 how to impose the position and the movement of the cilia. This action is naturally introduced in our problem by no-slip boundary conditions: the velocity $\mathbf{u}$ of the fluid at the level of a cilium is equal to the velocity $\mathbf{u}_{\text{cil}}$ of the cilium. Finally, the problem we consider to model the fluid is the following Stokes problem

$$\left\{\begin{array}{rcll} -\mu\triangle\mathbf{u}+\nabla p &=& 0 & \text{on } \Omega, \\ \text{div}(\mathbf{u}) &=& 0 & \text{on } \Omega, \\ \mathbf{u} &=& \mathbf{u}_{\text{cil}} & \text{on the cilia.} \end{array}\right. \tag{1.3.5}$$

1.3.1.4 Bifluid model

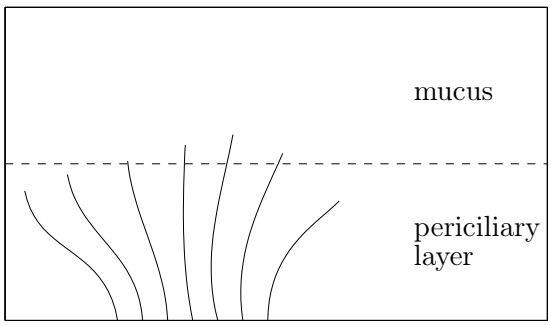

Figure 1.12: Domain Ω in the case of a two-viscosity fluid.

As described in Section 1.1.2, the airway surface liquid is composed of two overlayed layers, the mucus and the periciliary layer. In our model, we take into account this fact

defining the viscosity μ by the constant piecewise function

$$\mu(x,y,z) = \begin{cases} \mu_1 & \text{if } z \leqslant h_0, \\ \mu_2 & \text{if } z \geqslant h_0, \end{cases}$$

where h_0 is the height of the periciliary layer. Finally, Problem (1.3.5) becomes

$$\begin{cases} -2\mathrm{div}(\mu\mathbb{D}(\mathbf{u})) + \nabla p = 0 & \text{on } \Omega, \\ \mathrm{div}(\mathbf{u}) = 0 & \text{on } \Omega, \\ \mathbf{u} = \mathbf{u}_{\text{cil}} & \text{on the cilia.} \end{cases} \tag{1.3.6}$$

1.3.1.5 Boundary conditions

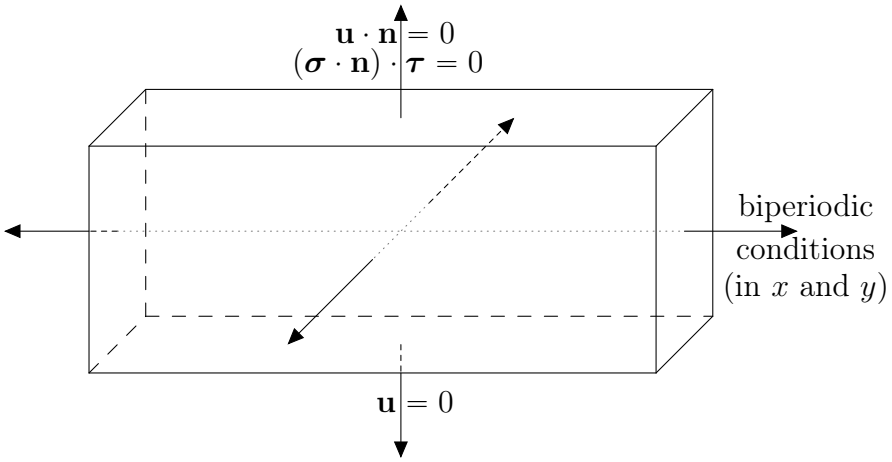

Figure 1.13: Illustration of the boundary conditions.

For now, we impose one boundary condition: $\mathbf{u} = \mathbf{u}_{\text{cil}}$ on the cilia (no-slip boundary conditions). In this section, we describe the different boundary conditions we impose to match reality. First, consider a box as the domain Ω (see Figure 1.13). The bottom corresponds to the lining of the bronchi, which is assumed to be flat, and we impose no-slip boundary condition: $\mathbf{u} = 0$. The box we consider is seen as a window focused on a part of a bronchus, with mucociliary transport which goes on outside the box. Therefore it is natural to impose in both directions x and y biperiodic boundary conditions. Lastly, if we pay attention to Figure 1.7, it seems reasonable to assume that the mucus surface remains flat. This approximation involves two boundary conditions on the top of the box:

$$\begin{cases} \mathbf{u} \cdot \mathbf{n} = 0 & \text{kinematic condition,} \\ (\boldsymbol{\sigma} \cdot \mathbf{n}) \cdot \boldsymbol{\tau} = 0 & \text{dynamic condition,} \end{cases}$$

where $\mathbf{n}$ is the normal vertor, $\boldsymbol{\tau}$ the tangential vector and $\boldsymbol{\sigma}$ the constraint tensor. The kinematic condition corresponds to a non-output condition while the dynamic condition

is a no-friction sliding condition. All the boundary conditions we impose in our model are summarized in Figure 1.13.

For the theoretical study, we do not consider these boundary conditons. Actually, they do not impact on the regularity of the solution and/or the approximation of the solution by finite element methods. Thus, we will consider homogeneous Dirichlet boundary conditions fir the sake of clarity, even if the results readily adapt with the boundary conditions that have been described in this section. They will be considered at the time of the computations (Chapter 4). In the meantime, Problem (1.3.6) is well-defined and we can discuss the regularity of the solution.

1.3.2 Modeling of a cilium

1.3.2.1 Hierarchy of thin-structure models for the cilium

The aim of this work is to solve Problem (1.3.6) by a finite-element method, so we have to mesh the domain Ω correctly. In the previously chosen model, in order to take into account the cilia in a conforming way, the mesh has to respect the complex geometry of domain Ω, especially at the neighbourhood of the cilia. The cilia are very slender bodies, as a consequence the mesh has to be very refined near the cilia. These considerations mean that computational costs will be very high, not to mention cilia beat very quickly and the mesh has to be redefined at each time step. If we could imagine this process for one cilium, it is clearly not adapted to a forest of cilia.

Another way to treat the cilia is to process by penalisation: the domain Ω includes the cilia, and the velocity of the fluid is penalized to be equal to the cilium velocity. Once more, it is important to have a very refined mesh on the volume occupied by the cilia; otherwise, cilia seen by the mesh would behave as a continuous layer where the velocity of the fluid is imposed (this model tends to the traction-layer model). Finally, this model yields the same computational cost issues as the previous model, and therefore is not adapted neither.

Our model is based on the fact that the cilium is a very slender body (the ratio cross-sectional radius over length is $r_0/L = 0.1/6$) and that it beats very quickly (frenquence $f = 15$ Hz), see Table 1.1. To avoid too prohibitive computational costs, we consider the asymptotic of a zero diameter cilium with an infinite velocity: the cilium is modeled by a line distribution of forces in source term. Again, in order to ease the computations, the line distribution of forces is approached by a sum of punctual forces distributed along the cilium, Figure 1.14.

In this section, we estimate the convergences between these different source terms: the volumic source term, the line distribution of forces and the distribution of punctual forces. More precisely, see Figure 1.14,

a. the cilium seen as a curved cylinder, which corresponds to a volumic source term of radius $\varepsilon > 0$,

$$f_\varepsilon = \frac{1}{\pi\varepsilon^2}\mathbb{1}_{\text{cil}} \in \mathbb{L}^2(\Omega),$$

and $\mathbf{u}_\varepsilon \in H^2(\Omega)$ the associated solution.

b. the cilium seen as a line distribution of forces on the curve Γ,

$$\delta_\Gamma \in H^{-1-\eta}(\Omega), \forall \eta > 0, \tag{1.3.7}$$

and $\mathbf{u}_\Gamma \in H^{1-\eta}(\Omega)$ the associated solution.

c. the previous line distribution replaced with a sum of N punctual forces located at the points x_i and of intensities c_i,

$$f_N = \sum_{i=1}^{N} c_i \delta_{x_i} \in H^{-3/2-\eta}(\Omega), \forall \eta > 0,$$

and $\mathbf{u}_N \in H^{1/2-\eta}(\Omega)$ the associated solution.

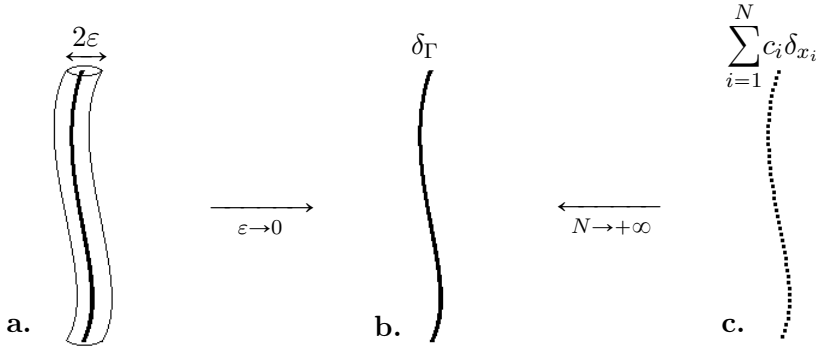

Figure 1.14: Three schematic source terms to model a cilium: **a.** A volumic cilium of small radius ε and force in ε^{-2} so that the mass stays constant when ε tends to 0. **b.** A line distribution of forces. **c.** A sum of N punctual forces distributed along the cilium.

Let us define

$$\begin{array}{rccc} \boldsymbol{\xi}: & [0,L] & \to & \mathbb{R}^3 \\ & s & \mapsto & \boldsymbol{\xi}(s) \end{array}$$

a regular parametrization of Γ such that $\boldsymbol{\xi} \in \mathscr{C}^\infty$ and $d_s\boldsymbol{\xi}$ is never zero. We recall the following properties of the Sobolev spaces:

Proposition 1 (Sobolev embeddings)**.** *Consider a regular domain Ω, we denote by d the dimension,*

$$H^m(\Omega) \hookrightarrow \mathscr{C}^k(\bar{\Omega}) \text{ for } m > k + \frac{d}{2}.$$

Proposition 2 (Trace operator)**.** *Consider $s > 1/2$ and an open domain Ω with a regular border $\partial\Omega$, there exists a continuous mapping T defined by*

$$\begin{array}{rccc} T: & H^s(\Omega) & \longrightarrow & H^{s-1/2}(\Omega) \\ & v & \longmapsto & Tv = v_{|_{\partial\Omega}}. \end{array}$$

We can now establish estimates of convergence between these different source terms and deduce convergences for the solutions. From now and until the end of this section, the study is led in dimension 3. We denote by η any (small) real such as $\eta > 0$.

Convergence of f_N to δ_Γ. We show a weak convergence result in $H^{3/2+\eta}(\Omega)$ and a strong convergence result in $H^{2+\eta}(\Omega)$.

Proposition 3 (Weak convergence)**.** *Let $(x_i)_{i\in[\![1,N]\!]}$ be N orderly points on Γ, there exist N reals $(c_i)_{i\in[\![1,N]\!]}$ such that, for all $v \in H_0^{3/2+\eta}(\Omega)$,*

$$\langle \sum_{i=1}^{N} c_{x_i}\delta_{x_i}, v\rangle \underset{N\to+\infty}{\longrightarrow} \langle \delta_\Gamma, v\rangle,$$

which means that $f_N = \sum c_{x_i}\delta_{x_i}$ weakly converges to δ_Γ in $H^{-3/2-\eta}$.

Proof. Consider $v \in H^{3/2+\eta}$. By Proposition 1, v is continuous, so that we can write:

$$\langle \sum_{i=1}^{N} c_{x_i}\delta_{x_i}, v\rangle = \sum_{i=1}^{N} c_{x_i} v(x_i).$$

Moreover, for all i, there exists $s_i \in [0, L]$ such that $x_i = \boldsymbol{\xi}(s_i)$, so we have

$$\sum_{i=1}^{N} c_{x_i} v(x_i) = \sum_{i=1}^{N} c_{\boldsymbol{\xi}(s_i)} v(\boldsymbol{\xi}(s_i)).$$

On the other hand,

$$\langle \delta_\Gamma, v\rangle = \int_\Gamma v(x)\mathrm{d}x = \int_0^L v(\boldsymbol{\xi}(s)) \left\| \frac{d\boldsymbol{\xi}}{ds}(s)\right\| \mathrm{d}s.$$

So, let us choose $(s_i)_i$ such as

$$0 = s_0 < s_1 < \cdots < s_N = L \text{ et } \max_i s_i - s_{i-1} \lesssim \frac{L}{N},$$

and

$$c_{\boldsymbol{\xi}(s_i)} = \left\| \frac{d\boldsymbol{\xi}}{ds}(s_i)\right\| (s_i - s_{i-1}).$$

Since the product $\left\|\frac{d\boldsymbol{\xi}}{ds}(\cdot)\right\| v(\boldsymbol{\xi}(\cdot))$ is continuous, By the Riemann sums theorem,

$$\sum_{i=1}^{N} (s_i - s_{i-1}) \left\| \frac{d\boldsymbol{\xi}}{ds}(s_i)\right\| v(\boldsymbol{\xi}(s_i)) \underset{N\to+\infty}{\longrightarrow} \int_0^L \left\| \frac{d\boldsymbol{\xi}}{ds}(s)\right\| v(\boldsymbol{\xi}(s))\mathrm{d}s = \int_\Gamma v(x)\mathrm{d}x.$$

Therefore, for all $v \in H_0^{3/2+\eta}(\Omega)$,

$$\langle \sum_{i=1}^{N} c_{x_i}\delta_{x_i}, v\rangle \underset{N\to+\infty}{\longrightarrow} \langle \delta_\Gamma, v\rangle,$$

which ends the proof of the weak converge. □

Proposition 4 (Strong convergence)**.** *The convergence rate of $f_N = \sum c_{x_i}\delta_{x_i}$ to δ_Γ depends on the space we consider:*

- *In $H^{-2-\eta}(\Omega)$, f_N converges to δ_Γ at the order $N^{-1/2}$.*
- *In $H^{-5/2-\eta}(\Omega)$, f_N converges to δ_Γ at the order N^{-1}.*

Proof. Consider $v \in H^{2+\eta}(\Omega)$, formally,

$$\begin{aligned}
\left|\langle\sum_{i=1}^{N} c_{x_i}\delta_{x_i}, v\rangle - \langle\delta_\Gamma, v\rangle\right| &= \left|\sum_{i=1}^{N}(s_i - s_{i-1})\left\|\frac{d\boldsymbol{\xi}}{ds}(s_i)\right\| v(\boldsymbol{\xi}(s_i)) - \int_0^L \left\|\frac{d\boldsymbol{\xi}}{ds}(s)\right\| v(\boldsymbol{\xi}(s))\mathrm{d}s\right| \\
&\leqslant \sum_{i=1}^{N}\int_{s_{i-1}}^{s_i}\left|\left\|\frac{d\boldsymbol{\xi}}{ds}(s_i)\right\| v(\boldsymbol{\xi}(s_i)) - \left\|\frac{d\boldsymbol{\xi}}{ds}(s)\right\| v(\boldsymbol{\xi}(s))\right|\mathrm{d}s \qquad (1.3.8)\\
&\leqslant \sum_{i=1}^{N}\int_{s_{i-1}}^{s_i}\left|\int_s^{s_i}\partial_s\left(\left\|\frac{d\boldsymbol{\xi}}{ds}(\cdot)\right\| v(\boldsymbol{\xi}(\cdot))\right)(\sigma)\mathrm{d}\sigma\right|\mathrm{d}s \qquad (1.3.9)\\
&\leqslant \sum_{i=1}^{N}\int_{s_{i-1}}^{s_i}(s_i - s_{i-1})^{1/2}\left\|\partial_s\left(\left\|\frac{d\boldsymbol{\xi}}{ds}(\cdot)\right\| v(\boldsymbol{\xi}(\cdot))\right)\right\|_{H^\eta(]0,L[)}\mathrm{d}s \qquad (1.3.10)\\
&\leqslant C(\boldsymbol{\xi})\|v\|_{H^{2+\eta}(\Omega)}\left(\frac{L}{N}\right)^{1/2}.
\end{aligned}$$

Let us derive this estimate in a rigorous way:

- from (1.3.8) to (1.3.9), since $v \in H^{2+\eta}(\Omega)$, the trace operator which restricts v to Γ defines a function $\widetilde{v} \in H^{1+\eta}(\Gamma)$, and thus the composition by the regular function $\boldsymbol{\xi}$ becomes a function of $H^{1+\eta}(]0, L[)$. So we can apply the fundamental theorem of calculus which writes a function as the integral of its derivative (mutliplying by the regular function $\|\frac{d\boldsymbol{\xi}}{ds}(\cdot)\|$ does not perturb this process).
- Inequality (1.3.10) comes from the Cauchy-Schwarz inequality.

Thus, we have shown that $f_N = \sum c_{x_i}\delta_{x_i}$ converges to δ_Γ in $H^{-2-\eta}(\Omega)$ at the order $N^{-1/2}$. Note that this result is *a priori* false in $H^{-3/2-\eta}(\Omega)$.

We can also specify the convergence rate in $H^{-5/2-\eta}$. Indeed, Riemann sums theorem ensures that the rate of convergence for $\mathscr{C}^1(\Omega)$-functions is $\mathcal{O}(N^{-1})$. More precisely,

$$\left|\langle\sum_{i=1}^{N} c_{x_i}\delta_{x_i}, v\rangle - \langle\delta_\Gamma, v\rangle\right| \leqslant C(\boldsymbol{\xi})\frac{L}{N}\|\nabla v\|_{\infty,\bar{\Omega}}.$$

By Proposition 1, for any $v \in H^{5/2+\eta}$, $\|\nabla v\|_{\infty,\bar{\Omega}} \leqslant C\|v\|_{H^{5/2+\eta}(\Omega)}$. We conclude that $f_N = \sum c_{x_i}\delta_{x_i}$ converges to δ_Γ in $H^{-5/2-\eta}(\Omega)$ at the order N^{-1}. □

Convergence of f_ε to δ_Γ By the definition of δ_Γ, Equation (1.3.7), the test function v has to belong to $H^{1+\eta}(\Omega)$, so that $\langle \delta_\Gamma, v\rangle$ is well-defined (actually, we need that the trace operator is defined on a submanifold of dimension $d-2$). Nevertheless, conversely to the previous case, no convergence (even weak) has been established in $H^{-1-\eta}(\Omega)$. We can however get an order of convergence in a weaker norm.

Proposition 5. *The convergence rate of f_ε to δ_Γ depends on the space we consider:*

- *In $H^{-2-\eta}(\Omega)$, f_ε strongly converges to δ_Γ at the order $\sqrt{\varepsilon}$.*
- *In $H^{-5/2-\eta}(\Omega)$, f_ε strongly converges to δ_Γ at the order ε.*

Proof. For $v \in H^{2+\eta}(\Omega)$,

$$|\langle f_\varepsilon, v\rangle - \langle \delta_\Gamma, v\rangle| = \left| \int_{\mathscr{C}_\varepsilon} \frac{1}{\pi\varepsilon^2} v(x)\mathrm{d}x - \int_\Gamma v(x)\mathrm{d}x \right| = \left| \int_{\mathscr{C}_\varepsilon} \frac{1}{\pi\varepsilon^2} \Big(v(x) - v(p_\Gamma(x)) \Big)\mathrm{d}x \right|,$$

where $\mathscr{C}_\varepsilon$ is the cylinder of center line Γ and of radius ε, and $p_\Gamma(x)$ is the orthogonal projection of x onto Γ. Moreover, since $v \in H^{2+\eta}(\Omega)$, its derivatives belong to $H^{1+\eta}(\Omega)$: their traces are well-defined on Γ. We can apply the fundamental theorem of calculus and the Cauchy-Schwarz inequality to obtain

$$\begin{aligned}
|\langle f_\varepsilon, v\rangle - \langle \delta_\Gamma, v\rangle| &= \left| \int_\Gamma \int_{D(y,\varepsilon)} \frac{1}{\pi\varepsilon^2} \int_y^x \partial_{x-y} v(\sigma)\mathrm{d}\sigma\mathrm{d}x\mathrm{d}y \right| \\
&\leqslant \int_\Gamma \frac{1}{\pi\varepsilon^2} \int_{D(y,\varepsilon)} |x-y|^{1/2} \|\partial_{x-y} v\|_{H^\eta(]y,x[)} \mathrm{d}x\mathrm{d}y \\
&\leqslant |\Gamma|\sqrt{\varepsilon}\|v\|_{H^{2+\eta}(\Omega)},
\end{aligned}$$

where $D(y,\varepsilon)$ is the cross-section of the cylinder $\mathscr{C}_\varepsilon$ at the point $y \in \Gamma$. We conclude that f_ε converges to δ_Γ at the order $1/2$ in $H^{-2-\eta}(\Omega)$.

We can also specify the convergence in $H^{-5/2-\eta}(\Omega)$. Indeed, for $v \in H^{5/2+\eta}(\Omega)$, from the above,

$$\begin{aligned}
|\langle f_\varepsilon, v\rangle - \langle \delta_\Gamma, v\rangle| &= \left| \int_{\mathscr{C}_\varepsilon} \frac{1}{\pi\varepsilon^2} \Big(v(x) - v(p_\Gamma(x)) \Big)\mathrm{d}x \right| \\
&\leqslant \int_{\mathscr{C}_\varepsilon} \frac{1}{\pi\varepsilon^2} \|\nabla v\|_{\infty,\Omega} |x - p_\Gamma(x)| \mathrm{d}x \\
&\leqslant \varepsilon|\Gamma|\|\nabla v\|_{\infty,\Omega}.
\end{aligned}$$

We conclude with Proposition 1 that f_ε converges to δ_Γ at the order 1 in $H^{-5/2-\eta}(\Omega)$. □

Convergence of the solutions. Now we have established convergence results for the source terms, we can specify the convergence results for the corresponding solutions. The results of this section are based on the following theorem, taken from [75] (Chapter 2, Theorem 6.3).

Theorem 1. *Define the space*

$$\Xi^r = \left\{ v \in \mathbb{L}^2(\Omega) \;\middle|\; \|v\|_{\Xi^r} = \sum_{|\alpha| \leqslant r} \|\rho^{|\alpha|} D_\alpha v\|_0 < +\infty \right\},$$

where ρ is a smooth function such that there exist $c_1, c_2 \in \mathbb{R}_+^*$ satisfying

$$c_1 \leqslant \frac{\rho(x)}{d(x, \partial\Omega)} \leqslant c_2, \;\; \forall x \in \Omega.$$

The space Ξ^{-r}, for $r \geqslant 0$, is defined as the dual space of Ξ^r. Consider the following elliptic problem

$$\begin{cases} Au = f & \text{in } \Omega, \\ u = 0 & \text{on } \partial\Omega, \end{cases} \tag{1.3.11}$$

where A is a "reasonable" elliptic operator (we assume that (1.3.11) *has a unique solution for any regular right-hand side f). Then, for any f in Ξ^{-r}, $r \geqslant 0$, there exists a solution u of* (1.3.11) *satisfying*

$$\|u\|_{m-r} \leqslant C \|f\|_{\Xi^{-r}},$$

where m is the highest order of derivation in the operator A.

Inspired by Scott [99], we apply Theorem 1 to $\delta_\Gamma - \sum c_{x_i} \delta_{x_i}$ and $f_\varepsilon - \delta_\Gamma$. But in order to do so we need to assume the cilium to be "far" from the border of Ω, that is, there exists $\Omega_0 \subset\subset \Omega$ such as supports of f_ε, δ_Γ and $\sum c_{x_i} \delta_{x_i}$ are included in Ω_0. Indeed, the H^{-r}-norm and the Ξ^{-r}-norm are equivalent on Ω_0, and for any f supported in Ω_0, we have

$$\|f\|_{\Xi^{-r}} \leqslant c d(\Omega_0, \partial\Omega)^{-r} \|f\|_{-r},$$

where c depends only on Ω_0 and on the choice of ρ. Finally, we conclude easily from the previous sections that for any $\eta > 0$,

$$\|u_\Gamma - u_N\|_{-\eta} \leqslant C \left\| \delta_\Gamma - \sum^N c_{x_i} \delta_{x_i} \right\|_{\Xi^{-2-\eta}} \leqslant C \left\| \delta_\Gamma - \sum^N c_{x_i} \delta_{x_i} \right\|_{-2-\eta} \leqslant \frac{C}{\sqrt{N}},$$

$$\|u_\Gamma - u_N\|_{-1/2-\eta} \leqslant C \left\| \delta_\Gamma - \sum^N c_{x_i} \delta_{x_i} \right\|_{\Xi^{-5/2-\eta}} \leqslant C \left\| \delta_\Gamma - \sum^N c_{x_i} \delta_{x_i} \right\|_{-5/2-\eta} \leqslant \frac{C}{N},$$

$$\|u_\varepsilon - u_\Gamma\|_{-\eta} \leqslant C \|f_\varepsilon - \delta_\Gamma\|_{\Xi^{-2-\eta}} \leqslant C \|f_\varepsilon - \delta_\Gamma\|_{-2-\eta} \leqslant C\sqrt{\varepsilon},$$

$$\|u_\varepsilon - u_\Gamma\|_{-1/2-\eta} \leqslant C \|f_\varepsilon - \delta_\Gamma\|_{\Xi^{-5/2-\eta}} \leqslant C \|f_\varepsilon - \delta_\Gamma\|_{-5/2-\eta} \leqslant C\varepsilon.$$

Remark 1. *The convergence of the solutions in weak spaces (relative to the solution's regularities) has been established under the assumption "the cilium is far from the border". In the case of mucociliary transport, the cilium is connected to the lining of the bronchi, which is the border of our domain Ω. Nevertheless, the velocity of the cilium at the border is zero, and so the active part of the cilium is not in contact with the border: the convergence of the solutions holds in this case.*

1.3.2.2 Parametrization of a cilium and of a forest of cilia

As explained in Sections 1.3.1.3 and 1.3.2.1, the effect of the cilia on the fluid ("one-way" model) is modeled by punctual forces distributed along the cilia. To complete this model, we have to define a parametrization of the movement of each cilium and the force it exerts on the fluid. Let us start with the parametrization of the movement of a cilium.

One cilium. Conversely to inert stiff or elastic solids, the cilia are "active": they have their own internal energy which allows them to beat. In our model, their movement is analytically imposed, as it is done for instance by Chatelin and Poncet in [30]. We use the parametrization established by Fulford and Blake in [48], based on the Fourier series decomposition of the beat of the cilium described by Sanderson and Sleigh in [96]. More precisely, at each time t the cilium is represented by the truncated Fourier series of the parametric curve

$$\boldsymbol{\xi}(s,t) = L\left[\frac{1}{2}\mathbf{a}_0(s) + \sum_{n=1}^{6} \mathbf{a}_n(s)\cos(2n\pi ft) + \mathbf{b}_n(s)\sin(2n\pi ft)\right],$$

where $s \in [0,1]$ measures arclength from the base of the cilium, L and f are respectively the length and the beat frequency of the cilium (see Table 1.1). The Fourier coefficients $\mathbf{a}_n$, $\mathbf{b}_n$ are vector quantities, which are approximated by the following 3-degree polynomial functions

$$\mathbf{a}_n(s) = \sum_{k=1}^{3} \mathbf{a}_{n,k} s^k \text{ and } \mathbf{b}_n(s) = \sum_{k=1}^{3} \mathbf{b}_{n,k} s^k$$

where $\mathbf{a}_{n,k}$ and $\mathbf{b}_{n,k}$ are constant vectors of $\mathbb{R}^3$, given in Table 1.3.

Figure 1.15 shows the beat of a cilium that we get with this parametrization and confirms the correspondance with the description made by Sanderson and Seligh in [96]. Let us note that the cilium crosses the interface between the mucus and the peryciliary layer (PCL) during the effective stroke (and only during this phase). This point is very important to guarantee an efficient mucus transport.

$\mathbf{a}_{n,k}$

	$n=0$	$n=1$	$n=2$	$n=3$	$n=4$	$n=5$	$n=6$
$k=1$	−0.449	0.130	−0.169	0.063	−0.050	−0.040	−0.068
	2.076	−0.003	0.054	0.007	0.026	0.022	0.010
$k=2$	−0.072	−1.502	0.260	−0.123	0.011	−0.009	0.196
	−1.074	−0.230	−0.305	−0.180	−0.069	0.001	−0.080
$k=3$	0.658	0.793	−0.251	0.049	0.009	0.023	−0.111
	0.381	0.331	0.193	0.082	0.029	0.002	0.048

$\mathbf{b}_{n,k}$

	$n=1$	$n=2$	$n=3$	$n=4$	$n=5$	$n=6$
$k=1$	−0.030	−0.093	0.037	0.062	0.016	−0.065
	0.080	−0.044	−0.017	0.052	0.007	0.051
$k=2$	1.285	−0.036	−0.244	−0.093	−0.137	0.095
	−0.298	0.513	0.004	−0.222	0.035	−0.128
$k=3$	−1.034	0.050	0.143	0.043	0.098	−0.054
	0.210	−0.367	0.009	0.120	−0.024	0.102

Table 1.3: Fourier-least squares coefficients for the cilia beat pattern. The upper and lower numbers in each entry correspond to the x and z components respectively, the y component is always zero.

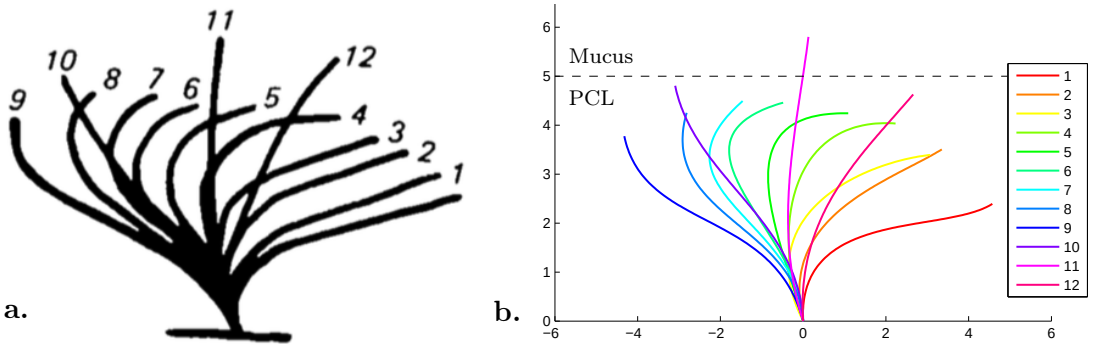

Figure 1.15: Traces of a cilium during one period of its beat. **a.** Description made by Sanderson and Sleigh [96]. **b.** Parametrization established by Fulford and Blake [48].

In [48], Fulford and Blake not only give a parametrization of one cilium, but they also explain how to parametrize a whole forest of cilia.

A forest of cilia. Now that we have described the beat of one cilium, parametrizing a whole forest is not more complicated if we take into account two important features of the forest: the space ℓ_0 between two cilia (in each direction) and the wavelength λ of the metachronal wave. These data are given in Table 1.1. More precisely, in order to model a forest of $n_x \times n_y$ cilia, with n_x (respectively n_y) the number of cilia in the direction x (respectively the direction y), the cilium (i,j), where $i \in [\![1, n_x]\!]$ and $j \in [\![1, n_y]\!]$, is

parametrized by the curve

$$\boldsymbol{\xi}_{i,j}(s,t) = i\ell_0\mathbf{e}_x + j\ell_0\mathbf{e}_y + \boldsymbol{\xi}\left(s, \frac{i\ell_0}{f\lambda} + t\right),$$

where $s \in [0,1]$. Let us note the phase shift $\varphi_i = i\ell_0/f\lambda$ in x (and only in x, not in y) which the metachronal wave comes from. As most of the models, we only consider the metachronal wave in the direction x, even if Figure 1.9 shows that activity is also propagated in the direction y. This approximation is classical and experiments [49] show that increasing viscosity causes the metachronal wave to become more orthoplectic (in the direction of mucociliary transport). We have drawn in Figure 1.16 a section of the forest in the direction x. The propagation of the metachronal wave (to the left on the picture) is in the opposite direction of mucus transport (to the right). Figure 1.17 shows a forest in 3d as we model it in the simulations (see Chapter 4), except on the value of the cilia spacing ℓ_0: it has been voluntarily increased for the sake of clarity.

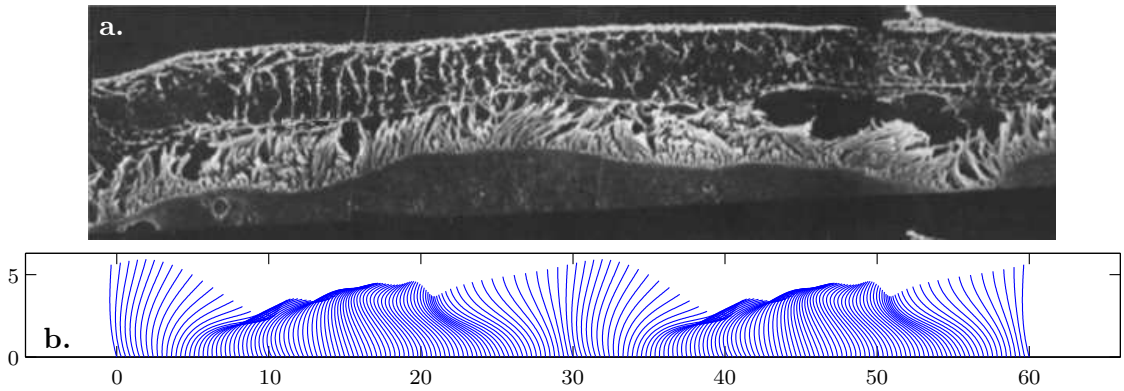

Figure 1.16: Parametrization of a forest of cilia. **a.** Another section of cultured rabbit tracheal epithelium examined by scanning electron microscopy, modified from [96]. **b.** Drawing of a section of a forest with the parametrization established by Fulford and Blake [48].

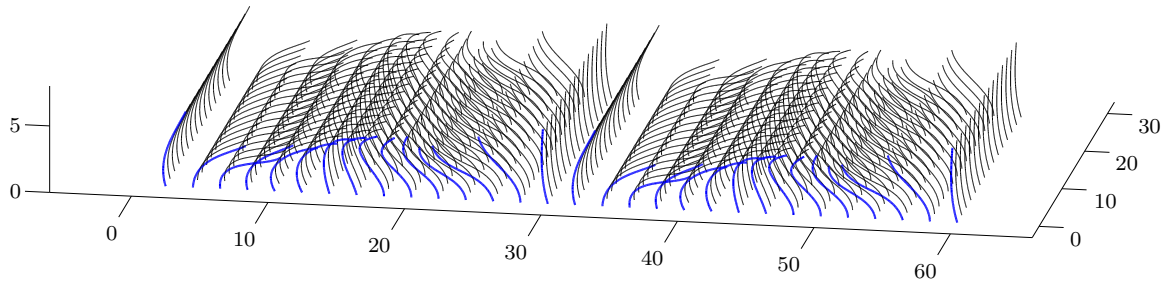

Figure 1.17: Drawing in 3d of a forest of cilia (with $\ell_0 = 2$ μm instead of 0.3 μm).

This section has been dedicated to the parametrization of the cilium and of a forest of cilia. Next section presents the model we have chosen for the force distributed along a cilium.

1.3.2.3 Distribution of forces along the cilium

There are two main theories to model the distribution of forces along a cilium. The simplier one is the resistive-force theory, and the second one is the slender-body theory. The resistive-force theory has been developed for flagella hydrodynamics in the pioneering work of Gray and Hancock [53]. It has been extensively used in subsequent studies of flagellar propulsion and bending [16, 21, 22]. The underlying assumption of this model is that the hydrodynamic forces are proportional to the local body velocity, where the constant of proportionality is defined as the force (or drag) coefficient. As pointed out by Lighthill [74], this assumption is inconsistent with the true hydrodynamic situation in which viscous effects dominate and produce long-range hydrodynamic interactions. Therefore, we have chosen to use the slender-body theory, although it requires more extensive numerical computations than the resistive-force theory.

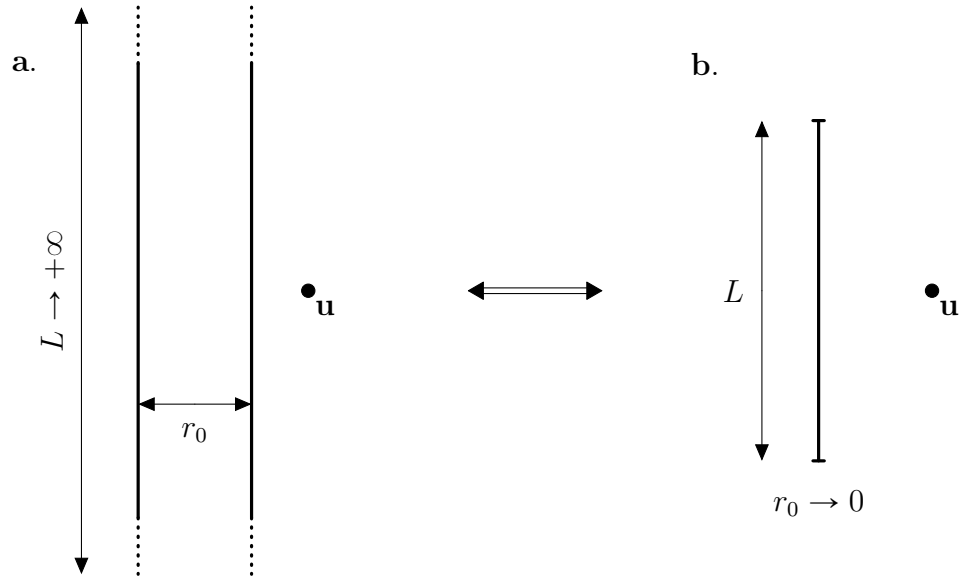

Figure 1.18: **a.** The inner expansion: $L \to +\infty$. **b.** The outer expansion: $r_0 \to 0$.

The slender-body theory model we use is based on asymptotic expansions when the ratio L/r_0 tends to infinity, where r_0 is the thickness of the cilium and L its length. Cox [36] established an asymptotic expansion of the force at each point of the cilium. If $\boldsymbol{\xi}$ is a parametrization of the cilium, the expression of the force at the point of curvilinear abscissa s is

$$\mathbf{f}(s,t) = \frac{2\pi\mu}{\ln(L/r_0)} \left(2\mathbb{I}_3 - \frac{\dot{\boldsymbol{\xi}}(s,t) \otimes \dot{\boldsymbol{\xi}}(s,t)}{\|\dot{\boldsymbol{\xi}}(s,t)\|^2} \right) \mathbf{u}_{\text{cil}}(s,t), \tag{1.3.12}$$

where $\dot{\boldsymbol{\xi}}$ is the derivative of $\boldsymbol{\xi}$ relative to s and $\mathbf{u}_{\text{cil}}$ is the derivative relative to t:

$$\dot{\boldsymbol{\xi}}(s,t) = \frac{\partial \boldsymbol{\xi}}{\partial s}(s,t) \text{ and } \mathbf{u}_{\text{cil}}(s,t) = \frac{\partial \boldsymbol{\xi}}{\partial t}(s,t).$$

Equation (1.3.12) has been established in [36] by confronting two different approaches:

a. the inner expansion consists in studying the fluid velocity near the cilium, which is thus seen as an infinite cylinder. The corresponding regime is L tends to infinity while r_0 remains constant.

b. the outer expansion considers the flow far from the cilium seen as a zero-thickness body, which corresponds to the regime r_0 goes to zero while L remains constant.

Both of these expansions are illustrated in Figure 1.18.

In the case of a two-viscosity fluid, the slender-body theory described by Cox [36] is not valid any longer. Fulford and Blake [47] established the expression of the distribution of forces along a slender body which straddles an interface. At the first order (in the regime $\ln(L/r_0)^{-1}$ tends to zero) the expression of the force is the one given by Equation (1.3.12) with μ the value of the viscosity at the origin point of the force. Actually, that point is not exact: the expression of the distribution of forces on the part of the cilium close to the interface (at a distance r_0 from the interface) is a little different. In our case, there are 20 punctual forces by cilium, so that the distance between two punctual forces is 0.3 μm, which is three times the radius $r_0 = 0.1$ μm of the cilium (see Table 1.1). Therefore, we do the following approximation: we consider Equation (1.3.12) for the distribution of forces all along the cilium.

1.3.3 Resulting mathematical problem

This subsection is a conclusion of the whole model presented in Section 1.3. Finally, the model leads us to the following problem

$$\left\{\begin{array}{rcll} -2\mathrm{div}(\mu\mathbb{D}(\mathbf{u})) + \nabla p &=& \displaystyle\sum_{i=1}^{N_{\mathrm{cx}}}\sum_{j=1}^{N_{\mathrm{cy}}}\left(\sum_{n=1}^{N}\delta_{\boldsymbol{\xi}_{i,j}(s_n,t)}\mathbf{f}\left(s_n, \frac{i\ell_0}{f\lambda}+t\right)\right) & \text{on } \Omega, \\ \mathrm{div}(\mathbf{u}) &=& 0 & \text{on } \Omega, \\ \mathbf{u} &=& 0 & \text{on } \partial\Omega, \end{array}\right. \tag{1.3.13}$$

where N_{cx} and N_{cy} are respectively the number of cilia in the directions x and y, and N is the number of punctual forces composing each cilium. We recall that ℓ_0, f, and λ are respectively the distance between two neighbouring cilia, the beat frequency and the wavelength of the metachronal wave, see Table 1.1. For a given cilium, s_n measures the arclength of the force application point from the base of the cilium. By linearity of the Stokes equations, studying Problem (1.3.13) consists in studying the following problem

$$\left\{\begin{array}{rcll} -2\mathrm{div}(\mu\mathbb{D}(\mathbf{u})) + \nabla p &=& \delta_{\mathbf{x}_0}\mathbf{F} & \text{on } \Omega, \\ \mathrm{div}(\mathbf{u}) &=& 0 & \text{on } \Omega, \\ \mathbf{u} &=& 0 & \text{on } \partial\Omega, \end{array}\right.$$

where $\mathbf{x}_0$ is a point of the domain Ω.

In what follows, we focus on the regularity of the solution and its approximations by finite element methods. In our model of a two-viscosity fluid, with $0 < \mu_1 < \mu_2$, the regularity of the solution (and so the convergence of the numerical solution) is not altered by the non-constant viscosity. Therefore, we consider the Stokes problem in a constant-viscosity fluid. In this case, the study is quite simplier and especially we can make explicit the solutions (at least in an infinite domain). Nevertheless, the two-viscosity fluid will be also considered in Chapter 4 in the computations. Finally, for the sake of clarity, we study the following problem

$$\left\{ \begin{array}{rcll} -\mu\triangle\mathbf{u} + \nabla p & = & \delta_{\mathbf{x}_0}\mathbf{F} & \text{on } \Omega, \\ \operatorname{div}(\mathbf{u}) & = & 0 & \text{on } \Omega, \\ \mathbf{u} & = & 0 & \text{on } \partial\Omega. \end{array} \right. \tag{1.3.14}$$

Before focusing on the numerical method to solve Problem (1.3.14), next section is dedicated to the study of this problem (regularity, existence of solutions...).

1.4 Elliptic problems with a singular right-hand side

This section is divided in two parts: the first one is devoted to the study of the Stokes problem with a punctual source term (Problem (1.3.14)); the second one introduces the Poisson problem with a Dirac mass in right-hand side, which is a scalar version of Problem (1.3.14). We take an interest in this problem because it is a simplier problem for a preliminary study, and because many results or methods that apply to the Poisson problem can be adaptated to the Stokes problem.

1.4.1 The Stokes problem with a punctual force in source term

1.4.1.1 The Stokeslet

The study is lead in 2-dimension, but the results will also be given in dimension 3. For the sake of simplicity, the location of the punctual force is the origin. Let us consider the Stokes problem on the whole domain:

$$\left\{ \begin{array}{rcll} -\mu\triangle\mathbf{u}_\delta + \nabla p_\delta & = & \delta_0\mathbf{F} & \text{in } \mathbb{R}^2, \\ \operatorname{div}(\mathbf{u}_\delta) & = & 0 & \text{in } \mathbb{R}^2. \end{array} \right. \tag{1.4.1}$$

The solution of this problem is not unique. Indeed, the homogeneous problem

$$\left\{ \begin{array}{rcll} -\mu\triangle\mathbf{u} + \nabla p & = & 0 & \text{in } \mathbb{R}^2, \\ \operatorname{div}(\mathbf{u}) & = & 0 & \text{in } \mathbb{R}^2. \end{array} \right.$$

has non-trivial solutions. For instance,

$$\mathbf{u}(\mathbf{x}) = \begin{bmatrix} \cos(x_1)\mathrm{e}^{x_2} \\ \sin(x_1)\mathrm{e}^{x_2} \end{bmatrix} \text{ and } p = 0.$$

In Proposition 6, we consider a particular solution, called "Stokeslet".

Proposition 6. *The 2d Stokeslet [31], defined by*

$$\begin{aligned}
\mathbf{u}_\delta(\mathbf{x}) &= \frac{1}{4\pi\mu}\left(-\ln\|\mathbf{x}\|\mathbb{I}_2 + \frac{\mathbf{x}\cdot{}^t\mathbf{x}}{\|\mathbf{x}\|^2}\right)\cdot\mathbf{F} && \in \mathbb{R}^2,\\
&= \frac{1}{4\pi\mu}\begin{bmatrix} -\ln\|\mathbf{x}\|f_1 + \dfrac{x_1^2 f_1 + x_1x_2f_2}{\|\mathbf{x}\|^2} \\ -\ln\|\mathbf{x}\|f_2 + \dfrac{x_1x_2 f_1 + x_2^2f_2}{\|\mathbf{x}\|^2}\end{bmatrix} && \in \mathbb{R}^2, \qquad (1.4.2)\\
p_\delta(\mathbf{x}) &= \frac{\mathbf{x}\cdot\mathbf{F}}{2\pi\|\mathbf{x}\|^2} = \frac{x_1f_1+x_2f_2}{2\pi\|\mathbf{x}\|^2} && \in \mathbb{R},
\end{aligned}$$

where $\mathbf{F} = {}^t[f_1, f_2]$ *and* $\mathbf{x} = {}^t[x_1, x_2]$*, is a solution of Problem* (1.4.1)*.*

Proof. Here, we present a constructive proof of the existence of the Stokeslet. As it will be done in the case of the Poisson problem (see Section 1.4.2.1), we first consider the following velocity

$$\mathbf{u}_\delta(\mathbf{x}) = -c\begin{bmatrix} \ln\|\mathbf{x}\|f_1 \\ \ln\|\mathbf{x}\|f_2 \end{bmatrix},$$

where c is constant. Defined in this way, $\mathbf{u}_\delta$ satisfies $-\triangle\mathbf{u}_\delta = \widetilde{c}\delta_0$, but the condition $\mathrm{div}(\mathbf{u}_\delta) = 0$ is not satisfied. Therefore $\mathbf{u}_\delta$ is modified by

$$\mathbf{u}_\delta(\mathbf{x}) = c\begin{bmatrix} -\ln\|\mathbf{x}\|f_1 + v_1(\mathbf{x})f_1 + v_2(\mathbf{x})f_2 \\ -\ln\|\mathbf{x}\|f_2 + w_1(\mathbf{x})f_1 + w_2(\mathbf{x})f_2 \end{bmatrix}.$$

Some calculations show that $\mathrm{div}(\mathbf{u}_\delta) = 0$ for any $\mathbf{F}$ in $\mathbb{R}^2$ is equivalent to the system

$$\begin{cases} \partial_1 v_1 + \partial_2 w_1 = \dfrac{x_1}{\|\mathbf{x}\|^2} \\ \partial_1 v_2 + \partial_2 w_2 = \dfrac{x_2}{\|\mathbf{x}\|^2}. \end{cases} \qquad (1.4.3)$$

The right hand side expression of System (1.4.3) encourages us to consider v_1 and w_1 defined by

$$v_1(\mathbf{x}) = \frac{x_1^{\alpha_1}x_2^{\beta_1}}{\|\mathbf{x}\|^2} \text{ et } w_1(\mathbf{x}) = \frac{x_1^{\alpha_2}x_2^{\beta_2}}{\|\mathbf{x}\|^2},$$

where α_1, α_2, β_1 et β_2 are some reals we have to set. We inject in the first equation of System (1.4.3), and we get the conditions

$$\begin{cases} \alpha_1 - 1 = 1 \\ \beta_1 = 0 \\ \alpha_2 = 1 \\ \beta_2 - 1 = 0 \\ \alpha_1 + \beta_2 = 3 \end{cases} \Longrightarrow \begin{cases} \alpha_1 = 2 \\ \beta_1 = 0 \\ \alpha_2 = 1 \\ \beta_2 = 1 \end{cases}$$

which gives

$$v_1(\mathbf{x}) = \frac{x_1^2}{\|\mathbf{x}\|^2} \text{ et } w_1(\mathbf{x}) = \frac{x_1 x_2}{\|\mathbf{x}\|^2}.$$

By injecting in the second equation of (1.4.3), we get

$$v_2(\mathbf{x}) = \frac{x_1 x_2}{\|\mathbf{x}\|^2} \text{ et } w_2(\mathbf{x}) = \frac{x_2^2}{\|\mathbf{x}\|^2}.$$

Finally, we have established the expression of the solution $\mathbf{u}$:

$$\mathbf{u}_\delta(\mathbf{x}) = \begin{bmatrix} u_1(\mathbf{x}) \\ u_2(\mathbf{x}) \end{bmatrix} = c \begin{bmatrix} -\ln\|\mathbf{x}\| f_1 + \dfrac{x_1^2 f_1 + x_1 x_2 f_2}{\|\mathbf{x}\|^2} \\ -\ln\|\mathbf{x}\| f_2 + \dfrac{x_1 x_2 f_1 + x_2^2 f_2}{\|\mathbf{x}\|^2} \end{bmatrix}.$$

Now, let us consider the pressure p_δ. We want $-\mu\triangle\mathbf{u}_\delta + \nabla p_\delta = 0$ (for $\mathbf{x} \neq 0$), so we set

$$\nabla p_\delta(\mathbf{x}) = c\mu\triangle\mathbf{u}_\delta(\mathbf{x}) = c\mu\triangle \begin{bmatrix} \dfrac{x_1^2 f_1 + x_1 x_2 f_2}{\|\mathbf{x}\|^2} \\ \dfrac{x_1 x_2 f_1 + x_2^2 f_2}{\|\mathbf{x}\|^2} \end{bmatrix}.$$

After some calculations, we have

$$\nabla p_\delta(\mathbf{x}) = \begin{bmatrix} \partial_1 p_\delta(\mathbf{x}) \\ \partial_2 p_\delta(\mathbf{x}) \end{bmatrix} = 2c\mu \begin{bmatrix} \dfrac{1}{\|\mathbf{x}\|^2} f_1 - \dfrac{2x_1}{\|\mathbf{x}\|^4}(x_1 f_1 + x_2 f_2) \\ \dfrac{1}{\|\mathbf{x}\|^2} f_2 - \dfrac{2x_2}{\|\mathbf{x}\|^4}(x_1 f_1 + x_2 f_2) \end{bmatrix}.$$

We identify

$$\nabla p_\delta(\mathbf{x}) = 2c\mu \begin{bmatrix} \partial_1 g(\mathbf{x}) h(\mathbf{x}) + g(\mathbf{x}) \partial_1 h(\mathbf{x}) \\ \partial_2 g(\mathbf{x}) h(\mathbf{x}) + g(\mathbf{x}) \partial_2 h(\mathbf{x}) \end{bmatrix}$$

with

$$g(\mathbf{x}) = x_1 f_1 + x_2 f_2 \text{ et } h(\mathbf{x}) = \frac{1}{\|\mathbf{x}\|^2}.$$

Finally, the pressure p_δ is given by

$$p_\delta(\mathbf{x}) = 2c\mu \left(\frac{x_1 f_1 + x_2 f_2}{\|\mathbf{x}\|^2} \right) + p_\infty = 2c\mu \frac{\mathbf{x} \cdot \mathbf{F}}{\|\mathbf{x}\|^2} + p_\infty,$$

where p_∞ is the value of the pressure at infinity. In what follows, we choose $p_\infty = 0$. In order to set the constant c, we fix a function $\boldsymbol{\varphi} \in \mathcal{C}_0^\infty(\mathbb{R}^2, \mathbb{R}^2)$ and assume that $\boldsymbol{\varphi}$ is radial

(to ease calculations): $\boldsymbol{\varphi}(\mathbf{x}) = \varphi(\|\mathbf{x}\|)$. For $\mathbf{F} = {}^t[1, 0]$:

$$\begin{aligned}
\langle -\mu\triangle\mathbf{u}_\delta + \nabla p_\delta, \boldsymbol{\varphi}\rangle &= \iint_{\mathbb{R}^2} \Big(-\mu\triangle u_1(\mathbf{x})\varphi_1(\mathbf{x}) - \mu\triangle u_2(\mathbf{x})\varphi_2(\mathbf{x}) + \nabla p_\delta(\mathbf{x})\cdot\boldsymbol{\varphi}(\mathbf{x})\Big)\mathrm{d}\mathbf{x} \\
&= -\iint_{\mathbb{R}^2} \Big(\mu u_1(\mathbf{x})\triangle\varphi_1(\mathbf{x}) + \mu u_2(\mathbf{x})\triangle\varphi_2(\mathbf{x})\Big)\mathrm{d}\mathbf{x} \\
&\quad - \iint_{\mathbb{R}^2} p_\delta(\mathbf{x})\Big(\partial_1\varphi_1(\mathbf{x}) + \partial_2\varphi_2(\mathbf{x})\Big)\mathrm{d}\mathbf{x} \\
&= -c\mu\Big(\iint_{\mathbb{R}^2} -\ln\|\mathbf{x}\|\triangle\varphi_1(\mathbf{x})\mathrm{d}\mathbf{x} + \iint_{\mathbb{R}^2} \frac{x_1^2}{\|\mathbf{x}\|^2}\triangle\varphi_1(\mathbf{x})\mathrm{d}\mathbf{x} \\
&\quad + \iint_{\mathbb{R}^2} \frac{x_1x_2}{\|\mathbf{x}\|^2}\triangle\varphi_2(\mathbf{x})\mathrm{d}\mathbf{x} + \iint_{\mathbb{R}^2} \frac{2x_1}{\|\mathbf{x}\|^2}(\partial_1\varphi_1(\mathbf{x}) + \partial_2\varphi_2(\mathbf{x}))\mathrm{d}\mathbf{x}\Big) \\
&= -c\mu\Big(I_1 + I_2 + I_3 + I_4\Big)
\end{aligned}$$

We recall the following results:

$$\int_0^{2\pi} \cos(\theta)\sin(\theta)\mathrm{d}\theta = 0 \quad \text{and} \quad \int_0^{2\pi} \cos^2(\theta)\mathrm{d}\theta = \pi.$$

- Calculation of I_1:

$$\begin{aligned}
I_1 &= \iint_{\mathbb{R}^2} -\ln\|\mathbf{x}\|\triangle\varphi_1(\mathbf{x})\mathrm{d}\mathbf{x} \\
&= -\int_0^{2\pi}\int_0^{+\infty} r\ln r\left(\partial^2_{r,r}\varphi_1(r) + \frac{1}{r}\partial_r\varphi_1(r)\right)\mathrm{d}r\mathrm{d}\theta \\
&= -\int_0^{2\pi}\left(\Big[r\ln r\partial_r\varphi_1(r)\Big]_0^{+\infty} + \int_0^{+\infty}\partial_r\varphi_1(r)\left(\ln r - \ln r - 1\right)\mathrm{d}r\right)\mathrm{d}\theta \\
&= -\int_0^{2\pi}\int_0^{+\infty} -\partial_r\varphi_1(r)\mathrm{d}r\mathrm{d}\theta \\
&= -2\pi\varphi_1(0).
\end{aligned}$$

- Calculation of I_2:

$$\begin{aligned}
I_2 &= \iint_{\mathbb{R}^2} \frac{x_1^2}{\|\mathbf{x}\|^2}\triangle\varphi_1(\mathbf{x})\mathrm{d}\mathbf{x} \\
&= \int_0^{2\pi}\int_0^{+\infty} r\cos^2(\theta)\left(\partial^2_r\varphi_1(r) + \frac{1}{r}\partial_r\varphi_1(r)\right)\mathrm{d}r\mathrm{d}\theta \\
&= \int_0^{2\pi}\cos^2(\theta)\mathrm{d}\theta\int_0^{+\infty}\Big(r\partial^2_r\varphi_1(r) + \partial_r\varphi_1(r)\Big)\mathrm{d}r \\
&= \pi\left(\Big[r\partial_r\varphi_1(r)\Big]_0^{+\infty} - \int_0^{+\infty}\partial_r\varphi_1(r)\mathrm{d}r + \int_0^{+\infty}\partial_r\varphi_1(r)\mathrm{d}r\right) \\
&= 0.
\end{aligned}$$

- Calculation of I_3:

$$\begin{aligned} I_3 &= \iint_{\mathbb{R}^2} \frac{x_1 x_2}{\|\mathbf{x}\|^2} \triangle \varphi_2(\mathbf{x}) \mathrm{d}\mathbf{x} \\ &= \int_0^{2\pi} \int_0^{+\infty} r\cos(\theta)\sin(\theta) \left(\partial_r^2 \varphi_2(r) + \frac{1}{r} \partial_r \varphi_2(r) \right) \mathrm{d}r\mathrm{d}\theta \\ &= \int_0^{2\pi} \cos(\theta)\sin(\theta)\mathrm{d}\theta \int_0^{+\infty} \left(r\partial_r^2 \varphi_2(r) + \partial_r \varphi_2(r) \right) \mathrm{d}r \\ &= 0. \end{aligned}$$

- Calculation of I_4:

$$\begin{aligned} I_4 &= \iint_{\mathbb{R}^2} \frac{2x_1}{\|\mathbf{x}\|^2} \Big(\partial_1 \varphi_1(\mathbf{x}) + \partial_2 \varphi_2(\mathbf{x}) \Big) \mathrm{d}\mathbf{x} \\ &= \int_0^{2\pi} \int_0^{+\infty} 2\cos(\theta) \Big(\cos(\theta)\partial_r \varphi_1(r) + \sin(\theta)\partial_r \varphi_2(r) \Big) \mathrm{d}r\mathrm{d}\theta \\ &= 2\int_0^{2\pi} \cos^2(\theta)\mathrm{d}\theta \int_0^{+\infty} \partial_r \varphi_1(r)\mathrm{d}r + 2\int_0^{2\pi} \cos(\theta)\sin(\theta)\mathrm{d}\theta \int_0^{+\infty} \partial_r \varphi_2(r)\mathrm{d}r \\ &= -2\pi\varphi_1(0). \end{aligned}$$

Finally, we get

$$\langle -\mu \triangle \mathbf{u}_\delta + \nabla p_\delta, \boldsymbol{\varphi} \rangle = 4\pi c \mu \varphi_1(0),$$

and we want

$$\langle -\mu \triangle \mathbf{u}_\delta + \nabla p_\delta, \boldsymbol{\varphi} \rangle = \langle \delta_0, \varphi_1 \rangle = \varphi_1(0).$$

We conclude that

$$c = \frac{1}{4\pi\mu}.$$

The same calculations with $\mathbf{F} = {}^t[0,1]$ give the same constant c. By linearity, it holds for any $\mathbf{F}$ in $\mathbb{R}^2$, which ends the proof. □

Proposition 7. *In 3-dimension, the "Stokeslet" is defined by*

$$\begin{aligned} \mathbf{u}_\delta(\mathbf{x}) &= \frac{1}{8\pi\mu} \left(\frac{\mathbb{I}_3}{\|\mathbf{x}\|} + \frac{\mathbf{x} \cdot {}^t\mathbf{x}}{\|\mathbf{x}\|^3} \right) \cdot \mathbf{F} && \in \mathbb{R}^3, \\ &= \frac{1}{8\pi\mu} \begin{bmatrix} \dfrac{f_1}{\|\mathbf{x}\|} + \dfrac{x_1^2 f_1 + x_1 x_2 f_2 + x_1 x_3 f_3}{\|\mathbf{x}\|^3} \\ \dfrac{f_2}{\|\mathbf{x}\|} + \dfrac{x_1 x_2 f_1 + x_2^2 f_2 + x_2 x_3 f_3}{\|\mathbf{x}\|^3} \\ \dfrac{f_3}{\|\mathbf{x}\|} + \dfrac{x_1 x_3 f_1 + x_2 x_3 f_2 + x_3^2 f_3}{\|\mathbf{x}\|^3} \end{bmatrix} && \in \mathbb{R}^3, \qquad (1.4.4) \\ p_\delta(\mathbf{x}) &= \frac{\mathbf{x} \cdot \mathbf{F}}{4\pi\|\mathbf{x}\|^3} = \frac{x_1 f_1 + x_2 f_2 + x_3 f_3}{4\pi\|\mathbf{x}\|^3} && \in \mathbb{R}, \end{aligned}$$

where $\mathbf{F} = {}^t[f_1, f_2, f_3]$ *and* $\mathbf{x} = {}^t[x_1, x_2, x_3]$.

Proof. The proof is the same as in 2-dimension. □

1.4.1.2 Regularity of the solution $(\mathbf{u}, p)$

Let us come back on the focus of Problem (1.3.14). The main difficulty in the study of this kind of problem is the singularity of the source term (and therefore of the solution). In 2-dimension, Problem (1.3.14) has a unique weak solution $(\mathbf{u}, p) \in W^{1,q}(\Omega)^2 \times \mathbb{L}^q_0(\Omega)$ for all $q \in [1, 2[$. Actually, the 2d Stokeslet $(\mathbf{u}_\delta, p_\delta)$ satisfies Problem (1.4.1), so that the Stokeslet $(\mathbf{u}_\delta(\cdot - \mathbf{x}_0), p_\delta(\cdot - \mathbf{x}_0))$ contains the singular part of $(\mathbf{u}, p)$, the solution of Problem (1.3.14). The solution $(\mathbf{u}, p)$ can be built by using a suitable lift procedure which consists in adding to $(\mathbf{u}_\delta, p_\delta)$ a corrector term $(\mathbf{w}, \pi) \in H^1(\Omega)^2 \times \mathbb{L}^2_0(\Omega)$ which satisfies the following problem:

$$\left\{ \begin{array}{rcll} -\triangle \mathbf{w} + \nabla \pi & = & 0 & \text{in } \Omega, \\ \operatorname{div}(\mathbf{w}) & = & 0 & \text{in } \Omega, \\ \mathbf{w} & = & -\mathbf{u}_\delta(\cdot - \mathbf{x}_0) & \text{on } \partial\Omega. \end{array} \right.$$

Then, the solution is given by:

$$\mathbf{u}(\mathbf{x}) = \mathbf{u}_\delta(\mathbf{x}) + \mathbf{w}(\mathbf{x}) = \frac{1}{4\pi} \left(-\ln \|\mathbf{x}\| \mathbb{I}_2 + \frac{\mathbf{x} \cdot {}^t\mathbf{x}}{\|\mathbf{x}\|^2} \right) \mathbf{F} + \mathbf{w}(\mathbf{x}),$$
$$p(\mathbf{x}) = p_\delta(\mathbf{x}) + \pi(\mathbf{x}) = \frac{\mathbf{x} \cdot \mathbf{F}}{2\pi \|\mathbf{x}\|^2} + \pi(\mathbf{x}).$$

Moreover, it is easy to show that $\mathbf{u}_\delta \notin H^1_0(\Omega)^2$ and $p_\delta \notin \mathbb{L}^2(\Omega)$. Actually, we can specify how the quantity $|\mathbf{u}_\delta|_{1,q,\Omega}$ goes to infinity when q goes to 2, with $q < 2$ (which is noted $q \underset{<}{\to} 2$). By (1.4.2), estimating $|\mathbf{u}_\delta|_{1,q,\Omega}$ when $q \underset{<}{\to} 2$ reduces to estimate $|\mathbf{u}_\delta|_{1,q,B}$, where B denotes the ball $B(\mathbf{x}_0, 1)$: we can easily show that there exists $C > 0$ depending only on $\mathbf{F}$ such that

$$\forall 1 \leqslant q < +\infty,\ \mathbf{u}_\delta \in \mathbb{L}^q(\Omega) \quad \text{and} \quad |\nabla \mathbf{u}_\delta| \leqslant \frac{C}{\|\mathbf{x}\|},$$

and so, using polar coordinates, we get for $q < 2$,

$$|\mathbf{u}_\delta|^q_{1,q,\Omega} = \int_B |\nabla \mathbf{u}_\delta(\mathbf{x})|^q \mathrm{d}\mathbf{x} \leqslant \int_B \frac{C^q}{\|\mathbf{x}\|^q} \mathrm{d}\mathbf{x} = C^q \int_0^1 \int_0^{2\pi} \frac{1}{r^{q-1}} \mathrm{d}\theta \mathrm{d}r = 2\pi C^q \frac{1}{2-q}.$$

Finally, there exists $C > 0$ independent of q such that, for $1 \leqslant q < 2$,

$$|\mathbf{u}_\delta|_{1,q,\Omega} \leqslant \frac{C}{\sqrt{2-q}}. \tag{1.4.5}$$

In the same way, we can easily show that there exists $C > 0$ independent of q such that, for $1 \leqslant q < 2$,

$$|p_\delta|_{0,q,\Omega} \leqslant \frac{C}{\sqrt{2-q}}. \tag{1.4.6}$$

In 3-dimension, the punctual force source term is more singular, and the solution $(\mathbf{u}, p)$ belongs to $W^{1,q}(\Omega)^2 \times \mathbb{L}^q_0(\Omega)$ for all $q \in [1, 3/2[$. The construction of the solution $(\mathbf{u}, p)$

is the same as in 2d, and we have: there exists $C > 0$ independent of q such that, for $1 \leqslant q < 3/2$,

$$|\mathbf{u}_\delta|_{1,q,\Omega} \leqslant \frac{C}{(3-2q)^{2/3}} \quad \text{and} \quad |p_\delta|_{0,q,\Omega} \leqslant \frac{C}{(3-2q)^{2/3}}.$$

Let us now do the same developments for the Poisson problem with a Dirac mass right-hand side, which is a scalar version of Problem (1.3.14).

1.4.1.3 Stokeslet in a confined domain

Even if Problem (1.3.14) is singular, each finite element space V_h we consider satisfies

$$V_h \subset \mathscr{C}(\bar{\Omega}),$$

so that the discrete problem (and so the finite element solution) is well-defined. The numerical analysis of such problem is led in Chapter 3. The solution of Problem (1.3.14) is the Stokeslet in a confined domain (in contrast to the Stokeslet defined in the whole domain, Propositions 6 and 7).

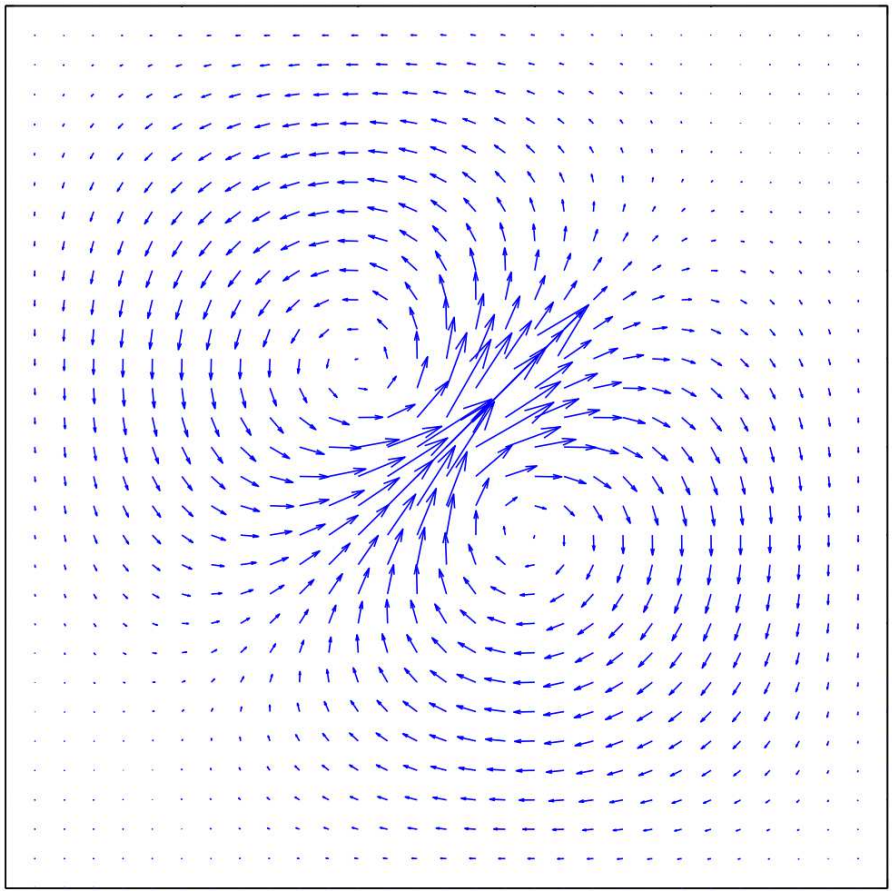

Figure 1.19: Stokeslet 2d in a confined domain.

A numerical solution of the problem 2d is illustrated in Figure 1.19, where Ω is the unit square, $\mathbf{x}_0 = (0.5, 0.5)$ and $\mathbf{F} = {}^t[1, 1]$. Notice that there are recirculations due to the boundedness of the domain.

1.4.2 The Poisson problem with a Dirac mass right-hand side

In this section, we consider the solution u of the following Poisson problem:

$$\left\{ \begin{array}{rcll} -\triangle u & = & \delta_{x_0} & \text{in } \Omega, \\ u & = & 0 & \text{on } \partial\Omega, \end{array} \right. \tag{1.4.7}$$

where Ω is a bounded open smooth subdomain of $\mathbb{R}^d$, $d = 2$ or 3, and $x_0 \in \Omega$. As said at the beginning of this section, we focus also on this problem because it is a scalar version of Problem (1.3.14), and so a simplier problem to lead a preliminary study (see Chapter 2). As it has been done in the case of the Stokes problem, we lead the study in 2-dimension and the results will be also given in 3-dimension.

1.4.2.1 The Green's function

Also for the sake of simplicity, the location of the punctual force is the origin. Let us consider the Poisson problem on the whole domain

$$-\triangle u_\delta = \delta_0 \in \mathbb{R}^2. \tag{1.4.8}$$

The solution of this problem is not unique: if u is a solution and v satisfies $\triangle v = 0$, then $u + v$ is another solution. Proposition 8 gives a particular solution of Problem (1.4.8).

Proposition 8. *The Green's function, defined in 2-dimension by*

$$u_\delta(x) = -\frac{1}{2\pi} \ln \|x\|,$$

is a solution of Problem (1.4.8).

Proof. We search the solution u_δ in the form

$$u_\delta(x) = U(\|x\|),$$

with $U : \mathbb{R}_+^* \to \mathbb{R}$. By the expression of the Laplacian in polar coordinates, we have for any $x \in \mathbb{R}^2 \backslash \{(0, 0)\}$

$$\triangle u_\delta(x) = U''(\|x\|) + \frac{1}{\|x\|} U'(\|x\|).$$

With $r = \|x\|$, u_δ is a solution of Problem (1.4.8) if and only if U satisfies on $\mathbb{R}_+^*$ the differential equation

$$U''(r) + \frac{1}{r} U(r) = 0.$$

The solutions of this equation satisfy

$$U'(r) = ae^{-\ln(r)} = \frac{a}{r},$$

and so are

$$U(r) = a\ln r + b,$$

where a and b are two real constants. It is clear that U is defined ignoring an additive contant so that we can choose $b = 0$. It remains to be determined the constant a: consider $\varphi \in \mathcal{C}_0^\infty(\mathbb{R}^2)$,

$$\begin{aligned}
\langle -\triangle u_\delta, \varphi\rangle &= -\int_{\mathbb{R}^2} u_\delta(x)\triangle\varphi(x)\mathrm{d}x \\
&= -\int_0^{2\pi}\int_0^{+\infty} U(r)\triangle\varphi(r,\theta) r\mathrm{d}r\mathrm{d}\theta \\
&= -\int_0^{2\pi}\int_0^{+\infty} ar\ln r\left(\partial^2_{r,r}\varphi(r,\theta) + \frac{1}{r}\partial_r\varphi(r,\theta) + \frac{1}{r^2}\partial^2_{\theta,\theta}\varphi(r,\theta)\right)\mathrm{d}r\mathrm{d}\theta \\
&= -a\int_0^{2\pi}\left(\Big[r\ln r\partial_r\varphi(r,\theta)\Big]_0^{+\infty} + \int_0^{+\infty}\partial_r\varphi(r,\theta)\left(\ln r - \ln r - 1\right)\mathrm{d}r\right)\mathrm{d}\theta \\
&\quad -a\int_0^{+\infty}\frac{\ln(r)}{r}\Big[\partial_\theta\varphi(r,\theta)\Big]_0^{2\pi}\mathrm{d}r \\
&= -\int_0^{2\pi}\int_0^{+\infty} -\partial_r\varphi(r,\theta)\mathrm{d}r\mathrm{d}\theta \\
&= -2a\pi\varphi(0).
\end{aligned}$$

We conclude that $-\triangle u_\delta = \delta_0$ involves $a = -\dfrac{1}{2\pi}$, and so

$$u_\delta(x) = -\frac{1}{2\pi}\ln\|x\|.$$

□

Remark 2. *Actually, we have shown that there exists an unique radial solution of Problem* (1.4.8) *up to an additive constant. The Green's function is the one for which this constant is zero.*

Proposition 9. *In 3-dimension, the Green's function is given by*

$$u_\delta(x) = \frac{1}{4\pi}\frac{1}{\|x\|}.$$

Proof. The proof is the same as in 2-dimension. □

1.4.2.2 Regularity of the solution u

In this subsection, we focus on the singularity of the solution, which is the main difficulty in the study of this kind of problems. In 2-dimension, Problem (1.4.7) has a unique weak solution $u \in W_0^{1,q}(\Omega)$ for all $q \in [1, 2[$ (see for instance [3]). In fact, the Green's function satisfies $-\triangle u_\delta = \delta_0$, so that $u_\delta(\cdot - x_0)$ contains the singular part of u. As it is done in [3], the solution u can be built by adding to $u_\delta(\cdot - x_0)$ a corrector term $\omega \in H^1(\Omega)$, solution of the Laplace Problem

$$\left\{ \begin{array}{rcll} -\triangle\omega & = & 0 & \text{in } \Omega, \\ \omega & = & -u_\delta(\cdot - x_0) & \text{on } \partial\Omega. \end{array} \right. \tag{1.4.9}$$

Then, the solution of Problem (1.4.7) is given by

$$u(x) = u_\delta(x - x_0) + \omega(x) = -\frac{1}{2\pi}\log(|x - x_0|) + \omega(x).$$

It is easy to verify that $u \notin H_0^1(\Omega)$. Actually, we can specify how the quantity $\|u\|_{1,q,\Omega}$ goes to infinity when q goes to 2, with $q < 2$. By the foregoing, if we write $u = u_\delta + \omega$, since $\omega \in H^1(\Omega)$, estimating $\|u\|_{1,q,\Omega}$ when q converges to 2 from below is reduced to estimate $\|u_\delta\|_{1,q,B}$, where $B = B(0,1)$: $u_\delta \in \mathbb{L}^q(\Omega)$ for all $1 \leqslant q < \infty$, and using polar coordinates, we get, for $q < 2$,

$$|u_\delta|_{1,q,B}^q = \int_B |\nabla u_\delta(x)|^q \mathrm{d}x = \int_0^1 \int_0^{2\pi} \left(\frac{1}{2\pi r}\right)^q r \mathrm{d}\theta \mathrm{d}r = (2\pi)^{1-q} \int_0^1 r^{1-q} \mathrm{d}r = \frac{(2\pi)^{1-q}}{2-q}.$$

Finally, when $q \underset{<}{\to} 2$,

$$\|u\|_{1,q,\Omega} \sim \frac{1}{\sqrt{2\pi}} \frac{1}{\sqrt{2-q}}. \tag{1.4.10}$$

1.4.2.3 Illustration of the solution u

In this case again, even if Problem (1.4.7) is singular, the finite element solution is well-defined. The numerical analysis of this problem is led in Chapter 2. Figure 1.20 illustrates the Green's function in a confined domain, with Ω the unit square and x_0 its center, $x_0 = (0.5, 0.5)$.

The study of the regularity of the solution of the Poisson problem (1.4.7) ends this chapter. The next chapter is devoted to the analysis of the finite element method applied to solve the Poisson problem with a Dirac mass right-hand side. In Chapter 3, we lead the study in the case of the Stokes problem with a punctual force in source term. In the last chapter, we detail a new numerical method to solve these problems and present numerical results got for the mucociliary transport.

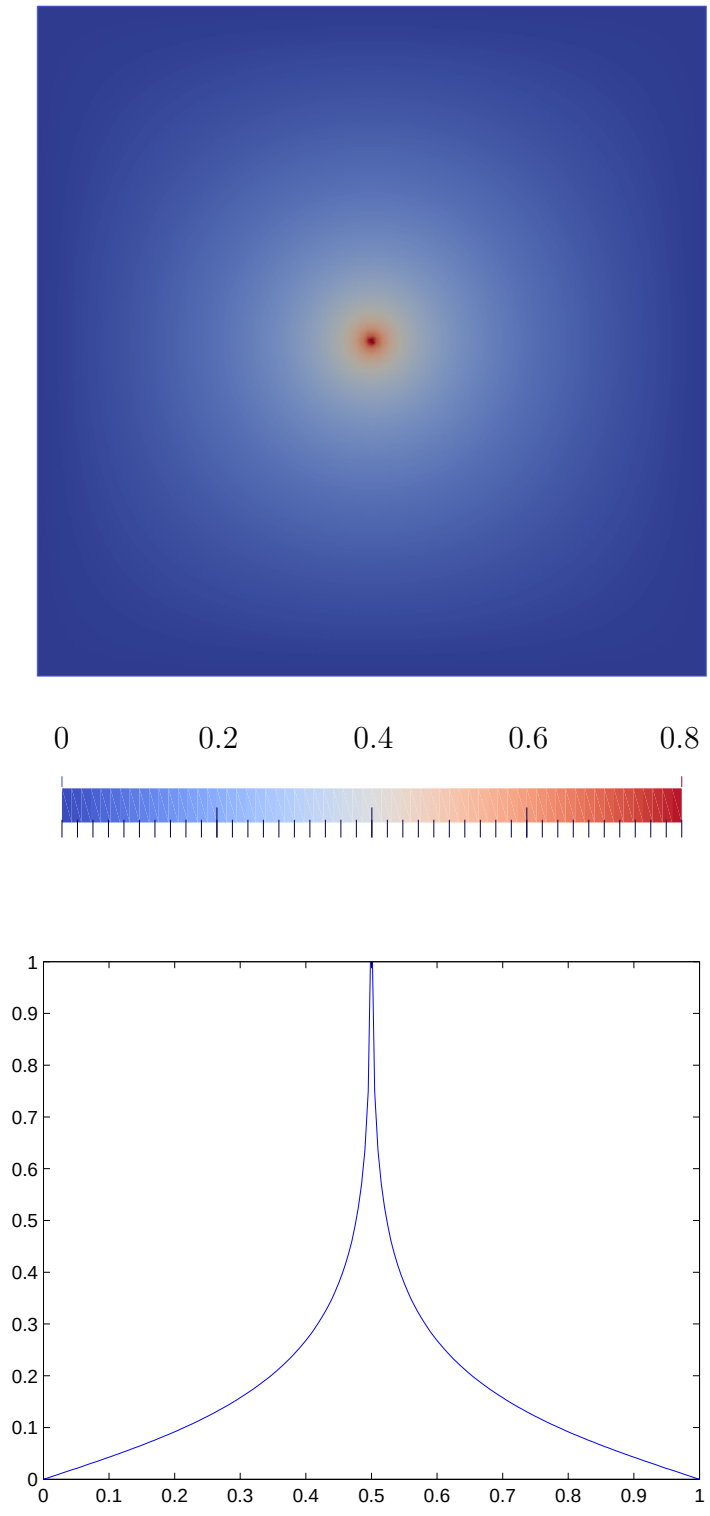

Figure 1.20: Solution u of Problem (1.4.7) in 2d and its section $\{y = 0.5\}$.

CHAPTER 2

LOCAL ERROR ESTIMATES OF THE FINITE ELEMENT METHOD FOR THE POISSON PROBLEM WITH A DIRAC RIGHT-HAND SIDE

Contents

The solutions of elliptic problems with a Dirac measure right-hand side are not H^1 and therefore the convergence of the finite element solutions is suboptimal. The use of graded meshes is standard remedy to recover quasi-optimality, namely optimality up to a log-factor, for low order finite elements in the $\mathbb{L}^2$-norm. Optimal (or quasi-optimal for the lowest order case) convergence for Lagrange finite elements has been shown, in the $\mathbb{L}^2$-norm, on a subdomain which excludes the singularity. Here, on such subdomains, we show a quasi-optimal convergence in the H^s-norm, for $s \geqslant 1$, and, in the particular case of Lagrange finite elements, an optimal convergence in H^1-norm, on a family of quasi-uniform meshes in dimension 2. The study of this problem is motivated by the use of the Dirac measure as a reduced model in physical problems, for which high accuracy of the finite element method at the singularity is not required. Our results are obtained using local Nitsche and Schatz-type error estimates, a weak version of Aubin-Nitsche duality lemma and a discrete inf-sup condition. These theoretical results are confirmed by numerical illustrations.

2.1 Introduction

This chapter deals with the accuracy of the finite element method on the Poisson problem with a singular right-hand side. More precisely, let us consider the Dirichlet problem

$$(P_\delta) \left\{ \begin{array}{rcll} -\triangle u & = & \delta_{x_0} & \text{in } \Omega, \\ u & = & 0 & \text{on } \partial\Omega, \end{array} \right.$$

where $\Omega \subset \mathbb{R}^2$ is a bounded open $\mathcal{C}^\infty$ domain or a square, and δ_{x_0} denotes the Dirac measure concentrated at a point $x_0 \in \Omega$ such that $\mathrm{dist}(x_0, \partial\Omega) > 0$.

Problems of this type occur in many applications from different areas, like in the mathematical modeling of electromagnetic fields [59]. Dirac measures can also be found on the right-hand side of adjoint equations in optimal control of elliptic problems with state constraints [26]. As further examples where such measures play an important role, we mention controllability for elliptic and parabolic equations [27, 28, 73] and parameter identification problems with pointwise measurements [93].

Our interest in (P_δ) is motivated by the modeling of the movement of a thin structure in a viscous fluid, such as cilia involved in the muco-ciliary transport in the lung [48]. In the asymptotic of a zero diameter cilium with an infinite velocity, the cilium is modelled by a line Dirac of force in the source term. In order to make the computations easier, the line Dirac of force can be approximated by a sum of punctual Dirac forces distributed along the cilium [67]. In this chapter, we address a scalar version of this problem: problem (P_δ).

In the regular case, namely the Poisson problem with a regular right-hand side, the finite element solution u_h is well-defined and for $u \in H^{k+1}(\Omega)$, we have, for all $0 \leqslant s \leqslant 1$,

$$\|u - u_h\|_s \leqslant C h^{k+1-s} \|u\|_{k+1}, \tag{2.1.1}$$

where k is the degree of the method [32] and h the mesh size. As can be noticed, the efficiency of the method critically depends on regularity of the solution. We aim at describing the impact of the loss of the regularity of the solution over the classical estimates

due to irregular source term. In dimension 1, the solution u of Problem (P_δ) belongs to $H^1(\Omega)$, but it is not $H^2(\Omega)$. In this case, the numerical solution u_h and the exact solution u can be computed explicitly. If x_0 matches with a node of the discretization, $u_h = u$. Otherwise, this equality is true only on the complementary of the element which contains x_0, and the convergence orders are $1/2$ and $3/2$ respectively in H^1-norm and $\mathbb{L}^2$-norm. In dimension 2, Problem (P_δ) has no $H^1(\Omega)$-solution, and so, although the finite element solution can be defined, the $H^1(\Omega)$-error has no sense and the $\mathbb{L}^2(\Omega)$-error estimates cannot be obtained by the Aubin-Nitsche method without modification.

Let us review the literature about error estimates for problem (P_δ), starting with discretizations on quasi-uniform meshes. Babuška [5] showed an $\mathbb{L}^2(\Omega)$-convergence of order $h^{1-\eta}$, $\eta > 0$, for a two-dimensional smooth domain. Scott proved in [99] an a priori error estimates of order $2 - \frac{d}{2}$, where the dimension d is 2 or 3. The same result has been proved by Casas [25] for general Borel measures on the right-hand side.

To the best of our knowledge, in order to improve the convergence order, Eriksson [44] was the first who studied the influence of locally refined meshes near x_0. Using results from [97], he proved convergence of order k and $k+1$ in the $W^{1,1}(\Omega)$-norm and the $\mathbb{L}^1(\Omega)$-norm respectively, for approximations with a $\mathbb{P}_k$-finite element method. Recently, by Apel and co-authors [2], an $\mathbb{L}^2(\Omega)$-error estimate of order $h^2|\ln h|^{3/2}$ has been proved in dimension 2, using graded meshes. Optimal convergence rates with graded meshes were also recovered by D'Angelo [38] using weighted Sobolev spaces. A posteriori error estimates in weighted spaces have been established by Agnelli and co-authors [1].

These theoretical a priori results are based upon graded meshes, which increase the complexity of the meshing and the computational cost, even if the mesh is refined only locally, especially when the right-hand side includes several Dirac measures, that can be static or moving. Therefore Eriksson [43] developed a numerical method to solve the problem and recover the optimal convergence rate: the numerical solution is searched in the form $u_0 + w_h$ where u_0 contains the singularity of the solution and w_h is the numerical solution of a smooth problem. This method is presented in the case of the Poisson and the Stokes problems in [67].

However, in applications, the Dirac measure at x_0 is often a model reduction approach, and a high accuracy at x_0 of the finite element method is not necessary. Thus, it is interesting to study the error on a fixed subdomain which excludes the singularity. Recently, Köppl and Wohlmuth have shown in [66] optimal convergence in $\mathbb{L}^2$-norm for the Lagrange finite elements (the result is quasi-optimal for the P^1-element). In this chapter, we consider the problem in dimension 2, and we show :

1. Quasi-optimal convergence in H^s-norm, for $s \geqslant 1$. This result applies to a wide class of finite-element methods and beyond, including Lagrange and Hermite finite elements and wavelets. The $\mathbb{L}^2$-error estimates established in [66] are not used and the proof is based on different arguments.

2. Optimal convergence in H^1-norm for the Lagrange finite elements. This result is obtained by direct use of the optimal $\mathbb{L}^2$-norm convergence result in [66].

3. Optimal convergence in H^1-norm in the particular case of the P^1-Lagrange finite element using different arguments than those used for the previous results.

These results imply that graded meshes are not required to recover optimality far from the singularity and that there are no pollution effects. In addition, by linearity of Problem (P_δ), the result holds in the case of several Dirac masses. The chapter is organized as follows. We begin with the 1-dimensional case, Section 2.2. Our main results are presented in Section 2.3 after recalling the Nitsche and Schatz Theorem, which is an important tool for the proof presented in Section 2.4. In Section 2.5 another argument is presented to obtain an optimal estimate in the particular case of the P_1-finite elements. We illustrate in Section 2.6 our theoretical results by numerical simulations and, in Section 2.7, we discuss the generalization of our approach to the three-dimensional case.

2.2 Preliminaries: one-dimensional case

Before getting to the heart of the matter, let us consider the problem in dimension 1. We consider $I =]a, b[$ and suppose that the Dirac mass δ is supported by $x_0 \in]a, b[$. In dimension 1, the problem (P_δ) can be written as

$$(P_\delta^1) \begin{cases} -u'' = \delta_{x_0} \text{ in }]a, b[, \\ u(a) = u(b) = 0. \end{cases}$$

It is easy to show that the solution u of the Poisson problem (P_δ^1) (drawn on Figure 2.1) is given by

$$u(x) = \begin{cases} \dfrac{b - x_0}{b - a}(x - a) & \text{if } x \in [a, x_0], \\ \dfrac{x_0 - a}{b - a}(b - x) & \text{if } x \in [x_0, b]. \end{cases} \tag{2.2.1}$$

In dimension 1 (and only in dimension 1), the solution u belongs to $H_0^1(I)$ (actually, it belongs to $H^{3/2-\eta}(I)$ for all $\eta > 0$). In this section, the study is limited to the case of the Lagrange finite elements $\mathbb{P}_1$ but the results can be easily extended to $\mathbb{P}_k$-finite elements. Moreover, it is possible to write an explicit form of the numerical solution u_h.

Theorem 2. *Let $\mathcal{T}_h$ be a discretization of the interval $I =]a, b[$, the numerical solution u_h satisfies one of the two following assertions :*

- *if x_0 is a point of the discretization $\mathcal{T}_h$ (mesh 1 on Figure 2.1), $u_h = u$.*
- *if x_0 is not a point of the discretization $\mathcal{T}_h$ (mesh 2 on Figure 2.1), by denoting x_i and x_{i+1} the two consecutive points of the discretization $\mathcal{T}_h$ such as $x_i < x_0 < x_{i+1}$, the numerical solution u_h is equal to the exact solution u on the closed sub-domain $[a, x_i] \cup [x_{i+1}, b]$, it is continue on I and affine on $[x_i, x_{i+1}]$ (see Figure 2.1). Actually, the numerical solution u_h is equal on I to the interpolation $I_h u$. Moreover, the convergence can be specified :*

$$\|u - u_h\|_{1,I} \leqslant C\sqrt{h} \quad \text{and} \quad \|u - u_h\|_{0,I} \leqslant Ch^{3/2}. \tag{2.2.2}$$

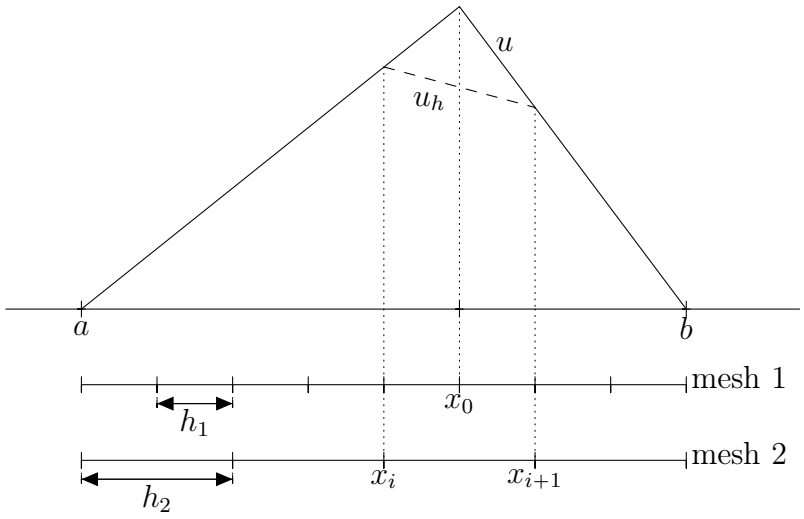

Figure 2.1: Exact solution and numerical solution in dimension 1.

Remark 3. *In dimension 1, the discretization $\mathcal{T}_h$ does not need to be uniform or quasi-uniform. Estimates* (2.2.2) *are true for $h = x_{i+1} - x_i$, the length of the segment which contains the point x_0.*

Proof. If x_0 is a point of the discretization $\mathcal{T}_h$, u belongs to the approximation space V_h, and a direct consequence of the Cea lemma is $u_h = u$. Otherwise, let us look at the discrete right-hand side corresponding to the Dirac measure δ_{x_0} : it is of the form

$$\begin{array}{c} \\ i \\ i+1 \end{array} \begin{bmatrix} 0 \\ \vdots \\ \alpha \\ \beta \\ \vdots \\ 0 \end{bmatrix} = \begin{bmatrix} 0 \\ \vdots \\ \alpha \\ 0 \\ \vdots \\ 0 \end{bmatrix} + \begin{bmatrix} 0 \\ \vdots \\ 0 \\ \beta \\ \vdots \\ 0 \end{bmatrix},$$

where $\alpha = v_i(x_0)$ and $\beta = v_{i+1}(x_0)$, with v_i and v_{i+1} the test functions corresponding to the points x_i and x_{i+1} of the mesh. By linearity of problem (P^1_δ), the numerical solution u_h is given by

$$u_h = u^h_\alpha + u^h_\beta,$$

where u^h_α and u^h_β are respectively the numerical solutions of problems

$$(P_\alpha) \begin{cases} -u''_\alpha = \alpha\delta_{x_i} \text{ in }]a,b[, \\ u_\alpha(a) = u_\alpha(b) = 0, \end{cases} \quad \text{and} \quad (P_\beta) \begin{cases} -u''_\beta = \beta\delta_{x_{i+1}} \text{ in }]a,b[, \\ u_\beta(a) = u_\beta(b) = 0. \end{cases}$$

Each of these problems satisfies the first item of Theorem 2, and thus, by (2.2.1),

$$u_\alpha^h(x) = \begin{cases} \alpha \dfrac{b - x_i}{b - a}(x - a) & \text{if } x \in [a, x_i], \\ \alpha \dfrac{x_i - a}{b - a}(b - x) & \text{if } x \in [x_i, b], \end{cases}$$

$$u_\beta^h(x) = \begin{cases} \beta \dfrac{b - x_{i+1}}{b - a}(x - a) & \text{if } x \in [a, x_{i+1}], \\ \beta \dfrac{x_{i+1} - a}{b - a}(b - x) & \text{if } x \in [x_{i+1}, b], \end{cases}$$

with

$$\alpha = \frac{x_{i+1} - x_0}{x_{i+1} - x_i} \quad \text{and} \quad \beta = \frac{x_0 - x_i}{x_{i+1} - x_i}.$$

Finally, since the function $u_h = u_\alpha^h + u_\beta^h$ is continuous and affine on each of the segments $[a, x_i]$, $[x_i, x_{i+1}]$ and $[x_{i+1}, b]$, it remains only to verify that the function u_h satisfies

$$u_h(a) = u_h(b) = 0, u_h(x_i) = u(x_i) \text{ and } u_h(x_{i+1}) = u(x_{i+1}).$$

Now that the analytic expressions of u and u_h are known, error Estimates (2.2.2) can be deduced from a direct calculation of the error on the segment $[x_i, x_{i+1}]$. □

Remark 4. *Since in one dimension the solution u belongs to $H^1(I)$, the finite element method is well-defined, but the solution does not belong to $H^2(I)$, and thus the classical error Estimates* (2.1.1) *are no longer valid: the order of convergence is 1/2 in H^1-norm and 3/2 in $\mathbb{L}^2$-norm against respectively 1 and 2 in the regular case.*

We have proved with Theorem 2 that in dimension 1 the numerical solution is equal to the exact solution outside the segment of the mesh which contains the singularity. Moreover, if the point x_0 matches with a point of the discretization, the numerical solution is actually the exact solution. Thus, if the mesh can be chosen conformed to the singularity, the error of the finite element method is zero. The following focuses on the local error far from the Dirac mass in dimension 2. As it will be seen, the 1-dimension arguments cannot be used anymore.

2.3 Main results

In this section, we define all the notations used in this chapter, recall an important tool for the proof, the Nitsche and Schatz Theorem, and formulate our main results.

2.3.1 Notations

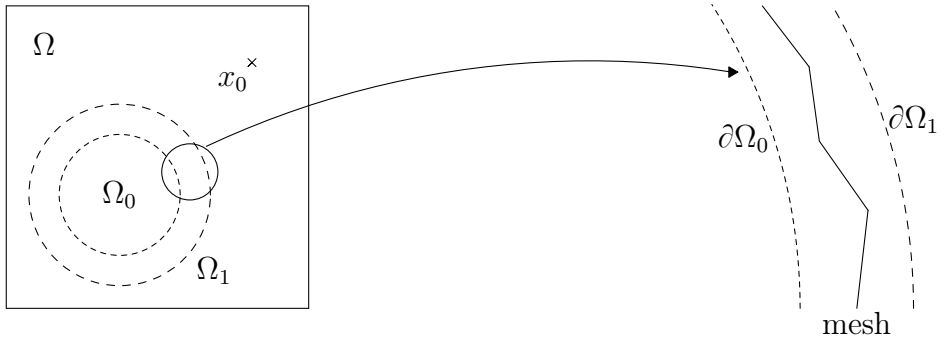

Figure 2.2: Domains Ω_0 and Ω_1.

For a domain D, we denote by $\|\cdot\|_{s,q,D}$ (respectively $|\cdot|_{s,q,D}$) the norm (respectively the semi-norm) of the Sobolev space $W^{s,q}(D)$, while $\|\cdot\|_{s,D}$ (respectively $|\cdot|_{s,D}$) stand for the norm (respectively the semi-norm) of the Sobolev space $H^s(D)$.

For the numerical solution, let us introduce a family of quasi-uniform simplicial triangulations $\mathcal{T}_h$ of Ω and a finite element space $V_h^k \subset H_0^1(\Omega)$, where k is the order of approximation. To ensure that the numerical solution is well-defined, the space V_h^k is assumed to contain only continuous functions. The finite element solution $u_h \in V_h^k$ of problem (P_δ) is defined by

$$\int_\Omega \nabla u_h \cdot \nabla v_h = v_h(x_0), \ \forall v_h \in V_h^k. \tag{2.3.1}$$

We also evaluate the H^s-norm of the error on a subdomain of Ω which does not contain the singularity, for $s \geqslant 2$, and, whenever we do so, we of course assume the finite elements are H^s-conform. We fix two subdomains of Ω, named Ω_0 and Ω_1, such that $\Omega_0 \subset\subset \Omega_1 \subset\subset \Omega$ and $x_0 \notin \overline{\Omega_1}$ (see Figure 2.2). We consider a mesh which satisfies the following condition:

Assumption 1. *For some h_0, we have for all $0 < h \leqslant h_0$ (see Figure 2.2),*

$$\overline{\Omega}_0^m \bigcap \Omega_1^c = \varnothing, \ \textit{where } \overline{\Omega}_0^m = \bigcup_{\substack{T\in\mathcal{T}_h \\ T\bigcap\Omega_0\neq\varnothing}} T,$$

and Ω_1^c is the complement of Ω_1 in Ω.

2.3.2 Nitsche and Schatz Theorem

Before stating the Nitsche and Schatz Theorem, let us introduce properties satisfied by the finite element spaces V_h^k.

Assumption 2. *Given two fixed concentric spheres B_0 and B with $B_0 \subset\subset B \subset\subset \Omega$, there exists an h_0 such that for all $0 < h \leqslant h_0$, we have for some $R \geqslant 1$ and $M > 1$:*

A1 *For any $0 \leqslant s \leqslant R$ and $s \leqslant \ell \leqslant M$, for each $v \in H^\ell(B)$, there exists $\eta \in V_h^k$ such that*

$$\|v - \eta\|_{s,B} \leqslant Ch^{\ell-s}\|v\|_{\ell,B}.$$

Moreover, if $v \in H_0^1(B_0)$ then η can be chosen to satisfy $\eta \in H_0^1(B)$.

A2 *Let $\varphi \in \mathscr{C}_0^\infty(B_0)$ and $v_h \in V_h^k$, then there exists $\eta \in V_h^k \bigcap H_0^1(B)$ such that*

$$\|\varphi v_h - \eta\|_{1,B} \leqslant C(\varphi, B, B_0)h\|v_h\|_{1,B}.$$

A3 *For each $h \leqslant h_0$ there exists a domain B_h with $B_0 \subset\subset B_h \subset\subset B$ such that if $0 \leqslant s \leqslant \ell \leqslant R$ then for all $v_h \in V_h^k$ we have*

$$\|v_h\|_{\ell,B_h} \leqslant Ch^{s-\ell}\|v_h\|_{s,B_h}.$$

We now state the following theorem, a key tool in the forthcoming proof of Theorem 3.

Theorem (Nitsche and Schatz [88])**.** *Consider $\Omega_0 \subset\subset \Omega_1 \subset\subset \Omega$ and let V_h^k satisfy Assumption 2. Let $v \in H^\ell(\Omega_1)$, let $v_h \in V_h^k$ and let t be a nonnegative integer, arbitrary but fixed. Let us suppose that $v - v_h$ satisfies*

$$\int_\Omega \nabla(v - v_h) \cdot \nabla\eta = 0, \ \forall \eta \in V_h^k \bigcap H_0^1(\Omega_1).$$

Then there exists h_1 such that if $h \leqslant h_1$ we have

(i) for $s = 0, 1$ and $1 \leqslant \ell \leqslant M$,

$$\|v - v_h\|_{s,\Omega_0} \leqslant C\left(h^{\ell-s}\|v\|_{\ell,\Omega_1} + \|v - v_h\|_{-t,\Omega_1}\right),$$

(ii) for $2 \leqslant s \leqslant \ell \leqslant M$ and $s \leqslant k < R$,

$$\|v - v_h\|_{s,\Omega_0} \leqslant C\left(h^{\ell-s}\|v\|_{\ell,\Omega_1} + h^{1-s}\|v - v_h\|_{-t,\Omega_1}\right).$$

For our study, we actually need a more general version of the assumptions on the approximation space V_h^k:

Assumption 3. *Given $B \subset \Omega$ and $q' \geqslant 2$, there exists an h_0 such that for all $0 < h \leqslant h_0$, we have for some $R \geqslant 1$ and $M > 1$:*

$\widetilde{\text{A1}}$ *For any $0 \leqslant s \leqslant R$ and $s \leqslant \ell \leqslant M$, for each $v \in H^\ell(B)$, there exists $\eta \in V_h^k$ such that, for any finite element $T \subset B$,*

$$|v - \eta|_{s,q',T} \leqslant Ch^{d(1/q'-1/2)}h^{\ell-s}|v|_{\ell,2,T}.$$

$\widetilde{\mathbf{A3}}$ *For $0 \leqslant s \leqslant \ell \leqslant R$, for all $v_h \in V_h^k$, for any finite element T in the family $\mathcal{T}_h$, we have*

$$\|v_h\|_{\ell,q',T} \leqslant Ch^{2(1/q'-1/2)}h^{s-\ell}\|v_h\|_{s,2,T}.$$

Assumptions $\widetilde{\mathbf{A1}}$ and $\widetilde{\mathbf{A3}}$ are generalizations of Assumptions **A1** and **A3**. They are quite standard and satisfied by a wide variety of approximation spaces, including all finite element spaces defined on quasi-uniform meshes [32]. The parameters R and M play respectively the role of the regularity and order of approximation of the approximation space V_h^k. For example, in the case of $\mathbb{P}_1$-finite elements, we have $R = 3/2 - \varepsilon$ and $M = 2$. Assumption **A2** is less common but also satisfied by a wide class of approximation spaces. Actually, for Lagrange and Hermite finite elements, a stronger property than Assumption **A2** can be shown as a consequence of Assumptions **A1** and **A3**:

Lemma 1. *Let us consider Lagrange finite elements, or Hermite finite elements if $s > 1$, we still denote by V_h^k the approximation space of degre k. Given two concentric spheres B_0 and B with $B_0 \subset\subset B \subset\subset \Omega$, and let us fix $\varphi \in \mathscr{C}_0^\infty(B_0)$. For any $0 \leqslant s \leqslant \ell \leqslant k$ and any $v_h \in V_h^k$, there exists $\eta \in V_h^k \bigcap H_0^1(B)$ such as*

$$\|\varphi v_h - \eta\|_{s,B} \leqslant C(\varphi)h^{\ell-s+1}\|v_h\|_{\ell,B}.$$

Applied for $s = \ell = 1$, Lemma 1 gives assumption **A2**. The proof is inspired from the ones presented in a more general case in [8].

Proof. Let $0 \leqslant s \leqslant k$. Since $\varphi \in \mathscr{C}_0^\infty(B)$, by Assumption **A1**, there exists $\eta \in V_h^k \bigcap H_0^1(B)$ such that

$$\|\varphi v_h - \eta\|_{s,B} \leqslant Ch^{k+1-s}\|\varphi v_h\|_{k+1,B}.$$

So we can write

$$\|\varphi v_h - \eta\|_{s,B}^2 \leqslant Ch^{2(k+1-s)} \sum_{T\in\mathcal{T}_h} \|\varphi v_h\|_{k+1,T}^2.$$

In order to bound the quantity $\|\varphi v_h\|_{k+1,T}$, we need the following result:

Proposition 10 (Ciarlet, page 192 [32])**.** *Let G be a subset of $\mathbb{R}^d$ and an integer $k \geqslant 1$, let $a \in W^{k,\infty}(G)$ and $b \in H^k(G)$. Then $ab \in H^k(G)$ and*

$$\|ab\|_{k,G} \leqslant C\left(|a|_{0,\infty,G}|b|_{k,G} + \|a\|_{k,\infty,G}\|b\|_{k-1,G}\right).$$

Applied for $G = T \in \mathcal{T}_h$, $a = \varphi$ and $b = v_h$, Proposition 10 gives

$$\|\varphi v_h\|_{k+1,T} \leqslant C\left(|\varphi|_{0,\infty,T}|v_h|_{k+1,T} + \|\varphi\|_{k,\infty,T}\|v_h\|_{k,T}\right).$$

Since $v_h \in \mathbb{R}_k[X]$, $|v_h|_{k+1,T} = 0$, and so

$$\|\varphi v_h\|_{k+1,T} \leqslant C\|\varphi\|_{k,\infty,T}\|v_h\|_{k,T}.$$

Thus, we get: there exists $\eta \in V_h^k \bigcap H_0^1(B)$ such that

$$\|\varphi v_h - \eta\|_{s,B} \leqslant C(\varphi)h^{k+1-s}\|v_h\|_{k,B}.$$

To end the proof, we use Assumption **A3**: for any $0 \leqslant \ell \leqslant k$,

$$\|v_h\|_{k,B} \leqslant Ch^{\ell-k}\|v_h\|_{\ell,B}.$$

Finally, there exists $\eta \in V_h^k \bigcap H_0^1(B)$ such that

$$\|\varphi v_h - \eta\|_{s,B} \leqslant C(\varphi)h^{\ell-s+1}\|v_h\|_{\ell,B}.$$

□

2.3.3 Statement of our main results

Our main results are Theorems 3, 4 and 5. The rest of the chapter is mostly concerned by the proof and the illustration of these results.

Theorem 3. *Let $\Omega_0 \subset\subset \Omega_1 \subset\subset \Omega$ satisfy Assumption 1, $1 \leqslant s \leqslant k$. Let u be the solution of problem (P_δ) and u_h its Galerkin projection onto V_h^k, satisfying* (2.3.1)*. Under Assumptions 2 and 3, there exists h_1 such that if $0 < h \leqslant h_1$, we have,*

$$\|u - u_h\|_{1,\Omega_0} \leqslant C(\Omega_0, \Omega_1, \Omega)h^k\sqrt{|\ln h|}. \tag{2.3.2}$$

In addition, for $s \geqslant 2$, if the finite elements are supposed H^k-conforming, we have

$$\|u - u_h\|_{s,\Omega_0} \leqslant C(\Omega_0, \Omega_1, \Omega)h^{k+1-s}\sqrt{|\ln h|}. \tag{2.3.3}$$

Remark 5. *The main tool in proving Theorem 3 is the Nitsche and Schatz Theorem, and the result holds for all the spaces verifying Assumptions 2 and 3. The class of such spaces includes spaces beyond finite elements, including, for instance, wavelets.*

Section 2.4 is dedicated to the proof of Theorem 3.

In the particular case of Lagrange finite elements, Köppl and Wohlmuth [66] showed, in the $\mathbb{L}^2$-norm of a subdomain which does not contain x_0, quasi-optimality for the lowest order case, and optimal a priori estimates for higher order. The proof is based on Wahlbin-type arguments, which are similar to the Nitsche and Schatz Theorem (see [112, 113]), and different arguments from the ones presented in this chapter, like the use of an operator of Scott and Zhang type [100]. Using this result it is possible to prove quite easily optimal convergence in H^1-norm for Lagrange finite elements. This result reads as follows:

Theorem 4. *Consider a domain Ω_2 such that $\Omega_0 \subset\subset \Omega_1 \subset\subset \Omega_2 \subset\subset \Omega$, $x_0 \notin \overline{\Omega_2}$, and satisfying Assumption 1. Let u be the solution of problem (P_δ) and u_h its Galerkin projection onto the space of Lagrange finite elements of order $k+1$. There exists h_1 such that if $0 < h \leqslant h_1$, we have*

$$\|u - u_h\|_{1,\Omega_0} \leqslant C(\Omega_1, \Omega_2, \Omega)h^k.$$

Remark 6. *This result is optimal and thus slightly stronger than Inequality* (2.3.2)*, but it is limited to Lagrange finite elements and to the H^1-norm, due to the use of an operator of Scott-Zhang type. Theorem 3 is more general: it holds for a wide class of finite elements and it allows to estimate the error in H^s-norm, for any $s \geqslant 1$.*

Proof of Theorem 4. In the particular case of Lagrange finite elements, Köppl and Wohlmuth proved in [66] the following convergence in the $\mathbb{L}^2$-norm of a subdomain which does not contain x_0:

$$\|u - u_h\|_{0,\Omega_1} \leqslant C(\Omega_1, \Omega_2, \Omega) \begin{cases} h^2 |\ln(h)| & \text{if } k = 1, \\ h^{k+1} & \text{if } k > 1. \end{cases} \tag{2.3.4}$$

Let us apply the Nitsche and Schatz Theorem on Ω_0 and Ω_1 for $l = k + 1$ and $t = 0$,

$$\|u - u_h\|_{1,\Omega_0} \leqslant C \left(h^k \|u\|_{2,\Omega_1} + \|u - u_h\|_{0,\Omega_1} \right).$$

Using (2.3.4), we get

$$\|u - u_h\|_{1,\Omega_0} \leqslant C h^k.$$

□

For the particular P_1-Lagrange finite elements, we prove the optimal convergence in H^1-norm using completely different arguments. This proof involves a technical assumption on the mesh, namely Assumption 4 in Section 2.5.2: the distance of the Dirac mass to the edges of the mesh triangles is assumed to be at least of the same order as the mesh size h. The result reads as follows:

Theorem 5. *Let $\Omega_0 \subset\subset \Omega_1 \subset\subset \Omega$ satisfy Assumption 1 and consider a mesh such that there exists a domain B_ε satisfying Assumption 4 with ε of the same order as the mesh size. The P_1-finite element method converges with order 1 for the $H^1(\Omega_0)$-norm. More precisely:*

$$\|u - u_h\|_{1,\Omega_0} \leqslant C(\Omega_0, \Omega_1, \Omega) h.$$

The proof of this result is detailed in Section 2.5.

2.4 Proof of Theorem 3

This section is devoted to the proof of Theorem 3. We first show a weak version of the Aubin-Nitsche duality lemma (Lemma 2) and establish a discrete inf-sup condition (Lemma 3). Then, we use these results to prove Theorem 3.

2.4.1 Aubin-Nitsche duality lemma with a singular right-hand side

The proof of Theorem 3 is based on Nitsche and Schatz Theorem. In order to estimate the quantity $\|u - u_h\|_{-t,\Omega_1}$, we first show a weak version of Aubin-Nitsche Lemma, in the case of the Poisson problem with a singular right-hand side.

Lemma 2. *Let $f \in W^{-1,q}(\Omega) = (W_0^{1,q'}(\Omega))'$, $1 < q < 2$, and $v \in W_0^{1,q}(\Omega)$ be the unique solution of*

$$\left\{ \begin{array}{rcl} -\triangle v & = & f \quad \textit{in } \Omega, \\ v & = & 0 \quad \textit{on } \partial\Omega. \end{array} \right.$$

Let $v_h \in V_h^k$ be the Galerkin projection of v. For finite elements of order k, letting $e = v - v_h$, we have for all $0 \leqslant t \leqslant k-1$,

$$\|e\|_{-t,\Omega} \leqslant Ch^{t+1}h^{2(1/q'-1/2)}|e|_{1,q,\Omega}. \tag{2.4.1}$$

Proof. We aim at estimating, for $t \geqslant 0$, the H^{-t}-norm of the error e:

$$\|e\|_{-t,\Omega} = \sup_{\phi \in \mathscr{C}_0^\infty(\Omega)} \frac{|\int_\Omega e\phi|}{\|\phi\|_{t,\Omega}}. \tag{2.4.2}$$

The error $e \in W_0^{1,q}(\Omega)$ satisfies

$$\int_\Omega \nabla e \cdot \nabla \eta = 0, \ \forall \eta \in V_h^k.$$

Let be $\phi \in \mathscr{C}_0^\infty(\Omega)$ and let $w^\phi \in H^{t+2}$ be the solution of

$$\left\{ \begin{array}{rcl} -\triangle w^\phi & = & \phi \quad \text{in } \Omega, \\ w^\phi & = & 0 \quad \text{on } \partial\Omega. \end{array} \right.$$

In dimension 2, by the Sobolev injections established in [20], $H^{t+2}(\Omega) \subset W^{1,q'}(\Omega)$ for all q' in $[2, +\infty[$. Thus, for any $w_h \in V_h^k$,

$$\left|\int_\Omega e\phi\right| = \left|\int_\Omega e\triangle w^\phi\right| = \left|\int_\Omega \nabla e \cdot \nabla w^\phi\right| = \left|\int_\Omega \nabla e \cdot \nabla(w^\phi - w_h)\right| \leqslant |w^\phi - w_h|_{1,q',\Omega}|e|_{1,q,\Omega}.$$

We have to estimate $|w^\phi - w_h|_{1,q',\Omega}$. It holds

$$|w^\phi - w_h|_{1,q',\Omega}^{q'} = \sum_T |w^\phi - w_h|_{1,q',T}^{q'}.$$

For all $0 \leqslant t \leqslant k-1$ and for all element T in $\mathcal{T}_h$, thanks to Assumption $\widetilde{\mathbf{A1}}$ applied for $s = 1$, $\ell = t+2$, there exists $w_h \in V_h^k$ such as

$$|w^\phi - w_h|_{1,q',T} \leqslant Ch^{2(1/q'-1/2)}h^{t+1}|w^\phi|_{t+2,2,T}. \tag{2.4.3}$$

We number the triangles of the mesh $\{T_i, i = 1, \cdots, N\}$ and we set

$$a = (a_i)_i \text{ and } b = (b_i)_i, \text{ where } a_i = |w^\phi - w_h|_{1,q',T_i} \text{ and } b_i = |w^\phi|_{t+2,2,T_i}.$$

By (2.4.3), we have, for all i in $[\![1, N]\!]$,

$$a_i \leqslant Ch^{2(1/q'-1/2)}h^{t+1}b_i.$$

We recall the norm equivalence in $\mathbb{R}^N$ for $0 < r < s$,

$$\|x\|_{\ell^s} \leqslant \|x\|_{\ell^r} \leqslant N^{1/r-1/s}\|x\|_{\ell^s}.$$

Remark that here $N \sim Ch^{-2}$. As $2 < q'$, we have $\|b\|_{\ell^{q'}} \leqslant \|b\|_{\ell^2}$. Then, we can write

$$\begin{aligned}|w^\phi - w_h|_{1,q',\Omega} = \|a\|_{\ell^{q'}} &\leqslant Ch^{t+1}h^{2(1/q'-1/2)}\|b\|_{\ell^{q'}},\\ &\leqslant Ch^{t+1}h^{2(1/q'-1/2)}\|b\|_{\ell^2},\\ &\leqslant Ch^{t+1}h^{2(1/q'-1/2)}|w^\phi|_{t+2,2,\Omega},\\ &\leqslant Ch^{t+1}h^{2(1/q'-1/2)}\|\phi\|_{t,\Omega}.\end{aligned}$$

Finally, using this estimate in (2.4.2), we obtain, for $t \leqslant k-1$,

$$\|e\|_{-t,\Omega} \leqslant Ch^{t+1}h^{2(1/q'-1/2)}|e|_{1,q,\Omega}.$$

□

Corollary 1. *For finite elements of order k, for any $0 < \varepsilon < 1$,*

$$\|u - u_h\|_{-k+1,\Omega} \leqslant Ch^k h^{-\varepsilon}|u - u_h|_{1,q_\varepsilon,\Omega}. \tag{2.4.4}$$

where $q_\varepsilon \in]1,2[$ is defined by

$$q_\varepsilon = \frac{2}{1+\varepsilon}\left(\textit{and so } q'_\varepsilon = \frac{2}{1-\varepsilon}\right). \tag{2.4.5}$$

Proof. We apply Lemma 2 to estimate $\|u - u_h\|_{-t,\Omega}$, for $(q_\varepsilon, q'_\varepsilon)$ defined in (2.4.5). In Inequality (2.4.1):

$$2\left(\frac{1}{q'_\varepsilon} - \frac{1}{2}\right) = 2\left(\frac{1-\varepsilon}{2} - \frac{1}{2}\right) = -\varepsilon. \tag{2.4.6}$$

Finally, for finite elements of order k, with $t = k-1$,

$$\|u - u_h\|_{-k+1,\Omega} \leqslant Ch^k h^{-\varepsilon}|u - u_h|_{1,q_\varepsilon,\Omega}.$$

□

2.4.2 Estimate of $|u - u_h|_{1,q_\varepsilon,\Omega}$

It remains to estimate the quantity $|u-u_h|_{1,q_\varepsilon,\Omega}$ by bounding $|u_h|_{1,q_\varepsilon,\Omega}$ in terms of $|u|_{1,q_\varepsilon,\Omega}$ (Equation (2.4.8)). To achieve this, we need the following discrete inf-sup condition.

Lemma 3. *For $0 < \varepsilon < 1$, q_ε and q'_ε defined in (2.4.5), we have the discrete inf-sup condition*

$$\inf_{u_h \in V_h^k} \sup_{v_h \in V_h^k} \frac{\int_\Omega \nabla u_h \cdot \nabla v_h}{\|u_h\|_{1,q_\varepsilon,\Omega}\|v_h\|_{1,q'_\varepsilon,\Omega}} \geqslant Ch^\varepsilon.$$

Proof. The continuous inf-sup condition

$$\inf_{u\in W_0^{1,q_\varepsilon}} \sup_{v\in W_0^{1,q'_\varepsilon}} \frac{\int_\Omega \nabla u\cdot\nabla v}{\|u\|_{1,q_\varepsilon}\|v\|_{1,q'_\varepsilon}} \geqslant \beta > 0$$

holds for β independent of q_ε and q'_ε (and thus independent of ε). It is a consequence of the duality of the two spaces $W_0^{1,q_\varepsilon}(\Omega)$ and $W_0^{1,q'_\varepsilon}(\Omega)$, see [62]. For $v\in W_0^{1,q'_\varepsilon}(\Omega)$, let $\Pi_h v$ denote the H_0^1-Galerkin projection of v onto V_h^k. This is well defined since $W_0^{1,q'_\varepsilon}(\Omega)\subset H_0^1(\Omega)$. We apply Assumption $\widetilde{\mathbf{A}}\mathbf{3}$ to $\Pi_h v$ for $\ell = s = 1$, and get

$$\|\Pi_h v\|_{1,q'_\varepsilon,\Omega} \leqslant Ch^{-2(1/2-1/q'_\varepsilon)}\|\Pi_h v\|_{1,2,\Omega} \leqslant Ch^{-2(1/2-1/q'_\varepsilon)}\|v\|_{1,2,\Omega} \leqslant Ch^{-2(1/2-1/q'_\varepsilon)}\|v\|_{1,q'_\varepsilon,\Omega}.$$

Moreover, for any $u_h\in V_h^k\subset W^{1,q_\varepsilon}(\Omega)$,

$$\begin{aligned}
\|u_h\|_{1,q_\varepsilon,\Omega} &\leqslant C \sup_{v\in W_0^{1,q'_\varepsilon}} \frac{\int_\Omega \nabla u_h\cdot\nabla v}{\|v\|_{1,q'_\varepsilon,\Omega}} = C \sup_{v\in W_0^{1,q'_\varepsilon}} \frac{\int_\Omega \nabla u_h\cdot\nabla \Pi_h v}{\|v\|_{1,q'_\varepsilon,\Omega}} \\
&\leqslant Ch^{-2(1/2-1/q'_\varepsilon)} \sup_{v\in W_0^{1,q'_\varepsilon}} \frac{\int_\Omega \nabla u_h\cdot\nabla \Pi_h v}{\|\Pi_h v\|_{1,q'_\varepsilon,\Omega}} \\
&\leqslant Ch^{-2(1/2-1/q'_\varepsilon)} \sup_{v_h\in V_h^k} \frac{\int_\Omega \nabla u_h\cdot\nabla v_h}{\|v_h\|_{1,q'_\varepsilon,\Omega}}.
\end{aligned}$$

Finally, thanks to Poincaré inequality, and to Inequality (2.4.6),

$$\inf_{u_h\in V_h^k} \sup_{v_h\in V_h^k} \frac{\int_\Omega \nabla u_h\cdot\nabla v_h}{\|u_h\|_{1,q_\varepsilon,\Omega}\|v_h\|_{1,q'_\varepsilon,\Omega}} \geqslant Ch^{\varepsilon}.$$

□

Then, we can estimate $|u-u_h|_{1,q_\varepsilon,\Omega}$:

Lemma 4. *With q_ε and q'_ε defined in* (2.4.5)*,*

$$|u-u_h|_{1,q_\varepsilon,\Omega} \leqslant C\frac{h^{-\varepsilon}}{\sqrt{\varepsilon}}. \tag{2.4.7}$$

Proof. By Lemma 3, it exists $v_h\in V_h^k$, with $\|v_h\|_{1,q'_\varepsilon,\Omega}=1$, such that

$$h^{2(1/2-1/q'_\varepsilon)}\|u_h\|_{1,q_\varepsilon,\Omega} \leqslant C\int_\Omega \nabla u_h\cdot\nabla v_h = C\int_\Omega \nabla u\cdot\nabla v_h \leqslant C\|u\|_{1,q_\varepsilon,\Omega}.$$

So we have

$$|u-u_h|_{1,q_\varepsilon,\Omega} \leqslant |u|_{1,q_\varepsilon,\Omega} + |u_h|_{1,q_\varepsilon,\Omega} \leqslant Ch^{-2(1/2-1/q'_\varepsilon)}\|u\|_{1,q_\varepsilon,\Omega}. \tag{2.4.8}$$

All that remains is to substitute $\|u\|_{1,q_\varepsilon,\Omega}$ for the expression established in (1.4.10) in Chapter 1, Section 1.4.2.2. For q_ε defined as in (2.4.5),

$$\|u\|_{1,q_\varepsilon,\Omega} \leqslant \frac{C}{\sqrt{2-q_\varepsilon}} \leqslant \frac{C}{\sqrt{\varepsilon}}.$$

Finally, with (2.4.6) and (2.4.8), we get

$$|u - u_h|_{1,q_\varepsilon,\Omega} \leqslant C\frac{h^{-\varepsilon}}{\sqrt{\varepsilon}}.$$

□

2.4.3 Proof of Theorem 3

We can now prove Theorem 3.

Proof. The function u is analytic on $\overline{\Omega}_1$, therefore the quantity $\|u\|_{k+1,\Omega_1}$ is bounded. If we suppose $s = 1$, Nitsche and Schatz Theorem gives, for $\ell = k+1$ and $t = k-1$,

$$\|u - u_h\|_{1,\Omega_0} \leqslant C\left(h^k + \|u - u_h\|_{-k+1,\Omega_1}\right).$$

Thanks to (2.4.4) and (2.4.7),

$$\|u - u_h\|_{-k+1,\Omega} \leqslant Ch^k\frac{h^{-2\varepsilon}}{\sqrt{\varepsilon}},$$

therefore, taking $\varepsilon = |\ln h|^{-1}$,

$$\|u - u_h\|_{-k+1,\Omega} \leqslant Ch^k\sqrt{|\ln h|}. \tag{2.4.9}$$

Finally, we get the result of Theorem 3 for $s = 1$ (Inequality (2.3.2)):

$$\|u - u_h\|_{1,\Omega_0} \leqslant Ch^k\sqrt{|\ln h|}.$$

Now, let us fix $2 \leqslant s \leqslant k$, Nitsche and Schatz Theorem gives, for $\ell = k+1$ and $t = k-1$,

$$\|u - u_h\|_{s,\Omega_0} \leqslant C\left(h^{k+1-s} + h^{1-s}\|u - u_h\|_{-k+1,\Omega_1}\right).$$

So, thanks to (2.4.9), we get the second result of Theorem 3 (Inequality (2.3.3)),

$$\|u - u_h\|_{s,\Omega_0} \leqslant Ch^{k+1-s}\sqrt{|\ln h|}.$$

which ends the proof of Theorem 3. □

2.5 Proof of Theorem 5

In the particular case of the $\mathbb{P}_1$-finite element method, different arguments from the ones presented in the general case permit us to recover optimality. The approach is as follows: we first regularize the right-hand side and prove that in our case the solution u of (P_δ) and the solution of the regularized problem are the same on the complementary of a neighbourhood of the singularity (Theorem 6). The proof of Theorem 5 is based once again on the Nitsche and Schatz Theorem and the observation that the discrete right-hand sides of problem (P_δ) and the regularized problem are exactly the same, so that the numerical solutions are the same too (Lemma 6).

2.5.1 Direct problem and regularized problem

The results presented in this section are valid in any dimension $d \geqslant 1$. However they are only applied in dimension 2 in Section 2.5.3 in order to prove Theorem 2. Let $\varepsilon > 0$, and f^ε be defined on Ω by

$$f^\varepsilon = \frac{d}{\sigma(\mathbb{S}_{d-1})\varepsilon^d} \mathbb{1}_{B_\varepsilon}, \tag{2.5.1}$$

where $B_\varepsilon = B(x_0, \varepsilon)$ and $\sigma(\mathbb{S}_{d-1})$ is the Lebesgue measure of the unit sphere in dimension d. The parameter ε is supposed to be small enough so that $\overline{B_\varepsilon} \subset\subset \Omega$. The function f^ε is a regularization of de the Dirac distribution δ_{x_0}. Let us consider the following problem:

$$(P_\varepsilon) \left\{ \begin{array}{rcll} -\triangle u^\varepsilon & = & f^\varepsilon & \text{in } \Omega, \\ u^\varepsilon & = & 0 & \text{on } \partial\Omega. \end{array} \right.$$

Since $f^\varepsilon \in \mathbb{L}^2(\Omega)$, it is possible to show that problem (P_ε) has a unique variational solution u^ε in $H_0^1(\Omega) \bigcap H^2(\Omega)$ [54]. We show the following result:

Theorem 6. *The solution u of (P_δ) and the solution u^ε of (P_ε) coincide on the closed set $\widetilde{\Omega} = \overline{\Omega} \backslash B_\varepsilon$, ie,*

$$u|_{\widetilde{\Omega}} = u^\varepsilon|_{\widetilde{\Omega}}.$$

The proof is based on the following lemma.

Lemma 5. *Let $d \in \mathbb{N}\backslash\{0\}$, $\varepsilon > 0$, $x \in \mathbb{R}^d$, v a function defined on $\mathbb{R}^d$, harmonic on $\overline{B}(x, \varepsilon)$, and $f \in L^1(\mathbb{R}^d)$ such that*

- *f is radial and positive,*
- *$supp(f) \subset B(0, \varepsilon)$, $\varepsilon > 0$,*
- *$\displaystyle\int_{\mathbb{R}^d} f(x)\,\mathrm{d}x = 1.$*

Then, $\displaystyle f * v(x) = \int_{\mathbb{R}^d} f(y)v(x-y)\,\mathrm{d}y = v(x).$

Proof. As $supp(f) \subset B(0, \varepsilon)$, using spherical coordinates, we have:

$$f * v(x) = \int_0^\varepsilon \int_{\mathbb{S}^{d-1}} f(r)v(x - r\omega)r^{d-1}\,\mathrm{d}\omega\,\mathrm{d}r = \int_0^\varepsilon r^{d-1} f(r) \left(\int_{\mathbb{S}^{d-1}} v(x - r\omega)\mathrm{d}\omega \right) \mathrm{d}r.$$

Besides, v is harmonic on $\overline{B}(x, \varepsilon)$, so that the mean value property gives, for $0 < r \leqslant \varepsilon$,

$$v(x) = \frac{1}{\sigma(\partial B(x, r))} \int_{\partial B(x,r)} v(y)\,\mathrm{d}y = \frac{r^{d-1}}{\sigma(\partial B(x, r))} \int_{\mathbb{S}^{d-1}} v(x - r\omega)\,\mathrm{d}\omega,$$

thus

$$\begin{aligned} f * v(x) &= \int_0^\varepsilon f(r)v(x)\sigma(\partial B(x,r))\,\mathrm{d}r \\ &= v(x)\int_0^\varepsilon \int_{\mathbb{S}^{d-1}} f(r)r^{d-1}\,\mathrm{d}\omega\,\mathrm{d}r \\ &= v(x)\int_{B(0,\varepsilon)} f(y)\,\mathrm{d}y \\ &= v(x). \end{aligned}$$

□

Now, let us prove Theorem 6.

Proof. First, let us leave out boundary conditions and consider the following problem

$$-\triangle v = f^\varepsilon \text{ in } \mathscr{D}'(\mathbb{R}^d). \tag{2.5.2}$$

With u_δ defined in Chapter 1, Section 1.4.2.1, $-\triangle u_\delta = \delta_0$ in $\mathscr{D}'(\mathbb{R}^d)$, so we can build a function v satisfying (2.5.2) as:

$$\begin{aligned} v(x) = f^\varepsilon * u_\delta(x) &= \int_{\mathbb{R}^d} f^\varepsilon(y)u_\delta(x-y)\,\mathrm{d}y \\ &= \int_{\mathbb{R}^d} f^\varepsilon(x_0+y)u_\delta(x-x_0-y)\,\mathrm{d}y \\ &= \Big(f^\varepsilon(x_0+\cdot) * u_\delta\Big)(x-x_0). \end{aligned}$$

Moreover, for all $x \in \Omega\backslash\overline{B_\varepsilon}$, u_δ is harmonic on $\overline{B}(x-x_0,\varepsilon)$, and $f^\varepsilon(\cdot+x_0)$ satisfies the assumptions of Lemma 5, so that $v(x) = \Big(f^\varepsilon(x_0+\cdot) * u_\delta\Big)(x-x_0) = u_\delta(x-x_0)$. We conclude that v and $u_\delta(\cdot - x_0)$ have the same trace on $\partial\Omega$, and so $v+\omega$, where ω is the solution of the Laplace Problem (1.4.9) (see Chapter 1, Section 1.4.2.2), is a solution of the problem (P_ε). By the uniqueness of the solution, we have $u^\varepsilon = v + \omega$. Finally, for all $x \in \Omega\backslash\overline{B_\varepsilon}$, $u^\varepsilon(x) = u(x)$. Since these functions are continuous on $\widetilde{\Omega} = \Omega\backslash B_\varepsilon$, this equality is true on the closure of $\widetilde{\Omega}$, which ends the proof of Theorem 6. □

Remark 7. *Theorem 6 holds for any radial nonnegative function $f \in \mathbb{L}^1(\mathbb{R}^d) \bigcap \mathbb{L}^2(\mathbb{R}^d)$ such that*

$$supp(f) \subset B(0,\varepsilon) \text{ and } \int_{\mathbb{R}^d} f(x)\,\mathrm{d}x = 1,$$

taking $f^\varepsilon = f(\cdot - x_0)$. It is a direct consequence of Lemma 5.

Remark 8. *The result is true in dimension 1, taking*

$$f^\varepsilon = \frac{1}{2\varepsilon}\mathbb{1}_{I_\varepsilon},$$

where $I_\varepsilon = [x_0 - \varepsilon, x_0 + \varepsilon] \subset]a, b[= I$. *In this case, we can easily write down the solutions* u *and* u^ε *explicitly,*

$$u(x) = \begin{cases} \dfrac{b - x_0}{b - a} x - a \dfrac{b - x_0}{b - a} & \text{if } x \in [a, x_0], \\ -\dfrac{x_0 - a}{b - a} x + b \dfrac{x_0 - a}{b - a} & \text{if } x \in [x_0, b]. \end{cases}$$

$$u^\varepsilon(x) = \begin{cases} \dfrac{b - x_0}{b - a} x - a \dfrac{b - x_0}{b - a} & \text{if } x \in [a, x_0 - \varepsilon], \\ -\dfrac{x^2}{4\varepsilon} + \left(\dfrac{x_0}{2\varepsilon} + \dfrac{a + b - 2x_0}{2(b - a)} \right) x & \\ \quad + \dfrac{a(x_0 - b) + b(x_0 - a)}{2(b - a)} - \dfrac{x_0^2 + \varepsilon^2}{4\varepsilon} & \text{if } x \in [x_0 - \varepsilon, x_0 + \varepsilon], \\ -\dfrac{x_0 - a}{b - a} x + b \dfrac{x_0 - a}{b - a} & \text{if } x \in [x_0 + \varepsilon, b]. \end{cases}$$

and observe, as shown in Figure 2.3, that u *and* u^ε *coincide outside* I_ε.

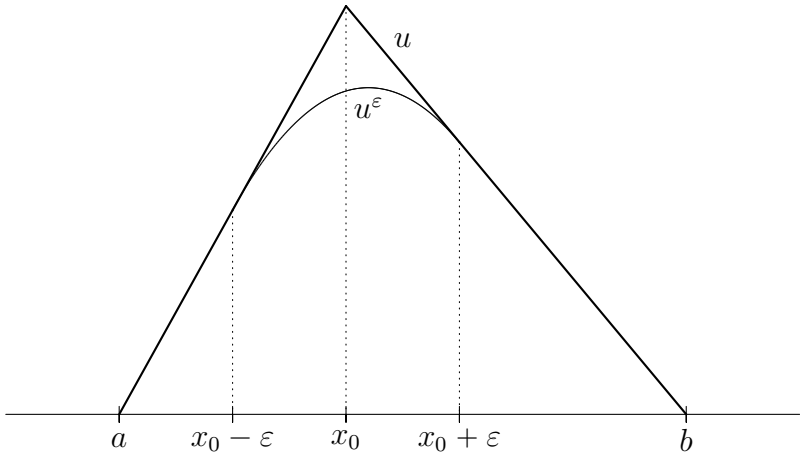

Figure 2.3: Illusration of Theorem 6 in 1D.

2.5.2 Discretizations of the right-hand side

At this point, we introduce a technical assumption on B_ε and the mesh.

Assumption 4. *The support B_ε of the function f^ε is supposed to satisfy*

$$B_\varepsilon \subset T_0,$$

where T_0 denotes the triangle of the mesh which contains the point x_0 (Figure 2.4).

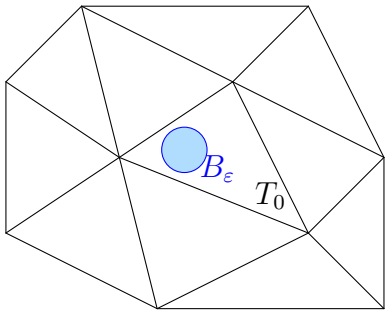

Figure 2.4: Assumption on B_ε.

Remark 9. *The parameter ε will be chosen to be $h/10$, so it remains to fix a "good" triangle T_0 and to build the mesh accordingly, so that Assumption 4 is satisfied. Notice that it is always possible to locally modify any given mesh so that it satisfies this assumption.*

Lemma 6. *Under Assumption 4,*

$$u_h^\varepsilon = u_h,$$

where u_h and u_h^ε are respectively the numerical solutions of problems (P_δ) and (P_ε).

Proof. Let us write down explicitly the discretized right-hand side F_h^ε associated to the function f^ε: for all node i and associated test function $v_i \in V_h^1$,

$$\left(F_h^\varepsilon\right)_i = \int_\Omega \frac{1}{\sigma(B_\varepsilon)} \mathbb{1}_{B_\varepsilon}(x) v_i(x)\,\mathrm{d}x = \int_{B_\varepsilon \subset T_0} \frac{1}{\sigma(B_\varepsilon)} v_i(x)\,\mathrm{d}x,$$

and v_i is affine (and so harmonic) on T_0, therefore

$$\left(F_h^\varepsilon\right)_i = \begin{cases} v_i(x_0) & \text{if } i \text{ is a node of the triangle } T_0, \\ 0 & \textit{otherwise.} \end{cases}$$

We note that $F_h^\varepsilon = D_h$, where D_h is the discretized right-hand side vector associated to the Dirac mass. That is why, with A_h the Laplacian matrix,

$$u_h^\varepsilon - u_h = \sum_{i \text{ node}} \left[A_h^{-1}\left(F_h^\varepsilon - D_h\right)\right]_i v_i = 0.$$

□

Remark 10. *$F_h^\varepsilon = D_h$ holds as long as $B_\varepsilon \subset T_0$. Otherwise, we still have $u_{|\Omega_0} = u^\varepsilon{}_{|\Omega_0}$ (Theorem 6), but $F_h^\varepsilon \neq D_h$, and so $u_h{}_{|\Omega} \neq u_h^\varepsilon{}_{|\Omega}$.*

2.5.3 Proof of Theorem 5

Theorem 5 can now be proved.

Proof. First, by triangular inequality, we can write, for $s \in \{0, 1\}$:

$$\|u - u_h\|_{s,\Omega_0} \leqslant \|u - u^\varepsilon\|_{s,\Omega_0} + \|u^\varepsilon - u_h^\varepsilon\|_{s,\Omega_0} + \|u_h^\varepsilon - u_h\|_{s,\Omega_0}.$$

Besides, thanks to Theorem 6, we have

$$\|u - u^\varepsilon\|_{s,\Omega_0} = 0, \tag{2.5.3}$$

and thanks to Lemma 6, we have

$$\|u_h - u_h^\varepsilon\|_{s,\Omega_0} = 0.$$

Finally we get

$$\|u - u_h\|_{s,\Omega_0} \leqslant \|u^\varepsilon - u_h^\varepsilon\|_{s,\Omega_0}. \tag{2.5.4}$$

We apply Nitsche and Schatz Theorem to $e = u^\varepsilon - u_h^\varepsilon$. With $\ell = 2$, $s = 1$, and $t = 0$,

$$\|e\|_{1,\Omega_0} \leqslant C\left(h\|u^\varepsilon\|_{2,\Omega_1} + \|e\|_{0,\Omega_1}\right). \tag{2.5.5}$$

The domain Ω is smooth and $f^\varepsilon \in \mathbb{L}^2(\Omega)$, so $u^\varepsilon \in H^2(\Omega) \bigcap H_0^1(\Omega)$, and then, thanks to Inequality (2.1.1),

$$\|e\|_{0,\Omega_1} \leqslant \|e\|_{0,\Omega} \leqslant Ch^2\|u^\varepsilon\|_{2,\Omega} \leqslant Ch^2\|f^\varepsilon\|_{0,\Omega}.$$

As $\|f^\varepsilon\|_{0,\Omega}$ can be calculated,

$$\|f^\varepsilon\|_{0,\Omega} = \left(\int_\Omega \left(\frac{1}{\pi\varepsilon^2}\mathbb{1}_{B_\varepsilon}(y)\right)^2 \mathrm{d}y\right)^{1/2} = \frac{1}{\varepsilon\sqrt{\pi}}, \tag{2.5.6}$$

for $\varepsilon \sim h/10$ (in order to satisfy the assumption on B_ε), we get

$$\|e\|_{0,\Omega_1} \leqslant Ch. \tag{2.5.7}$$

Finally, by Theorem 6, $u_{|_{\Omega_1}} = u^\varepsilon{}_{|_{\Omega_1}}$, therefore combining (2.5.5) and (2.5.7), we get

$$\|u^\varepsilon - u_h^\varepsilon\|_{1,\Omega_0} = \|e\|_{1,\Omega_0} \leqslant Ch. \tag{2.5.8}$$

At last, we obtain from Inequalities (2.5.4) and (2.5.8) the expected error estimate, that is

$$\|u - u_h\|_{1,\Omega_0} \leqslant Ch.$$

□

2.5.4 Limits of the method

This proof cannot be adapted to prove the same rate of convergence for a higher order. Indeed, in dimension 2, numerical results make us expect a result in the form of:

$$\|u - u_h\|_{1,\Omega_0} = O(h^k), \tag{2.5.9}$$

for a numerical solution of the problem (P_δ) using the finite element method $\mathbb{P}_k$, $k \geqslant 2$. The are two natural ways to adapt the proof to show Inequality (2.5.9):

- we can keep f^ε as it is defined in (2.5.1), so that Equation (2.5.3) holds. Nevertheless, the finite elements $\mathbb{P}_k$ for $k \geqslant 2$ are not harmonic functions, and so Lemma 6 cannot be used.
- we can use instead of f^ε a polynomial function Q_k, depending on x_0, T_0 and k, and supported by T_0 (see [99]). But in this case, Q_k is not a radial non negative function of mass 1, and Lemma 5 can not be applied.

None of these adaptative methods permits to prove the expected result (2.5.9).

2.6 Numerical illustrations

In this section, we illustrate our theorical results by numerical examples.

Concentration of the error around the singularity. First, we present one of the computations which drew our attention to the fact that the convergence could be better far from the singularity. For this example, we define Ω as the unit disk,

$$\Omega = \{x = (x_1, x_2) \in \mathbb{R}^2 : \|x\|_2 < 1\},$$

Ω_0 as the portion of Ω

$$\Omega_0 = \{x = (x_1, x_2) \in \mathbb{R}^2 : 0.2 < \|x\|_2 < 1\},$$

and finally $x_0 = (0, 0)$ the origin. In this case, the exact solution u of problem (P_δ) is given by

$$u(x) = -\frac{1}{4\pi} \log\left(x_1^2 + x_2^2\right).$$

When problem (P_δ) is solved by the $\mathbb{P}_1$-finite element method, the numerical solution u_h converges to the exact solution u at the order 1 on the entire domain Ω for the $\mathbb{L}^2$-norm (see [99]). The previous example has shown that the convergence far from the singularity is faster, since the order of convergence in this case is 2 (see [66]). The difference of convergence rates for $\mathbb{L}^2$-norm on Ω and Ω_0 let us suppose that the preponderant part of the error is concentrated around the singularity, as can be seen in Figures 2.5, 2.6, 2.7,

and 2.8. Indeed, they respectively show the repartition of the error for $1/h \simeq 10, 15, 20$ and 30.

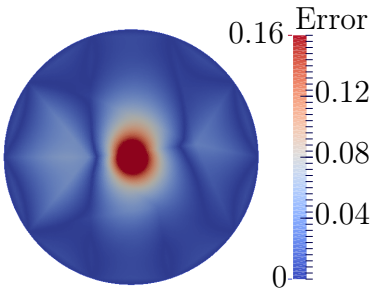

Figure 2.5: Error for $1/h \simeq 10$.

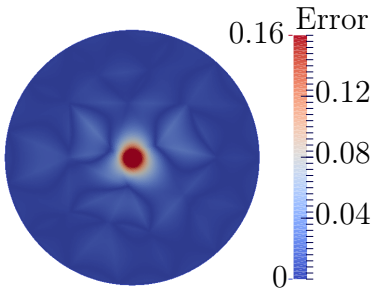

Figure 2.6: Error for $1/h \simeq 15$.

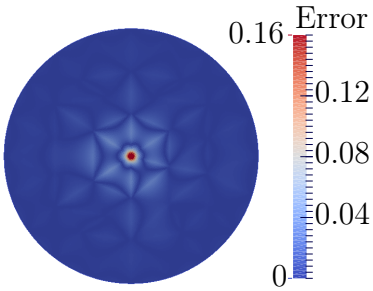

Figure 2.7: Error for $1/h \simeq 20$.

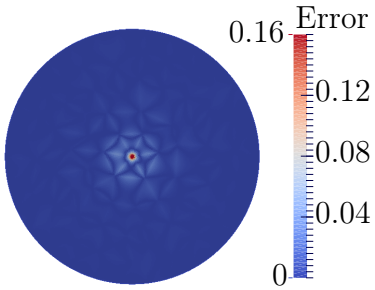

Figure 2.8: Error for $1/h \simeq 30$.

Estimated orders of convergence. Figure 2.9 shows the order of convergence for $\mathbb{L}^2(\Omega_0)$-norm for the $\mathbb{P}_k$-finite element method, where $k = 1, 2, 3$ and 4. In this case too, the convergence far from the singularity is the same as in the regular case: the $\mathbb{P}_k$-finite element method seems to converge at the order $k+1$ on Ω_0 for the $\mathbb{L}^2$-norm. This result has been proved by Köppl and Wohlmuth in [66].

Figure 2.10 shows the estimated order of convergence for the $H^1(\Omega_0)$-norm for the $\mathbb{P}_k$-finite element method, where $k = 1, 2, 3$ and 4, in dimension 2. The convergence far from the singularity (i.e. excluding a neighborhood of the point x_0) is the same as in the regular case: the $\mathbb{P}_k$-finite element method converges at the order k on Ω_0 for the H^1-norm, as proved previously with a $\sqrt{|\ln(h)|}$ multiplier.

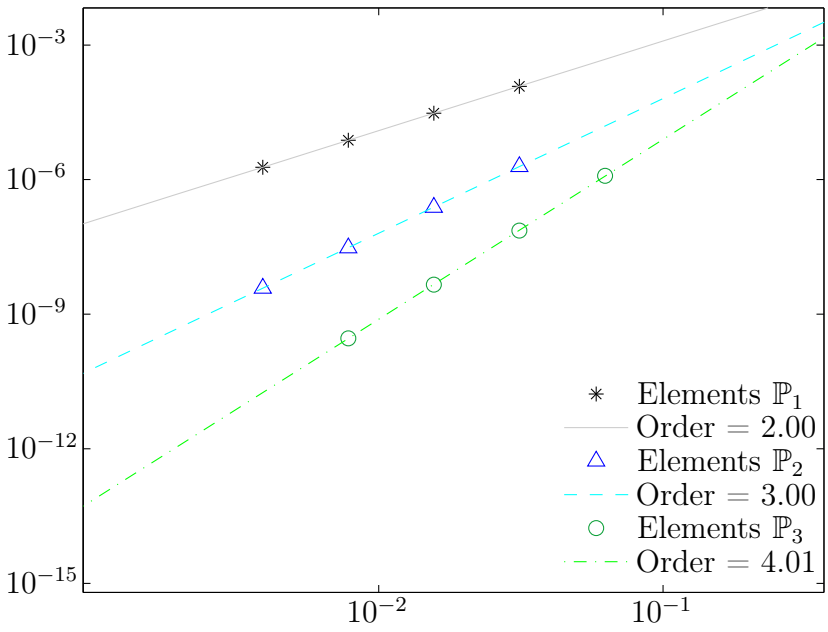

Figure 2.9: Estimated order of convergence for $\mathbb{L}^2(\Omega_0)$-norm for the finite element method $\mathbb{P}_k$, $k = 1, 2, 3$.

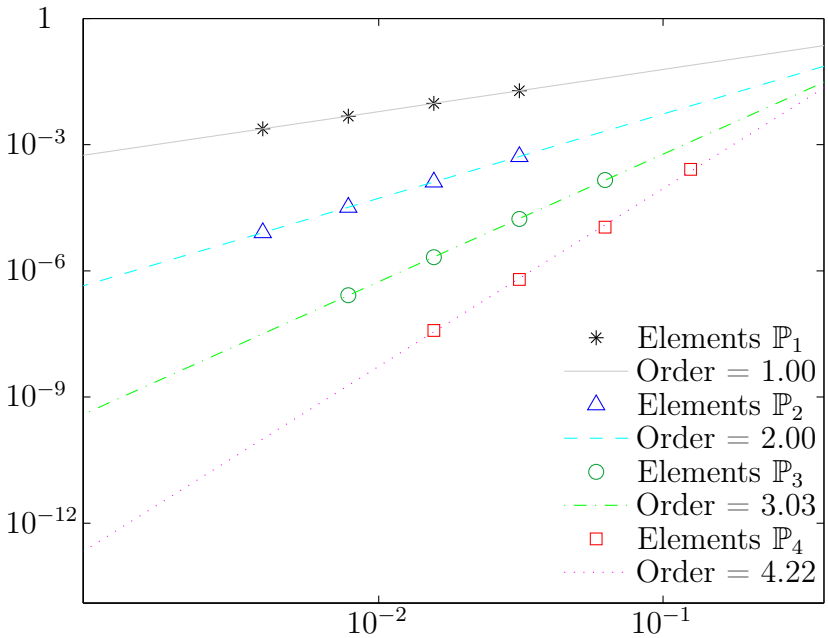

Figure 2.10: Estimated order of convergence for $H^1(\Omega_0)$-norm for the finite element method $\mathbb{P}_k$, $k = 1, 2, 3, 4$.

2.7 Discussion

2.7.1 The three-dimensional case

Dirac mass. The approach presented in this chapter can be extended to the three-dimensional case but straighforward adaptations of the proofs lead to a suboptimal result. In the case of Theorem 3, the solution u belongs to $W_0^{1,q}(\Omega)$ for all q in $[1, 3/2[$. As a consequence the couple $(q_\varepsilon, q'_\varepsilon)$ defined in (2.4.5) has to be taken near from $(3/2, 3)$. For instance,

$$q_\varepsilon = \frac{3}{2+\varepsilon} \text{ and } q'_\varepsilon = \frac{3}{1-\varepsilon},$$

so that, with the same notations, the result of Corollary 1 becomes

$$\|u - u_h\|_{-k+1,\Omega} \leqslant Ch^k h^{-\varepsilon-1/2} |u - u_h|_{1,q_\varepsilon,\Omega}.$$

Moreover, the discrete inf-sup condition in dimension 3 is

$$\inf_{u_h \in V_h^k} \sup_{v_h \in V_h^k} \frac{\int_\Omega \nabla u_h \cdot \nabla v_h}{\|u_h\|_{1,q_\varepsilon,\Omega} \|v_h\|_{1,q'_\varepsilon,\Omega}} \geqslant Ch^{\varepsilon+1/2}.$$

Thus when dealing with the estimaye for $|u - u_h|_{1,q_\varepsilon,\Omega}$, we get

$$|u - u_h|_{1,q_\varepsilon,\Omega} \leqslant Ch^{-\varepsilon-1/2} |u|_{1,q_\varepsilon,\Omega}.$$

Finally, with the asymptotics in 3d

$$\|u\|_{1,q_\varepsilon,\Omega} \sim \frac{1}{\sqrt[3]{4\pi}} \frac{1}{\sqrt[3]{3-2q_\varepsilon}^2},$$

we get the estimate

$$\|u - u_h\|_{1,\Omega_0} \leqslant C(\Omega_0, \Omega_1, \Omega) h^{k-1} \sqrt[3]{|\ln h|}^2.$$

which is clearly suboptimal.

Theorem 5 is also suboptimal in 3d, even if better. Indeed, in 2d or in 3d, the proof readily adapts until the computation of $\|f^\varepsilon\|_{0,\Omega}$, which is in 3d

$$\|f^\varepsilon\|_{0,\Omega} = \frac{1}{2}\sqrt{\frac{3}{\pi}} \frac{1}{\varepsilon\sqrt{\varepsilon}},$$

so that we get

$$\|u - u_h\|_{1,\Omega_0} \leqslant C\sqrt{h}.$$

Line Dirac along a curve. In 3-dimension, a line Dirac δ_Γ along a curve $\Gamma \subset\subset \Omega$ belongs to $H^{-1-\eta}$ for all $\eta > 0$, so that the solution u_Γ of the Poisson problem with the line Dirac δ_Γ belongs to $H^{1-\eta}$. Actually, we have $u_\Gamma \in W^{1,q}(\Omega)$ for all $q \in [1, 2[$. In this case, with the same notations and assumptions as in Theorem 3, we have the following estimate for u_Γ and its Galerkin projection u_Γ^h,

$$\|u_\Gamma - u_\Gamma^h\|_{1,\Omega_0} \leqslant C(\Omega_0, \Omega_1, \Omega) h^k \sqrt{|\ln h|},$$

which is quasi-optimal. This result is shown using the same arguments as the ones presented in Section 2.4, but cannot be obtained with the tools given in the proof detailed in [66].

2.7.2 Dirac mass near the boundary

Theorem 5 excludes some critical cases: Dirac mass should not be closer and closer to the border of the domain Ω. Indeed, for example in the case $\mathrm{d}(x_0, \partial\Omega) \sim h^2$, Assumption 4 cannot be satisfied with $\varepsilon \sim h/10$, but only with $\varepsilon \sim h^2/10$. Nevertheless, this small value of ε implies

$$\|u - u_h\|_{1,\Omega_0} \leqslant C,$$

so that our method does not even prove the convergence of the approximate solution in this case. Actually, if the distance $\mathrm{d}(x_0, \partial\Omega)$ tends to 0, the norm $\|u\|_{1,q,\Omega}$, for a fixed $1 \leqslant q < 2$, tends to $+\infty$, so that the problem becomes more and more singular. But this question is a completely different problem and should be treated in a different way.

This discussion ends this chapter, devoted to the study of the Poisson problem with a Dirac mass in right-hand side. In next chapter we focus on the analysis of local errors for the finite element method applied to the Stokes problem with a punctual force in source term, and show in this case quasi-optimal convergences on subdomains which exclude the singularity [68].

CHAPTER 3

LOCAL ERROR ANALYSIS FOR THE STOKES EQUATIONS WITH A PUNCTUAL FORCE IN SOURCE TERM

Contents

The solution of the Stokes problem with a punctual force in source term is not $H^1 \times \mathbb{L}^2$ and therefore the approximation by a finite element method is suboptimal. In the case of the Poisson problem with a Dirac mass in the right-hand side, an optimal convergence for the Lagrange finite elements has been shown on a subdomain which excludes the singularity in $\mathbb{L}^2$-norm by Köppl and Wohlmuth, and, independently, we have proved a quasi-optimal convergence in H^s-norm, for $s \geqslant 1$ (see Chapter 2). In this chapter, we show a quasi-optimal local convergence in $H^1 \times \mathbb{L}^2$-norm for a $\mathbb{P}_k/\mathbb{P}_{k-1}$ finite element method, $k \geqslant 2$, and for the $\mathbb{P}_1\mathrm{b}/\mathbb{P}_1$ finite elements. The error is still analysed on a subdomain which does not contain the singularity. The proof is based on local Arnold and Liu error estimates, a weak version of Aubin-Nitsche duality lemma applied to the Stokes problem and discrete inf-sup conditions. These theoretical results are generalized to a wide class of finite element methods, before being illustrated by numerical simulations.

3.1 Introduction

This chapter is about the accuracy of the finite element method to solve the Stokes problem with a punctual force in source term. Let us consider this following problem

$$\left\{\begin{array}{rcll} -\triangle \mathbf{u} + \nabla p & = & \delta_{\mathbf{x}_0}\mathbf{F} & \text{in } \Omega, \\ \mathrm{div}(\mathbf{u}) & = & 0 & \text{in } \Omega, \\ \mathbf{u} & = & 0 & \text{on } \partial\Omega, \end{array}\right. \tag{3.1.1}$$

where $\Omega \subset \mathbb{R}^2$ is a square, and $\delta_{\mathbf{x}_0}\mathbf{F}$ denotes the punctual force $\mathbf{F}$ located at $\mathbf{x}_0 \in \Omega$ such that $\mathrm{dist}(\mathbf{x}_0, \Omega) > 0$.

Our interest in Problem (3.1.1) is motivated by the modeling of the movement of thin structures in a viscous fluid, such as flagella connected to bacteria or cilia involved in the muco-ciliary transport in the lung [48]. Indeed, for instance in the lung, the cilium is very thin and a direct simulation with a graded mesh would be too expensive. In the asymptotics of a zero diameter cilium and an infinite velocity, the cilium is thus replaced by a line Dirac of forces in source term. In order to ease the computations, the line Dirac of forces is approached by a sum of punctual forces distributed along the cilium [67]. Finally, by linearity of the Stokes problem, the analysis of the subsequent problem reduces to Problem (3.1.1).

In dimension 2, Problem (3.1.1) has no $H^1(\Omega)^2 \times \mathbb{L}^2(\Omega)$-solution. Although the numerical solution can be defined in this case, the $H^1(\Omega)$-error (respectively $\mathbb{L}^2(\Omega)$-error) for the velocity (respectively the pressure) has no sense, and the $\mathbb{L}^2$-estimates of the velocity cannot be derived like in the regular case without suitable modifications.

Let us notice that the scalar version of this problem, the Poisson problem with a Dirac mass in right-hand side, has already been widely studied. It occurs in many applications from different areas like in optimal control of elliptic problems with state contraints [26] or in the mathematical modeling of electromagnetic fields [59]. Problems of this type are found in controllability for elliptic parabolic equations [27, 28, 73] and in parameter identification problems with pointwise measurements [93]. In this case, Babuška proved

in [5] for two-dimension smooth domain an $\mathbb{L}^2(\Omega)$-convergence of order $h^{1-\varepsilon}$, $\varepsilon > 0$, where h is the mesh size, and Scott has shown in [99] an a priori error estimates of order $2 - \frac{d}{2}$, where the dimension d is 2 or 3. Casas has got the same result in [25] for general Borel measures on the right-hand side.

To the best of our knowledge, there is no finite element method convergence result for the Stokes problem with a punctual force in source term. Moreover, in applications, the punctual force (or the Dirac measure) at the point $\mathbf{x}_0$ is often a model reduction approach and the finite element solution does not need to approximate precisely the exact solution at the point $\mathbf{x}_0$. Thus, it is interesting to estimate the error on a fixed subdomain which does not contain the singularity. In the case of the Poisson problem, Köppl and Wohlmuth recently showed in [66] a quasi-optimal local convergence for low order in $\mathbb{L}^2$-norm for Lagrange finite elements and optimal local convergence for higher orders. A quasi-optimal local convergence in H^s-norm, $s \geqslant 1$ and an optimal local convergence in the case of low order have been proved in dimension 2 in [9]. In this chapter, we establish still in dimension 2 local error estimates for the Stokes problem with a punctual force in source term, Problem (3.1.1), and show a quasi-optimal convergence in $H^1 \times \mathbb{L}^2$-norm. The proof is based on the Arnold and Liu Theorem [4] that establishes local error estimates for finite element discretizations of the Stokes equations with regular source term. It is written in the case of the $\mathbb{P}_k/\mathbb{P}_{k-1}$ elements for $k \geqslant 2$, and the MINI finite element method $\mathbb{P}_1\mathrm{b}/\mathbb{P}_1$ if $k = 1$. No graded meshes are required for these results and they imply that there is no pollution effects far from the singularity.

The chapter is organized as follows. Our main result is formulated in Section 3.2 followed by the Arnold and Liu Theorem [4], an important tool for the proof presented in Section 3.3. Our theoretical results are generalized in Section 3.4 and summarized in Section 3.5, before being illustrated in Section 3.6 by some numerical simulations.

3.2 Main results

In this section, we first set all the notations used in this chapter. Then, we formulate our main result and give an important tool for the proof: the Arnold and Liu Theorem. For the sake of clarity, this result is first set and proved in the particular case of the $\mathbb{P}_k/\mathbb{P}_{k-1}$ finite elements ($k \geqslant 2$) and the $\mathbb{P}_1\mathrm{b}/\mathbb{P}_1$ elements. It is generalized in Section 3.4.

3.2.1 Notations

For a domain D, we denote by $\|\cdot\|_{s,q,D}$ (respectively $|\cdot|_{s,q,D}$) the norm (respectively semi-norm) of the Sobolev space $W^{s,q}(D)$, and by $\|\cdot\|_{s,D}$ (respectively $|\cdot|_{s,D}$) the norm (respectively semi-norm) of the Sobolev space $H^s(\Omega)$. Letters in bold refer to a vector of $\mathbb{R}^2$ or a function with values in $\mathbb{R}^2$.

For the numerical solution, let us introduce a family of quasi-uniform simplical triangulations $\mathcal{T}_h$ of Ω, where h is the meshsize. For the approximation spaces V_h^k and W_h^k, we

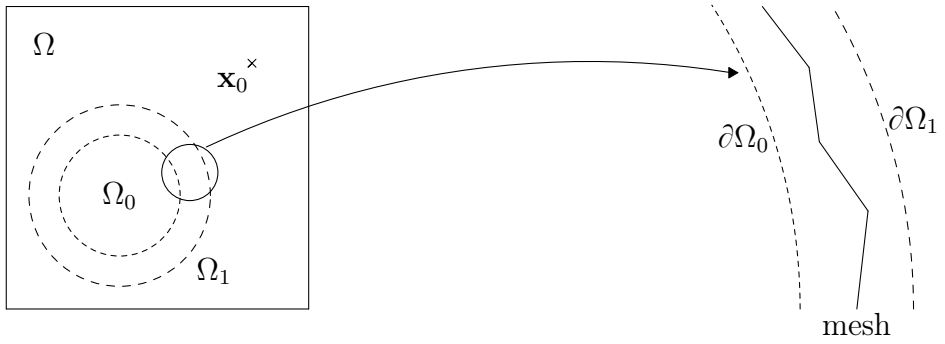

Figure 3.1: Domains Ω_0 and Ω_1.

use the $\mathbb{P}_k/\mathbb{P}_{k-1}$ finite elements, for $k \geqslant 2$, defined as

$$V_h^k = \left\{ \mathbf{v}_h \in \mathscr{C}(\bar{\Omega})^2 \;\middle|\; \mathbf{v}_{h|_T} \in P_k[T], \forall T \in \mathcal{T}_h \right\},$$
$$W_h^k = \left\{ p_h \in \mathscr{C}(\bar{\Omega}) \;\middle|\; p_{h|_T} \in P_{k-1}[T], \forall T \in \mathcal{T}_h \right\},$$

and if $k = 1$, we use the MINI finite element method $\mathbb{P}_1\mathrm{b}/\mathbb{P}_1$, where $\mathbb{P}_1\mathrm{b}$ denotes the continous piecewise linear and bubble functions. For a finite element T, the bubble function b is defined by

$$b(x) = \begin{cases} \lambda_1^T(x)\lambda_2^T(x)\lambda_3^T(x) & \text{if } x \in T, \\ 0 & \text{else,} \end{cases}$$

where λ_1^T, λ_2^T and λ_3^T are the barycentric coordinates of x in relation to the triangle T.

We fix two subdomains of Ω, called Ω_0 and Ω_1, such that $\Omega_0 \subset\subset \Omega_1 \subset\subset \Omega$ and $\mathbf{x}_0 \notin \overline{\Omega_1}$ (see Figure 3.1). We consider a mesh which satisfies the following condition:

Assumption 5. *For some h_0, we have for all $0 < h \leqslant h_0$ (see Figure 3.1),*

$$\overline{\Omega}_0^m \bigcap \Omega_1^c = \varnothing, \text{ where } \overline{\Omega}_0^m = \bigcup_{\substack{T \in \mathcal{T}_h \\ T \bigcap \Omega_0 \neq \varnothing}} T.$$

3.2.2 Statement of our main results

Our main result is given by Theorem 7. The rest of the chapter is mostly concerned by the proof, the generalization and the illustration of this theorem.

Theorem 7. *Consider $\Omega_0 \subset\subset \Omega_1 \subset\subset \Omega$ satisfying Assumption 5, $k \geqslant 1$, $1 \leqslant q < 2$, let $(\mathbf{u}, p) \in W_0^{1,q}(\Omega) \times \mathbb{L}_0^q(\Omega)$ be the solution of Problem (3.1.1) and $(\mathbf{u}_h, p_h)$ its Galerkin*

projection onto $V_h^k \times W_h^k$ *satisfying* $\int_\Omega p_h = 0$ *and*

$$\begin{aligned} \int_\Omega \nabla(\mathbf{u}-\mathbf{u}_h) :: \nabla\eta - \int_\Omega (p-p_h)\mathrm{div}(\eta) &= 0 \quad \textit{for all } \eta \in V_h^k, \\ \int_\Omega \mathrm{div}(\mathbf{u}-\mathbf{u}_h)\xi &= 0 \quad \textit{for all } \xi \in W_h^k. \end{aligned} \tag{3.2.1}$$

Under the assumption that $(\mathbf{u},p) \in H^{k+1}(\Omega_1)^2 \times H^k(\Omega_1)$*, there exists* h_1 *such that if* $0 < h \leqslant h_1$*, we have,*

$$\|\mathbf{u}-\mathbf{u}_h\|_{1,\Omega_0} + \|p-p_h\|_{0,\Omega_0} \leqslant C(\Omega_0,\Omega_1,\Omega)h^k\sqrt{|\ln h|}.$$

3.2.3 Arnold and Liu Theorem

Before stating Arnold and Liu Theorem, let us enumerate the assumptions that the finite element spaces $\mathcal{V}_h^k$ and $\mathcal{W}_h^k$ have to satisfy so that the theorem is true.

Assumption 6. *Given two fixed concentric disks* B_0 *and* B *with* $B_0 \subset\subset B \subset\subset \Omega$*, there exists an* h_0 *such that for all* $0 < h \leqslant h_0$*, we have for some integers* k_1 *and* k_2*:*

B1 *For any* $1 \leqslant \ell$*, for each* $\mathbf{v} \in H^\ell(B)^2$*, there exists* $\eta \in \mathcal{V}_h^k$ *such that*

$$\|\mathbf{v}-\eta\|_{1,B} \leqslant Ch^{\widetilde{r}_1-1}\|\mathbf{v}\|_{\ell,B}, \quad \widetilde{r}_1 = \min(k_1+1,\ell).$$

For any $0 \leqslant s$*, for each* $\pi \in H^s(B)$*, there exists* $\xi \in \mathcal{W}_h^k$ *such that*

$$\|\pi-\xi\|_{0,B} \leqslant Ch^{\widetilde{r}_2}\|\pi\|_{s,B}, \quad \widetilde{r}_2 = \min(k_2+1,s).$$

Moreover, if $\mathbf{v} \in H_0^1(B_0)^2$ *(respectively* π *vanishes on* $B\backslash\overline{B}_0$*) then* η *(respectively* ξ*) can be chosen to satisfy* $\eta \in H_0^1(B)^2$ *(respectively* ξ *vanishes on* $\Omega\backslash\overline{B}$*).*

B2 *Let* $\varphi \in \mathscr{C}_0^\infty(B_0)$*,* $\mathbf{v}_h \in \mathcal{V}_h^k$ *and* $\pi_h \in \mathcal{W}_h^k$*, then there exist* $\eta \in \mathcal{V}_h^k \bigcap H_0^1(B)$ *and* $\xi \in \mathcal{W}_h^k$ *with* $\mathrm{supp}\ \xi \subset \overline{B}$ *such that*

$$\begin{aligned} \|\varphi\mathbf{v}_h - \eta\|_{1,B} &\leqslant C(\varphi,B,B_0)h\|\mathbf{v}_h\|_{1,B}, \\ \|\varphi\pi_h - \xi\|_{0,B} &\leqslant C(\varphi,B,B_0)h\|\pi_h\|_{0,B}. \end{aligned}$$

B3 *For each* $0 < h \leqslant h_0$ *there exists a domain* B_h *with* $B_0 \subset\subset B_h \subset\subset B$ *such that for any* $0 \leqslant \ell$*, for all* $\mathbf{v}_h \in \mathcal{V}_h^k$ *and* $\pi_h \in \mathcal{W}_h^k$*, we have*

$$\begin{aligned} \|\mathbf{v}_h\|_{1,B_h} &\leqslant Ch^{-1-\ell}\|\mathbf{v}_h\|_{-\ell,B_h}, \\ \|\pi_h\|_{0,B_h} &\leqslant Ch^{-\ell}\|\pi_h\|_{-\ell,B_h}. \end{aligned}$$

B4 *There exists* $\beta > 0$ *such that for all* $0 < h \leqslant h_0$*, there is a domain* B_h*, with* $B_0 \subset\subset B_h \subset\subset B$ *for which*

$$\inf_{\substack{\pi_h \in \mathcal{W}_h^k \\ \mathrm{supp}\ \pi_h \subset B_h}} \sup_{\substack{\mathbf{v}_h \in \mathcal{V}_h^k \\ \mathrm{supp}\ \mathbf{v}_h \subset B_h}} \frac{\int_{B_h} \mathrm{div}(\mathbf{v}_h)\pi_h}{|\pi_h|_{0,B_h}|\mathbf{v}_h|_{1,B_h}} \geqslant \beta > 0.$$

We now state the following theorem by Arnold and Liu [4], a key tool in the forthcoming proof of Theorem 7.

Theorem (Arnold and Liu [4]). *Consider $\Omega_0 \subset\subset \Omega_1 \subset\subset \Omega$ and V_h^k and W_h^k satisfy Assumption 6. Suppose that the continuous solution $(\mathbf{v}, \pi) \in H^1(\Omega)^2 \times \mathbb{L}^2(\Omega)$ satisfies $(\mathbf{v}, \pi)_{|\Omega_1} \in H^\ell(\Omega_1)^2 \times H^{\ell-1}(\Omega_1)$ for some $\ell > 0$. Suppose that the finite element solution $(\mathbf{v}_h, \pi_h) \in V_h^k \times W_h^k$ satisfies $\int_\Omega \pi - \pi_h = 0$ and*

$$\begin{aligned} \int_\Omega \nabla(\mathbf{v} - \mathbf{v}_h) :: \nabla\eta - \int_\Omega (\pi - \pi_h)\mathrm{div}(\eta) &= 0 \quad \textit{for all } \eta \in V_h^k, \\ \int_\Omega \mathrm{div}(\mathbf{v} - \mathbf{v}_h)\xi &= 0 \quad \textit{for all } \xi \in W_h^k. \end{aligned}$$

Let t be a nonnegative integer. Then there exist a constant $C > 0$ and a real $h_1 > 0$ depending only on Ω_1, Ω_0, and t, such that if $0 < h \leqslant h_1$ we have

$$\begin{aligned} \|\mathbf{v} - \mathbf{v}_h\|_{1,\Omega_0} + \|\pi - \pi_h\|_{0,\Omega_0} \leqslant & C(h^{r_1-1}\|\mathbf{v}\|_{\ell,\Omega_1} + h^{r_2-1}\|\pi\|_{\ell-1,\Omega_1} \\ & + \|\mathbf{v} - \mathbf{v}_h\|_{-t,\Omega_1} + \|\pi - \pi_h\|_{-t-1,\Omega_1}), \end{aligned}$$

where $r_1 = \min(k_1 + 1, \ell)$, $r_2 = \min(k_2 + 2, \ell)$, and k_1, k_2 as in Assumption **B1**.

Assumptions **B1** and **B3** are quite standard and satisfied by a wide class of finite element spaces, including all finite element spaces defined on quasi-uniform meshes [32]. The parameters k_1 and k_2 play respectively the role of the order of approximation of the spaces $\mathcal{V}_h^k$ and $\mathcal{W}_h^k$. In this section, for $k \geqslant 2$, we have $k_1 = k$ and $k_2 = k - 1$, and for $k = 1$, we have $k_1 = k_2 = k = 1$. Assumption **B2** is less common but also satisfied by a wide variety of approximation spaces, including the $\mathbb{P}_1$b-finite elements [4]. Actually, for Lagrange finite elements, a stronger property than assumption **B2** is shown in [8]: let $0 \leqslant s \leqslant \ell \leqslant k$, $\varphi \in \mathscr{C}_0^\infty(B)$ and $\mathbf{v}_h \in V_h^k$, then there exists $\eta \in V_h^k$ such that

$$\|\varphi\mathbf{v}_h - \eta\|_{s,B} \leqslant C(\varphi)h^{\ell-s+1}\|\mathbf{v}_h\|_{\ell,B}. \tag{3.2.2}$$

Applied for $s = \ell = 1$, Inequality (3.2.2) gives assumption **B2**. When $B_h = \Omega$, Assumption **B4** is the standard stability condition or discrete inf-sup condition of the Stokes elements. It usually holds as long as B_h is a union of elements.

Remark 11. *The assumption $(\mathbf{v}, \pi) \in H^1(\Omega)^2 \times \mathbb{L}^2(\Omega)$ is not necessary, but it ensures that the finite element solution $(\mathbf{v}_h, \pi_h)$ is well-defined. In the Dirac right-hand side case, as $V_h^k \subset \mathscr{C}(\Omega)$, the discrete solution $(\mathbf{u}_h, p_h)$ is well-defined and Arnold and Liu Theorem holds.*

3.3 Proof of Theorem 7

This section is devoted to the proof of Theorem 7. We first show a weak version of Aubin-Nitsche duality lemma (Lemma 7), then we establish two discrete inf-sup conditions (Lemmas 8 and 9), and finally we use these results to prove Theorem 7.

3.3.1 Aubin-Nitsche duality lemma with a singular source term

The proof of Theorem 7 is based on Arnold and Liu Theorem. In order to estimate the quantities $\|\mathbf{u}-\mathbf{u}_h\|_{-t,\Omega_1}$ and $\|p-p_h\|_{-t-1,\Omega_1}$, we first show a weak version of Aubin-Nitsche Lemma in the case of the Stokes problem with a singular source term.

Lemma 7. *Consider the source term* $\mathbf{f} \in W^{-1,q}(\Omega)^2 = (W_0^{1,q'}(\Omega)^2)'$, $1 < q < 2$, *and let* $(\mathbf{w}, \pi) \in W_0^{1,q}(\Omega) \times \mathbb{L}^q(\Omega)$ *be the unique solution of*

$$\left\{ \begin{array}{rcl} -\triangle \mathbf{w} + \nabla \pi &=& \mathbf{f} \quad \textit{in } \Omega, \\ \mathrm{div}(\mathbf{w}) &=& 0 \quad \textit{in } \Omega, \\ \mathbf{w} &=& 0 \quad \textit{on } \partial\Omega. \end{array} \right.$$

Let $(\mathbf{w}_h, \pi_h)$ *be the Galerkin projection of* $(\mathbf{w}, \pi)$ *in* $V_h^k \times W_h^k$. *For any integer* $0 \leqslant t \leqslant k-1$,

$$\begin{aligned} &\|\mathbf{w}-\mathbf{w}_h\|_{-t,\Omega} + \|\pi - \pi_h\|_{-t-1,\Omega} \\ &\qquad \leqslant C h^{2(1/q'-1/2)} h^{t+1} \left(|\mathbf{w} - \mathbf{w}_h|_{1,q,\Omega} + |\pi - \pi_h|_{0,q,\Omega} \right). \end{aligned} \tag{3.3.1}$$

Proof. We aim at estimating, for $t \geqslant 0$, the $H^{-t}(\Omega)$-norm and the $H^{-t-1}(\Omega)$-norm respectively of the errors $\mathbf{w} - \mathbf{w}_h$ and $\pi - \pi_h$:

$$\|\mathbf{w} - \mathbf{w}_h\|_{-t,\Omega} = \sup_{\varphi \in \mathscr{C}_0^\infty(\Omega)^2} \frac{1}{\|\varphi\|_{t,\Omega}} \left| \int_\Omega (\mathbf{w} - \mathbf{w}_h) \cdot \varphi \right| \tag{3.3.2}$$

$$\|\pi - \pi_h\|_{-t-1,\Omega} = \sup_{\psi \in \mathscr{C}_0^\infty(\Omega)} \frac{1}{\|\psi\|_{t+1,\Omega}} \left| \int_\Omega (\pi - \pi_h) \psi \right| \tag{3.3.3}$$

The Galerkin projection $(\mathbf{w}_h, \pi_h)$ satisfies $\displaystyle\int_\Omega \pi - \pi_h = 0$ and

$$\begin{aligned} \int_\Omega \nabla(\mathbf{w} - \mathbf{w}_h) :: \nabla \eta - \int_\Omega (\pi - \pi_h) \mathrm{div}(\eta) &= 0 \quad \text{for all } \eta \in V_h^k, \\ \int_\Omega \mathrm{div}(\mathbf{w} - \mathbf{w}_h) \xi &= 0 \quad \text{for all } \xi \in W_h^k. \end{aligned} \tag{3.3.4}$$

Consider $\varphi \in \mathscr{C}_0^\infty(\Omega)^2$ and let $(\mathbf{w}^\varphi, \pi^\varphi) \in H^{t+2}(\Omega) \times H^{t+1}(\Omega)$ be the solution of

$$\left\{ \begin{array}{rcl} -\triangle \mathbf{w}^\varphi + \nabla \pi^\varphi &=& \varphi \quad \text{in } \Omega, \\ \mathrm{div}(\mathbf{w}^\varphi) &=& 0 \quad \text{in } \Omega, \\ \mathbf{w}^\varphi &=& 0 \quad \text{on } \partial\Omega. \end{array} \right.$$

Existence and uniqueness of the solution to this problem are given in [111] (see Chapter I, §2), and we have the estimate

$$\|\mathbf{w}^\varphi\|_{t+2,\Omega} + \|\pi^\varphi\|_{t+1,\Omega} \leqslant C \|\varphi\|_{t,\Omega}. \tag{3.3.5}$$

In dimension 2, by the Sobolev injections established for instance in [20], we have

$$\begin{aligned} &H^{t+2}(\Omega) \subset W^{1,q'}(\Omega), \\ &H^{t+1}(\Omega) \subset \mathbb{L}^{q'}(\Omega), \end{aligned} \tag{3.3.6}$$

for all q' in $[2, +\infty[$. Thus

$$\int_\Omega (\mathbf{w}-\mathbf{w}_h)\cdot\varphi = -\int_\Omega (\mathbf{w}-\mathbf{w}_h)\cdot\triangle\mathbf{w}^\varphi + \int_\Omega (\mathbf{w}-\mathbf{w}_h)\cdot\nabla\pi^\varphi$$
$$= \int_\Omega \nabla(\mathbf{w}-\mathbf{w}_h) :: \nabla\mathbf{w}^\varphi - \int_\Omega \mathrm{div}(\mathbf{w}-\mathbf{w}_h)\pi^\varphi.$$

By adding (3.3.4) in the last equation, we get for any $\eta \in V_h^k$ and any $\xi \in W_h^k$,

$$\int_\Omega (\mathbf{w}-\mathbf{w}_h)\cdot\varphi = \int_\Omega \nabla(\mathbf{w}-\mathbf{w}_h) :: \nabla(\mathbf{w}^\varphi-\eta) - \int_\Omega \mathrm{div}(\mathbf{w}-\mathbf{w}_h)(\pi^\varphi-\xi)$$
$$+ \int_\Omega \mathrm{div}(\eta)(\pi-\pi_h).$$

By definition of $\mathbf{w}^\varphi$, $\mathrm{div}(\mathbf{w}^\varphi)=0$ on Ω, so

$$\int_\Omega (\mathbf{w}-\mathbf{w}_h)\cdot\varphi = \int_\Omega \nabla(\mathbf{w}-\mathbf{w}_h) :: \nabla(\mathbf{w}^\varphi-\eta) - \int_\Omega \mathrm{div}(\mathbf{w}-\mathbf{w}_h)(\pi^\varphi-\xi)$$
$$+ \int_\Omega \mathrm{div}(\eta-\mathbf{w}^\varphi)(\pi-\pi_h)$$
$$\leqslant |\mathbf{w}-\mathbf{w}_h|_{1,q,\Omega}\left(|\mathbf{w}^\varphi-\eta|_{1,q',\Omega} + |\pi^\varphi-\xi|_{0,q',\Omega}\right)$$
$$+ |\pi-\pi_h|_{0,q,\Omega}|\mathbf{w}^\varphi-\eta|_{1,q',\Omega}.$$

Now let us deal with the pressure estimate. For any $\psi \in \mathscr{C}_0^\infty(\Omega)$, we denote by $\widetilde{\psi}$ the function

$$\widetilde{\psi} = \psi - \frac{1}{|\Omega|}\int_\Omega \psi.$$

By definition, it is easy to see that $\widetilde{\psi}$ satisfies

$$\int_\Omega \widetilde{\psi} = 0 \quad \text{and} \quad \forall t \geqslant 0,\ \|\widetilde{\psi}\|_{t+1,\Omega} \leqslant C(\Omega)\|\psi\|_{t+1,\Omega}.$$

We can now establish the result for the pressure: consider $\psi \in \mathscr{C}_0^\infty(\Omega)$ and the solution $(\mathbf{w}^\psi, \pi^\psi) \in H^{t+2}(\Omega)\times H^{t+1}(\Omega)$ of

$$\left\{\begin{array}{rcl} -\triangle\mathbf{w}^\psi + \nabla\pi^\psi &=& 0 \quad \text{in } \Omega,\\ \mathrm{div}(\mathbf{w}^\psi) &=& \widetilde{\psi} \quad \text{in } \Omega,\\ \mathbf{w}^\psi &=& 0 \quad \text{on } \partial\Omega, \end{array}\right.$$

See [111] (Chapter I, §2) for the existence and the uniqueness, and the following estimate

$$\|\mathbf{w}^\psi\|_{t+2,\Omega} + \|\pi^\psi\|_{t+1,\Omega} \leqslant C\|\widetilde{\psi}\|_{t+1,\Omega} \leqslant C\|\psi\|_{t+1,\Omega}. \tag{3.3.7}$$

Moreover, $\displaystyle\int_\Omega \pi-\pi_h = 0$, so that

$$\int_\Omega (\pi-\pi_h)\psi = \int_\Omega (\pi-\pi_h)\widetilde{\psi} + \frac{1}{|\Omega|}\int_\Omega \psi\int_\Omega \pi-\pi_h = \int_\Omega (\pi-\pi_h)\widetilde{\psi}.$$

By the Sobolev injections recalled in (3.3.6), and the Galerkin projection property (3.3.4), we can write for all $\eta \in V_h^k$,

$$\begin{aligned}\int_\Omega (\pi - \pi_h)\psi &= \int_\Omega (\pi - \pi_h)\widetilde{\psi} \\ &= \int_\Omega (\pi - \pi_h)\mathrm{div}(\mathbf{w}^\psi) \\ &= \int_\Omega (\pi - \pi_h)\mathrm{div}(\mathbf{w}^\psi - \eta) + \int_\Omega \nabla(\mathbf{w} - \mathbf{w}_h) :: \nabla\eta.\end{aligned}$$

Then, for all $\mathbf{v} \in W_0^{1,q}(\Omega)$

$$\int_\Omega \nabla\mathbf{w}^\psi :: \nabla\mathbf{v} - \int_\Omega \pi^\psi \mathrm{div}(\mathbf{v}) = 0,$$

so, with $\mathbf{v} = \mathbf{w} - \mathbf{w}_h$, and for any $\xi \in W_h^k$,

$$\begin{aligned}\int_\Omega (\pi - \pi_h)\psi &= \int_\Omega (\pi - \pi_h)\mathrm{div}(\mathbf{w}^\psi - \eta) + \int_\Omega \nabla(\mathbf{w} - \mathbf{w}_h) :: \nabla(\eta - \mathbf{w}^\psi) \\ &\quad + \int_\Omega \pi^\psi \mathrm{div}(\mathbf{w} - \mathbf{w}_h) \\ &= \int_\Omega (\pi - \pi_h)\mathrm{div}(\mathbf{w}^\psi - \eta) + \int_\Omega \nabla(\mathbf{w} - \mathbf{w}_h) :: \nabla(\eta - \mathbf{w}^\psi) \\ &\quad + \int_\Omega (\pi^\psi - \xi)\mathrm{div}(\mathbf{w} - \mathbf{w}_h) \\ &\leqslant |\pi - \pi_h|_{0,q,\Omega}|\mathbf{w}^\psi - \eta|_{1,q',\Omega} \\ &\quad + |\mathbf{w} - \mathbf{w}_h|_{1,q,\Omega}\left(|\mathbf{w}^\psi - \eta|_{1,q',\Omega} + |\pi^\psi - \xi|_{0,q',\Omega}\right).\end{aligned}$$

Finally, for any $(\eta_1, \xi_1) \in V_h^k \times W_h^k$,

$$\begin{aligned}\int_\Omega (\mathbf{w} - \mathbf{w}_h)\cdot\varphi &\leqslant |\mathbf{w} - \mathbf{w}_h|_{1,q,\Omega}\left(|\mathbf{w}^\varphi - \eta_1|_{1,q',\Omega} + |\pi^\varphi - \xi_1|_{0,q',\Omega}\right) \\ &\quad + |\pi - \pi_h|_{0,q,\Omega}|\mathbf{w}^\varphi - \eta_1|_{1,q',\Omega},\end{aligned} \tag{3.3.8}$$

and for any $(\eta_2, \xi_2) \in V_h^k \times W_h^k$,

$$\begin{aligned}\int_\Omega (\pi - \pi_h)\psi &\leqslant |\pi - \pi_h|_{0,q,\Omega}|\mathbf{w}^\psi - \eta_2|_{1,q',\Omega} \\ &\quad + |\mathbf{w} - \mathbf{w}_h|_{1,q,\Omega}\left(|\mathbf{w}^\psi - \eta_2|_{1,q',\Omega} + |\pi^\psi - \xi_2|_{0,q',\Omega}\right).\end{aligned} \tag{3.3.9}$$

In order to estimate $|\mathbf{w}^\varphi - \eta_1|_{1,q',\Omega}$, $|\mathbf{w}^\psi - \eta_2|_{1,q',\Omega}$, $|\pi^\varphi - \xi_1|_{0,q',\Omega}$ and $|\pi^\psi - \xi_2|_{0,q',\Omega}$, we need the following result:

Proposition 11 (Girault, Raviart, Corollary A.2, page 97 [52]). *Let $\mathcal{T}_h$ be a family of quasi-uniform simplicial triangulations of $\Omega \subset \mathbb{R}^2$, where h is the meshsize. For any $0 \leqslant m \leqslant t+1 \leqslant k$, for any mesh element T in the family, for any $v \in W^{k+1,q'}(\Omega)$, any real $q' \geqslant 2$,*

$$|v - \Pi_h v|_{m,q',T} \leqslant Ch^{2(1/q'-1/2)} h^{t+2-m} |v|_{t+2,2,T}, \tag{3.3.10}$$

where $\Pi_h v$ is the P_k-interpolant of the function v.

Up to now and until the end of this proof, we take

$$\eta_1 = \Pi_h \mathbf{w}^\varphi \text{ and } \eta_2 = \Pi_h \mathbf{w}^\psi \in V_h^k,$$
$$\xi_1 = \widetilde{\Pi}_h \pi^\varphi \text{ and } \xi_2 = \widetilde{\Pi}_h \pi^\psi \in W_h^k,$$

where $\Pi_h \mathbf{v}$ is the P_k-interpolant of the function $\mathbf{v}$ and $\widetilde{\Pi}_h v$ is the P_{k-1}-interpolant of the function v. By (3.3.10), with $m = 1$, $0 \leqslant t \leqslant k-1$, for all T finite element in the family,

$$\begin{aligned} |\mathbf{w}^\varphi - \eta_1|_{1,q',T} &\leqslant Ch^{2(1/q'-1/2)} h^{t+1} |\mathbf{w}^\varphi|_{t+2,2,T}, \\ |\mathbf{w}^\psi - \eta_2|_{1,q',T} &\leqslant Ch^{2(1/q'-1/2)} h^{t+1} |\mathbf{w}^\psi|_{t+2,2,T}, \end{aligned} \tag{3.3.11}$$

and with $m = 0$,

$$\begin{aligned} |\pi^\varphi - \xi_1|_{0,q',T} &\leqslant Ch^{2(1/q'-1/2)} h^{t+1} |\pi^\varphi|_{t+1,2,T}, \\ |\pi^\psi - \xi_2|_{0,q',T} &\leqslant Ch^{2(1/q'-1/2)} h^{t+1} |\pi^\psi|_{t+1,2,T}. \end{aligned}$$

We denote the triangles of the mesh by $\{T_i\}_{i=1,\cdots,N}$, and we set

$$a = (a_i)_i \text{ and } b = (b_i)_i, \text{ where } a_i = |\mathbf{w}^\varphi - \eta_1|_{1,q',T_i} \text{ and } b_i = |\mathbf{w}^\varphi|_{t+2,2,T_i}.$$

By (3.3.11), we have, for all i in $[\![1, N]\!]$,

$$a_i \leqslant Ch^{2(1/q'-1/2)} h^{t+1} b_i.$$

We recall the norm equivalence in $\mathbb{R}^N$ for $0 < r < s$,

$$\|x\|_{\ell^s} \leqslant \|x\|_{\ell^r} \leqslant N^{1/r-1/s} \|x\|_{\ell^s},$$

with here $N \sim Ch^{-2}$. As $2 < q'$, we have $\|b\|_{\ell^{q'}} \leqslant \|b\|_{\ell^2}$. Then, we can write

$$\begin{aligned} |\mathbf{w}^\varphi - \eta_1|_{1,q',\Omega} = \|a\|_{\ell^{q'}} &\leqslant Ch^{t+1} h^{2(1/q'-1/2)} \|b\|_{\ell^{q'}}, \\ &\leqslant Ch^{t+1} h^{2(1/q'-1/2)} \|b\|_{\ell^2}, \\ &\leqslant Ch^{t+1} h^{2(1/q'-1/2)} |\mathbf{w}^\varphi|_{t+2,2,\Omega}. \end{aligned}$$

Similarly, we get

$$\begin{aligned} |\mathbf{w}^\psi - \eta_2|_{1,q',\Omega} &\leqslant Ch^{t+1} h^{2(1/q'-1/2)} |\mathbf{w}^\psi|_{t+2,2,\Omega}, \\ |\pi^\varphi - \xi_1|_{0,q',\Omega} &\leqslant Ch^{t+1} h^{2(1/q'-1/2)} |\pi^\varphi|_{t+1,2,\Omega}, \\ |\pi^\psi - \xi_2|_{0,q',\Omega} &\leqslant Ch^{t+1} h^{2(1/q'-1/2)} |\pi^\psi|_{t+1,2,\Omega}, \end{aligned}$$

and by (3.3.5) and (3.3.7), we get

$$\begin{aligned}
|\mathbf{w}^{\varphi} - \eta_1|_{1,q',\Omega} &\leqslant Ch^{t+1}h^{2(1/q'-1/2)}\|\varphi\|_{t,2,\Omega},\\
|\mathbf{w}^{\psi} - \eta_2|_{1,q',\Omega} &\leqslant Ch^{t+1}h^{2(1/q'-1/2)}\|\psi\|_{t+1,2,\Omega},\\
|\pi^{\varphi} - \xi_1|_{0,q',\Omega} &\leqslant Ch^{t+1}h^{2(1/q'-1/2)}\|\varphi\|_{t,2,\Omega},\\
|\pi^{\psi} - \xi_2|_{0,q',\Omega} &\leqslant Ch^{t+1}h^{2(1/q'-1/2)}\|\psi\|_{t+1,2,\Omega},
\end{aligned}$$

Finally, the proof is ended by combining (3.3.2), (3.3.3), (3.3.8), (3.3.9), and the last inequalities. □

Corollary 2. *Let* $(\mathbf{u}_h, p_h) \in V_h^k \times W_h^k$ *be the Galerkin projection of the solution* $(\mathbf{u}, p)$ *of Problem* (3.1.1)*, for any* $0 < \varepsilon < 1$*,*

$$\begin{aligned}
&\|\mathbf{u}-\mathbf{u}_h\|_{-k+1,\Omega} + \|p - p_h\|_{-k,\Omega}\\
&\qquad \leqslant Ch^{-\varepsilon}h^k \left(|\mathbf{u} - \mathbf{u}_h|_{1,q_\varepsilon,\Omega} + |p - p_h|_{0,q_\varepsilon,\Omega}\right),
\end{aligned}$$

where $q_\varepsilon \in [1, 2[$ *is defined by*

$$q_\varepsilon = \frac{2}{1+\varepsilon} \left(\textit{and so } q'_\varepsilon = \frac{2}{1-\varepsilon} \right). \tag{3.3.12}$$

Proof. We apply Lemma 7 with $\mathbf{f} = \delta_{\mathbf{x}_0}\mathbf{F}$, $\mathbf{w} = \mathbf{u}$, $\pi = p$ and $t = k - 1$. We can explicit Inequality (3.3.1):

$$2\left(\frac{1}{q'_\varepsilon} - \frac{1}{2}\right) = 2\left(\frac{1-\varepsilon}{2} - \frac{1}{2}\right) = -\varepsilon, \tag{3.3.13}$$

and so, it follows

$$\begin{aligned}
&\|\mathbf{u}-\mathbf{u}_h\|_{-k+1,\Omega} + \|p - p_h\|_{-k,\Omega}\\
&\qquad \leqslant Ch^{-\varepsilon}h^k \left(|\mathbf{u} - \mathbf{u}_h|_{1,q_\varepsilon,\Omega} + |p - p_h|_{0,q_\varepsilon,\Omega}\right).
\end{aligned}$$

□

3.3.2 Discrete inf-sup conditions in $\mathbb{L}^{q_\varepsilon}$-norm

Section 3.3.3 is devoted to estimate of $|\mathbf{u} - \mathbf{u}_h|_{1,q_\varepsilon,\Omega}$ and $|p - p_h|_{0,q_\varepsilon,\Omega}$. In that prospect, we need to establish two discrete inf-sup conditions.

Lemma 8. *With* q_ε *and* q'_ε *defined in* (3.3.12)*, the approximation space* $\mathring{V}_h^k$ *defined by*

$$\mathring{V}_h^k = \left\{ \mathbf{v}_h \in V_h^k \,\middle|\, \int_\Omega \operatorname{div}(\mathbf{v}_h) p_h = 0, \forall p_h \in W_h^k \right\},$$

satisfies the following discrete inf-sup condition:

$$\inf_{\mathbf{u}_h \in \mathring{V}_h^k} \sup_{\mathbf{v}_h \in \mathring{V}_h^k} \frac{\int_\Omega \nabla \mathbf{u}_h :: \nabla \mathbf{v}_h}{|\mathbf{u}_h|_{1,q_\varepsilon,\Omega}|\mathbf{v}_h|_{1,q'_\varepsilon,\Omega}} \geqslant Ch^{\varepsilon}.$$

Proof. The bilinear form

$$a(\mathbf{u},\mathbf{v}) = \int_\Omega \nabla\mathbf{u} :: \nabla\mathbf{v}$$

is continuous and coercive on $H_0^1(\Omega)$, so for $\mathring{V}_h^k$ vector subspace of $H_0^1(\Omega)$, we have the inf-sup condition:

$$\inf_{\mathbf{u}_h\in\mathring{V}_h^k}\sup_{\mathbf{v}_h\in\mathring{V}_h^k}\frac{\int_\Omega \nabla\mathbf{u}_h :: \nabla\mathbf{v}_h}{|\mathbf{u}_h|_{1,\Omega}|\mathbf{v}_h|_{1,\Omega}} \geqslant \alpha > 0,$$

where α only depends on Ω. We recall the following inverse inequality:

Proposition 12 (Ciarlet, Theorem 3.2.6, page 140 [32])**.** *Let $\mathcal{T}_h$ a family of quasi-uniform simplicial triangulations of $\Omega\subset\mathbb{R}^d$, where h is the meshsize. For $\mathbf{v}_h\in V_h^k$, $1\leqslant r,s<+\infty$, $0\leqslant\ell\leqslant m$,*

$$\left(\sum_{T\in\mathcal{T}_h}|\mathbf{v}_h|_{m,r,T}^r\right)^{1/r} \leqslant Ch^{-d[\max\{0,1/s-1/r\}]}h^{-(m-\ell)}\left(\sum_{T\in\mathcal{T}_h}|\mathbf{v}_h|_{\ell,s,T}^s\right)^{1/s}.$$

We apply this to any $\mathbf{v}_h\in\mathring{V}_h^k\subset\mathscr{C}(\Omega)$, with $d=2$, $m=l=1$, $s=2$ and $r=q_\varepsilon'$ to get:

$$|\mathbf{v}_h|_{1,q_\varepsilon',\Omega}\leqslant Ch^{-2(1/2-1/q_\varepsilon')}|\mathbf{v}_h|_{1,2,\Omega} = Ch^{-\varepsilon}|\mathbf{v}_h|_{1,2,\Omega},$$

using Equation (3.3.13). Moreover, for any $\mathbf{u}_h\in\mathring{V}_h^k$,

$$|\mathbf{u}_h|_{1,q_\varepsilon,\Omega}\leqslant C|\mathbf{u}_h|_{1,2,\Omega}\leqslant C\sup_{\mathbf{v}_h\in\mathring{V}_h^k}\frac{\int_\Omega\nabla\mathbf{u}_h::\nabla\mathbf{v}_h}{|\mathbf{v}_h|_{1,2,\Omega}}\leqslant Ch^{-\varepsilon}\sup_{\mathbf{v}_h\in\mathring{V}_h^k}\frac{\int_\Omega\nabla\mathbf{u}_h::\nabla\mathbf{v}_h}{|\mathbf{v}_h|_{1,q_\varepsilon',\Omega}}.$$

Finally,

$$\inf_{\mathbf{u}_h\in\mathring{V}_h^k}\sup_{\mathbf{v}_h\in\mathring{V}_h^k}\frac{\int_\Omega\nabla\mathbf{u}_h::\nabla\mathbf{v}_h}{|\mathbf{u}_h|_{1,q_\varepsilon,\Omega}|\mathbf{v}_h|_{1,q_\varepsilon',\Omega}}\geqslant Ch^{\varepsilon}.$$

□

The second discrete inf-sup condition we need is given by the following lemma:

Lemma 9. *With q_ε and q_ε' defined in* (3.3.12)*, the approximations spaces V_h^k and W_h^k satisfy the following discrete inf-sup condition:*

$$\inf_{p_h\in W_h^k}\sup_{\mathbf{v}_h\in V_h^k}\frac{\int_\Omega\operatorname{div}(\mathbf{v}_h)p_h}{|p_h|_{0,q_\varepsilon,\Omega}|\mathbf{v}_h|_{1,q_\varepsilon',\Omega}}\geqslant Ch^{\varepsilon}.$$

Proof. The proof is similar to the proof of Lemma 8. By Assumption **B4**,

$$\inf_{p_h\in W_h^k}\sup_{\mathbf{v}_h\in V_h^k}\frac{\int_\Omega\operatorname{div}(\mathbf{v}_h)p_h}{|p_h|_{0,\Omega}|\mathbf{v}_h|_{1,\Omega}}\geqslant\beta>0.$$

By Proposition 12, for any $\mathbf{v}_h\in V_h^k$,

$$|\mathbf{v}_h|_{1,q_\varepsilon',\Omega}\leqslant Ch^{-\varepsilon}|\mathbf{v}_h|_{1,2,\Omega}.$$

So, we have, for any $p_h \in W_h^k$ and $q_\varepsilon < 2$,

$$|p_h|_{0,q_\varepsilon,\Omega} \leqslant C|p_h|_{0,\Omega} \leqslant C \sup_{\mathbf{v}_h \in V_h^k} \frac{\int_\Omega \operatorname{div}(\mathbf{v}_h) p_h}{|\mathbf{v}_h|_{1,2,\Omega}} \leqslant Ch^{-\varepsilon} \sup_{\mathbf{v}_h \in V_h^k} \frac{\int_\Omega \operatorname{div}(\mathbf{v}_h) p_h}{|\mathbf{v}_h|_{1,q'_\varepsilon,\Omega}}.$$

Finally, we get

$$\inf_{p_h \in W_h^k} \sup_{\mathbf{v}_h \in V_h^k} \frac{\int_\Omega \operatorname{div}(\mathbf{v}_h) p_h}{|p_h|_{0,q_\varepsilon,\Omega} |\mathbf{v}_h|_{1,q'_\varepsilon,\Omega}} \geqslant Ch^{\varepsilon}.$$

□

3.3.3 Estimates of $|\mathbf{u} - \mathbf{u}_h|_{1,q_\varepsilon,\Omega}$ and $|p - p_h|_{0,q_\varepsilon,\Omega}$

Following Corollary 2, the quantities $|\mathbf{u} - \mathbf{u}_h|_{1,q_\varepsilon,\Omega}$ and $|p - p_h|_{0,q_\varepsilon,\Omega}$ have to be estimated to prove Theorem 7. We apply the last two results to bound them in terms of $|\mathbf{u}|_{1,q_\varepsilon,\Omega}$ and $|p|_{0,q_\varepsilon,\Omega}$.

Lemma 10. *Let $(\mathbf{u}_h, p_h) \in V_h^k \times W_h^k$ be the Galerkin projection of the solution $(\mathbf{u}, p)$ of Problem* (3.1.1)*, for any small enough real $\varepsilon > 0$,*

$$|\mathbf{u} - \mathbf{u}_h|_{1,q_\varepsilon,\Omega} \leqslant Ch^{-\varepsilon} \left(|\mathbf{u}|_{1,q_\varepsilon,\Omega} + |p|_{0,q_\varepsilon,\Omega} \right).$$

Proof. First, we estimate $|\mathbf{u}_h|_{1,q_\varepsilon,\Omega}$ in terms of $|\mathbf{u}|_{1,q_\varepsilon,\Omega}$. As we have $\operatorname{div}(\mathbf{u}) = 0$ on Ω, by Equation (3.2.1) we have

$$\int_\Omega \operatorname{div}(\mathbf{u}_h) q_h = 0, \ \forall q_h \in W_h^k,$$

and so, $\mathbf{u}_h \in \mathring{V}_h^k$. By Lemma 8, there exists $\mathbf{v}_h \in \mathring{V}_h^k$ such as $|\mathbf{v}_h|_{1,q'_\varepsilon,\Omega} = 1$, and

$$|\mathbf{u}_h|_{1,q_\varepsilon,\Omega} \leqslant Ch^{-\varepsilon} \int_\Omega \nabla \mathbf{u}_h :: \nabla \mathbf{v}_h.$$

Moreover, Equation (3.2.1) gives

$$\int_\Omega \nabla \mathbf{u}_h :: \nabla \mathbf{v}_h = \int_\Omega \nabla \mathbf{u} :: \nabla \mathbf{v}_h - \int_\Omega \operatorname{div}(\mathbf{v}_h)(p - p_h).$$

Now, $\mathbf{v}_h \in \mathring{V}_h^k$, so

$$\int_\Omega \operatorname{div}(\mathbf{v}_h) p_h = 0.$$

Finally, as $|\mathbf{v}_h|_{1,q'_\varepsilon,\Omega} = 1$, we get

$$\begin{aligned} |\mathbf{u}_h|_{1,q_\varepsilon,\Omega} &\leqslant Ch^{-\varepsilon} \left(\int_\Omega \nabla \mathbf{u} :: \nabla \mathbf{v}_h - \int_\Omega \operatorname{div}(\mathbf{v}_h) p \right), \\ &\leqslant Ch^{-\varepsilon} \left(|\mathbf{u}|_{1,q_\varepsilon,\Omega} + |p|_{0,q_\varepsilon,\Omega} \right). \end{aligned}$$

We conclude with the triangulary inequality,

$$|\mathbf{u} - \mathbf{u}_h|_{1,q_\varepsilon,\Omega} \leqslant |\mathbf{u}|_{1,q_\varepsilon,\Omega} + |\mathbf{u}_h|_{1,q_\varepsilon,\Omega} \leqslant Ch^{-\varepsilon} \left(|\mathbf{u}|_{1,q_\varepsilon,\Omega} + |p|_{0,q_\varepsilon,\Omega} \right).$$

□

We can now estimate $|p - p_h|_{0,q_\varepsilon,\Omega}$.

Lemma 11. *Let $(\mathbf{u}_h, p_h) \in V_h^k \times W_h^k$ be the Galerkin projection of the solution $(\mathbf{u}, p)$ of Problem (3.1.1), for any small enough real $\varepsilon > 0$,*

$$|p - p_h|_{1,q_\varepsilon,\Omega} \leqslant Ch^{-2\varepsilon} \left(|\mathbf{u}|_{1,q_\varepsilon,\Omega} + |p|_{0,q_\varepsilon,\Omega} \right).$$

Proof. The proof is similar to the velocity case: by Lemma 9, there exists $\mathbf{v}_h \in V_h^k$ such as $|\mathbf{v}_h|_{1,q'_\varepsilon,\Omega} = 1$ and

$$|p_h|_{0,q_\varepsilon,\Omega} \leqslant Ch^{-\varepsilon} \int_\Omega \operatorname{div}(\mathbf{v}_h) p_h.$$

By Equation (3.2.1), we have

$$\int_\Omega \operatorname{div}(\mathbf{v}_h) p_h = -\int_\Omega \nabla(\mathbf{u} - \mathbf{u}_h) :: \nabla \mathbf{v}_h + \int_\Omega \operatorname{div}(\mathbf{v}_h) p.$$

By applying Lemma 10, as $|\mathbf{v}_h|_{1,q'_\varepsilon,\Omega} = 1$, we get

$$\begin{aligned} |p_h|_{0,q_\varepsilon,\Omega} &\leqslant Ch^{-\varepsilon} \left(-\int_\Omega \nabla(\mathbf{u} - \mathbf{u}_h) :: \nabla \mathbf{v}_h + \int_\Omega \operatorname{div}(\mathbf{v}_h) p \right), \\ &\leqslant Ch^{-\varepsilon} \left(|\mathbf{u} - \mathbf{u}_h|_{1,q_\varepsilon,\Omega} + |p|_{0,q_\varepsilon,\Omega} \right), \\ &\leqslant Ch^{-2\varepsilon} \left(|\mathbf{u}|_{1,q_\varepsilon,\Omega} + |p|_{0,q_\varepsilon,\Omega} \right). \end{aligned}$$

□

3.3.4 Proof of Theorem 7

We can now prove Theorem 7.

Proof. The functions $\mathbf{u}$ and p are analytic on $\overline{\Omega}_1$, so the quantities $\|\mathbf{u}\|_{k+1,\Omega_1}$ and $\|p\|_{k,\Omega_1}$ are bounded. Let us note that in this case $(\mathbf{u}, p) \notin H_0^1(\Omega)^2 \times \mathbb{L}_0^2(\Omega)$, but Remark 11 allows us to apply Arnold and Liu Theorem. For $k_1 = k$ and

$$k_2 = \begin{cases} 1 & \text{if } k = 1, \\ k - 1 & \text{if } k \geqslant 2, \end{cases}$$

and $l = k + 1 = \widetilde{r}_1$ and $t = k - 1$, we have

$$\|\mathbf{u} - \mathbf{u}_h\|_{1,\Omega_0} + \|p - p_h\|_{0,\Omega_0} \leqslant C(h^k + \|\mathbf{u} - \mathbf{u}_h\|_{-k+1,\Omega_1} + \|p - p_h\|_{-k,\Omega_1}).$$

By combining Corollary 2, Lemmas 10 and 11, and Inequalities (1.4.5) and (1.4.6) (see Chapter 1, Section 1.4.1.2), we get

$$\|\mathbf{u} - \mathbf{u}_h\|_{-k+1,\Omega_1} + \|p - p_h\|_{-k,\Omega_1} \leqslant Ch^k \frac{h^{-3\varepsilon}}{\sqrt{2 - q_\varepsilon}}.$$

By (3.3.12), with $\varepsilon \leqslant 1$,

$$\frac{1}{\sqrt{2-q_\varepsilon}} = \frac{\sqrt{1+\varepsilon}}{\sqrt{2\varepsilon}} \leqslant \frac{1}{\sqrt{\varepsilon}}, \tag{3.3.14}$$

therefore, taking $\varepsilon = |\ln h|^{-1}$,

$$\|\mathbf{u} - \mathbf{u}_h\|_{1,\Omega_0} + \|p - p_h\|_{0,\Omega_0} \leqslant Ch^k\sqrt{|\ln h|},$$

which ends the proof of Theorem 7. □

3.4 General case

Theorem 7 and its proof have been written in the particular case of the $\mathbb{P}_k/\mathbb{P}_{k-1}$ finite element method, $k \geqslant 2$, and the $\mathbb{P}_1$b/$\mathbb{P}_1$ elements (which corresponds to the case $k = 1$). But we can state two more general results.

3.4.1 Some more general assumptions

First, we focus on the assumptions. Let $\mathcal{T}_h$ be a family of quasi-uniform simplicial triangulations of Ω, let $V_h^{k_1}$ and $W_h^{k_2}$ be two approximation spaces satisfying Assumption 6. We also assume that $V_h^{k_1} \in \mathscr{C}(\Omega)$: this assumption ensures that the finite element solution is well-defined. Moreover, we need two more assumptions, they play the role of Propositions 11 and 12:

Assumption 7. *Given $B \subset \Omega$, consider $q' \geqslant 2$, there exists an h_0 such that for all $0 < h \leqslant h_0$, we have for some positive integers k_1, k_2, and some reals $R_1, R_2 \geqslant 1$:*

$\widetilde{\mathbf{B}}$1 *For any $0 \leqslant m \leqslant R_1$ and $m \leqslant \ell$, for each $\mathbf{v} \in H^\ell(B)^2$, there exists $\eta \in V_h^{k_1}$ such that, for any mesh element $T \subset B$,*

$$|\mathbf{v} - \eta|_{m,q',T} \leqslant Ch^{d(1/q'-1/2)}h^{\widetilde{r}_1-m}|\mathbf{v}|_{\ell,2,T}, \quad \widetilde{r}_1 = \min(k_1+1, \ell).$$

For any $0 \leqslant m \leqslant R_2$ and $m \leqslant \ell$, for each $\pi \in H^\ell(B)$, there exists $\xi \in W_h^{k_2}$ such that, for any mesh element $T \subset B$,

$$|\pi - \xi|_{m,q',T} \leqslant Ch^{d(1/q'-1/2)}h^{\widetilde{r}_2-m}|\pi|_{\ell,2,T}, \quad \widetilde{r}_2 = \min(k_2+1, \ell).$$

$\widetilde{\mathbf{B}}$3 *For $0 \leqslant m \leqslant \ell \leqslant R_1$, for all $\mathbf{v}_h \in V_h^{k_1}$, for any mesh element $T \in \mathcal{T}_h$, we have*

$$\|\mathbf{v}_h\|_{\ell,q',T} \leqslant Ch^{2(1/q'-1/2)}h^{m-\ell}\|\mathbf{v}_h\|_{m,2,T}.$$

For $0 \leqslant m \leqslant \ell \leqslant R_2$, for all $\pi_h \in W_h^{k_2}$, for any mesh element $T \in \mathcal{T}_h$, we have

$$\|\pi_h\|_{\ell,T} \leqslant Ch^{m-\ell}\|\pi_h\|_{m,T}.$$

Assumptions $\widetilde{\mathbf{B1}}$ and $\widetilde{\mathbf{B3}}$ are also satisfied by a wide class of finite element spaces, including all finite element spaces defined on quasi-uniform meshes [32]. They are actually common generalisations of Assumptions **B1** and **B3**. The parameters R_1 and R_2 play the roles of the regularities of the approximation spaces $V_h^{k_1}$ and $W_h^{k_2}$.

3.4.2 Generalization of Theorem 7

We can now state the following result:

Theorem 8. *Consider $\Omega_0 \subset\subset \Omega_1 \subset\subset \Omega$ satisfying Assumption 5, $1 \leqslant q < 2$, the solution $(\mathbf{u}, p) \in W_0^{1,q}(\Omega)^2 \times \mathbb{L}_0^q(\Omega)$ of Problem (3.1.1) and $(\mathbf{u}_h, p_h)$ its Galerkin projection onto $V_h^{k_1} \times W_h^{k_2}$ satisfying $\int_\Omega p_h = 0$ and*

$$\begin{aligned} \int_\Omega \nabla(\mathbf{u}-\mathbf{u}_h) :: \nabla\eta - \int_\Omega (p-p_h)\mathrm{div}(\eta) &= 0 \quad \textit{for all } \eta \in V_h^k, \\ \int_\Omega \mathrm{div}(\mathbf{u}-\mathbf{u}_h)\xi &= 0 \quad \textit{for all } \xi \in W_h^k. \end{aligned}$$

Under the assumption that $(\mathbf{u}, p) \in H^{k_0+1}(\Omega_1)^2 \times H^{k_0}(\Omega_1)$, there exists h_1 such that if $0 < h \leqslant h_1$, we have,

$$\|\mathbf{u}-\mathbf{u}_h\|_{1,\Omega_0} + \|p-p_h\|_{0,\Omega_0} \leqslant C(\Omega_0,\Omega_1,\Omega) h^{k_0} \sqrt{|\ln h|},$$

where $k_0 = \min(k_1, k_2+1)$.

Proof. We do not develop the complete proof here because it is essentially the same as the proof of Theorem 7 (see Section 3.3). But we explain two differences between both proofs:

- the result of Lemma 7 holds in this case, but for $0 \leqslant t \leqslant \min(k_1-1, k_2)$.
- the result of Corollary 2 becomes

$$\begin{aligned} &\|\mathbf{u}-\mathbf{u}_h\|_{-k_0+1,\Omega} + \|p-p_h\|_{-k_0,\Omega} \\ &\qquad \leqslant C h^{-\varepsilon} h^{k_0} \left(|\mathbf{u}-\mathbf{u}_h|_{1,q_\varepsilon,\Omega} + |p-p_h|_{0,q_\varepsilon,\Omega} \right), \end{aligned} \tag{3.4.1}$$

  where $k_0 = \min(k_1, k_2+1)$.

The end of the proof is the same. □

The next two sections are dedicated to the local error analysis for the Stokes equations with a punctual force in source term in $H^s \times H^{s-1}$-norm, with $s \geqslant 2$.

3.4.3 Local error estimates in $H^s \times H^{s-1}$-norm, with $s \geqslant 2$

Before proceeding, we have to state the following result. It can be seen as a complement of the Arnold and Liu Theorem.

Theorem 9. *Consider $\Omega_0 \subset\subset \Omega_1 \subset\subset \Omega$, $V_h^{k_1}$ and $W_h^{k_2}$ satisfy Assumption 5. Moreover, we assume that $V_h^{k_1}$ and $W_h^{k_2}$ also satisfy Assumption 6, and Assumption 7 for $q' = 2$. Suppose that $(\mathbf{v}, \pi)_{|\Omega_1} \in H^\ell(\Omega_1)^2 \times H^{\ell-1}(\Omega_1)$ for some $\ell > 0$, and $(\mathbf{v}_h, \pi_h) \in V_h^k \times W_h^k$ satisfies $\int_\Omega \pi - \pi_h = 0$ and*

$$\begin{aligned} \int_\Omega \nabla(\mathbf{v} - \mathbf{v}_h) :: \nabla\eta - \int_\Omega (\pi - \pi_h)\mathrm{div}(\eta) &= 0 \quad \textit{for all } \eta \in V_h^k, \\ \int_\Omega \mathrm{div}(\mathbf{v} - \mathbf{v}_h)\xi &= 0 \quad \textit{for all } \xi \in W_h^k. \end{aligned}$$

Let t be a nonnegative integer. Then, there exist a constant $C > 0$ and a real $h_1 > 0$ depending only on Ω_1, Ω_0, and t, such that for $0 < h \leqslant h_1$, and $2 \leqslant s \leqslant \ell$, with $s \leqslant k_1 < R_1$ and $s \leqslant k_2 + 1 < R_2 + 1$, we have

$$\begin{aligned} \|\mathbf{v} - \mathbf{v}_h\|_{s,\Omega_0} + \|\pi - \pi_h\|_{s-1,\Omega_0} \leqslant & C\big[h^{r_1-s}\|\mathbf{v}\|_{\ell,\Omega_1} + h^{r_2-s}\|\pi\|_{\ell-1,\Omega_1} \\ & + h^{1-s}(\|\mathbf{v} - \mathbf{v}_h\|_{-t,\Omega_1} + \|\pi - \pi_h\|_{-t-1,\Omega_1})\big], \end{aligned} \tag{3.4.2}$$

where $r_1 = \min(k_1 + 1, \ell)$, $r_2 = \min(k_2 + 2, \ell)$.

We first prove a local version of Theorem 9.

Lemma 12. *Suppose the conditions of Theorem 9 are satisfied, then* (3.4.2) *holds with Ω_0 and Ω_1 replaced by G_0 and G, two concentric disks such as $G_0 \subset\subset G \subset\subset \Omega_1$.*

Proof. Let us fix $2 \leqslant s \leqslant \ell$ such as $s \leqslant k_1 < R_1$ and $s \leqslant k_2 + 1 < R_2 + 1$, and consider $G_0 \subset\subset G_h \subset\subset G_1 \subset\subset G \subset\subset \Omega_1$ where G_0, G_1 and G are concentric disks, and G_h is a union of mesh elements. Then, for any $(\eta, \xi) \in V_h^{k_1} \times W_h^{k_2}$,

$$\begin{aligned} &\|\mathbf{v} - \mathbf{v}_h\|_{s,G_0} + \|\pi - \pi_h\|_{s-1,G_0} \\ &\quad \leqslant \|\mathbf{v} - \eta\|_{s,G} + \|\eta - \mathbf{v}_h\|_{s,G_h} + \|\pi - \xi\|_{s-1,G} + \|\xi - \pi_h\|_{s-1,G_h}. \end{aligned}$$

Thanks to Assumption $\widetilde{\mathbf{B}}\mathbf{3}$, applied for $q' = 2$,

$$\begin{aligned} \|\eta - \mathbf{v}_h\|_{s,G_h} &\leqslant h^{1-s}\|\eta - \mathbf{v}_h\|_{1,G_h}, \\ \|\xi - \pi_h\|_{s-1,G_h} &\leqslant h^{1-s}\|\xi - \pi_h\|_{0,G_h}, \end{aligned}$$

so that we have

$$\begin{aligned} &\|\mathbf{v} - \mathbf{v}_h\|_{s,G_0} + \|\pi - \pi_h\|_{s-1,G_0} \\ &\quad \leqslant \|\mathbf{v} - \eta\|_{s,G} + h^{1-s}\|\eta - \mathbf{v}_h\|_{1,G_h} + \|\pi - \xi\|_{s-1,G} + h^{1-s}\|\xi - \pi_h\|_{0,G_h}, \\ &\quad \leqslant \|\mathbf{v} - \eta\|_{s,G} + \|\pi - \xi\|_{s-1,G} + h^{1-s}(\|\mathbf{v} - \mathbf{v}_h\|_{1,G_1} + \|\pi - \pi_h\|_{0,G_1}) \\ &\qquad + h^{1-s}(\|\mathbf{v} - \eta\|_{1,G} + \|\pi - \xi\|_{0,G}). \end{aligned} \tag{3.4.3}$$

We now estimate all the terms in Equation (3.4.3):

- thanks to Assumption $\widetilde{\mathbf{B}}1$, applied for $q' = 2$, there exists $\eta \in V_h^{k_1}$ such that

$$\|\mathbf{v} - \eta\|_{s,G} \leqslant Ch^{r_1 - s}\|\mathbf{v}\|_{\ell,G} \text{ and } \|\mathbf{v} - \eta\|_{1,G} \leqslant Ch^{r_1 - 1}\|\mathbf{v}\|_{\ell,G}, \tag{3.4.4}$$

  where $r_1 = \min(k_1 + 1, \ell)$.

- still thanks to Assumption $\widetilde{\mathbf{B}}1$, there exists $\xi \in W_h^{k_2}$ such that

$$\|\pi - \xi\|_{s-1,G} \leqslant Ch^{r_2 - s}\|\pi\|_{\ell-1,G} \text{ and } \|\pi - \xi\|_{0,G} \leqslant Ch^{r_2 - 1}\|\pi\|_{\ell-1,G}, \tag{3.4.5}$$

  where $r_2 = \min(k_2 + 2, \ell)$.

- applying Arnold and Liu Theorem for $\Omega_0 = G_1$ and $\Omega_1 = G$, we get

$$\begin{aligned}\|\mathbf{v} - \mathbf{v}_h\|_{1,G_1} + \|\pi - \pi_h\|_{0,G_1} \leqslant & C(h^{r_1 - 1}\|\mathbf{v}\|_{\ell,G} + h^{r_2 - 1}\|\pi\|_{\ell-1,G} \\ & + \|\mathbf{v} - \mathbf{v}_h\|_{-t,G} + \|\pi - \pi_h\|_{-t-1,G}).\end{aligned} \tag{3.4.6}$$

Finally, combining (3.4.3), (3.4.4), (3.4.5), and (3.4.6), we get the result of Theorem 9 with $\Omega_0 = G_0$ and $\Omega_1 = G$:

$$\begin{aligned}\|\mathbf{v} - \mathbf{v}_h\|_{s,G_0} + \|\pi - \pi_h\|_{s-1,G_0} \leqslant & C\big[h^{r_1 - s}\|\mathbf{v}\|_{\ell,G} + h^{r_2 - s}\|\pi\|_{\ell-1,G} \\ & + h^{1-s}(\|\mathbf{v} - \mathbf{v}_h\|_{-t,G} + \|\pi - \pi_h\|_{-t-1,G})\big].\end{aligned}$$

□

We can now prove Theorem 9.

Proof. The argument is the same as in Theorem 5.1 in [88]. Consider $d = d_0/2$ where $d_0 = \operatorname{dist}(\bar{\Omega}_0, \partial\Omega_1)$. Cover $\bar{\Omega}_0$ with a finite number of disks $G_0(x_i)$, $i = 1, 2, ..., N$ centered at $x_i \in \Omega_0$ with diam $G_0(x_i) = d$. Let us note that the number N of disks depends only on Ω_0 and Ω_1. For all $i \in [\![1, N]\!]$, we define $G(x_i)$ corresponding concentric disks with diam $G(x_i) = 2d$, so that we have:

$$\bar{\Omega}_0 \subset \bigcup_{i=1}^{N} G_0(x_i) \subset \bigcup_{i=1}^{N} G(x_i) \subset \Omega_1.$$

We apply Lemma 12 to each couple (G_0, G), so that we get:

$$\begin{aligned}\|\mathbf{v} - \mathbf{v}_h\|_{s,\Omega_0} + \|\pi - \pi_h\|_{s-1,\Omega_0} &\leqslant \sum_{i=1}^{N} \|\mathbf{v} - \mathbf{v}_h\|_{s,G_0(x_i)} + \|\pi - \pi_h\|_{s-1,G_0(x_i)}, \\ &\leqslant C \sum_{i=1}^{N} \big[h^{r_1 - s}\|\mathbf{v}\|_{\ell,G(x_i)} + h^{r_2 - s}\|\pi\|_{\ell-1,G(x_i)} \\ &\quad + h^{1-s}(\|\mathbf{v} - \mathbf{v}_h\|_{-t,G(x_i)} + \|\pi - \pi_h\|_{-t-1,G(x_i)})\big], \\ &\leqslant C_N\big[h^{r_1 - s}\|\mathbf{v}\|_{\ell,\Omega_1} + h^{r_2 - s}\|\pi\|_{\ell-1,\Omega_1} \\ &\quad + h^{1-s}(\|\mathbf{v} - \mathbf{v}_h\|_{-t,\Omega_1} + \|\pi - \pi_h\|_{-t-1,\Omega_1})\big],\end{aligned}$$

which ends the proof of Theorem 9. □

3.4.4 Local error analysis in $H^s \times H^{s-1}$-norm for the Stokes equations with a punctual force in source term, $s \geqslant 2$

In the same way we proved Theorem 8 based on Arnold and Liu Theorem, we apply Theorem 9 to prove the following result.

Theorem 10. *Consider $\Omega_0 \subset\subset \Omega_1 \subset\subset \Omega$, $V_h^{k_1}$ and $W_h^{k_2}$ satisfy Assumption 5. Moreover, we assume that $V_h^{k_1}$ and $W_h^{k_2}$ also satisfy Assumption 6 and Assumption 7. Consider $1 \leqslant q < 2$, let $(\mathbf{u}, p) \in W_0^{1,q}(\Omega)^2 \times \mathbb{L}_0^q(\Omega)$ be the solution of Problem (3.1.1) and $(\mathbf{u}_h, p_h)$ its Galerkin projection onto $V_h^{k_1} \times W_h^{k_2}$ satisfying $\int_\Omega p_h = 0$ and*

$$\begin{aligned} \int_\Omega \nabla(\mathbf{u} - \mathbf{u}_h) :: \nabla\eta - \int_\Omega (p - p_h)\mathrm{div}(\eta) &= 0 \quad \textit{for all } \eta \in V_h^k, \\ \int_\Omega \mathrm{div}(\mathbf{u} - \mathbf{u}_h)\xi &= 0 \quad \textit{for all } \xi \in W_h^k. \end{aligned}$$

Under the assumption that $(\mathbf{u}, p) \in H^{k_0+1}(\Omega_1)^2 \times H^{k_0}(\Omega_1)$, there exists h_1 such that if $0 < h \leqslant h_1$, we have for $2 \leqslant s \leqslant k_0 < \min(R_1, R_2 + 1)$,

$$\|\mathbf{u} - \mathbf{u}_h\|_{s,\Omega_0} + \|p - p_h\|_{s-1,\Omega_0} \leqslant C(\Omega_0, \Omega_1, \Omega) h^{k_0+1-s} \sqrt{|\ln h|},$$

where $k_0 = \min(k_1, k_2 + 1)$.

Proof. The proof is similar to the one of Theorem 7. The functions $\mathbf{u}$ and p are analytic on $\overline{\Omega}_1$, so the quantities $\|\mathbf{u}\|_{k_0+1,\Omega_1}$ and $\|p\|_{k_0,\Omega_1}$ are bounded. Let us apply Theorem 9 taking $\ell = k_0 + 1$ and $t = k_0 - 1$. For $2 \leqslant s \leqslant \min(k_1, k_2 + 1) < \min(R_1, R_2 + 1)$, we have:

$$\|\mathbf{u} - \mathbf{u}_h\|_{s,\Omega_0} + \|p - p_h\|_{s-1,\Omega_0} \leqslant C\big[h^{k_0+1-s} + h^{1-s}(\|\mathbf{u} - \mathbf{u}_h\|_{-k_0+1,\Omega_1} + \|p - p_h\|_{-k_0,\Omega_1})\big].$$

Assumptions of Theorem 10 imply that assumptions of Theorem 8 are satisfied. We conclude that Estimate (3.4.1) holds, so that:

$$\|\mathbf{u} - \mathbf{u}_h\|_{s,\Omega_0} + \|p - p_h\|_{s-1,\Omega_0} \leqslant C h^{k_0+1-s} h^{-\varepsilon}\big[|\mathbf{u} - \mathbf{u}_h|_{1,q_\varepsilon,\Omega} + |p - p_h|_{0,q_\varepsilon,\Omega}\big],$$

where q_ε is defined in (3.3.12). By combining Lemmas 10 and 11, and Inequalities (1.4.5) and (1.4.6) (see Chapter 1, Section 1.4.1.2), we get

$$\|\mathbf{u} - \mathbf{u}_h\|_{s,\Omega_0} + \|p - p_h\|_{s-1,\Omega_0} \leqslant C h^{k_0+1-s} \frac{h^{-3\varepsilon}}{\sqrt{2 - q_\varepsilon}}.$$

By (3.3.14), with $\varepsilon = |\ln h|^{-1}$, we have

$$\|\mathbf{u} - \mathbf{u}_h\|_{s,\Omega_0} + \|p - p_h\|_{s-1,\Omega_0} \leqslant C h^{k_0+1-s} \sqrt{|\ln h|},$$

which ends the proof of Theorem 10. □

3.5 Summary of the main theoretical results of this chapter

The aim of this section is to collect the results of this chapter to have a clear view of them. We have proved the following results:

Theorem 11. *Consider $\Omega_0 \subset\subset \Omega_1 \subset\subset \Omega$, $V_h^{k_1} \subset \mathscr{C}(\Omega)$ and $W_h^{k_2}$ satisfy Assumption 5. Moreover, we assume that $V_h^{k_1}$ and $W_h^{k_2}$ also satisfy Assumption 6, and Assumption 7. Consider $1 \leqslant q < 2$, let $(\mathbf{u}, p) \in W_0^{1,q}(\Omega)^2 \times \mathbb{L}_0^q(\Omega)$ be the solution of Problem (3.1.1) and $(\mathbf{u}_h, p_h)$ its Galerkin projection onto $V_h^{k_1} \times W_h^{k_2}$ satisfying $\int_\Omega p_h = 0$ and*

$$\begin{aligned} \int_\Omega \nabla(\mathbf{u}-\mathbf{u}_h) :: \nabla\eta - \int_\Omega (p-p_h)\mathrm{div}(\eta) &= 0 \quad \textit{for all } \eta \in V_h^k, \\ \int_\Omega \mathrm{div}(\mathbf{u}-\mathbf{u}_h)\xi &= 0 \quad \textit{for all } \xi \in W_h^k. \end{aligned}$$

Under the assumption that $(\mathbf{u}, p) \in H^{k_0+1}(\Omega_1)^2 \times H^{k_0}(\Omega_1)$, there exists h_1 such that if $0 < h \leqslant h_1$, for $1 \leqslant s \leqslant k_0 < \min(R_1, R_2+1)$, we have

$$\|\mathbf{u}-\mathbf{u}_h\|_{s,\Omega_0} + \|p-p_h\|_{s-1,\Omega_0} \leqslant C(\Omega_0,\Omega_1,\Omega) h^{k_0+1-s}\sqrt{|\ln h|}.$$

where $k_0 = \min(k_1, k_2+1)$.

First, the case $s = 1$ in Theorem 11 has been proved in the particular context of the $\mathbb{P}_k/\mathbb{P}_{k-1}$ finite elements, for $k \geqslant 2$, and the $\mathbb{P}_1\mathrm{b}/\mathbb{P}_1$ finite elements (which corresponds to the situation $k = 1$). It is Theorem 7.

Theorem 11 is a mix of Theorem 8 (case $s = 1$) and Theorem 10 (case $s \geqslant 2$), which have been proved in Section 3.4. For $s = 1$, the proof is based on the Arnold and Liu Theorem [4]. For $s \geqslant 2$, the result is a consequence of Theorem 9, proved in Section 3.4.3.

Next section is devoted to the numerical illustrations of these theoretical results.

3.6 Numerical illustrations

In this section, we present some computations which illustrate the theoretical results proved in this chapter.

Concentration of the error around the singularity. First, we define Ω as the unit square,

$$\Omega = [0,1]^2.$$

and solve the following Stokes problem with $\mathbf{F} = {}^t[1,1]$ and $\mathbf{x}_0 = (0.5, 0.5)$,

$$\left\{ \begin{array}{rcll} -\triangle\mathbf{u} + \nabla p &=& \delta_{\mathbf{x}_0}\mathbf{F} & \text{in } \Omega, \\ \mathrm{div}(\mathbf{u}) &=& 0 & \text{in } \Omega, \\ \mathbf{u} &=& \mathbf{u}_\delta & \text{on } \partial\Omega, \end{array} \right. \tag{3.6.1}$$

where $\mathbf{u}_\delta$ is the 2d Stokeslet defined in (1.4.2) (see Chapter 1, Section 1.4.1.1).

Remark 12. *Unlike Problem* (3.1.1), *Problem* (3.6.1) *has non homogeneous Dirichlet boundary conditions, but in this case, the exact solution is known:* $\mathbf{u}_\delta$. *Thus, it is easier to get some information on the error.*

Figures 3.2, 3.3, 3.4 and 3.5 show the repartition of the error on the velocity with a $\mathbb{P}_1\text{b}/\mathbb{P}_1$ method for respectively $1/h \simeq 5, 10, 20$ and 30. Figures 3.6, 3.7, 3.8 and 3.9 show the repartition of the error on the pressure for the same values of h. In both cases, they illustrate the fact that the error concentrates around the singularity. These simulations made us think that the convergence could be optimal on a subdomain which does not contain the singularity: quasi-optimality has been proved in this chapter (Theorem 7).

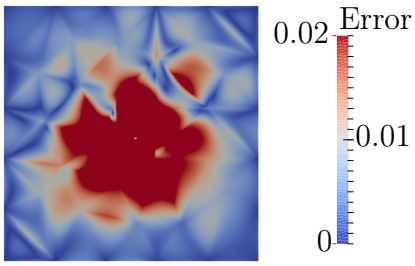

Figure 3.2: Error in velocity, $1/h \simeq 5$.

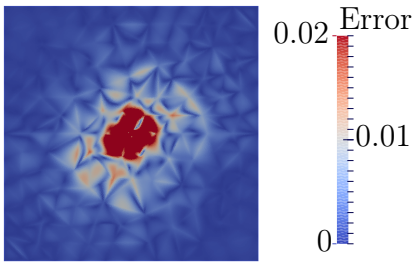

Figure 3.3: Error in velocity, $1/h \simeq 10$.

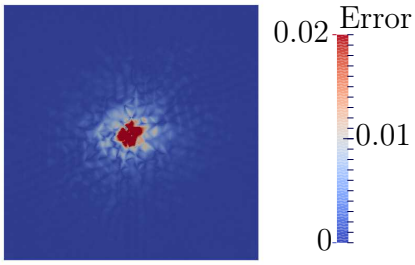

Figure 3.4: Error in velocity, $1/h \simeq 20$.

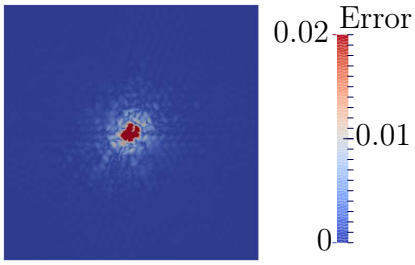

Figure 3.5: Error in velocity $1/h \simeq 30$.

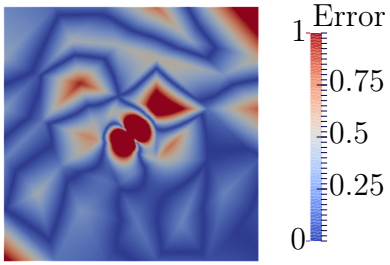

Figure 3.6: Error in pressure, $1/h \simeq 5$.

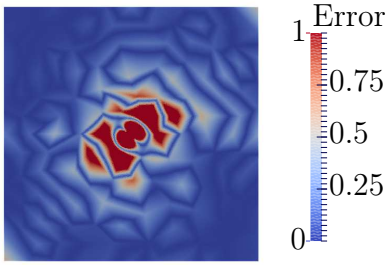

Figure 3.7: Error in pressure, $1/h \simeq 10$.

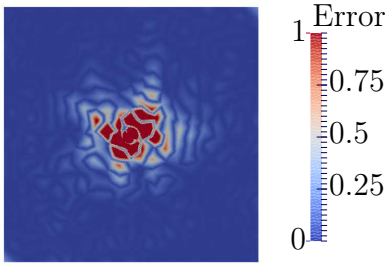

Figure 3.8: Error in pressure, $1/h \simeq 20$.

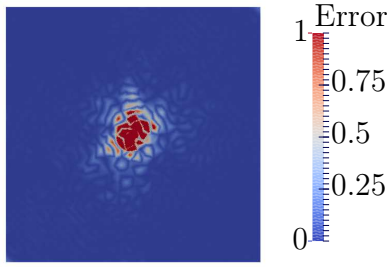

Figure 3.9: Error in pressure $1/h \simeq 30$.

Estimated orders of convergence. For this second example, the domain Ω is still the unit square, and Ω_0 is defined as the following portion of Ω,

$$\Omega_0 = \{\mathbf{x} \in \Omega : \|\mathbf{x} - \mathbf{x}_0\|_2 > 0.4\},$$

where $\mathbf{x}_0 = (0.5, 0.5)$. We fix $\mathbf{F} = {}^t[1, 1]$ and solve Problem 3.1.1 for different mesh sizes h with the $\mathbb{P}_1\text{b}/\mathbb{P}_1$, $\mathbb{P}_2/\mathbb{P}_1$ and $\mathbb{P}_3/\mathbb{P}_2$ finite element methods.

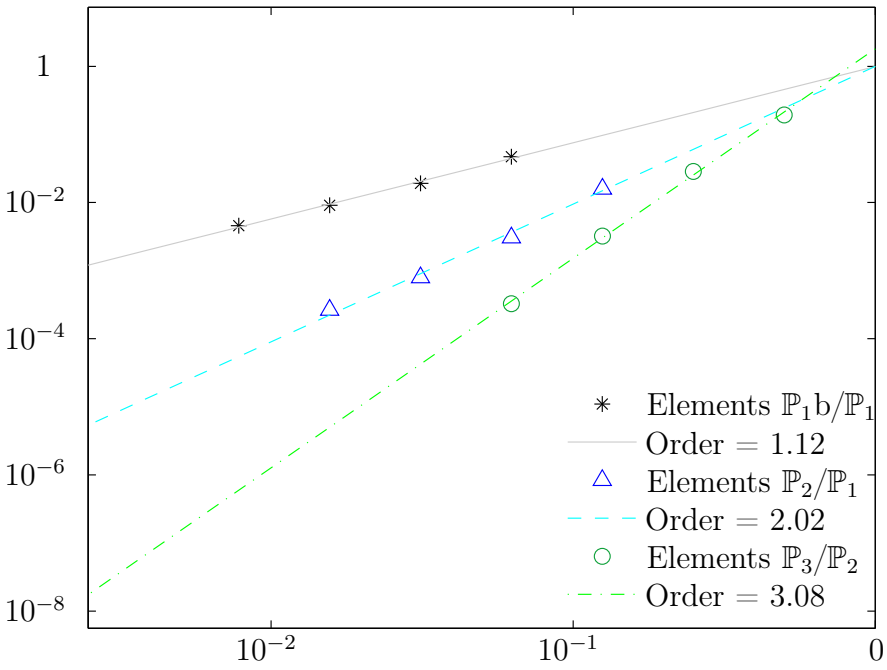

Figure 3.10: Estimated order of convergence for the $H^1(\Omega_0)$-norm of the velocity.

Figure 3.10 (respectively Figure 3.11) presents the estimated orders of convergence for the $H^1(\Omega_0)$-norm of the velocity (respectively the $\mathbb{L}^2(\Omega_0)$-norm of the pressure) for these three methods. The convergence far from the singularity (*i.e.* on Ω_0) is the same as in the regular case: the $\mathbb{P}_k/\mathbb{P}_{k-1}$ method (or the $\mathbb{P}_1\text{b}/\mathbb{P}_1$ method if $k = 1$) converges at the order k on Ω_0 in H^1-norm for the velocity and in $\mathbb{L}^2$-norm for the pressure, as proved

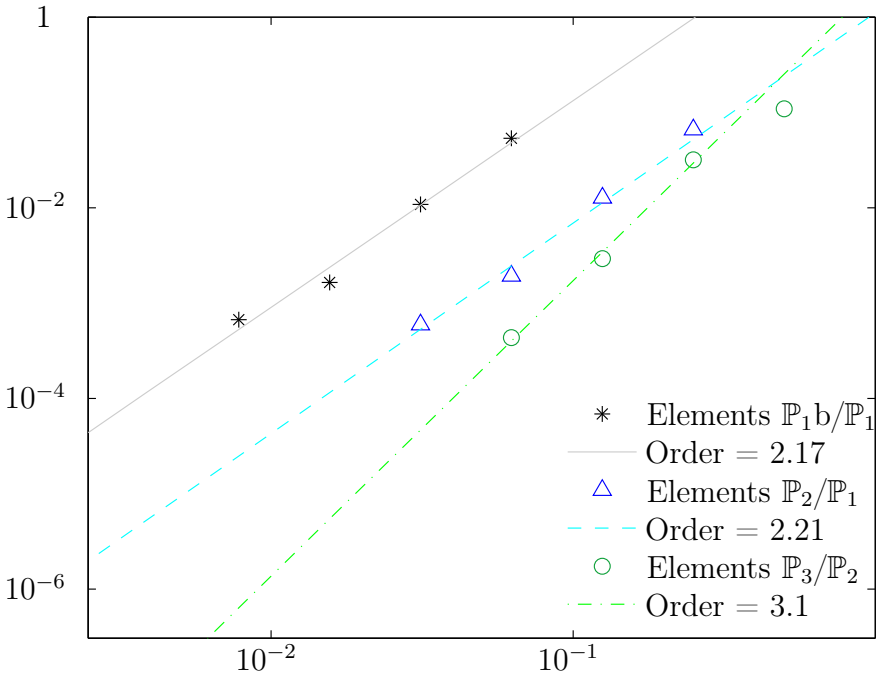

Figure 3.11: Estimated order of convergence for the $\mathbb{L}^2(\Omega_0)$-norm of the pressure.

in this chapter. Let us just note that there is an over-convergence in pressure for the $\mathbb{P}_1$b/$\mathbb{P}_1$ elements: the estimated order of convergence is approximately 2, greater than the convergence expected by Theorem 7.

About the error in $\mathbb{L}^2(\Omega_0)$-norm for the velocity, Figure 3.12 suggests that the $\mathbb{P}_k/\mathbb{P}_{k-1}$ finite element method (or $\mathbb{P}_1$b/$\mathbb{P}_1$ if $k = 1$) converges at the order $k+1$ on Ω_0. This result has only been observed numerically but it is still an open question.

3.7 Discussion

3.7.1 The three-dimensional case

Punctual force. The approach presented in this chapter can be also extended to the three-dimensional case, but like is the case of the Poisson problem, straighforward adaptations of the proofs lead to a suboptimal result. First, the solution $(\mathbf{u}, p)$ belongs to $W_0^{1,q}(\Omega) \times \mathbb{L}_0^q(\Omega)$ for all q in $[1, 3/2[$, as a consequence the couple $(q_\varepsilon, q'_\varepsilon)$ defined in (3.3.12) has to be once again taken near from $(3/2, 3)$. We fix

$$q_\varepsilon = \frac{3}{2+\varepsilon} \text{ and } q'_\varepsilon = \frac{3}{1-\varepsilon},$$

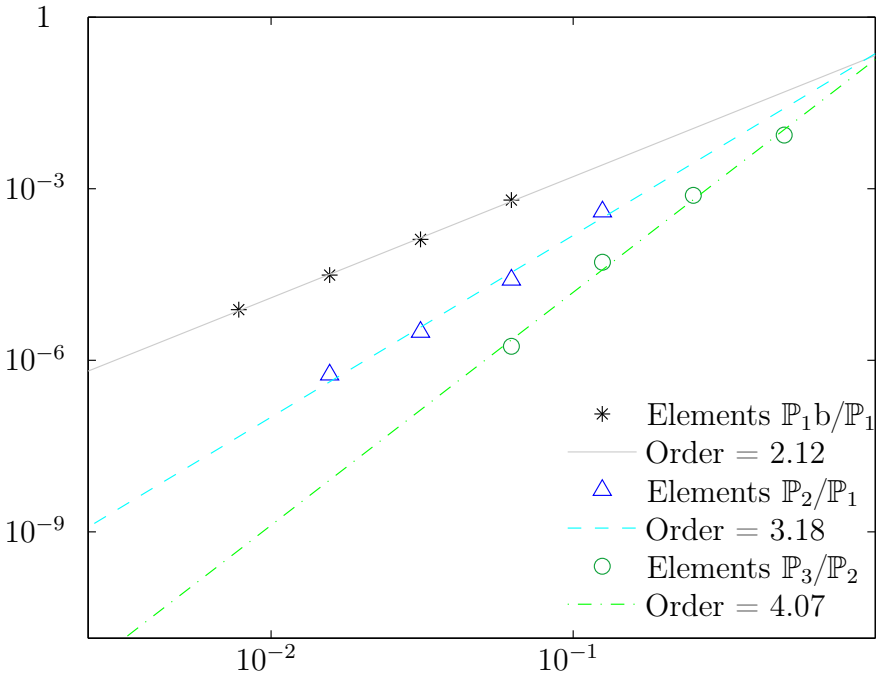

Figure 3.12: Estimated order of convergence for the $\mathbb{L}^2(\Omega_0)$-norm of the velocity.

so that, with the same notations, the result of Corollary 2 becomes

$$\begin{aligned}\|\mathbf{u}-\mathbf{u}_h\|_{-k+1,\Omega} + \|p-p_h\|_{-k,\Omega} \\ \leqslant Ch^{-\varepsilon-1/2}h^k\left(|\mathbf{u}-\mathbf{u}_h|_{1,q_\varepsilon,\Omega} + |p-p_h|_{0,q_\varepsilon,\Omega}\right).\end{aligned}$$

Moreover, the discrete inf-sup conditions in dimension 3 are

$$\inf_{\mathbf{u}_h\in\mathring{V}_h^k}\sup_{\mathbf{v}_h\in\mathring{V}_h^k}\frac{\int_\Omega \nabla\mathbf{u}_h\cdot\nabla\mathbf{v}_h}{\|\mathbf{u}_h\|_{1,q_\varepsilon,\Omega}\|\mathbf{v}_h\|_{1,q'_\varepsilon,\Omega}} \geqslant Ch^{\varepsilon+1/2},$$

and

$$\inf_{p_h\in W_h^k}\sup_{\mathbf{v}_h\in V_h^k}\frac{\int_\Omega \operatorname{div}(\mathbf{v}_h)p_h}{|p_h|_{0,q_\varepsilon,\Omega}|\mathbf{v}_h|_{1,q'_\varepsilon,\Omega}} \geqslant Ch^{\varepsilon+1/2}.$$

The rest of the proof is exactly the same, and we finally get the estimate

$$\|\mathbf{u}-\mathbf{u}_h\|_{1,\Omega_0} + \|p-p_h\|_{0,\Omega_0} \leqslant C(\Omega_0,\Omega_1,\Omega)h^{k-1}\sqrt[3]{|\ln h|}^2.$$

which is clearly suboptimal.

Line Dirac of force. The proof presented in the case of the punctual force, and the adaptations in 3d suggest that the method lead to a local quasi-optimal convergence in the case where the solution $(\mathbf{u},p)$ belongs to $\in W_0^{1,q}(\Omega)\times\mathbb{L}_0^q(\Omega)$ for all q in $[1,2[$. For

example, in 3-dimension, a line Dirac of force along a curve $\Gamma \subset\subset \Omega$ belongs to $H^{-1-\eta}(\Omega)$ for all $\eta > 0$, so that the solution $(\mathbf{u}^\Gamma, p^\Gamma)$ of the Stokes problem with the line Dirac of forces δ_Γ belongs to $\in W_0^{1,q}(\Omega) \times \mathbb{L}_0^q(\Omega)$, $q \in [1, 2[$. In this case, we can proof the following estimate

$$\|\mathbf{u}^\Gamma - \mathbf{u}_h^\Gamma\|_{1,\Omega_0} + \|p^\Gamma - p_h^\Gamma\|_{0,\Omega_0} \leqslant C(\Omega_0, \Omega_1, \Omega) h^k \sqrt{|\ln h|},$$

which is quasi-optimal. This result is shown using the same arguments as the ones presented in Section 3.3.

3.7.2 Punctual force near the boundary

The conclusions about this critical case are strictly the same as for the Poisson problem. Curious reader is encouraged to see Chapter 2, Section 2.7.2 for further information.

Chapters 2 and 3 establish the analysis of local errors for the finite element methods to solve elliptic problem (Poisson and Stokes problems) with a singular source term. Last chapter presents a new method to solve these problems and recover the optimal convergence rate: it is based on the knowledge of the singularity of the solutions [67]. Once set, this method is applied to the study of mucociliary transport.

CHAPTER 4

SIMULATION IN 3D OF A DENSE FOREST OF CILIA IN A VISCOUS FLUID

Contents

The modelling of thin structures in a viscous fluid leads to consider elliptic problems with a singular right-hand side: a Dirac mass for the Poisson problem or a punctual force for the Stokes problem. In Chapters 2 and 3, we have established local error estimates for the finite element method. But it is well known that the convergence over the whole domain is suboptimal (see for example [99]). In this chapter, we propose a numerical method which preserves optimality for any approximation order even with a singular source term. It is based on the knowledge of a fundamental solution of the associated operator over the whole space. Unlike Chapters 2 and 3, in which the study is limited to the 2-dimensional case, the method is detailed in dimensions 2 and 3. Besides, it is applied in dimension 3 to the direct simulation of a large forest of cilia. Actually, this method is a performing tool to study muco-ciliary transport efficiency and related diseases: direct simulation allows for example to understand better the influence of some parameters on mucus transport, such as the thickness of periciliary layer (and thus of mucus) or the density of cilia.

4.1 A numerical method to solve elliptic problems with a singular source term

As it has been already done in previous chapters, we present the method in the case of the Poisson problem with a Dirac mass right-hand side and in the case of the Stokes problem with a punctual force in source term. The calculations are detailed in 2-dimension only, but the results are also given in dimension 3.

The method is based on the explicit knowledge of the singularity of the solution. The main idea relies on the extraction of the singularity from the solution to reduce initial problem to an auxiliary regular problem. This approach fits on the class of *subtraction methods*, introduced in [120] in the context of electroencephalography.

4.1.1 The Poisson problem with a Dirac mass right-hand side

Even if we aim at applying the method in the case of the Stokes problem, let us start with the Poisson problem for two reasons. First, all the important steps to explain the method are contained in the explanations related to the Poisson problem, and since this problem is the scalar version of Stokes problem, the method is a little simplier in this case. Second, the Poisson problems with a Dirac mass right-hand side appear naturally for example in electromagnetism [120].

4.1.1.1 Principle of the subtraction method

First, let us recall the Poisson problem with a Dirac mass in right-hand side

$$\left\{ \begin{array}{rcll} -\triangle u & = & \delta_0 & \text{in } \Omega, \\ u & = & 0 & \text{on } \partial\Omega. \end{array} \right. \tag{4.1.1}$$

For the sake of clarity, in all the results of this section the location x_0 of the Dirac mass is the origin. The fundamental solution of the no-boundary condition problem is still denoted u_δ,

$$-\triangle u_\delta = \delta_0 \text{ in } \mathscr{D}'(\mathbb{R}^d). \tag{4.1.2}$$

By Propositions 8 and 9, Chapter 1, Section 1.4.2.1, the fundamental solution of this problem is given by

$$\begin{array}{l} \bullet \text{ in dimension } d = 2, \quad u_\delta(x) = -\dfrac{1}{2\pi} \ln \|x\|, \\ \bullet \text{ in dimension } d = 3, \quad u_\delta(x) = \dfrac{1}{4\pi} \dfrac{1}{\|x\|}. \end{array} \tag{4.1.3}$$

Since a regular lift is sufficient to get the exact solution u (see Chapter 1, Section 1.4.2.2), the singularity of u is contained in the Green's function u_δ and is located at the Dirac point x_0 (here, the origin). The following method is based on this observation.

In order to extract the singularity, let us fix $0 < a < b < d(x_0, \partial\Omega)$ and define χ by Definition 1:

Definition 1. *Assume that χ is a bump function satisfying for some $k \geqslant 0$,*

- $\chi \in H^{2+k}(\mathbb{R}^d)$,
- $\chi|_{B(x_0,\, a)} = 1$,
- $\chi|_{B(x_0,\, b)^c} = 0$.

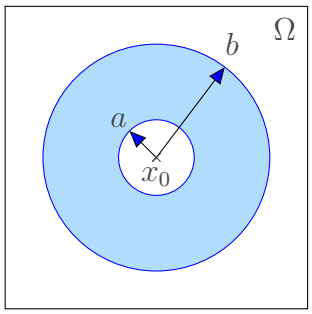

Figure 4.1: Definition of χ.

Then we set

$$u_0 = u_\delta \chi, \tag{4.1.4}$$

and the function g is defined by

$$-\triangle u_0 = -\triangle(u_\delta \chi) = \delta_0 + g. \tag{4.1.5}$$

By Definition 1, we can specify $u_\delta \chi$:

- on $B(x_0, a)$, $\chi = 1$, so $u_\delta \chi = u_\delta$, and therefore

$$g = -\triangle u_\delta - \delta_{x_0} = 0.$$

- on $B(x_0, b)^c$, $\chi = 0$, so $u_\delta \chi = 0$, and therefore

$$g = -\triangle(0) = 0.$$

Finally, $supp(g) \subset \mathcal{R}_a^b(x_0)$, where $\mathcal{R}_a^b(x_0)$ is the ring centered around x_0, of internal radius a and external radius b, see Figure 4.1. Moreover, since u_δ is analytic on a neighbourhood of $\mathcal{R}_a^b(x_0)$ and $\chi \in H^{2+k}(\mathbb{R}^d)$, the function g belongs to $H^k(\Omega)$. Thus, Problem (4.1.1) is reduced to the following regular problem

$$\left\{ \begin{array}{rcll} -\triangle v & = & -g & \text{in } \Omega, \\ v & = & 0 & \text{on } \partial\Omega, \end{array} \right. \tag{4.1.6}$$

and the solution u of Problem (4.1.1) is given by

$$u = v + u_0 = v + u_\delta \chi,$$

where u_0 is explicitly known and v is the solution of Problem (4.1.6). With v_h the finite element solution of Problem (4.1.6), the numerical solution u_h of Problem (4.1.1) is set as

$$u_h = v_h + u_0 = v_h + u_\delta \chi.$$

Even if the solutions u and u_h do not belong to $H^1(\Omega)$ (because of the singularity at the point x_0), the difference $u - u_h$ does, and we have

$$\|u - u_h\|_{s,\Omega} = \|v - v_h\|_{s,\Omega}, \text{ for } 0 \leqslant s \leqslant k+1.$$

Remark 13. *This method allows us to switch from the numerical computation of the solution of a singular problem with Dirac source term (with a poor convergence rate) to the numerical computation of the solution of a regular problem with an optimal convergence rate, at any required precision in terms of regularity.*

4.1.1.2 Practical aspects

First of all, a suitable function χ has to be defined: to take advantage of the use of a P_ℓ-finite element method, $\ell \geqslant 1$, the function χ has to belong to $\mathscr{C}^\ell(\mathbb{R}^d) \bigcap H^{\ell+1}(\mathbb{R}^d)$, so that $g \in H^{\ell-1}(\Omega)$, and finally get an optimal convergence. We could choose $\chi \in \mathscr{C}_0^\infty(\mathbb{R}^d)$, but the calculations to make g be explicit would be unnecessarily complicated. For example, for $\ell = 1$, we can take the radial function defined by

$$\chi(r) = \left\{ \begin{array}{ll} 1 & \text{si } r \in [0, a], \\ \dfrac{2r^3 - 3(a+b)r^2 + 6abr + b^2(b-3a)}{(b-a)^3} & \text{si } r \in [a, b], \\ 0 & \text{si } r > b, \end{array} \right. \tag{4.1.7}$$

where the function r is the Euclidean distance from the origin

$$r(x) = \|x\|.$$

The expression of g can now be explicited. We detail the calculations only in 2-dimension, but the results are also be given in 3-dimension.

Proposition 13. *In dimension $d = 2$, the function g is given by*

$$g(x) = \frac{3}{\pi(b-a)^3 r}\left((3r^2 - 2(a+b)r + ab)\ln r + 2r^2 - 2(a+b)r + 2ab\right)\mathbb{1}_{\mathcal{R}_a^b(x_0)}(x).$$

Proof. First, we have already shown that

$$supp(g) \subset \mathcal{R}_a^b(x_0),$$

so for $\|x\| \leqslant a$ or $b \leqslant \|x\|$,

$$g(x) = 0.$$

For $a < \|x\| < b$, in polar coordinates, since χ and u_δ are radial functions,

$$\begin{aligned}\triangle(u_\delta\chi) &= \chi\triangle(u_\delta) + 2\nabla u_\delta \cdot \nabla\chi + u_\delta\triangle\chi \\ &= \chi\triangle u_\delta + 2\partial_r(u_\delta)\partial_r(\chi) + u_\delta\left(\partial^2_{r,r}(\chi) + \frac{1}{r}\partial_r(\chi)\right).\end{aligned}$$

Now, u_δ is a solution of Problem (4.1.2), so $\triangle(u_\delta) = 0$ on $\mathcal{R}_a^b(x_0)$. That is why

$$\triangle(u_\delta\chi) = 2\partial_r(u_\delta)\partial_r(\chi) + u_\delta\left(\partial^2_{r,r}(\chi) + \frac{1}{r}\partial_r(\chi)\right). \tag{4.1.8}$$

Moreover, by Equations (4.1.3) and (4.1.7),

$$\begin{aligned}&\bullet\ \partial_r(u_\delta) = -\frac{1}{2\pi r}, \\ &\bullet\ \partial_r(\chi) = \frac{6}{(b-a)^3}(r^2 - (a+b)r + ab), \\ &\bullet\ \partial^2_{r,r}(\chi) = \frac{6}{(b-a)^3}(2r - (a+b)).\end{aligned} \tag{4.1.9}$$

Finally, by injecting (4.1.9) into (4.1.8), we get

$$g(x) = -\triangle(u_\delta\chi) = \frac{3}{\pi(b-a)^3 r}\left((3r^2 - 2(a+b)r + ab)\ln r + 2r^2 - 2(a+b)r + 2ab\right).$$

□

Proposition 14. *In dimension $d = 3$, the function g is given by*

$$g(x) = -\frac{3}{2\pi(b-a)^3 r}(2r - (a+b))\mathbb{1}_{\mathcal{R}_a^b(x_0)}(x).$$

4.1.1.3 Numerical illustrations

In this section, we illustrate our theorical results by a numerical example. We define Ω the unit disk and $x_0 = (0,0)$ the origin. Table 4.2 presents the $\mathbb{L}^2$-error for a direct method and the subtraction method respectively, for characteristic mesh sizes h, and the estimated order of convergence (e.o.c.). Figure 4.2 illustrates the section $\{y = 0\}$ of the error $|u - u_h|$ in both cases. Numerical simulations evidence the fact that solving the auxiliary problem associated to the subtraction procedure of the singularity is more efficient than solving directly the problem with the punctual force source term.

h	Direct method	Subtraction method
2^{-3}	1.58×10^{-2}	2.11×10^{-3}
2^{-4}	3.72×10^{-3}	4.63×10^{-4}
2^{-5}	3.89×10^{-3}	1.22×10^{-4}
2^{-6}	1.45×10^{-3}	2.99×10^{-5}
2^{-7}	6.51×10^{-4}	8.73×10^{-6}
e.o.c.	1.06	1.98

Table 4.1: $\mathbb{L}^2$-error for the direct method and the subtraction method

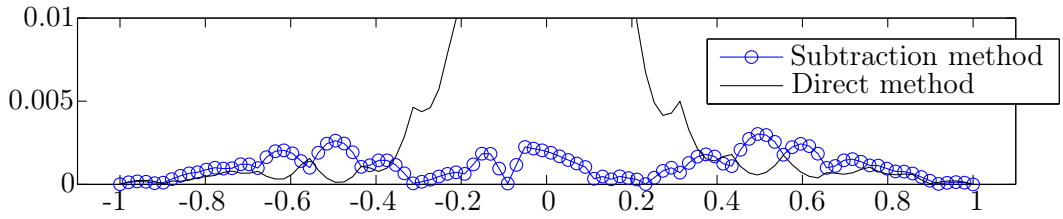

Figure 4.2: Section $\{y = 0\}$ of the error $\|u - u_h\|$ for the direct method and the subtraction method with $h = 0.125$.

Remark 14. *Figure 4.2 illustrates the concentration of the error around the singularity, with a wide and infinite peak located at the point x_0 for the direct method.*

4.1.2 The Stokes problem with a punctual force in source term

The previous method has been presented in the case of the Poisson problem. In this section, we adapt the method to the Stokes problem. As in Section 4.1.1, the calculations are detailed in dimension 2 but the results in dimension 3 are also given. Actually, we apply this method in dimension 3, in the case of the Stokes problem, to study muco-ciliary transport.

4.1.2.1 Principle of the subtraction method

The principle of the method is essentially the same as in the case of the Poisson problem. Let us consider the following problem,

$$\left\{\begin{array}{rcll} -\mu\triangle\mathbf{u}+\nabla p &=& \delta_{\mathbf{x}_0}\mathbf{F} & \text{in } \Omega,\\ \text{div } \mathbf{u} &=& 0 & \text{in } \Omega,\\ \mathbf{u} &=& 0 & \text{on } \partial\Omega, \end{array}\right. \tag{4.1.10}$$

where $\mathbf{x}_0$ is fixed in Ω and $\mathbf{F}$ is a vector of $\mathbb{R}^d$. For the sake of clarity, we assume $\mathbf{x}_0$ to be the origin. We still denote by $(\mathbf{u}_\delta, p_\delta)$ the fundamental solution of the no-boundary condition problem

$$\left\{\begin{array}{rcll} -\mu\triangle\mathbf{u}_\delta+\nabla p_\delta &=& \delta_0\mathbf{F} & \\ \text{div } \mathbf{u} &=& 0 & \end{array}\right. \text{in } \mathscr{D}'(\mathbb{R}^d). \tag{4.1.11}$$

We recall that the solution of Problem (4.1.11) in dimension d is given by Propositions 6 and 7, Chapter 1, Section 1.4.1.1:

$$\begin{array}{ll} \bullet\ d=2, & \mathbf{u}_\delta(\mathbf{x}) = \dfrac{1}{4\pi\mu}\left(-\ln\left(\|\mathbf{x}\|\right)\mathbb{I}_2+\dfrac{\mathbf{x}^t\mathbf{x}}{\|\mathbf{x}\|^2}\right)\mathbf{F} \quad \text{and} \quad p_\delta(\mathbf{x}) = \dfrac{1}{2\pi}\dfrac{\mathbf{x}\cdot\mathbf{F}}{\|\mathbf{x}\|^2},\\ \bullet\ d=3, & \mathbf{u}_\delta(\mathbf{x}) = \dfrac{1}{8\pi\mu}\left(\dfrac{\mathbb{I}_3}{\|\mathbf{x}\|}+\dfrac{\mathbf{x}^t\mathbf{x}}{\|\mathbf{x}\|^3}\right)\mathbf{F}, \quad \text{and} \quad p_\delta(\mathbf{x}) = \dfrac{1}{4\pi}\dfrac{\mathbf{x}\cdot\mathbf{F}}{\|\mathbf{x}\|^3}, \end{array} \tag{4.1.12}$$

where $\mathbb{I}_d$ is the identity matrix in dimension d. The fundamental solution $(\mathbf{u}_\delta, p_\delta)$ does not satisfy the boundary conditions, and so is not the solution of Problem (4.1.10). But this solution can be retrieved by adding a regular lift, therefore the whole information on the singularity of the solution $(\mathbf{u}, p)$ is contained in the fundamental solution $(\mathbf{u}_\delta, p_\delta)$ and is located at $\mathbf{x}_0$. In order to extract this singularity, let us fix $0 < a < b < d(\mathbf{x}_0, \partial\Omega)$ and define χ by Definition 1. Then, with $\mathbf{u}_0 = \chi\mathbf{u}_\delta$ and $p_0 = \chi p_\delta$, we define $\mathbf{g}$ and h as

$$\mathbf{g} = -\mu\triangle\mathbf{u}_0 + \nabla p_0 - \delta_{\mathbf{x}_0}\mathbf{F}, \tag{4.1.13}$$

$$h = \text{div } \mathbf{u}_0. \tag{4.1.14}$$

By the definitions of $\mathbf{u}_\delta$, p_δ and χ, $supp(\mathbf{g}) \subset \mathcal{R}_a^b(\mathbf{x}_0)$ and $supp(h) \subset \mathcal{R}_a^b(\mathbf{x}_0)$, where $\mathcal{R}_a^b(\mathbf{x}_0)$ is still the ring centered around $\mathbf{x}_0$, of internal radius a and external radius b, see Figure 4.1. Since $\mathbf{u}_\delta$ and p_δ are analytic on $\Omega\backslash\{\mathbf{x}_0\}$, the regularity of functions $\mathbf{g}$ and h directly depends on the regularity of function χ, namely $\mathbf{g} \in H^k(\Omega)$ and $h \in H^{k+1}(\Omega)$. Finally, it only remains to correct the terms $\mathbf{u}_0$ and p_0 by solving the regular elliptic problem

$$\left\{\begin{array}{rcll} -\mu\triangle\mathbf{v}+\nabla q &=& -\mathbf{g} & \text{in } \Omega,\\ \text{div } \mathbf{v} &=& -h & \text{in } \Omega,\\ \mathbf{v} &=& 0 & \text{on } \partial\Omega, \end{array}\right. \tag{4.1.15}$$

and the solution of Problem (4.1.10) is given by

$$(\mathbf{u}, p) = (\mathbf{u}_0 + \mathbf{v}, p_0 + q) = (\chi\mathbf{u}_\delta + \mathbf{v}, \chi p_\delta + q),$$

where $\mathbf{u}_0$ and p_0 are explicitly known functions and $(\mathbf{v}, q)$ is the solution of Problem (4.1.15). Noting $(\mathbf{v}_h, q_h)$ the numerical solution of Problem (4.1.15) and defining $\mathbf{u}_h = \mathbf{v}_h + \mathbf{u}_0$ and $p_h = q_h + p_0$, we have,

$$\|\mathbf{u} - \mathbf{u}_h\|_{H^s(\Omega)} = \|\mathbf{v} - \mathbf{v}_h\|_{H^s(\Omega)}, \quad \text{for } 0 \leqslant s \leqslant k+1,$$
$$\|p - p_h\|_{H^s(\Omega)} = \|q - q_h\|_{H^s(\Omega)}, \quad \text{for } 0 \leqslant s \leqslant k.$$

Again, the method allows us to switch from the numerical computation of the solution of a singular problem with a punctual force in source term (with a poor convergence rate) to the numerical computation of the solution of a regular problem with an optimal convergence rate, at any required precision in terms of regularity.

4.1.2.2 Practical aspects

We still take (4.1.7) for the choice of χ, and we can establish the expressions of the functions $\mathbf{g}$ and h.

Proposition 15. *In dimension 2, the functions* $\mathbf{g}$ *and* h *are given on* $\mathcal{R}_a^b(\mathbf{x}_0)$ *by*

$$\mathbf{g}(\mathbf{x}) = \frac{3}{2\pi(b-a)^3 r}\left[\left((3r^2 - 2(a+b)r + ab)\ln r + 2r^2 - 2(a+b)r + 2ab\right)\mathbb{I}_2 + (ab - r^2)\frac{\mathbf{x}^t\mathbf{x}}{r^2}\right]\mathbf{F},$$

$$h(\mathbf{x}) = \frac{3(1-\ln r)(r^2 - (a+b)r + ab)}{2\pi\mu(b-a)^3 r}\mathbf{x}\cdot\mathbf{F}.$$

where $r = r(\mathbf{x}) = \|\mathbf{x}\|$, *and are zero outside.*

Proof. We already know that $supp(\mathbf{g}) \subset \mathcal{R}_a^b(\mathbf{x}_0)$ and $supp(h) \subset \mathcal{R}_a^b(\mathbf{x}_0)$. Let us begin with the calculation of h. For $a < \|\mathbf{x}\| < b$,

$$h = \mathrm{div}(\chi\mathbf{u}_\delta) = \nabla\chi\cdot\mathbf{u}_\delta + \chi\mathrm{div}(\mathbf{u}_\delta) = \nabla\chi\cdot\mathbf{u}_\delta, \tag{4.1.16}$$

as $\mathrm{div}(\mathbf{u}_\delta) = 0$ on $\mathcal{R}_a^b(\mathbf{x}_0)$, since $(\mathbf{u}_\delta, p_\delta)$ is solution of Problem (4.1.11). We need to establish the expression of $\nabla\chi$. Noting that

$$\partial_i r = \frac{x_i}{r},$$

with $\mathbf{x} = {}^t[x_1, x_2]$, we have

$$\partial_i\chi = \frac{6x_i}{(b-a)^3 r}(r^2 - (a+b)r + ab),$$

and so

$$\nabla\chi = \frac{6(r^2 - (a+b)r + ab)}{(b-a)^3 r}\mathbf{x}. \tag{4.1.17}$$

By combining (4.1.16) and (4.1.17), we get:

$$h = \frac{3(r^2 - (a+b)r + ab)}{2\pi\mu(b-a)^3 r}(1 - \ln r)\mathbf{x}\cdot\mathbf{F}.$$

Let us now calculate $\mathbf{g}$. As we did previously,

$$\begin{aligned}\mathbf{g} &= -\mu\triangle(\chi\mathbf{u}_\delta) + \nabla(\chi p_\delta)\\ &= -\mu\left(\chi\triangle\mathbf{u}_\delta + 2\nabla\mathbf{u}_\delta\nabla\chi + \triangle\chi\mathbf{u}_\delta\right) + \chi\nabla p_\delta + p_\delta\nabla\chi\\ &= -\mu\left(2\nabla\mathbf{u}_\delta\nabla\chi + \triangle\chi\mathbf{u}_\delta\right) + p_\delta\nabla\chi, \qquad (4.1.18)\end{aligned}$$

because $(\mathbf{u}_\delta, p_\delta)$ satisfies $-\mu\triangle\mathbf{u}_\delta + \nabla p_\delta = 0$ on $\mathcal{R}_a^b(\mathbf{x}_0)$. We need to calculate $\triangle\chi$: with Equations (4.1.9),

$$\triangle\chi = \partial^2_{r,r}(\chi) + \frac{1}{r}\partial_r(\chi) = \frac{6(3r^2 - 2(a+b)r + ab)}{(b-a)^3 r}.$$

All that remains for us is to calculate $\nabla\mathbf{u}_\delta$. With $\mathbf{F} = {}^t[f_1, f_2]$,

$$\nabla\mathbf{u}_\delta = \frac{1}{4\pi\mu r^2}\left(\begin{bmatrix}\mathbf{x}\cdot\mathbf{F} & x_1f_2 - x_2f_1\\ x_2f_1 - x_1f_2 & \mathbf{x}\cdot\mathbf{F}\end{bmatrix} - \frac{2}{r^2}\mathbf{x}^t\mathbf{x}\mathbf{F}^t\mathbf{x}\right).$$

We can now make all the term in (4.1.18) be explicit:

$$-2\mu\nabla\mathbf{u}_\delta\nabla\chi = \frac{3(r^2 - (a+b)r + ab)}{\pi(b-a)^3 r}\mathbf{F},$$

$$-\mu\triangle\chi\mathbf{u}_\delta = \frac{3(3r^2 - 2(a+b)r + ab)}{2\pi(b-a)^3 r}\left(\ln(r)\mathbb{I}_2 - \frac{\mathbf{x}^t\mathbf{x}}{r^2}\right)\mathbf{F},$$

$$p_\delta\nabla\chi = \frac{3(r^2 - (a+b)r + ab)}{\pi(b-a)^3}\frac{\mathbf{x}^t\mathbf{x}}{r^3}\mathbf{F}.$$

And finally we deduce the expression of $\mathbf{g}$:

$$\mathbf{g}(\mathbf{x}) = \frac{3}{2\pi(b-a)^3 r}\left[\left((3r^2 - 2(a+b)r + ab)\ln r + 2r^2 - 2(a+b)r + 2ab\right)\mathbb{I}_2 + (ab - r^2)\frac{\mathbf{x}^t\mathbf{x}}{r^2}\right]\mathbf{F}$$

□

Proposition 16. *In dimension 3, the functions* $\mathbf{g}$ *and* h *are given on* $\mathcal{R}_a^b(\mathbf{x}_0)$ *by*

$$\mathbf{g}(\mathbf{x}) = \frac{3}{4\pi(b-a)^3 r^2}\left[((a+b)r - 2r^2)\mathbb{I}_3 + (2ab - (a+b)r)\frac{\mathbf{x}^t\mathbf{x}}{r^2}\right]\mathbf{F},$$

$$h(\mathbf{x}) = \frac{3(r^2 - (a+b)r + ab)}{2\pi\mu(b-a)^3 r^2}\mathbf{x}\cdot\mathbf{F},$$

where $r = r(\mathbf{x}) = \|\mathbf{x}\|$, *and are zero outside.*

4.1.2.3 Numerical illustrations

As it has been done in the case of the Poisson problem, we illustrate here our theorical results by a numerical example. We define Ω as the unit square and $\mathbf{x}_0 = (0.5, 0.5)$. Table 4.2 presents the $\mathbb{L}^2$-error for a direct method and the subtraction method respectively, for characteristic mesh sizes h, and the estimated order of convergence (e.o.c.). Figure 4.3 illustrates the section $\{y = 0.5\}$ of the error $|\mathbf{u} - \mathbf{u}_h|$ in both cases. Again, numerical simulations evidence the fact that solving the auxiliary problem associated to the subtraction procedure of the singularity is more efficient than solving directly the problem with the punctual force source term.

h	Direct method	Subtraction method
2^{-3}	1.02×10^{-2}	4.12×10^{-3}
2^{-4}	4.87×10^{-3}	1.33×10^{-3}
2^{-5}	2.36×10^{-3}	2.92×10^{-4}
2^{-6}	1.21×10^{-3}	6.86×10^{-5}
2^{-7}	5.89×10^{-4}	2.71×10^{-5}
e.o.c.	1.02	1.88

Table 4.2: $\mathbb{L}^2$-error for the direct method and the subtraction method

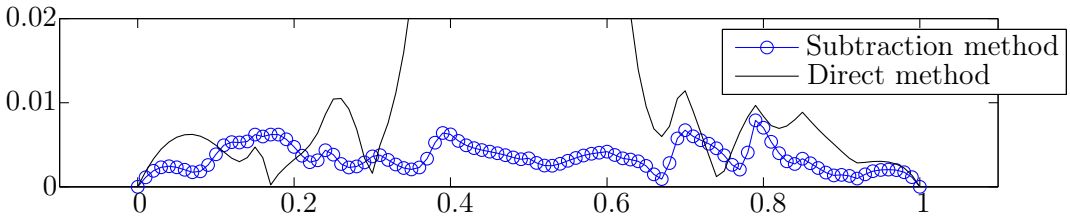

Figure 4.3: Section $\{y = 0.5\}$ of the error $\|\mathbf{u} - \mathbf{u}_h\|$ for the direct method and the subtraction method with $h = 0.125$.

4.1.3 Adaptations of the subtraction method to more general problems

In this section, we focus on the advantages and drawbacks of implementing and using the method.

4.1.3.1 Linear elliptic problems

The subtraction method has been presented in the particular cases of the Poisson and the Stokes problems. Actually, it can be detailed in the case of other linear elliptic problems.

Consider a linear elliptic operator A, for example of the form

$$Au = -\sum_{i,j=1}^{d} a_{i,j} D_i D_j u + \sum_{k=1}^{d} b_k D_k u + cu,$$

where the coefficients $a_{i,j}$, b_k, c are smooth functions, and assume that we know explicitly a smooth fundamental solution $\widetilde{u}_\delta$, that is to say $\widetilde{u}_\delta$ is smooth except on the point x_0 and satisfies

$$A\widetilde{u}_\delta = \delta_{x_0} \text{ in } \mathscr{D}'(\mathbb{R}^d). \tag{4.1.19}$$

Then the subtraction method can be applied to solve the following problem

$$\begin{cases} Au &= \delta_{x_0} & \text{in } \Omega, \\ u &= 0 & \text{on } \partial\Omega. \end{cases}$$

In this example, A is a partial operator of order 2, but the order of derivation does not matter. Moreover, the method can be extended to mixed problems, such as the Stokes problem. In fact, the key points are the linearity of the operator and the explicit knowledge of a fundamental solution smooth out of a compact. Notice that in the general case, it is very difficult to solve explicitly Problem (4.1.19) and that the method cannot be applied without such a solution.

4.1.3.2 About boundary conditions

Consider the following problem

$$\begin{cases} Au &= \delta_{x_0} & \text{in } \Omega, \\ Bu &= 0 & \text{on } \partial\Omega. \end{cases}$$

where A is a linear elliptic operator for which there exists a smooth fundamental solution $\widetilde{u}_\delta$, and B a boundary condition operator. This operator B is assumed to satisfy the condition

$$B(v + v_0) = B(v) \tag{4.1.20}$$

for any function v_0 such that $v_0 = 0$ on a neighbourhood of the border $\partial\Omega$ (for instance, $B(v + u_0) = Bv$, where u_0 is defined in (4.1.4)). Then the method can be applied in this case and the finite element solution u_h is given by

$$u_h = v_h + \widetilde{u}_0$$

where $\widetilde{u}_0 = \widetilde{u}_\delta \chi$ (Definition 1) and v_h is the finite element solution of the following problem

$$\begin{cases} Au &= -g & \text{in } \Omega, \\ Bu &= 0 & \text{on } \partial\Omega, \end{cases}$$

with g defined as in (4.1.5). Note that if B is a linear operator which depends only on the trace on $\partial\Omega$ of u and its derivatives, for example Dirichlet or Neumann boundary conditions, Equation (4.1.20) still holds. Besides, the subtraction method is compatible

with periodic boundary conditions, and these conditions are imposed on the auxiliary problem. Lastly, the method is of course compatible with mixed boundary conditions. For example, in 3-dimension, we can consider biperiodic conditions in directions x and y, homogeneous Dirichlet boundary conditions on the bottom, no-output conditions with no-friction sliding on the top of the box (see Figure 4.4).

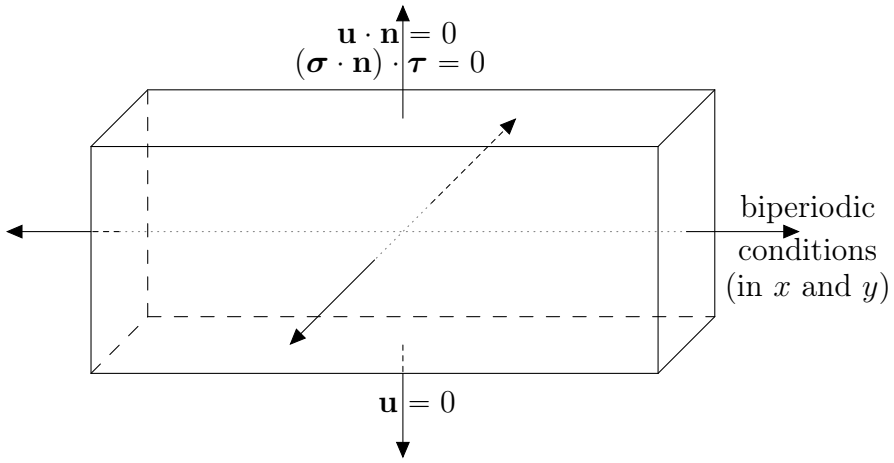

Figure 4.4: Illustration of mixed boundary conditions.

These boundary conditions are chosen in the modeling of the mucociliary transport in the lung.

4.1.3.3 More general source terms

In order to clarify the explanations, let us deal with the Stokes problem, even if the principle also extends to other linear elliptic problems concerned by Section 4.1.3.1.

A punctual force plus a smooth function in source term. Let $\mathbf{f}$ be a smooth function, and consider the following problem

$$\left\{\begin{array}{rcll} -\mu\triangle\mathbf{u} + \nabla p &=& \delta_{\mathbf{x}_0}\mathbf{F} + \mathbf{f} & \text{in } \Omega, \\ \text{div}(\mathbf{u}) &=& 0 & \text{in } \Omega, \\ \mathbf{u} &=& 0 & \text{on } \partial\Omega. \end{array}\right.$$

By linearity, the subtraction method can be applied to get a numerical solution of such problems solving the following auxiliary problem

$$\left\{\begin{array}{rcll} -\mu\triangle\mathbf{u} + \nabla p &=& -\mathbf{g} + \mathbf{f} & \text{in } \Omega, \\ \text{div}(\mathbf{u}) &=& -h & \text{in } \Omega, \\ \mathbf{u} &=& 0 & \text{on } \partial\Omega, \end{array}\right.$$

where the functions $\mathbf{g}$ and h are defined in (4.1.13) and (4.1.14). Note that the regularity of this problem is directly linked to the regularity of the function $\mathbf{f}$. Actually, if the

function $\mathbf{f}$ is also singular, the method allows the user to separate the difficulties and deal with one singularity after the other.

High number of punctual forces in source term. Let us now consider the Stokes problem with several punctual forces in source term:

$$\begin{cases} -\mu\triangle\mathbf{u} + \nabla p &= \displaystyle\sum_{i=1}^{N} \delta_{\mathbf{x}_i}\mathbf{F}_i & \text{in } \Omega, \\ \operatorname{div}(\mathbf{u}) &= 0 & \text{in } \Omega, \\ \mathbf{u} &= 0 & \text{on } \partial\Omega. \end{cases}$$

For each punctual force $\delta_{\mathbf{x}_i}\mathbf{f}_i$, we define $\mathbf{g}_i$ and h_i as in (4.1.13) and (4.1.14). No matter the number of punctual forces, the method can be applied and by linearity, only one auxiliary regular problem has to be solved:

$$\begin{cases} -\mu\triangle\mathbf{u} + \nabla p &= \displaystyle -\sum_{i=1}^{N} \mathbf{g}_i & \text{in } \Omega, \\ \operatorname{div}(\mathbf{u}) &= \displaystyle -\sum_{i=1}^{N} h_i & \text{in } \Omega, \\ \mathbf{u} &= 0 & \text{on } \partial\Omega. \end{cases}$$

A high number of punctual forces may involve some bad convergence: even if the source term $\sum \mathbf{g}_i$ (respectively $\sum h_i$) is regular, its $\mathbb{L}^2$-norm (respectively H^1-norm) can be very large, and the convergence depends directly on this norm, even if the convergence rate remains the same. Figure 4.5 draws the $\mathbb{L}^2$-norm of the term source in function of the number of cilia, knowing that a cilium is composed of 20 punctual forces. The $\mathbb{L}^2$-norm of the source term does not linearly depend on the number of cilia, and even if it can be very large, it stops growing after some number of cilia This screening effect is due to the high density of cilia. The dotted line corresponds to the number of cilia we consider in the simulation, namely 6885 cilia (135 in the direction x and 51 in the direction y).

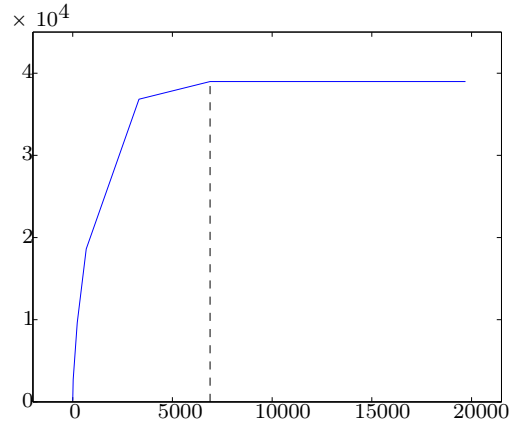

Figure 4.5: $\mathbb{L}^2$-norm of the right-hand side in function of the number of cilia.

Note that the required time to numerically build the source term $\sum \mathbf{g}_i$ may become preponderant for a high number of cilia compared to the required time to solve the Stokes problem.

4.1.3.4 Punctual force close to the border

The issue is the same for the Stokes problem as for the Poisson problem. When presenting the method, we introduce the ring $\mathcal{R}_a^b(\mathbf{x}_0)$ centred on $\mathbf{x}_0$, of internal radius a and external radius b. The natural question is: what happens if the Dirac mass is close to the border of Ω? Indeed, even if we can always define the ring, the mesh size h could be bigger than one of these distances: the radius a, the width of the ring $b-a$, the distance of the ring $\mathcal{R}_a^b(\mathbf{x}_0)$ to the border $\partial\Omega$. Moreover, even if h small enough, is the convergence of the finite element solution to the exact solution still optimal? Actually, the convergence is related to the regularity and the norm of the right-hand side $\mathbf{g}$. In our case, we have:

$$\|\mathbf{g}\|_{0,\Omega} \leqslant \|\chi\|_{2,\mathbb{R}_a^b(\mathbf{x}_0)} \|\mathbf{u}_\delta\|_{1,\mathbb{R}_a^b(\mathbf{x}_0)}.$$

Moreover, we can show that there exists C independent of a and b such that

$$\|\chi\|_{2,\mathbb{R}_a^b(\mathbf{x}_0)} \leqslant \frac{C}{(b-a)^3}.$$

As a result, if the distance $b-a$ is small, the norm $\|\chi\|_{2,\mathbb{R}_a^b(\mathbf{x}_0)}$ is very big (and the growth is cubic). We conclude that the optimal rate of convergence can be counterbalanced by the constant, leading to a deterioration of the results in practice.

A solution to counter-balance this fact is to consider a so-called "Stokeslet in a no-slip boundary", that is to say a Stokeslet defined in the half-space, and satisfying $\mathbf{u} = 0$ on the border (see Figure 4.6). This Stokeslet is built in [11]. For the sake of clarity, consider the problem

$$\left\{ \begin{array}{rcll} -\mu\triangle\widetilde{\mathbf{u}}_\delta + \nabla\widetilde{p}_\delta &=& \delta_{\mathbf{x}_0}\mathbf{F} & \text{in } \mathbb{R}^2 \times \mathbb{R}_+^*, \\ \operatorname{div}(\widetilde{\mathbf{u}}_\delta) &=& 0 & \text{in } \mathbb{R}^2 \times \mathbb{R}_+^*, \\ \widetilde{\mathbf{u}}_\delta &=& 0 & \text{on the plan } \{z=0\}, \end{array} \right.$$

where $\mathbf{F} \in \mathbb{R}^3$ and $\mathbf{x}_0 = (x_0, y_0, z_0)$, with $z_0 > 0$. The solution is the Stokeslet in a no-slip boundary, and it is defined by:

$$\widetilde{\mathbf{u}}_\delta = \frac{1}{8\pi\mu}\left[\left(\frac{1}{r} - \frac{1}{R}\right)\mathbb{I}_3 + \frac{\mathbf{X}_+ \otimes \mathbf{X}_+}{r^3} - \frac{\mathbf{X}_- \otimes \mathbf{X}_-}{R^3} + 2z_0\mathbf{W}(R_1, R_2, R_3)\right] \cdot \mathbf{F},$$

and

$$\widetilde{p}_\delta = \frac{1}{4\pi}\left[\frac{\mathbf{X}_+}{r^3} - \frac{\mathbf{X}_-}{R^3} - 2z_0\mathbf{S}(R_1, R_2, R_3)\right] \cdot \mathbf{F},$$

where

$$\mathbf{X}_+ = {}^t[x - x_0, y - y_0, z - z_0], \quad \mathbf{X}_- = {}^t[x - x_0, y - y_0, z + z_0],$$

$$r = \|\mathbf{X}_+\|, \quad R = \|\mathbf{X}_-\| = \sqrt{R_1^2 + R_2^2 + R_3^2},$$

$$R_1 = x - x_0, \quad R_2 = y - y_0, \quad R_3 = z + z_0,$$

$$\mathbf{W}(R_1, R_2, R_3) = \begin{bmatrix} \partial_{R_1}\left(\frac{z_0 R_1}{R^3} - \frac{R_1 R_3}{R^3}\right) & \partial_{R_2}\left(\frac{z_0 R_1}{R^3} - \frac{R_1 R_3}{R^3}\right) & -\partial_{R_3}\left(\frac{z_0 R_1}{R^3} - \frac{R_1 R_3}{R^3}\right) \\ \partial_{R_1}\left(\frac{z_0 R_2}{R^3} - \frac{R_2 R_3}{R^3}\right) & \partial_{R_2}\left(\frac{z_0 R_2}{R^3} - \frac{R_2 R_3}{R^3}\right) & -\partial_{R_3}\left(\frac{z_0 R_2}{R^3} - \frac{R_2 R_3}{R^3}\right) \\ \partial_{R_1}\left(\frac{z_0 R_3}{R^3} - \frac{1}{R} - \frac{R_3^2}{R^3}\right) & \partial_{R_2}\left(\frac{z_0 R_3}{R^3} - \frac{1}{R} - \frac{R_3^2}{R^3}\right) & -\partial_{R_3}\left(\frac{z_0 R_3}{R^3} - \frac{1}{R} - \frac{R_3^2}{R^3}\right) \end{bmatrix},$$

and

$$\mathbf{S}(R_1, R_2, R_3) = \begin{bmatrix} \partial_{R_1}\left(\frac{R_3}{R^3}\right) \\ \partial_{R_2}\left(\frac{R_3}{R^3}\right) \\ \partial_{R_3}\left(\frac{R_3}{R^3}\right) \end{bmatrix} = \begin{bmatrix} \partial_{R_1} \\ \partial_{R_2} \\ \partial_{R_3} \end{bmatrix} \left(\frac{R_3}{R^3}\right).$$

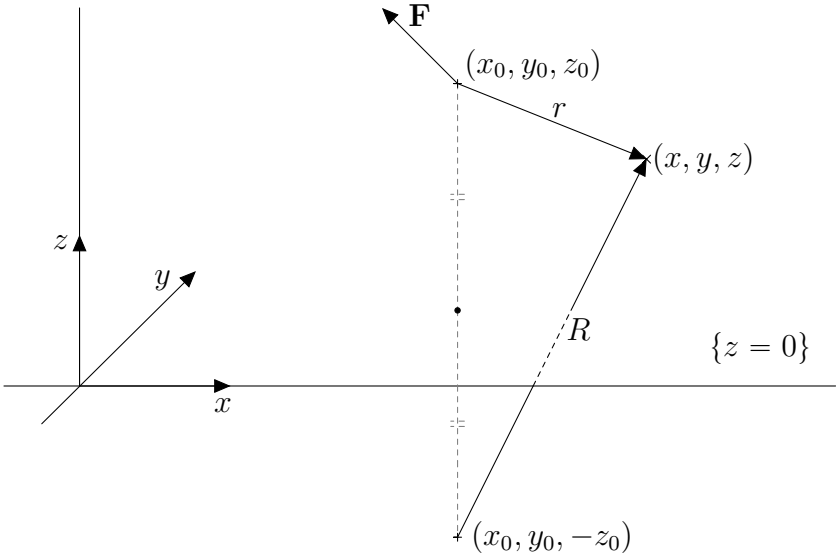

Figure 4.6: Construction of the Stokeslet in a no-slip boundary.

Once we have a fundamental solution, we can apply the subtraction method. To help in this process, we have to define a "good" function χ, but Definition 1 does not match in this case. Let us make another choice for χ:

Definition 2. *Assume that χ is a bump function satisfying for some $k \geqslant 0$, $\chi \in H^{2+k}(\Omega)$. Moreover, let us split the domain Ω in two parts and define χ on each of these parts:*

- *in the half-space* $\{z \geqslant z_0\}$, χ *is a radial function centred on* $\mathbf{x}_0$ *such as*

$$\chi|_{B(\mathbf{x}_0, a)} = 1 \text{ and } \chi|_{B(\mathbf{x}_0, b)^c} = 0,$$

  as defined in Definition 1.

- *in the half-space* $\{z \leqslant z_0\}$, χ *is a cylindrical function of axis* $\mathcal{D}$ *(the straight line* $\{x = x_0$ *and* $y = y_0\}$*, see Figure 4.7) such as*

$$\begin{aligned} \chi(x, y, z) &= 1 \quad \text{if } r(x, y) \leqslant a, \\ \chi(x, y, z) &= 0 \quad \text{if } b \leqslant r(x, y), \end{aligned}$$

  where $r(x, y) = \sqrt{(x - x_0)^2 + (y - y_0)^2}$.

From this point, the method can be applied as in Sections 4.1.1.1 and 4.1.2.1. With this adaptation, we can compute punctual forces $\delta_{\mathbf{x}_0}\mathbf{F}$ close to the border of Ω, even if an issue persists if the punctual force is near a corner. Note that if we consider periodic boundary conditions, punctual forces can be close to the border (or corner): the part of the support of χ which is out the box is deferred at the other side of the box.

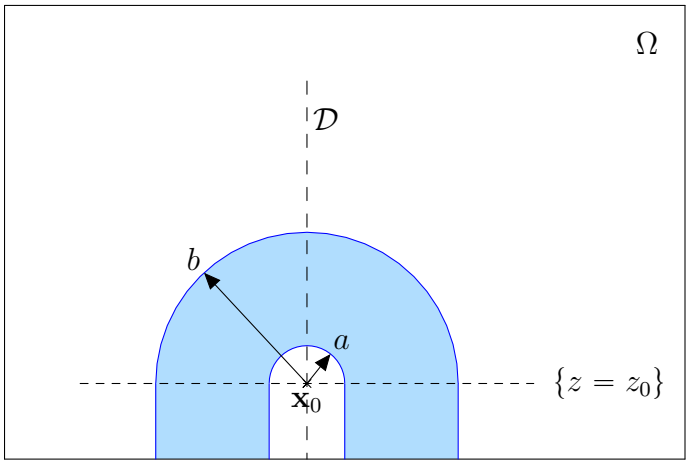

Figure 4.7: Definition of χ. Section $\{y = y_0\}$.

Calculations of functions $\mathbf{g}$ and h have not been done in this case. Actually, in our model, the cilium is connected to the bottom of the box (domain Ω) and therefore, we should use the Stokeslet in a no-slip boundary. But the lower part of the cilium does not beat a lot, the velocity near the base is low, and so the force $\mathbf{F}$ distributed near the border is also very small and vanishes at the border. As a consequence, heavy computations related to the treatment of the near boundary punctual forces can be avoided in the case of mucociliary transport.

4.1.3.5 Non-constant viscosity

The method has been presented in the case of a constant-viscosity fluid. Actually, this assumption is not really necessary, but the difficulty remains the existence of the fundamental solution. In some cases, we can still define the method with suitable adaptations. For instance, the two-viscosity case is very interesting, as the mucociliary escalator relies on a bifluid mechanism. Consider Ω a viscous fluid domain in 3d of viscosity μ defined by

$$\mu(x,y,z) = \begin{cases} \mu_1 & \text{if } z < h_0, \\ \mu_2 & \text{if } z > h_0, \end{cases}$$

where h_0 is the height of the bottom layer. Let us denote by Ω_1 this bottom layer and the top layer by Ω_2 (see Figure 4.8). In applications, the domain Ω_1 corresponds to the periciliary layer while the domain Ω_2 refers to the mucus. Let us assume that the punctual force is located at the point $\mathbf{x}_0 = (x_0, y_0, z_0)$ with $z_0 < h_0$, so that it is located in the bottom layer, as in Figure 4.8 (else, the development is the same exchanging the subscripts $i = 1, 2$ for μ_i and Ω_i).

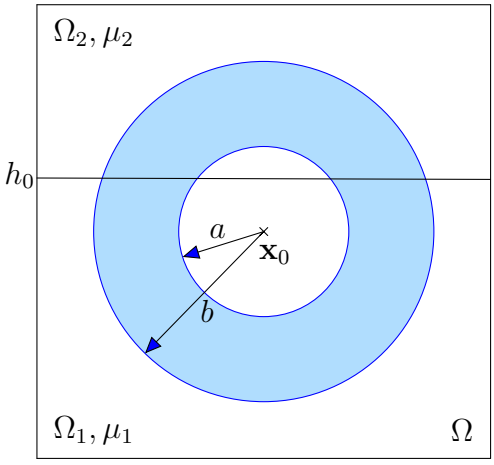

Figure 4.8: Illustration of the subtraction method for a two-viscosity fluid

Let us thus define the Stokeslet $(\mathbf{u}_\delta, p_\delta)$ as in (4.1.12) with $\mu = \mu_1$, and the functions $\mathbf{g}$ and h are given in 3d by Proposition 16, still with $\mu = \mu_1$ and χ defined in (4.1.7). Consider $\mathbf{u} = \mathbf{u}_0 + \mathbf{v} = \chi\mathbf{u}_\delta + \mathbf{v}$ and $p = p_0 + q = \chi p_\delta + q$, where $(\mathbf{v}, p)$ is the solution of Problem (4.1.15), and calculate for any test function $\varphi \in \mathscr{C}_0^\infty(\Omega)$,

$$
\begin{aligned}
2\int_\Omega \mu(\mathbf{x})\mathbb{D}(\mathbf{u})(\mathbf{x}) :: \mathbb{D}(\varphi)(\mathbf{x})\mathrm{d}\mathbf{x} &+ \int_\Omega \nabla p(\mathbf{x})\cdot\varphi(\mathbf{x})\mathrm{d}\mathbf{x} \\
=&2\int_\Omega \mu(\mathbf{x})\mathbb{D}(\mathbf{u}_0)(\mathbf{x}) :: \mathbb{D}(\varphi)(\mathbf{x})\mathrm{d}\mathbf{x} + \int_\Omega \nabla p_0(\mathbf{x})\cdot\varphi(\mathbf{x})\mathrm{d}\mathbf{x} \\
&+ 2\int_\Omega \mu(\mathbf{x})\mathbb{D}(\mathbf{v})(\mathbf{x}) :: \mathbb{D}(\varphi)(\mathbf{x})\mathrm{d}\mathbf{x} + \int_\Omega \nabla q(\mathbf{x})\cdot\varphi(\mathbf{x})\mathrm{d}\mathbf{x} \\
=&2\int_{\Omega_1} \mu_1\mathbb{D}(\mathbf{u}_0)(\mathbf{x}) :: \mathbb{D}(\varphi)(\mathbf{x})\mathrm{d}\mathbf{x} + 2\int_{\Omega_2} \mu_2\mathbb{D}(\mathbf{u}_0)(\mathbf{x}) :: \mathbb{D}(\varphi)(\mathbf{x})\mathrm{d}\mathbf{x} \\
&+ \int_\Omega \nabla p_0(\mathbf{x})\cdot\varphi(\mathbf{x})\mathrm{d}\mathbf{x} - \int_\Omega \mathbf{g}(\mathbf{x})\cdot\varphi(\mathbf{x})\mathrm{d}\mathbf{x} \\
=&2\int_{\Omega_1} \mu_1\mathbb{D}(\mathbf{u}_0)(\mathbf{x}) :: \mathbb{D}(\varphi)(\mathbf{x})\mathrm{d}\mathbf{x} + 2\int_{\Omega_2} \mu_2\mathbb{D}(\mathbf{u}_0)(\mathbf{x}) :: \mathbb{D}(\varphi)(\mathbf{x})\mathrm{d}\mathbf{x} \\
&+ \langle\delta_{\mathbf{x}_0},\varphi\rangle_{\mathscr{D}'(\Omega)} - 2\int_\Omega \mu_1\mathbb{D}(\mathbf{u}_0)(\mathbf{x}) :: \mathbb{D}(\varphi)(\mathbf{x})\mathrm{d}\mathbf{x} \\
=&\langle\delta_{\mathbf{x}_0},\varphi\rangle_{\mathscr{D}'(\Omega)} + 2\int_{\Omega_2} (\mu_2-\mu_1)\mathbb{D}(\mathbf{u}_0)(\mathbf{x}) :: \mathbb{D}(\varphi)(\mathbf{x})\mathrm{d}\mathbf{x}.
\end{aligned}
$$

In the light of this calculation, let us define $\widetilde{\mathbf{g}}$ by: for all $\varphi \in \mathscr{C}_0^\infty(\Omega)$,

$$
\langle\widetilde{\mathbf{g}},\varphi\rangle = \int_\Omega \mathbf{g}(\mathbf{x})\cdot\varphi(\mathbf{x})\mathrm{d}\mathbf{x} + 2\int_{\Omega_2} (\mu_2-\mu_1)\mathbb{D}(\mathbf{u}_0)(\mathbf{x}) :: \mathbb{D}(\varphi)(\mathbf{x})\mathrm{d}\mathbf{x},
$$

and denote by $(\widetilde{\mathbf{v}},\widetilde{q})$ the solution of the following auxiliary regular problem

$$
\left\{\begin{array}{rcll} -2\mathrm{div}(\mu\mathbb{D}(\widetilde{\mathbf{v}})) + \nabla\widetilde{q} &=& -\widetilde{\mathbf{g}} & \text{in } \Omega, \\ \mathrm{div}(\widetilde{\mathbf{v}}) &=& -h & \text{in } \Omega, \\ \widetilde{\mathbf{v}} &=& 0 & \text{on } \partial\Omega. \end{array}\right.
$$

We conclude that $(\mathbf{u},p) = (\mathbf{u}_0+\widetilde{\mathbf{v}}, p_0+\widetilde{q})$ is the solution of

$$
\left\{\begin{array}{rcll} -2\mathrm{div}(\mu\mathbb{D}(\mathbf{u})) + \nabla p &=& \delta_{\mathbf{x}_0}\mathbf{F} & \text{in } \Omega, \\ \mathrm{div}(\mathbf{u}) &=& 0 & \text{in } \Omega, \\ \mathbf{u} &=& 0 & \text{on } \partial\Omega. \end{array}\right.
$$

To complete this adaptated method, it remains to explicit $\nabla\mathbf{u}_0$ on Ω_2:

- on $\Omega_2 \bigcap B(\mathbf{x}_0,b)^c$, $\chi = 0$, and so $\nabla\mathbf{u}_0 = 0$.
- on $\Omega_2 \bigcap B(\mathbf{x}_0,a)$, $\chi = 1$, and so $\nabla\mathbf{u}_0 = \nabla\mathbf{u}_\delta$, with

$$
\nabla\mathbf{u}_\delta(\mathbf{x}) = \frac{1}{8\pi\mu_1 r^3}\left(\begin{bmatrix} \mathbf{x}\cdot\mathbf{F} & xf_2-yf_1 & xf_3-zf_1 \\ yf_1-xf_2 & \mathbf{x}\cdot\mathbf{F} & yf_3-zf_2 \\ zf_1-xf_3 & zf_2-yf_3 & \mathbf{x}\cdot\mathbf{F} \end{bmatrix} - \frac{1}{r^2}\mathbf{x}^t\mathbf{x}\mathbf{F}^t\mathbf{x}\right).
$$

- on $\Omega_2 \bigcap \mathcal{R}_a^b(\mathbf{x}_0)$, $\nabla \mathbf{u}_0 = \nabla(\chi \mathbf{u}_\delta) = \chi \nabla \mathbf{u}_\delta + {\mathbf{u}_\delta}^t \nabla \chi$, with χ given in (4.1.7), $\nabla \mathbf{u}_\delta$ explicited above, and

$$ {\mathbf{u}_\delta}^t \nabla \chi = \frac{3(r^2 - (a+b)r + ab)}{4\pi\mu_1 (b-a)^3 r^2} \left(\mathbb{I}_3 + \frac{\mathbf{x}^t \mathbf{x}}{r^2} \right) \mathbf{F}^t \mathbf{x}. $$

The method adaptated to the two-viscosity case is used in Section 4.2.4 for the simulation of a forest of cilia and the study of the influences of some parameters, like the thickness of the periciliary layer or the density of cilia.

4.2 Application to mucociliary transport in the lung

The complexity of the process is high (cilia, two layers, several interfaces, several scales, etc) and only a few data are available. Although a wide variety of works can be found in the literature about mucociliary clearance, the numerical modeling remains at present time a challenge for the scientists. One of the main difficulties is the model of the cilia. For instance, Smith and coworkers [107] replaced the forest by an active porous medium in which the cilia are modeled by a volumic resistive force directly dependent on the local velocity of the cilia. They considered in 2-dimension a three-layer fluid: a Maxwell fluid for the mucus and a Newtonian fluid for the periciliary layer and the layer of transition. This model leads to a quasi-uniform mucus transport but no collective movement in the periciliary layer emerges from this model. Another way to model the cilia is the discrete-cilia model. Dillon and coworkers [40] tried to model the internal elastic and force-generating structures of the cilia. They considered in 2D only a few cilia but observed that the interface between the mucus and the periciliary layer stays flat, which justifies the two-layers (sometimes three) models with invariant interfaces. Nevertheless, how the internal ciliary engine affects the ciliary beat form remains an open question. That is why most of the works focus on the flow fields produced by cilia with given beat pattern and frequency. Smith and coworkers [106] considered a discrete-cilia model and used regularized Stokeslet to model in 3D the transport by an infinite array of cilia. Lee and coworkers [71] modeled the cilia by discrete Dirac delta functions distributed all along the cilium. They considered a 2D two-layer flow and the governing equations are solved using the immersed boundary method combined with the projection method. The same techniques were used in 3D by Jayathilake and coworkers [60] to simulate a 3D two-layer flow in order to better understand some pathological cases. Finally, Chatelin and Poncet [30] proposed a 3D model with a variable viscosity: the viscosity is the solution of a convection-diffusion equation. The beat of the cilia is imposed and the effects of the cilia on the fluid are treated by penalization. Most of these approaches are discussed in [108].

4.2.1 Implementation

The code CAFES (Cartesian Finite Element Solver) has been developed by Benoit Fabrèges, in collaboration with Loïc Gouarin and Bertrand Maury [45]. It is written in C/C++ and uses the library PETSc. It works with the 4Q1/Q1-finite element to solve a class of problems for which a solver on a Cartesian grid is needed. The library PETSc is used for the parallel structure of matrices and vectors, as well as the parallel solvers for the linear systems.

The simulations presented below are obtained with the code CAFES, used for the resolution of the regular auxiliary Stokes problem. My contribution to the code is the implementation of the subtraction method, described in Section 4.1, from the construction of the right-hand side to the corrective terms added to the numerical solution of the auxiliary regular problem.

4.2.2 Choice of the different parameters for the computations

Before beginning the computations, let us fix the values of the parameters. Consider the Stokes problem

$$\left\{\begin{array}{rcll} -\triangle \mathbf{u} + \nabla p & = & \widetilde{\mathbf{F}} & \text{in } \Omega, \\ \operatorname{div}(\mathbf{u}) & = & 0 & \text{in } \Omega, \\ \mathbf{u} & = & 0 & \text{on } \partial\Omega, \end{array}\right.$$

where $\widetilde{\mathbf{F}}$ is independent of the viscosity μ. By denoting $(\mathbf{u}, p)$ the solution of this problem, for any viscosity μ the couple $(\mathbf{u}, \mu p)$ is solution of the problem

$$\left\{\begin{array}{rcll} -\mu\triangle \mathbf{u} + \nabla p & = & \widetilde{\mathbf{F}}\mu & \text{in } \Omega, \\ \operatorname{div}(\mathbf{u}) & = & 0 & \text{in } \Omega, \\ \mathbf{u} & = & 0 & \text{on } \partial\Omega. \end{array}\right.$$

This remark leads us to consider the viscosity $\widetilde{\mu} = 1$ in the computations: the velocity flow remains the same, and the pressure is multiplied by the real viscosity μ. In the case of the bifluid model, the observation is the same: it is only necessary to keep the ratio between both viscosities $r_\mu = \mu_{mucus}/\mu_{PCL}$ constant.

Remark 15. *We can take the viscosity we want for the computations because we focus on the flow fields produced by cilia with given beat pattern and frequency. If we would impose the force and not the movement of the cilia, this simplification would not be possible.*

Table 4.3 recalls the data related to the cilia. These parameters are the ones used in all the simulations (unless otherwise stated). It remains to choose the parameters a and b to complete the definition of χ. Let us take $a = d/5$ and $b = 4d/5$, with d defined by

$$d = \min(z_0, h_z - z_0),$$

where z_0 is the third component of the position of the punctual force, and h_z the height of the box of calculations. This choice of a and b is consistant with the biperiodic boundary conditions.

Length of cilium	L	6 μm
Cross-sectional radius	r_0	0.1 μm
Beat frequency	f	15 Hz
Cilia spacing	ℓ_0	0.3 μm
Metachronal wavelength	λ	30 μm

Table 4.3: Summary of data for cilia in the lung, from [48].

The simulations should present the time evolution of flow. In our case, the movement of the cilia is periodic (the period T is $1/f$), and the movement of the cilia is imposed: there is no effect of the fluid on the cilia. Due to the instantaneousness of the Stokes equations, the simulation of one period is sufficient. The time step $\triangle t$ is taken equal to $T/20$. For the sake of clarity, the time t is not given in seconds but in the form $t = n\triangle t$, where n is an integer between 0 and 19, and represents the associated step in the period T. In all the simulations presented in this chapter, the number of punctual force composing each cilium is 20. Lastly, we do not present convergence results but we ensured that the computations have indeed converged for the meshsize used in the simulations.

Next sections are devoted to the presentation of the various results obtained using the code CAFES and applying the subtraction method to the mucociliary transport. In particular, this numerical tool allows us to study the influence of some parameters of the mucociliary clearance.

4.2.3 Simulations in a constant-viscosity fluid

In the light of the review of the works related to mucociliary clearance, it is clear that modeling the airway surface liquid as a constant-viscosity fluid is not sufficient. However, comparing the constant-viscosity case to the two-viscosity fluid allows to highlight the impact of the bifluid flow for the mucus transport efficiency. Therefore we start with computing cilia beating in a constant-viscosity fluid.

4.2.3.1 Simulation of a small patch of cilia

In order to validate the model and the method, we start the computations with the simulation of a small patch of cilia. For this computation, we consider a $20 \times 10 \times 10$ μm^3 box, discretized by a $64 \times 32 \times 32$ mesh. The patch of cilia is a 15×15 array of cilia. Figure 4.9 shows the 3-dimensional flow generated by a patch of cilia in a constant-viscosity fluid at times $t = \triangle t$ s (during the effective stroke) and $t = 11\triangle t$ s (during the recovery stroke). It illustrates the efficiency of transport during the effective stroke compared to a low flow in the opposite direction during the recovery stroke. This observation is a consequence of the non-reversibility of the cilia beat pattern. Note also that the average flow over a period is non-zero.

A whole 3-dimensional forest of cilia is computed in a constant-viscosity fluid in the next section.

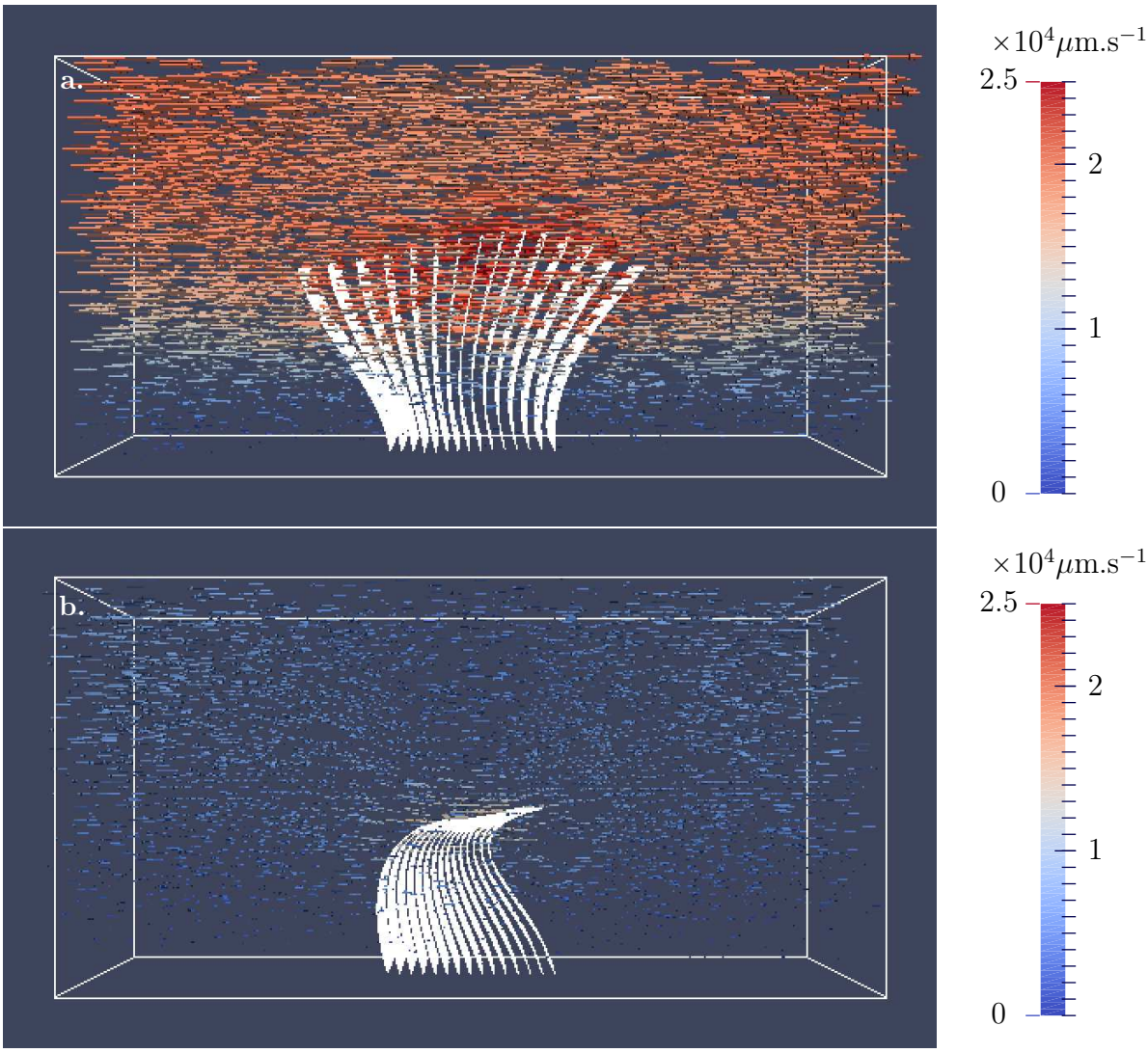

Figure 4.9: 3D-Simulation of a patch of cilia in a constant-viscosity fluid. **a.** Effective stroke ($t = \triangle t$ s). **b.** Recovery stroke ($t = 11\triangle t$ s).

4.2.3.2 Simulation of a forest of cilia

Figure 4.10 illustrates the flow produced by a whole forest of cilia. The parameters are the same as in the previous case, except for the domain and the number of cilia: we consider a $30 \times 5 \times 10$ μm^3 box, discretized by a $128 \times 17 \times 33$ mesh. The bottom of the box is filled with cilia, an "infinite" array in each direction modeled by a 153×51 array of cilia and the biperiodic boundary conditions. The length of the box is exactly the length of one metachronal wave, and the boundary conditions in the directions x and y are biperiodic, so that the flow does not depend on time, up to a translation at the velocity of the metachronal wave. As a consequence, drawing one time step only is sufficient. In the following simulation of a whole forest, the box has the same length as the metachronal wave, and therefore this observation holds.

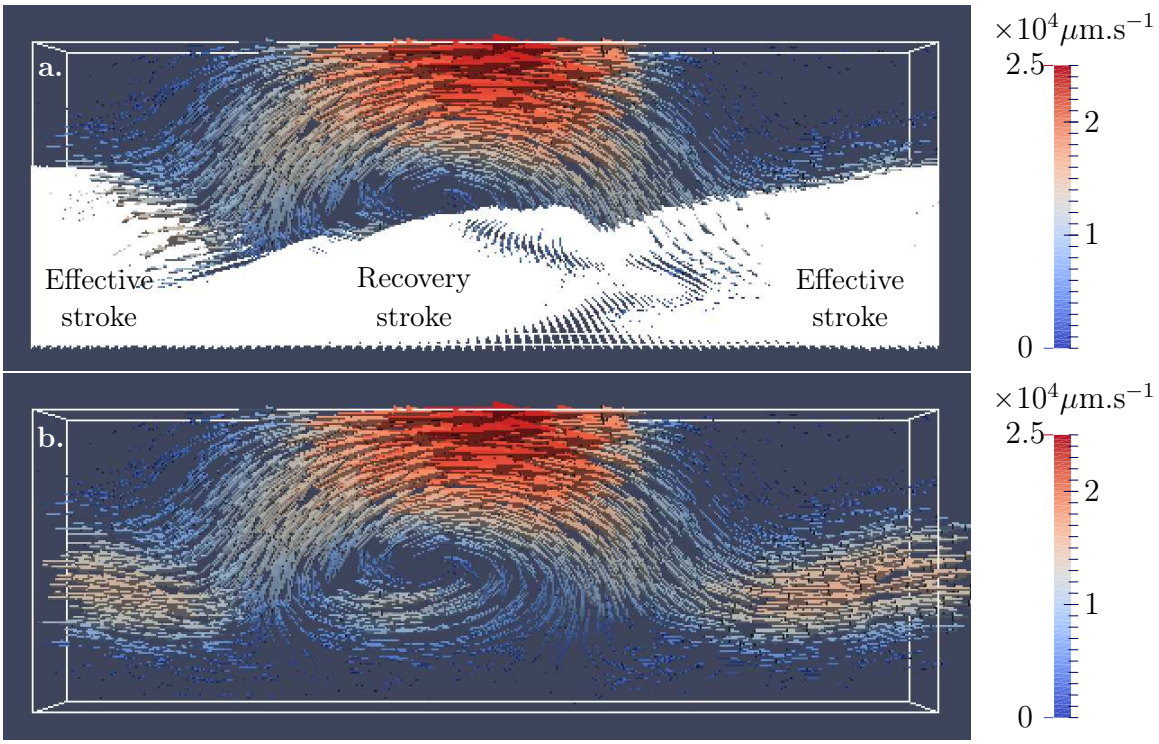

Figure 4.10: 3D-Simulation of a whole forest of cilia in a constant-viscosity fluid. **a.** Drawing with the cilia. **b.** The same flow drawn without the cilia.

Figure 4.10 illustrates the mucus transport which emerges from the collective movement of the high number of cilia. Let us note the presence of recirculations over the cilia during their recovery stroke, which results in a loss of energy and therefore a sub-efficiency of the mucus transport, compared to the bifluid case (see below).

4.2.4 Simulations with the bifluid model

The simulation of a constant-viscosity fluid leads to first conclusive observations but is not sufficient for the study of mucociliary transport in the lung. From now, we present simulations with the bifluid model: the periciliary layer and the mucus.

4.2.4.1 Simulation of a forest of cilia

Let us start with the non-pathological case. Figure 4.11 illustrates the flow produced by a whole forest of cilia in a two-viscosity fluid. All the parameters (among the computational box) are the same as in previous case, but we consider here a bifluid model for which the ratio between the viscosity in the mucus and the viscosity in the periciliary layer is $r_\mu = 50$, the ratio measured in the experiments [71, 107].

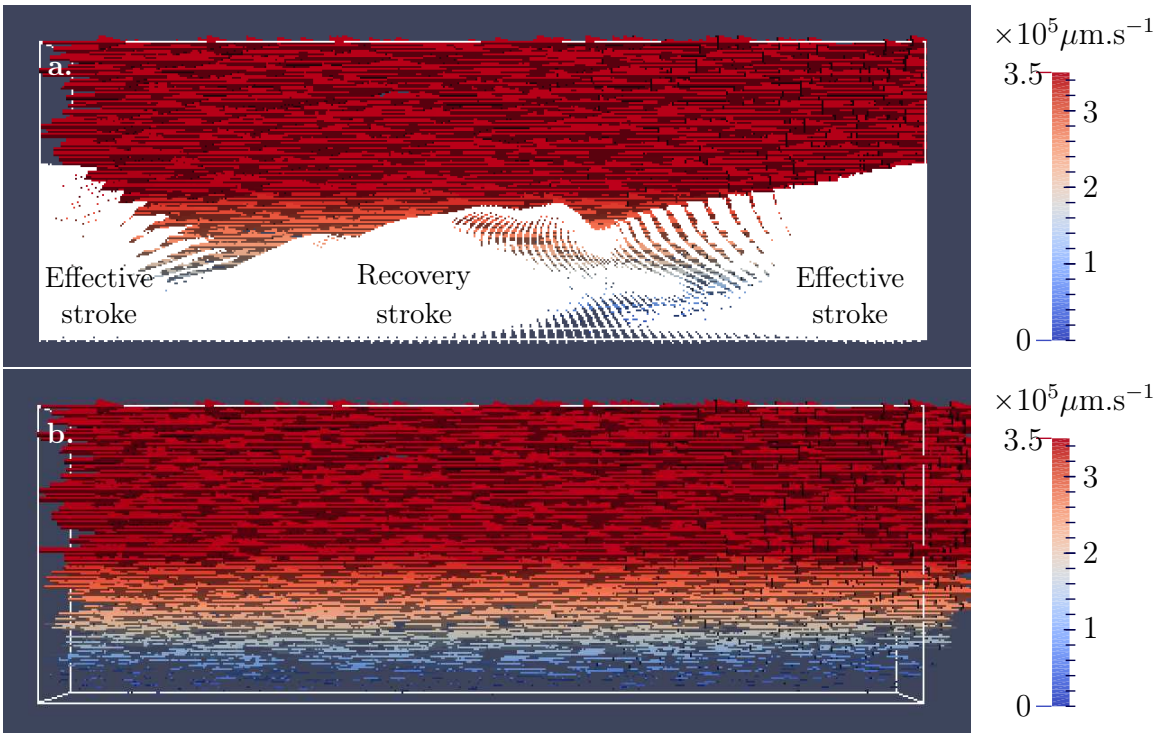

Figure 4.11: 3D-Simulation of a whole forest of cilia in a constant-viscosity fluid. **a.** Drawing with the cilia. **b.** The same flow drawn without the cilia.

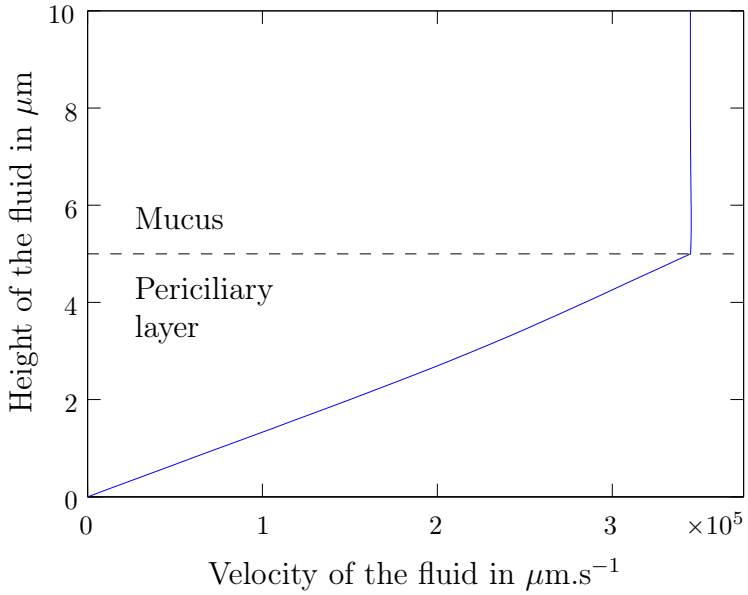

Figure 4.12: Velocity of the fluid as a function of the height.

First of all, note that the mucus, corresponding to the top block in Figure 4.11, is transported at near constant velocity. Note also that the components in y and z are zero in the whole fluid. The velocity in the periciliary layer does not appear to depend on x

and y, but only on the height z. It seems to grow linearly from 0 (at the bottom of the domain, against the epithelial lining) to the mucus velocity. There are no recirculations as in the constant-viscosity case. The conclusion is that high viscosity in the mucus allows a more efficient transport. Actually, the viscosity effect is the primary mechanism by which mucus transport is produced. Moreover, mucus is transported at a constant velocity, as a block "sliding" over the periciliary layer, which means it is not transported by fits and starts, and there is no turning back, contrary to the case of a patch of cilia [30]. This fact results from the collective movement of the high number of cilia. Note that there is no difference between the area in which cilia are in their effective stroke and the area in which they are in their recovery stroke, which is different from the constant-viscosity case (compare Figures 4.10 and 4.11): it is a consequence of the collective dynamics of the cilia.

In Figure 4.12, the velocity of the fluid is drawn as a function of the height of the fluid. This figure confirms that velocity is constant in the mucus and that it linearly grows in the periciliary layer. The simulation allows us to reproduce the profiles described in [84, 108].

In what follows, the simulation of the standard case serves as a reference case to study the influence of some parameters and their related pathologies.

4.2.4.2 Influence of the density of cilia

Now that the non-pathological case has been simulated, we can study the influence of some parameters, and for instance, let us look at the consequences of a low density of cilia. By linearity of the Stokes equations, if we divide the number of cilia by 2 (keeping the same length λ for the metachronal wave), we can expect the same qualitative flow, but with an average transport velocity divided by a factor 2. Nevertheless, it is possible that a low density of cilia causes the loss of the collective dynamics. The aim of the following simulations is to evaluate the limit where the collective dynamics disappear.

Figure 4.13 shows the flows produced by lower densities of cilia. Figure 4.13**a** illustrates the flow when the number of cilia is divided by 2 in each direction of the array of cilia. The total number of cilia is therefore divided by 4. As expected, the average velocity in the mucus is 4 times lower. In the case where the number of cilia is divided by 4 in each direction (Figure 4.13**b**), the velocity in the mucus is divided by 16, and by 64 when the number of cilia in each direction is divided by 8 (Figure 4.13**c**). Finally, we conclude that the flow produced by the cilia is proportional to the number of cilia. This fact was forseeable by linearity of the Stokes equations. Note that the collective dynamics hold in these cases.

However, when the number of cilia is divided by 8 in each direction, and therefore a total number of cilia divided by 64, the produced flow is not quite constant over a cilium beat. Figure 4.14 draws the average velocity in the mucus layer at the times $t = n\triangle t$ s, for $n \in [0, 19]$ (over one beat). The order of magnitude is significantly the same. The difference in the absolute value comes from the ratio between the number of cilia which are in their effective stroke and the number of cilia which are in their recovery stroke: this ratio is not the same all over the beat, but the variations are small. Actually, this

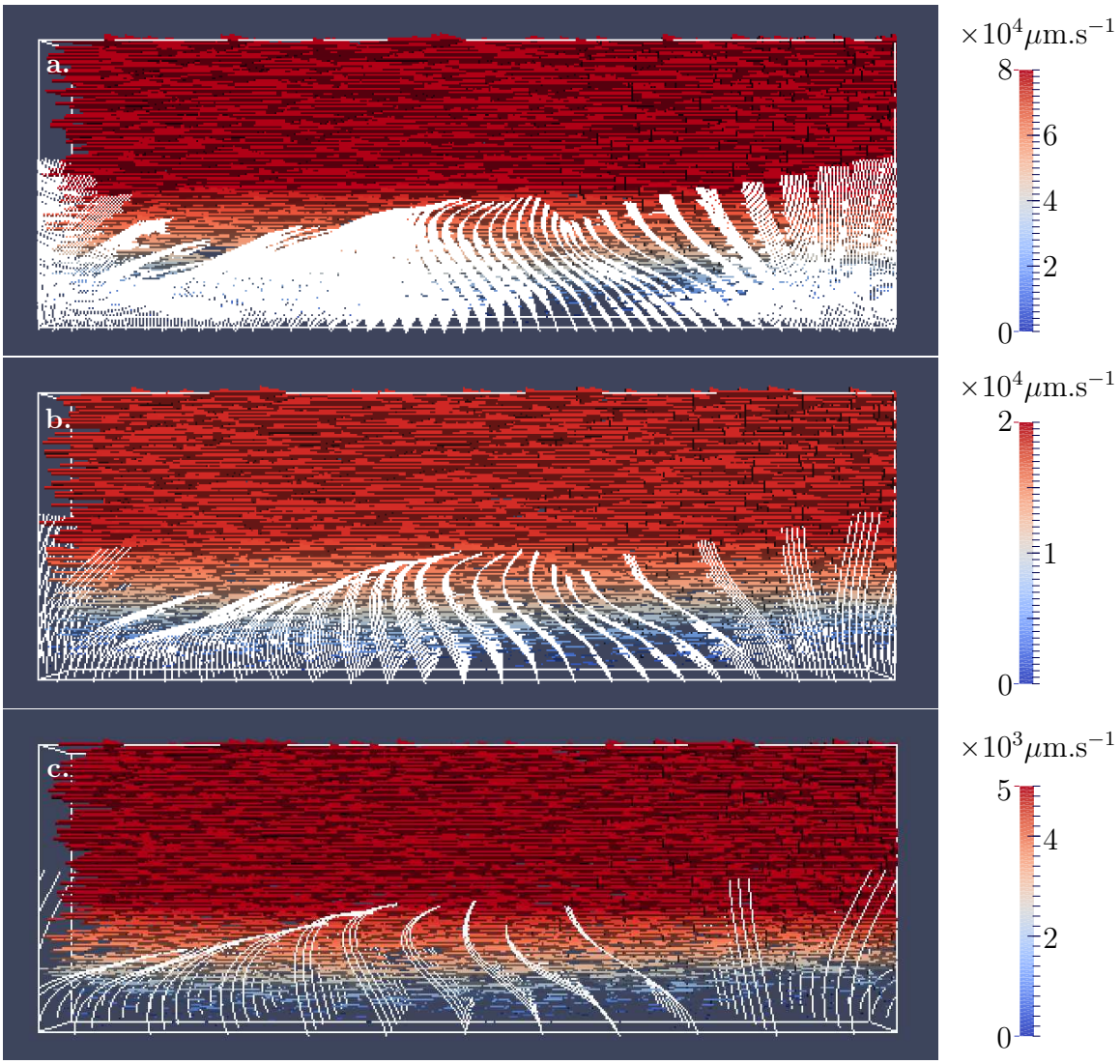

Figure 4.13: Influence of the density on the mucus transport. **a.** Number of cilia divided by 2 in both directions x and y. **b.** Number of cilia divided by 4 in both directions x and y. **c.** Number of cilia divided by 8 in both directions x and y.

observation is a consequence of a computational artefact: the size of the box related to the metachronal wave length, artefact which disappears when the number of cilia increases.

But, what happens when the number of cilia in each direction is even lower? Let us devide it by 16 for a total number of cilia divided by 256. Figure 4.15 shows the flow generated in this case at two different times of the beat: $t = 0$ s (Figure 4.15**a**) and $t = 4\triangle t$ s (Figure 4.15**b**). At time $t = 0$ s, there are cilia which penetrate into the mucus, and therefore it can be transported. The velocity in this case follows the proportionnality observed previously. But if there is no cilium which penetrates into the mucus (time $t = 4\triangle t$ s), it is not transported and only a bit of periciliary layer is propelled. In this situation, we lose the collective dynamics and fall in a pathological case. Actually, with the simulation of Figure 4.15**b**, we recover the fact that mucus transport requires cilia to reach the mucus layer in situation of low ciliary density, whereas in the case of a high

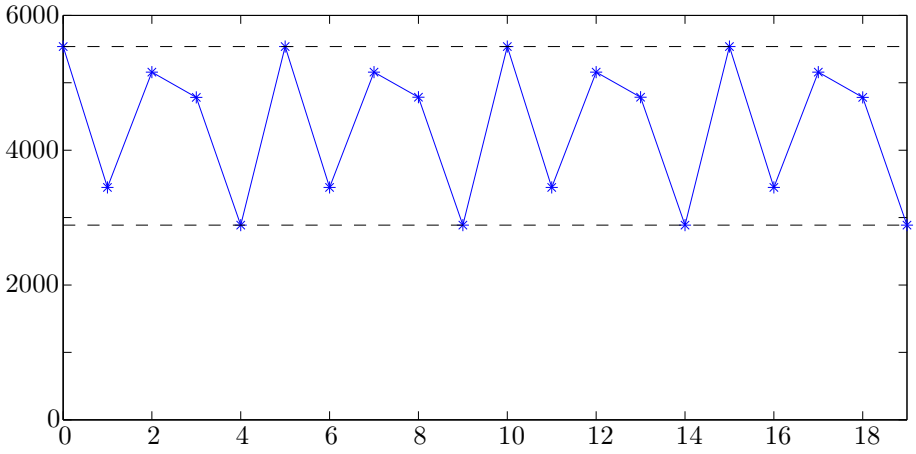

Figure 4.14: Velocity in the mucus layer over a beat for a density divided by 8 in each direction.

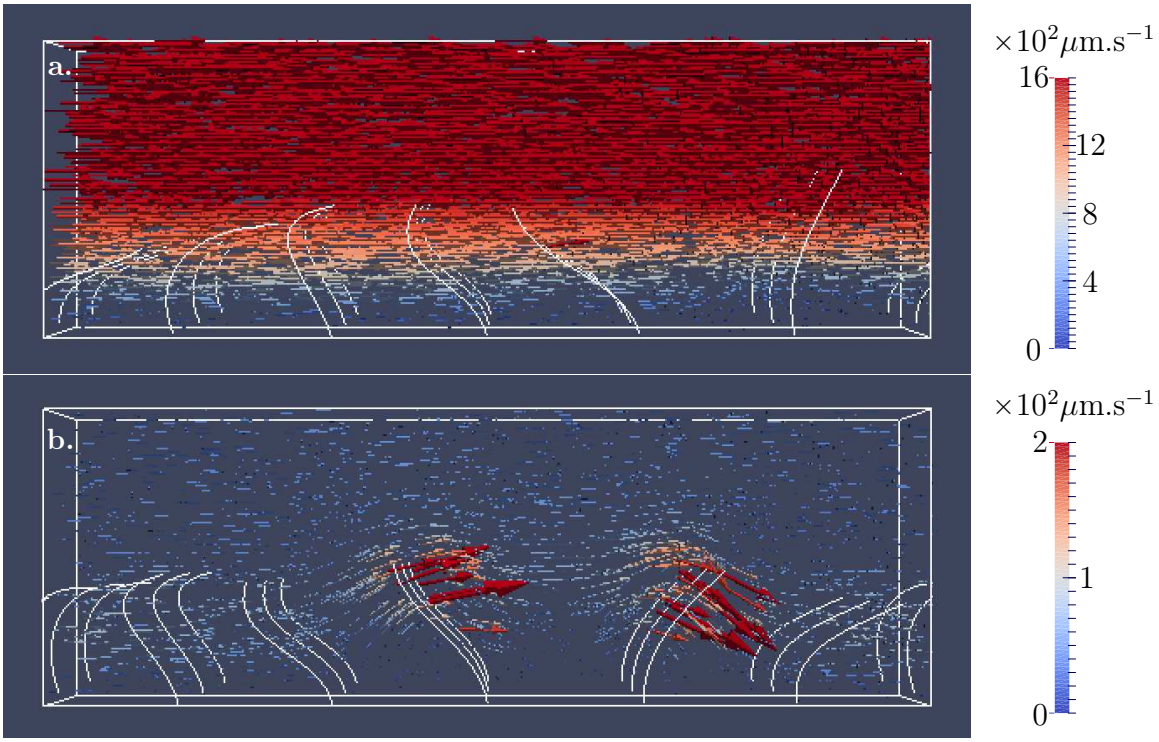

Figure 4.15: Flow produced by a low-density array of cilia (divided by 16 in each direction). **a.** Flow at the time $t = 0$ s. **b.** Flow at the time $t = 4\triangle t$ s.

ciliary activity, the penetration into the mucus is not necessary to obtain ample velocities of propulsion [105, 108].

As a conclusion of this section, let us remark that the too small length of the computational box does not allow us to bring to light a potential threshold where the collective dynamics disappear. Actually, the box should be of the length of several metachronal waves to hope to observe the loss of collective dynamics, but it involves too expansive

computational costs.

4.2.4.3 Influence of the thickness of the periciliary layer

It is clearly reported in the litterature [105, 108] that the penetration of cilia into the mucus is very important for its transport: mucus is propelled by cilia during their effective stroke (and only during this stroke) and the penetration accentuates the irreversible nature of the beat of the cilia. Two natural pathological cases emerge:

- the first one is the case where the periciliary layer is too thick, so that the cilia do not reach the mucus layer.
- the second one concerns the case where, on the contrary, periciliary layer is so thin that the cilia reach the mucus not only during their effective stroke but also during their recovery stroke, propulsing the mucus towards the opposite direction.

A too thick periciliary layer. Let us start with studying the first case. We compute a dense forest of cilia with the parameters described above, but assume the periciliary layer is a 6.5 μm thickness layer (against 5 μm in the non-pathological case). For this height of periciliary layer, the cilia cannot reach the mucus and never penetrate into it. Figure 4.16 draws the flow produced by a dense forest of cilia beating in a too thick periciliary layer.

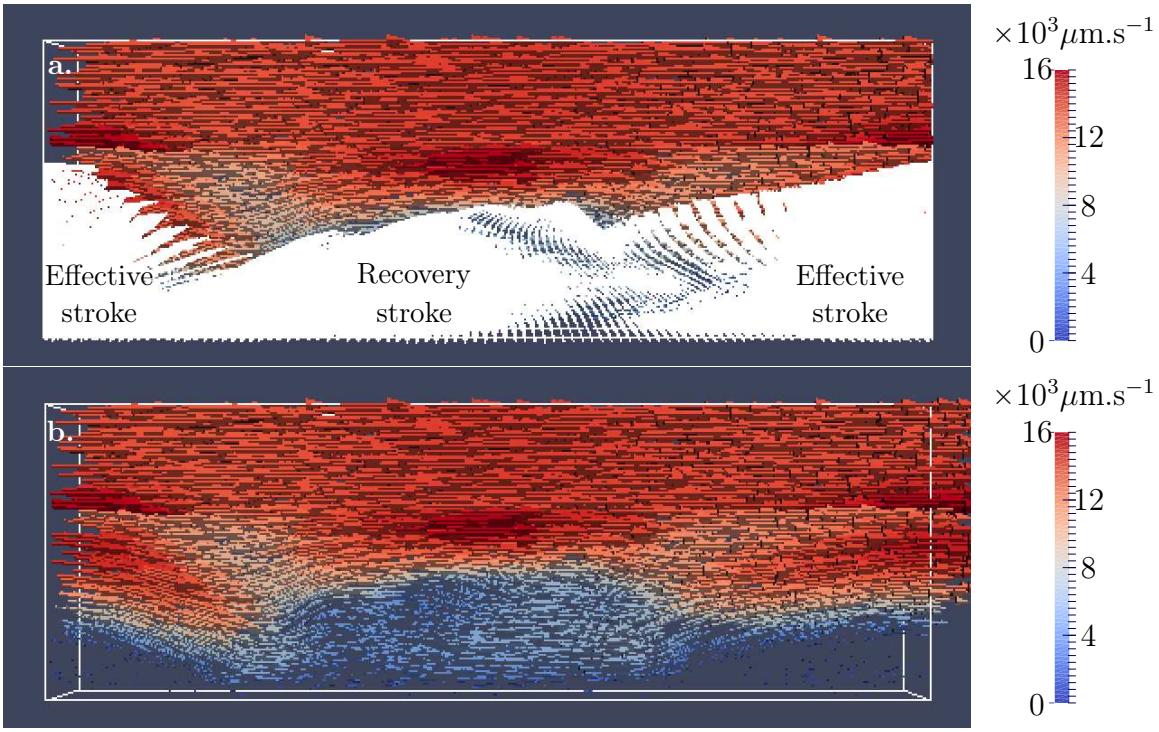

Figure 4.16: 3D-Simulation of the thick periciliary layer case. **a.** Drawing with the cilia. **b.** The same flow drawn without the cilia.

As it has been observed experimentally [105] and recovered numerically [108], a high ciliary activity does not require penetration of the cilia into the mucus to obtain an efficient mucus transport, even if of course the velocity in the mucus layer is lower. Figure 4.16 shows that this observation is reproduced by our simulations. The robustness of the process results in it: if an overproduction of periciliary liquid occured, so that the cilia could not reach the mucus layer, the periciliary layer and the mucus would be transported and a return to the standard situation could be expected.

We can also take advantage of the thick periciliary layer case to study the influence of the viscosity in the mucus on the transport, that is to say the influence of the ratio of viscosities. In order to do that, we compute the flow for three values of this ratio of viscosities: $r_\mu = 20$, $r_\mu = 50$ and $r_\mu = 70$. Note that $r_\mu = 50$ is our reference case, illustrated above (see Figure 4.16). Figure 4.17 draws the mean velocity for each of these three values of the ratio of viscosities, as a function of the height. The flow produced in the periciliary layer is the same in the three cases: the cilia do not see the mucus, and the mucus seems to have no effect on the periciliary layer. Nevertheless, the viscosity in the mucus changes its velocity: the more the mucus is viscous (which corresponds to a high ratio of viscosities r_μ) the more the transport is efficient. Note that the loss of velocity between the cases $r_\mu = 50$ and $r_\mu = 20$ is only about 5% whereas the ratio is divided by 2.5 (same remark between the cases $r_\mu = 50$ and $r_\mu = 70$: the gain is about 3.5% for a ratio multiplied by 1.4). The dependence of the transport on the viscosity in the mucus is clearly not linear and not very sensitive.

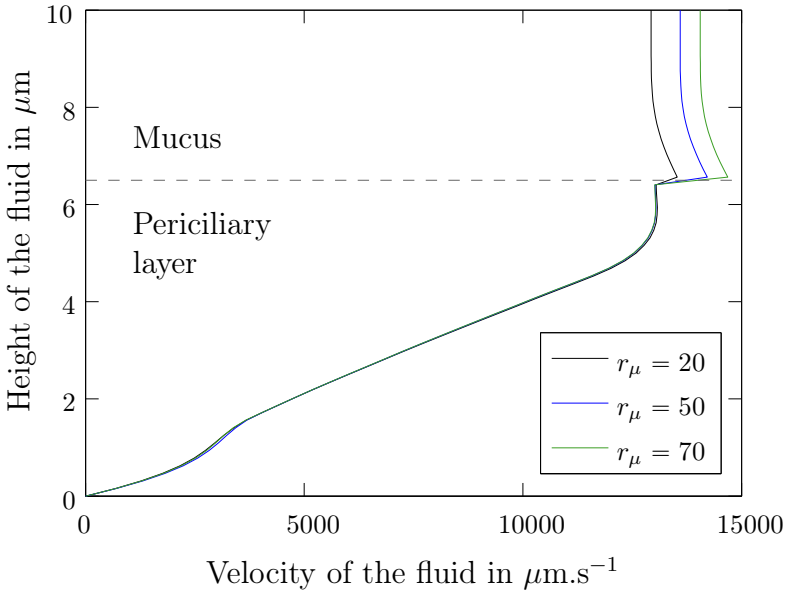

Figure 4.17: Variation of the viscosity in the mucus in the case of a too thick periciliary layer (PCL).

A too thin periciliary layer. Let us now consider the opposite phenomena: a thin periciliary layer. In this situation, the height of the interface mucus-periciliary layer is so low that the cilia reach the mucus layer also in their recovery stroke. The mucus is

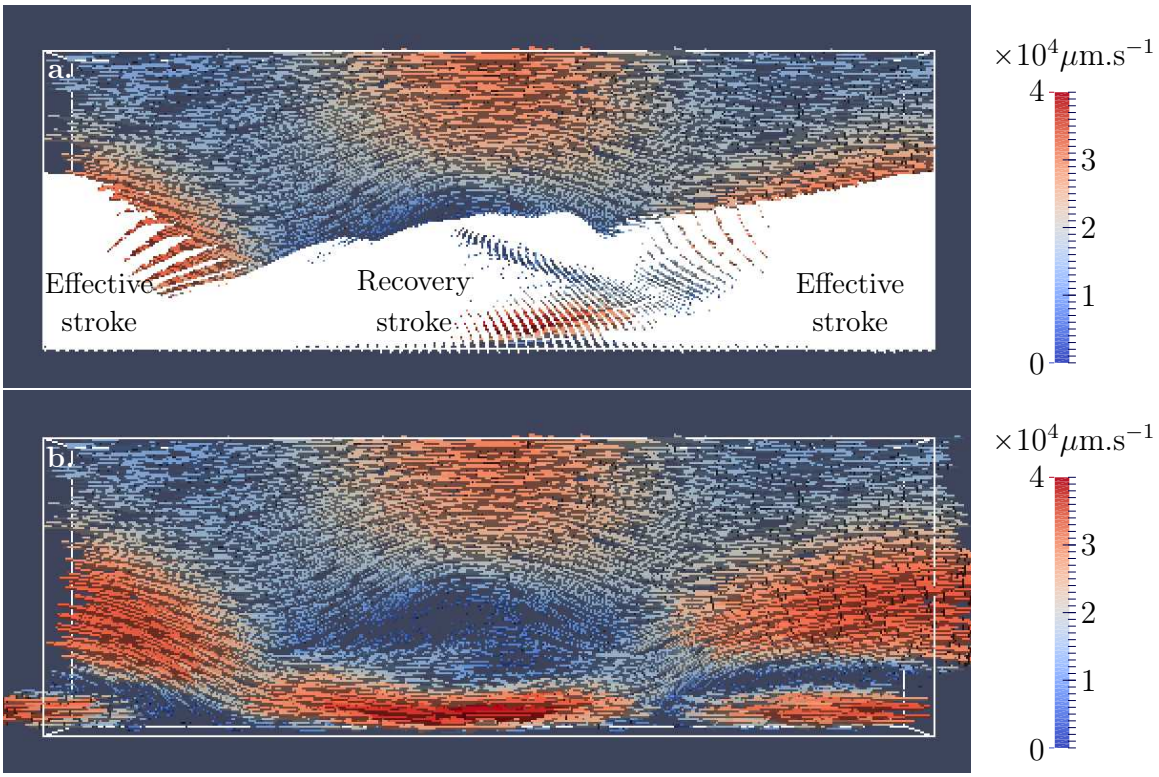

Figure 4.18: 3D-Simulation of the thin periciliary layer case. **a.** Drawing with the cilia. **b.** The same flow drawn without the cilia.

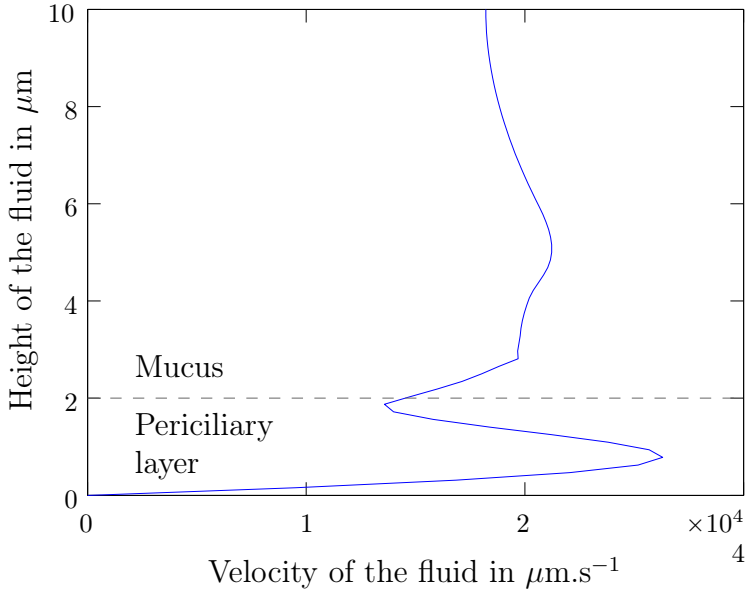

Figure 4.19: Velocity of the fluid as a function of the height for the thin-periciliary layer case.

therefore also propelled in the opposite direction during this phase. Figure 4.18 shows

the flow produced in this case. Note that there are big recirculations and very different velocities in the periciliary layer: even if the mucus is propelled also in this case, the transport is not optimal because of the important loss of energy in the periciliary layer. Figure 4.19 draws the average velocity as a function of the height and confirms the ample variations of the velocity in the periciliary layer.

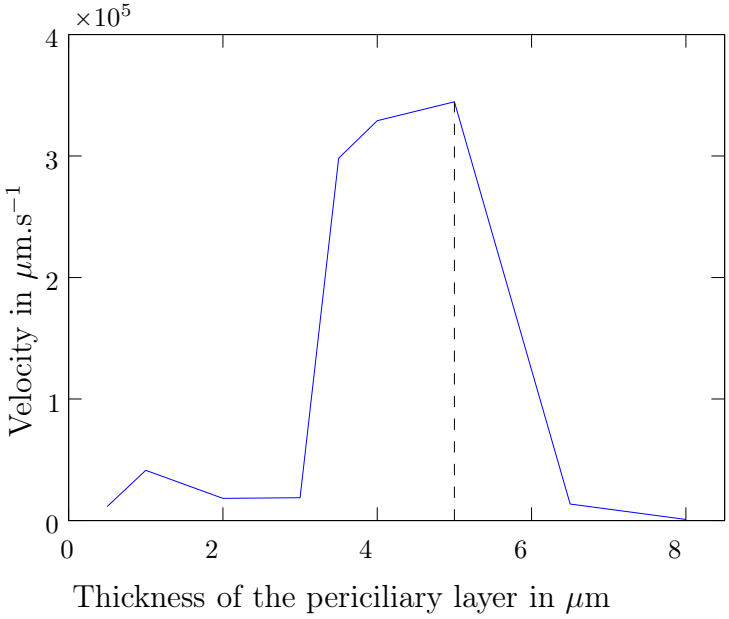

Figure 4.20: Average velocity in the mucus for different thicknesses of periciliary layer.

To conclude this section, the average velocity in the top of mucus layer is drawn in Figure 4.20 for different thicknesses of periciliary layer. First of all, let us note that the most efficient case is where the thickness of the periciliary layer is 5 μm, that is the same thickness for periciliary layer and mucus. This configuration corresponds to the non-pathological case: the case selected by the nature is the most efficient. Moreover, Figure 4.20 also shows the robustness of the transport efficiency related to the thickness of the periciliary layer. Nevertheless, the velocity magnitude falls significantly if the thickness of the periciliary is not between 3.5 and 6 μm.

4.2.5 Limits of the model

To end this chapter, we discuss the limits of our model. The first one, and maybe the main one, is that the cilia beat is imposed. Even if most of the works related to mucociliary transport do this assumption, it is not realistic. The second limit is the too high order of magnitude we obtain compared to the experimental data. These differences can be explained by the model, which should be improved.

Imposed beat pattern. In our model, as it is done in nearly all the models (see for instance [30, 71, 107, 108]), the movement of the cilia is imposed, independently on the

environment: no matter if the fluid viscosity is high or low, the cilium beat remains the same. When the cilium penetrates the mucus, its velocity is imposed through the movement, and the cilium beat pattern is not sensitive to the change of viscosity. The resistance of mucus is much higher than the resistance of the periciliary layer, but the movement of the cilium is not affected by this difference of resistance, as if the cilium could adapt its internal force to keep a constant velocity. This assumption is not realistic. Actually, experiments show that the cilium is slowed down by the mucus and ends its beat when it goes out the mucus, as if the mucus had stopped it [96]. In our model, this is not taken into account, and thus, the internal force of the cilium increases artificially to adapt to the viscosity of the mucus. Indeed, the force is linear in μ and therefore, when the cilium crosses the interface mucus-periciliary layer, the force is multiplied by 50 in the upper part of the cilium.

In order to illustrate this remark, we compute the flow produced by a forest of cilia in a bifluid model with the force generated as if the cilia were in a constant-viscosity fluid (the periciliary layer). Actually, we recall the expression of the force at each point of the cilium (see Chapter 1, Equation (1.3.12) for more details)

$$\mathbf{f}(s,t) = \frac{2\pi\mu}{\ln(L/r_0)} \left(2\mathbb{I}_3 - \frac{\dot{\boldsymbol{\xi}}(s,t) \otimes \dot{\boldsymbol{\xi}}(s,t)}{\|\dot{\boldsymbol{\xi}}(s,t)\|^2} \right) \mathbf{u}_{\text{cil}}(s,t),$$

where μ is the local viscosity at the point $\boldsymbol{\xi}(s,t)$. Figure 4.21 shows the flow produced when we keep $\mu = \mu_{\text{PCL}}$ all along the cilium, as if the force generated by the cilium were the same in the periciliary layer and the mucus.

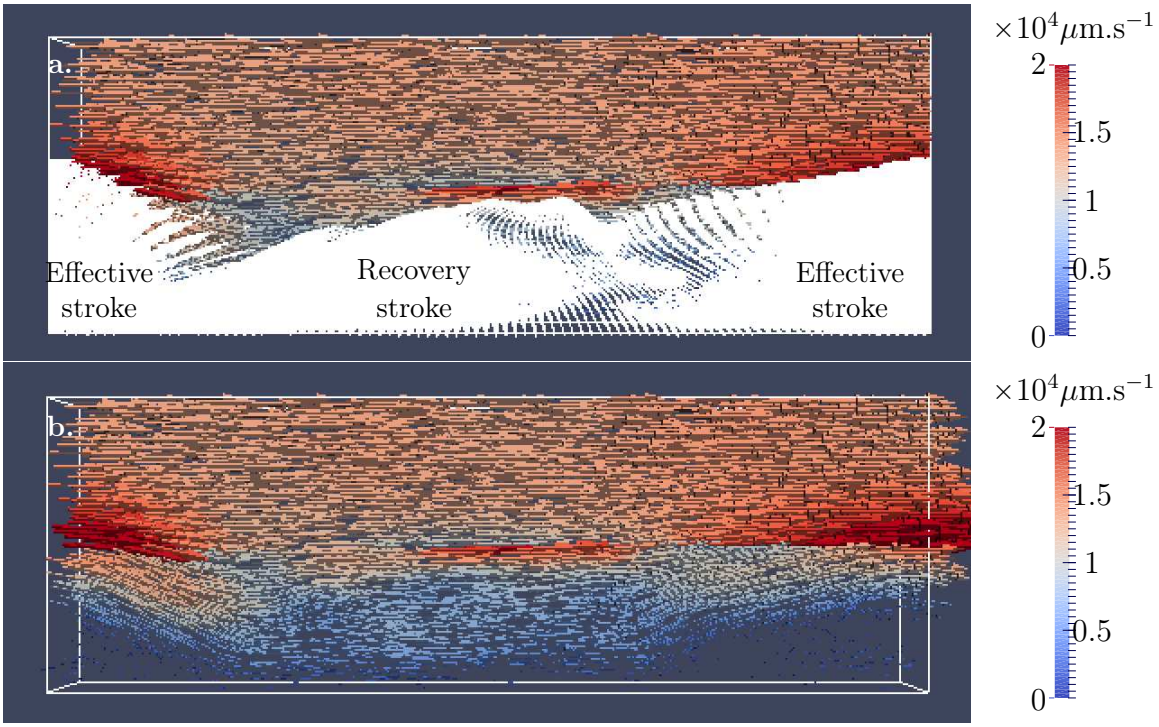

Figure 4.21: Flow generated with the modified force in each point of the upper part of the cilia. **a.** Drawing with the cilia. **b.** The same flow drawn without the cilia.

Even if this definition of the force is not consistant with the movement of the cilia, the simulation illustrates the important difference between the standard case computed in Section 4.2.4.1 and a "more realistic case", in which the force but not the movement of the cilia would be imposed. By comparing Figures 4.12 and 4.22, which draw the vertical profiles of velocity, we can see a ratio 27 between the two velocities in the upper part of the mucus (where the velocities are constant). Finally, imposing the movement and deducing the force increases artificially the velocity of the fluid, which is one of the reasons of high orders of magnitude (see below). But even if it is not the most realistic model we can develop, it allows us to compute simulations and study the influence of some parameters on the transport and thus understand the mucociliary clearance. Note that imposing the force rather than the movement of the cilia involves a description of the internal mechanism of the cilium, which is not really well-understood. Moreover, this approach requires the model to take into account the feedback of the fluid on the cilium. Finally, imposing the force is an altogether different model.

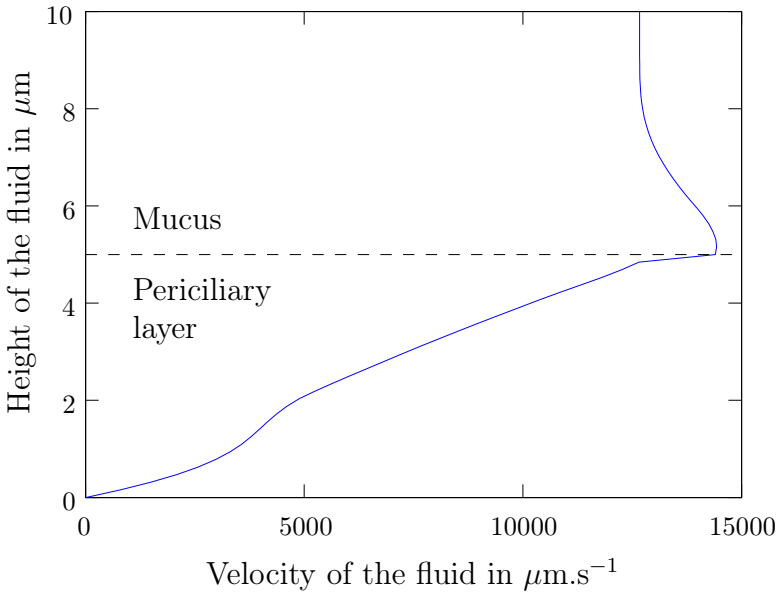

Figure 4.22: Average velocity of the fluid as a function of the height, flow produced by the modified force.

High order of magnitude. In the non-pathological case, Section 4.2.4.1, the order of magnitude of the predicted velocity in the mucus is $3.5 \times 10^5 \mu\text{ms}^{-1}$, which is 1000 times higher than the experimental measurements: Wanner [115] measured rates of 300 μm.s^{-1}. This difference of order of magnitude can be explained by several reasons related to the model, among them:

- the movement of the cilia is imposed; this first point has been explained in the last paragraph, and we have shown that a loss of a factor 27 can be expected by imposing the force rather than the movement.

- the biperiodic boundary conditions.
- the whole forest is computed.

The biperiodic conditions can also explain the high order of magnitude we obtain with our model. Indeed, the mucus is transported along the bronchi until the end of the trachea, and for a portion of bronchus, the mucus input and output have no reason to be equal. We consider biperiodic boundary conditions because they are natural at the scale of the metachronal wave, and because of the difficulty of imposing realistic conditions of input and output.

Lastly, for most of the simulations presented in this chapter, we compute a whole forest of cilia with no area of inactivity. Actually, as it has been observed by Sanderson and Sleigh [96], only small areas of cilia are beating at each time, a lot of the cilia being at rest (see Chapter 1, Figures 1.8 and 1.9). By linearity of the Stokes equations, we can expect a higher order of magnitude of the flow produced by a whole forest of cilia than the flow produced by only small areas of ciliary activity. But the study of the collective dynamics generated by several small areas of ciliary activity requires a very big box of computation, which increases significantly the computational costs. That is why the simulation of a whole forest in a box of one-metachronal wave length is a good deal between realistic orders of magnitude and reasonable computational costs.

CONCLUSION ET PERSPECTIVES

L'objectif de la thèse est de modéliser et de simuler de manière directe en 3D le mouvement de cils dans un fluide visqueux, c'est-à-dire prise en compte des mécanismes à l'échelle où ils se produisent, à savoir celle du cil. Il s'agit de décrire en détail le mouvement d'un ou plusieurs cils en interaction avec le fluide environnant, et de développer un outil numérique capable de simuler un très grand nombre de cils battant dans un fluide complexe, cet outil permettant de mieux comprendre le processus de transport mucociliaire et les pathologies associées.

Un des points clés du modèle présenté dans le Chapitre 1 est la façon dont nous avons choisi de prendre en compte les effets des cils sur l'écoulement bifluide. Nous travaillons à mouvement imposé et donc la rétro-action du fluide sur les cils n'est pas prise en considération. Le cil étant un corps très fin et battant à une fréquence très élevée, dans l'asymptotique où le rapport entre épaisseur et longueur tend vers 0, mais à résultante de force constante, il est modélisé par une distribution linéique de forces, elle-même approchée pour des raisons purement numériques par une distribution de forces ponctuelles le long du cil. Cette modélisation conduit à l'étude de problèmes elliptiques singuliers, dont l'analyse numérique est présentée dans le Chapitre 2 pour le problème de Poisson avec une masse de Dirac en second membre, et dans le Chapitre 3 pour le problème de Stokes avec une force ponctuelle en terme source. En particulier, on s'intéresse à des estimations d'erreurs locales, sur des sous-domaines qui ne contiennent pas la singularité. Cette analyse numérique nous a poussé à développer une nouvelle méthode numérique pour la résolution de ces deux problèmes. Basée sur celle des éléments finis, elle s'appuie sur la connaissance explicite d'une solution fondamentale, et permet de retrouver une convergence optimale de la solution approchée vers la solution exacte. Enfin, dans le Chapitre 4, cette méthode est appliquée à l'étude du transport mucociliaire. Elle nous permet notamment de simuler en 3D l'écoulement bifluide généré par toute une forêt de cils. Des pathologies liées à la clairance mucociliaire sont illustrées à travers l'étude de l'influence de certains paramètres telles la hauteur de mucus ou la densité de cil.

Nous terminons ce manuscrit en donnant des pistes naturelles de recherche à explorer pour compléter ce travail.

Analyse numérique

L'analyse numérique des problèmes de Poisson et de Stokes singuliers a soulevé plusieurs problèmes. Le principal étant que les preuves présentées en dimension 2 ne s'étendent pas au cas de la dimension 3 : les résultats qu'on obtient ne sont pas optimaux. Une perspective de ce travail est donc la recherche d'autres techniques que celles présentées et qui pourraient être étendues à la dimension 3.

Dans le cas du problème de Poisson, Köppl et Wholmuth [66] ont obtenu des estimations d'erreurs locales optimales en norme $\mathbb{L}^2$ pour les éléments finis de Lagrange. Même si les estimations que nous avons obtenues en norme H^s, $s \geqslant 1$, ne sont que quasi-optimales (présence d'un facteur log qui, numériquement, ne se voit pas), elles sont valables pour une très grande classe d'éléments finis : les éléments de Lagrange, de Hermite, les ondelettes, etc. Un des points clés de la preuve de Köppl et Wholmuth [66] est le résultat de Scott [99] : sur l'ensemble du domaine, il y a convergence en norme $\mathbb{L}^2$ à l'ordre 1 en dimension 2 et 1/2 en dimension 3, contre l'ordre 2 dans le cas régulier. Il n'y a pas de résultat équivalent pour le problème de Stokes : pas de résultat de convergence en norme $\mathbb{L}^2$ pour la vitesse sur l'ensemble du domaine. Un axe de recherche consisterait donc à établir des estimations d'erreur sur l'ensemble du domaine dans ce cas-là aussi, et à les utiliser pour démontrer des estimations d'erreurs locales optimales en normes $\mathbb{L}^2$ et H^s, pour $s \geqslant 1$.

Enfin, la question a été soulevée mais laissée en suspens : que se passe-t-il lorsque la masse de Dirac (ou la force ponctuelle) est proche du bord ? Cette question intéressante change complètement la nature du problème et mérite réflexion car, dans les applications, elle intervient lorsque l'on souhaite simuler la dynamique d'un micro-nageur autopropulsé par un flagelle ou des cils. Dans ce cas, remailler le domaine à chaque itération est coûteux et par ailleurs un nouveau maillage ne suffirait pas à obtenir de bonnes estimations.

Méthode de soustraction

Comme expliqué dans le Chapitre 4, la méthode dite de *soustraction*, que nous avons développée et présentée pour la résolution numérique des problèmes de Poisson et de Stokes singuliers, peut être généralisée à d'autres problèmes elliptiques. Mais qu'en est-il si on remplace le terme source par un autre lui aussi singulier ? Par exemple, considérons le problème de Stokes avec en second membre un *doublet de Stokes* D_F, défini par

$$D_S = \lim_{\varepsilon \to 0} \frac{\delta_{\mathbf{x}_0}\mathbf{F} - \delta_{\widetilde{\mathbf{x}}_0}\mathbf{F}}{\varepsilon},$$

où $\mathbf{F}$ est la force du doublet, $\mathbf{x}_0$ son origine, et $\widetilde{\mathbf{x}}_0 = \mathbf{x}_0 - \varepsilon\mathbf{e}$ (dans le cas d'un *pusher*, voir plus loin). Le vecteur unitaire $\mathbf{e}$ est défini par $\mathbf{e} = \mathbf{F}/\|\mathbf{F}\|$. Un doublet de Stokes est en fait la limite de la somme de deux forces ponctuelles de même intensité, de même direction mais de sens opposés, lorsque leur distance ε tend vers 0 (voir Figure 4.23).

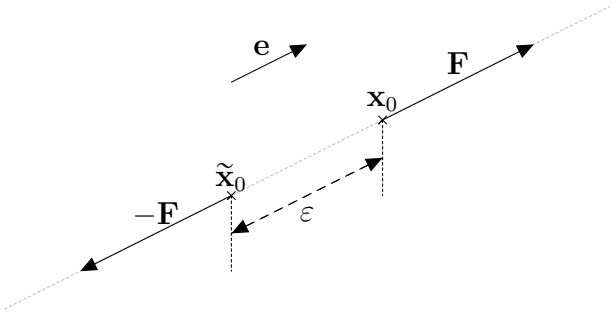

FIGURE 4.23: Doublet de Stokes.

Une solution du problème de Stokes en domaine infini est connue pour ce terme source : on l'appelle la *Stresslet* [7]. Elle est définie par :

$$\mathbf{u}_S(\mathbf{x}) = \frac{1}{2^d \pi \mu}\left[-\frac{\|\mathbf{F}\|}{r^d} + \frac{3(\mathbf{F}\cdot\mathbf{x})(\mathbf{e}\cdot\mathbf{x})}{r^{d+2}}\right]\mathbf{x},$$
$$p_S(\mathbf{x}) = \frac{1}{2^{d-1}\pi}\left[-\frac{\|\mathbf{F}\|}{r^d} + \frac{3(\mathbf{F}\cdot\mathbf{x})(\mathbf{e}\cdot\mathbf{x})}{r^{d+2}}\right],$$

où d est la dimension de l'espace. Comme on connaît une solution en domaine infini, on peut adapter la méthode de soustraction à ce problème défini sur un domaine borné, et pallier les problèmes de convergence liés à la résolution numérique d'un problème singulier. Une extension méthodologique des travaux présentés dans ce manuscrit consisterait donc à dérouler les calculs et à appliquer la méthode, par exemple, à la simulation d'un grand nombre de micro-nageurs dans le but de retrouver des signatures rhéologiques observées expérimentalement [39].

D'autres choix de modélisation

Un modèle viscoélastique pour le mucus. Dans la littérature scientifique consacrée au transport mucociliaire, les auteurs s'accordent sur le fait que la couche périciliaire est essentiellement de l'eau, et a donc un comportement newtonien, même si cette affirmation a récemment été mise en cause par Boucher [17]. En revanche, pour le mucus, les modèles proposés peuvent être très différents [30, 37, 86]. Pour notre modèle, nous avons choisi de considérer un fluide newtonien, pour la couche périciliaire et pour le mucus. Un autre modèle naturel serait de considérer un modèle bifluide, avec un fluide newtonien pour la couche périciliaire et un fluide viscoélastique pour le mucus, dans l'espoir de retrouver des effets non captés par le modèle bifluide newtonien.

Un modèle diphasique pour le fluide. En s'appuyant sur des expériences de Sanderson and Sleigh [96] et sur des travaux numériques de Dillon et ses co-auteurs [40], nous avons supposé dans notre modèle que l'interface entre le mucus et la couche périciliaire restait plane et invariante. Cette hypothèse peut être relaxée en considérant un modèle diphasique pour le fluide [18], notamment s'il s'agit de mettre en évidence des phénomènes de régulation de la hauteur de la couche périciliaire. Par exemple, Boyer et ses co-auteurs [19] considèrent le modèle d'Oldroyd pour les fuides viscoélastiques et l'interface diffuse entre les deux fluides est modélisée par le modèle de Cahn-Hilliard. Cependant, ce modèle couplé est non linéaire et n'a pas été étudié avec des termes sources singuliers. De manière générale, se pose la question de comment adapter la méthode de soustraction à des opérateurs non linéaires.

Travail à force imposée. Même si travailler à mouvement imposé, comme nous l'avons fait dans la thèse, permet de retrouver des comportements et des champs de vitesses observés expérimentalement et numériquement, on a bien vu dans le Chapitre 4 que ce modèle est limité. Son principal défaut est que la partie haute du cil adapte sa vitesse à la résistance du mucus quand il pénètre dedans. Un modèle plus réaliste serait de non pas imposer le mouvement du cil, mais la force que le cil génère en chaque point sur le fluide. De cette force serait induit le mouvement du cil, et on pourrait alors aussi prendre en compte la rétro-action du fluide sur le cil. Le problème est qu'il n'est pas simple de définir cette force, notamment car les mécanismes internes du cil ne sont pas encore bien compris.

Application à la nage de micro-organismes

Le travail effectué dans cette thèse et l'outil numérique que nous y avons développé, possèdent un champ d'applications plus large que le transport mucociliaire. Parmi ces applications se trouvent l'étude et la simulation de la nage de micro-organismes. On distingue deux types de micro-nageurs :

- le *pusher*, qui est propulsé par des flagelles, à l'instar de la bactérie *Escherichia Coli* ou du spermatozoïde.
- le *puller*, tracté par des cils, comme la micro-algue *Chlamydomonas reinhardtii* (voir Figure 4.24).

Dans chacun des deux cas, nous pouvons simuler la nage à l'échelle du cil (ou du flagelle) et espérer retrouver des signatures rhéologiques observées expérimentalement. Pour un fluide de viscosité constante, travailler à mouvement imposé peut aussi être un bon premier modèle, mais il semble alors naturel de prendre en compte la rétro-action du fluide. En particulier, pour des bactéries nageant dans un écoulement donné (cisaillement par exemple), les effets du fluide sur les cils peuvent être prépondérants. Ce travail serait l'occasion de confronter le modèle à des données réelles.

FIGURE 4.24: *Chlamydomonas reinhardtii*, image modifiée à partir de [119].

BIBLIOGRAPHIE

[1] J. P. Agnelli, E. M. Garau, and P. Morin. *A posteriori* error estimates for elliptic problems with Dirac measure terms in weighted spaces. ESAIM Math. Model. Numer. Anal., 48(6) :1557–1581, 2014.

[2] T. Apel, O. Benedix, D. Sirch, and B. Vexler. A priori mesh grading for an elliptic problem with Dirac right-hand side. SIAM J. Numer. Anal., 49(3) :992–1005, 2011.

[3] R. Araya, E. Behrens, and R. Rodríguez. A posteriori error estimates for elliptic problems with Dirac delta source terms. Numer. Math., 105(2) :193–216, 2006.

[4] D. N. Arnold and X. B. Liu. Local error estimates for finite element discretizations of the Stokes equations. RAIRO Modél. Math. Anal. Numér., 29(3) :367–389, 1995.

[5] I. Babuška. Error-bounds for finite element method. Numer. Math., 16 :322–333, 1970/1971.

[6] C. Barton and S. Raynor. Analytical investigation of cilia induced mucous flow. Bull. of Math. Biophys., 29(3) :419–428, 1967.

[7] G. K. Batchelor. The stress system in a suspension of force-free particles. J. Fluid Mech., 41 :545–570, 1970.

[8] S. Bertoluzza. The discrete commutator property of approximation spaces. C. R. Acad. Sci. Paris Sér. I Math., 329(12) :1097–1102, 1999.

[9] S. Bertoluzza, A. Decoene, L. Lacouture, and S. Martin. Local error estimates of the finite element method for an elliptic problem with a dirac source term. Submitted for publication, 2015.

[10] J. R. Blake. Infinite models for ciliary propulsion. J. Fluid Mech., 49 :209–222, 1971.

[11] J. R. Blake. A note on the image system for a stokeslet in a no-slip boundary. Math. Proc. Camb. Phil. Soc., 70 :303–310, 1971.

[12] J. R. Blake. A spherical envelope approach to ciliary propulsion. J. Fluid Mech., 46 :199–208, 1971.

[13] J. R. Blake. A model for the micro-structure in ciliated organisms. J. Fluid Mech., 55 :1–23, 1972.

[14] J. R. Blake and G. R. Fulford. Mechanics of ciliary transport. Physico. Chem. Hyd., 5 :401–411, 1984.

[15] J. R. Blake and H. Winet. On the mechanics of muco-ciliary transport. Biorheology, 17 :125–134, 1980.

[16] J. J. Blum and J. Lubliner. Biophysics of flagellar motility. Annu. Rev. Biophys., 2(1) :181–219, 1973.

[17] R. C. Boucher. Airway surface dehydration in cystic fibrosis : Pathogenesis and therapy. Annu. Rev. Med., 58(1) :157–170, 2007.

[18] F. Boyer. A theoretical and numerical model for the study of incompressible mixture flows. Comput. Fluids, 31(1) :41–68, 2002.

[19] F. Boyer, L. Chupin, and P. Fabrie. Numerical study of viscoelastic mixtures through a Cahn-Hilliard flow model. Eur. J. Mech. B Fluids, 23(5) :759–780, 2004.

[20] H. Brézis. Analyse fonctionnelle : théorie et applications. Paris : Masson, 1983.

[21] C. J. Brokaw. Non-sinusoidal bending waves of sperm flagella. J. Exp. Biol., 43(1) :155–169, 1965.

[22] C. J. Brokaw. Bending moments in free-swimming flagella. J. Exp. Biol., 53(2) :445–464, 1970.

[23] P. Camner, C. Jarstrand, and K. Philipson. Tracheobronchial clearance in patients with influenza. Am. Rev. Respir. Dis., 108(1) :131–135, 1973.

[24] P. Camner, B. Mossberg, and B. A. Afzelius. Measurements of tracheobronchial clearance in patients with immotile-cilia syndrome and its value in differential diagnosis. Eur. J. Respir. Dis. Suppl., 127 :57–63, 1983.

[25] E. Casas. L^2 estimates for the finite element method for the Dirichlet problem with singular data. Numer. Math., 47(4) :627–632, 1985.

[26] E. Casas. Control of an elliptic problem with pointwise state constraints. SIAM J. Control Optim., 24(6) :1309–1318, 1986.

[27] E. Casas, C. Clason, and K. Kunisch. Parabolic control problems in measure spaces with sparse solutions. SIAM J. Control Optim., 51(1) :28–63, 2013.

[28] E. Casas and E. Zuazua. Spike controls for elliptic and parabolic PDEs. Systems Control Lett., 62(4) :311–318, 2013.

[29] R. C. Causey. Mucus and the mare : how little we know. Theriogenology, 68(3) :386–394, 2007.

[30] R. Chatelin and P. Poncet. A hybrid grid-particle method for moving bodies in 3D Stokes flow with variable viscosity. SIAM J. Sci. Comput., 35(4) :925–949, 2013.

[31] A. T. Chwang and T. Y.-T. Wu. Hydromechanics of low-Reynolds-number flow. II. Singularity method for Stokes flows. J. Fluid Mech., 67 :787–815, 1975.

[32] P. G. Ciarlet. The finite element method for elliptic problems, volume 40 of Classics in Applied Mathematics. Society for Industrial and Applied Mathematics (SIAM), Philadelphia, PA, 2002.

[33] J. R. Clamp and J. M. Creeth. Some non-mucin components of mucus and their possible biological roles. Ciba Found. Symp., 109 :157–172, 1984.

[34] S. J. Coles, K. R. Bhaskar, D. D. O'Sullivan, K. H. Neill, and L. M. Reid. Airway mucus : composition and regulation of its secretion by neuropeptides *in vitro*. Ciba Found. Symp., 109 :40–60, 1984.

[35] A. M. Collier and W. A. Clyde. Relationships between *mycoplasma pneumoniae* and human respiratory epithelium. Infect. Immun., 3(5) :694–701, 1971.

[36] R. G. Cox. The motion of long slender bodies in a viscous fluid. Part 1. General theory. J. Fluid Mech., 44 :791–810, 1970.

[37] R. V. Craster and O. K. Matar. Surfactant transport on mucus films. J. Fluid Mech., 425 :235–258, 2000.

[38] C. D'Angelo. Finite element approximation of elliptic problems with Dirac measure terms in weighted spaces : applications to one- and three-dimensional coupled problems. SIAM J. Numer. Anal., 50(1) :194–215, 2012.

[39] A. Decoene, S. Martin, and B. Maury. Microscopic modelling of active bacterial suspensions. Math. Model. Nat. Phenom., 6(5) :98–129, 2011.

[40] R. H. Dillon, L. J. Fauci, C. Omoto, and X. Yang. Fluid dynamic models of flagellar and ciliary beating. Ann. N. Y. Acad. Sci., 1101(1) :494–505, 2007.

[41] M. Del Donno, D. Bittesnich, A. Chetta, D. Olivieri, and M.T. Lopez-Vidriero. The effect of inflammation on mucociliary clearance in asthma : An overview. Chest, 118(4) :1142–1149, 2000.

[42] S. Enault, D. Lombardi, P. Poncet, and M. Thiriet. Mucus dynamics subject to air and wall motion. ESAIM : Proceedings, 30 :125–141, 2010.

[43] K. Eriksson. Finite element methods of optimal order for problems with singular data. Math. Comp., 44(170) :345–360, 1985.

[44] K. Eriksson. Improved accuracy by adapted mesh-refinements in the finite element method. Math. Comp., 44(170) :321–343, 1985.

[45] Benoit Fabrèges. A smooth extension method for the simulation of fluid/particles flows. PhD thesis, Université Paris Sud - Paris XI, 2012.

[46] B. Foliguet and E. Puchelle. Apical structure of human respiratory cilia. Bull. Eur. Physiopathol. Respir., 22(1) :43–47, 1986.

[47] G. R. Fulford and J. R. Blake. Force distribution along a slender body straddling an interface. J. Austral. Math. Soc. Ser. B, 27(3) :295–315, 1986.

[48] G. R. Fulford and J. R. Blake. Muco-ciliary transport in the lung. J. Theor. Biol., 121(4) :381–402, 1986.

[49] L. Gheber, A. Korngreen, and Z. Priel. Effect of viscosity on metachrony in mucus propelling cilia. Cell Motil. Cytoskel., 39(1) :9–20, 1998.

[50] I. R. Gibbons. Cilia and flagella of eukaryotes. J. Cell. Biol., 91(3) :107–124, 1981.

[51] A. Gilboa and A. Silberberg. *In situ* rheological characterization of epithelial mucus. Biorheology, 13 :59–65, 1976.

[52] V. Girault and P.-A. Raviart. Finite element methods for Navier-Stokes equations, volume 5 of Springer Series in Computational Mathematics. Springer-Verlag, Berlin, 1986.

[53] J. Gray and G. J. Hancock. The propulsion of sea-urchin spermatozoa. J. Exp. Biol., 32(4) :802–814, 1955.

[54] P. Grisvard. Elliptic problems in nonsmooth domains, volume 24 of Monographs and Studies in Mathematics. Pitman (Advanced Publishing Program), Boston, MA, 1985.

[55] D. A. Groneberg, U. Wagner, and K. F. Chung. Mucus and fatal asthma. Am. J. Med., 116(1) :66–67, 2004.

[56] A. C. Hilding. Ciliary streaming in the lower respiratory tract. Am. J. Physiol., 191(2) :404–410, 1957.

[57] J. C. Hogg, P. T. Macklem, and W. M. Thurlbeck. Site and nature of airway obstruction in chronic obstructive lung disease. N. Engl. J. Med., 278(25) :1355–1360, 1968.

[58] J. Iravani and A. Van As. Mucus transport in the tracheobronchial tree of normal and bronchitic rats. J. Pathol., 106 :81–93, 1972.

[59] J. D. Jackson. Classical electrodynamics. John Wiley & Sons, Inc., New York-London-Sydney, second edition, 1975.

[60] P. G. Jayathilake, Z. Tan, D. V. Le, H. P. Lee, and B. C. Khoo. Three-dimensional numerical simulations of human pulmonary cilia in the periciliary liquid layer by the immersed boundary method. Comput. & Fluids, 67 :130–137, 2012.

[61] P. K. Jeffrey and L. M. Reid. The respiratory mucous membrane. In J. D. Brain, D. F. Proctor, and L. M. Reid, editors, Respiratory defense mechanisms. Part I, pages 193–245. New York : Marcel Dekker, 1977.

[62] D. Jerison and C. E. Kenig. The inhomogeneous Dirichlet problem in Lipschitz domains. J. Funct. Anal., 130(1) :161–219, 1995.

[63] S. Keller, T. Y. Wu, and C. Brennan. A traction layer model for ciliary propulsion. In T. Y. Wu, C. Brokaw, and C. Brennan, editors, Swimming and flying in nature, pages 253–271. New York : Plenum, 1975.

[64] M. K. Khelloufi. Physique de la dynamique mucociliaire. Dispositif d'étude de la migration cellulaire 3D. Application à l'asthme et à la BPCO. PhD thesis, Aix-Marseille Université, 2015.

[65] M. R. Knowles and R. C. Boucher. Mucus clearance as a primary innate defense mechanism for mammalian airways. J. Clin. Invest., 109(5) :571–577, 2002.

[66] T. Köppl and B. Wohlmuth. Optimal a priori error estimates for an elliptic problem with Dirac right-hand side. SIAM J. Numer. Anal., 52(4) :1753–1769, 2014.

[67] L. Lacouture. A numerical method to solve the Stokes problem with a punctual force in source term. C. R. Mecanique, 343(3) :187–191, 2015.

[68] L. Lacouture. Local error analysis for the stokes equations with a singular source term. Submitted for publication, 2016.

[69] L. A. Laitinen, M. Heino, A. Laitinen, T. Kava, and T. Haahtela. Damage of the airway epithelium and bronchial reactivity in patients with asthma. Am. Rev. Respir. Dis., 131(4) :599–606, 1985.

[70] J. M. Lauweryns and J. H. Baert. Alveolar clearance and the role of the pulmonary lymphatics. Am. Rev. Respir. Dis., 115(4) :625–683, 1977.

[71] W. L. Lee, P. G. Jayathilake, Zhijun Tan, D. V. Le, H. P. Lee, and B. C. Khoo. Muco-ciliary transport : effect of mucus viscosity, cilia beat frequency and cilia density. Comput. & Fluids, 49 :214–221, 2011.

[72] D. E. Leith. Cough. In J. D. Brain, D. F. Proctor, and L. M. Reid, editors, Respiratory defense mechanisms. Part II, pages 545–592. New York : Marcel Dekker, 1977.

[73] D. Leykekhman, D. Meidner, and B. Vexler. Optimal error estimates for finite element discretization of elliptic optimal control problems with finitely many pointwise state constraints. Comput. Optim. Appl., 55(3) :769–802, 2013.

[74] J. Lighthill. Flagellar hydrodynamics. SIAM Rev., 18(2) :161–230, 1976.

[75] J.-L. Lions and E. Magenes. Problèmes aux limites non homogènes et applications. Vol. 1. Travaux et Recherches Mathématiques, No. 17. Dunod, Paris, 1968.

[76] N. Liron and S. Mochon. The discrete-cilia approach to propulsion of ciliated microorganisms. J. Fluid Mech., 75 :593–607, 1976.

[77] N. Liron and M. Rozenson. Muco-ciliary transport. J. Submicrosc. Cytol., 15 :317–321, 1983.

[78] M. Litt. Mucus rheology : Relevance to mucociliary clearance. Arch. Intern. Med., 126(3) :417–423, 1970.

[79] M. Litt. Flow behavior of mucus. Ann. Otol. Rhinol. Laryngol., 80(3) :330–335, 1971.

[80] M. T. Lopez-Vidriero, I. Das, and L. M. Reid. Airway secretion : source, biochemical and rheologicol properties. In J. D. Brain, D. F. Proctor, and L. M. Reid, editors, Respiratory defense mechanisms. Part I, pages 289–356. New York : Marcel Dekker, 1977.

[81] A. M. Lucas and L. C. Douglas. Principles underlying ciliary activity in the respiratory tract : II. A comparison of nasal clearance in man, monkey and other mammals. Arch. Otolaryngol., 20(4) :518–541, 1934.

[82] M. R. Marino and E. Aiello. Cinemicrographic analysis of beat dynamics of human respiratory cilia. Cell Motil., 2 :35–39, 1982.

[83] O. K. Matar and P. D. M. Spelt. Dynamics of thin free films with reaction-driven density and viscosity variations. Phys. Fluids, 17(12) :122102, 15, 2005.

[84] H. Matsui, S. H. Randell, S. W. Peretti, C. W. Davis, and R. C. Boucher. Coordinated clearance of periciliary liquid and mucus from airway surfaces. J. Clin. Invest., 102(6) :1125–1131, 1998.

[85] B. Mauroy, C. Fausser, D. Pelca, J. Merckx, and P. Flaud. Toward the modeling of mucus draining from the human lung : role of the geometry of the airway tree. Phys. Biol., 8(5) :056006, 12, 2011.

[86] S. M. Mitran. Metachronal wave formation in a model of pulmonary cilia. Comput. Struct., 85(11-14) :763–774, 2007.

[87] J. A. Nadel. New approaches to regulation of fluid secretion in airways. Chest, 80(6 Suppl) :849–851, 1981.

[88] J. A. Nitsche and A. H. Schatz. Interior estimates for Ritz-Galerkin methods. Math. Comp., 28 :937–958, 1974.

[89] D. Pavia, J. E. Agnew, J. R. Bateman, N. F. Sheahan, R. K. Knight, W. F. Hendry, and S. W. Clarke. Lung mucociliary clearance in patients with Young's syndrome. Chest, 80(6) :892–895, 1981.

[90] M. Pedersen, Y. Sakakura, B. Winther, S. Brofeldt, and N. Mygind. Nasal mucociliary transport, number of ciliated cells, and beating pattern in naturally acquired common colds. Eur. J. Respir. Dis. Suppl., 128 :355–365, 1983.

[91] M. Pedersen and G. Stafanger. Bronchopulmonary symptoms in primary ciliary dyskinesia. A clinical study of 27 patients. Eur. J. Respir. Dis. Suppl., 127 :118–128, 1983.

[92] E. Puchelle, J. M. Zahm, and P. Sadoul. Mucociliary frequency of frog palate epithelium. Am. J. Physiol., 242(1) :C31–C35, 1982.

[93] R. Rannacher and B. Vexler. A priori error estimates for the finite element discretization of elliptic parameter identification problems with pointwise measurements. SIAM J. Control Optim., 44(5) :1844–1863, 2005.

[94] S. M. Ross and S. Corrsin. Results of an analytical model of mucociliary pumping. J. Appl. Physiol., 37(3) :333–340, 1974.

[95] M. J. Sanderson and E. R. Dirksen. A versatile and quantitative computer-assisted photoelectronic technique used for the analysis of ciliary beat cycles. Cell Motil., 5 :267–292, 1985.

[96] M. J. Sanderson and M. A. Sleigh. Ciliary activity of cultured rabbit tracheal epithelium : beat pattern and metachrony. J. Cell Sci., 47(1) :331–347, 1981.

[97] A. H. Schatz and L. B. Wahlbin. Maximum norm estimates in the finite element method on plane polygonal domains. II. Refinements. Math. Comp., 33(146) :465–492, 1979.

[98] E. E. Schneeburger. The integrity of the air-blood barrier. In J. D. Brain, D. F. Proctor, and L. M. Reid, editors, Respiratory defense mechanisms. Part II, pages 687–708. New York : Marcel Dekker, 1977.

[99] L. R. Scott. Finite element convergence for singular data. Numer. Math., 21 :317–327, 1973/74.

[100] L. R. Scott and S. Zhang. Finite element interpolation of nonsmooth functions satisfying boundary conditions. Math. Comp., 54(190) :483–493, 1990.

[101] W. Sharpey. Cilia. In R. B. Todd, editor, Cyclopaedia of anatomy and physiology, pages 606–638. London, Sherwood, Gilbert, and Piper, 1835.

[102] M. A. Sleigh. The biology of cilia and flagella. International series of monographs on pure and applied biology : Division, Zoology. Pergamon Press, 1962.

[103] M. A. Sleigh. Movement and coordination of tracheal cilia and the relation of these to mucus transport. Cell Motil., 2 :19–24, 1982.

[104] M. A. Sleigh. Ciliary activity in the respiratory tract and the effects of tobacco smoke. In G. Cumming and G. Bonsignore, editors, Smoking and the Lung, Ettore Majorana International Science Series, pages 333–351. Springer US, 1984.

[105] M. A. Sleigh, J. R. Blake, and N. Liron. The propulsion of mucus by cilia. Am. Rev. Respir. Dis., 137(3) :726–741, 1988.

[106] D. J. Smith, E. A. Gaffney, and J. R. Blake. Discrete cilia modelling with singularity distributions : application to the embryonic node and the airway surface liquid. Bull. Math. Biol., 69(5) :1477–1510, 2007.

[107] D. J. Smith, E. A. Gaffney, and J. R. Blake. A viscoelastic traction layer model of muco-ciliary transport. Bull. Math. Biol., 69(1) :289–327, 2007.

[108] D.J. Smith, E.A. Gaffney, and J.R. Blake. Modelling mucociliary clearance. Physiol. Neurobiol., 163(1–3) :178–188, 2008.

[109] B. Spungin and A. Silberberg. Stimulation of mucus secretion, ciliary activity, and transport in frog palate epithelium. Am. J. Physiol., 247(5) :C299–C308, 1984.

[110] J. Sturgess. The mucus lining of major bronchi in the rabbit lung. Am. Rev. Respir. Dis., 115 :819–827, 1977.

[111] R. Temam. Navier-Stokes equations. AMS Chelsea Publishing, Providence, RI, 2001.

[112] L. B. Wahlbin. Local behavior in finite element methods. In Handbook of numerical analysis, Vol. II, Handb. Numer. Anal., II, pages 353–522. North-Holland, Amsterdam, 1991.

[113] L. B. Wahlbin. Superconvergence in Galerkin finite element methods, volume 1605 of Lecture Notes in Mathematics. Springer-Verlag, Berlin, 1995.

[114] A. Wanner. Clinical aspects of mucociliary transport. Am. Rev. Respir. Dis., 116(1) :73–125, 1977.

[115] A. Wanner. Alteration of tracheal mucociliary transport in airway disease : effect of pharmacologic agents. Chest, 80(6 Suppl) :867–870, 1981.

[116] F. D. Warner. The fine structure of the ciliary and flagella axoneme. In M. A. Sleigh, editor, Cilia and flagella, pages 11–37. London : Academic Press, 1974.

[117] E. R. Weibel. Morphometry of the human lung. Academic Press, 1963.

[118] E. R. Weibel, B. Sapoval, and M. Filoche. Design of peripheral airways for efficient gas exchange. Physiol. Neurobiol., 148(1-2) :3–21, 2005.

[119] M. Wirschell, H. Olbrich, C. Werner, D. Tritschler, R. Bower, W. S. Sale, N. T. Loges, P. Pennekamp, S. Lindberg, U. Stenram, B. Carlén, E. Horak, G. Köhler, P. Nürnberg, G. Nürnberg, M. E. Porter, and H. Omran. The nexin-dynein regulatory complex subunit DRC1 is essential for motile cilia function in algae and humans. Nat. Genet., 45(5) :262–268, 2013.

[120] C. H. Wolters, H. Köstler, C. Möller, J. Härdtlein, L. Grasedyck, and W. Hackbusch. Numerical mathematics of the subtraction method for the modeling of a current dipole in EEG source reconstruction using finite element head models. SIAM J. Sci. Comput., 30(1) :24–45, 2007/08.